Mémoire pour l'obtention de

l'Habilitation à Diriger les Recherches

présenté par

**Stéphane Pleutin**

à l'Université de Lille 1

Spécialité : Physique

---

# Courant, bruit et relaxation dans des dispositifs à base de matériaux organiques en couches minces.

---

Composition du jury

| | |
|---|---|
| Prof. G. Dambrine | (Président) |
| Dr. J. Cornil | (Rapporteur) |
| Dr. C. Godet | (Rapporteur) |
| Prof. S. Roche | (Rapporteur) |
| Prof. G.-L. Ingold | (Examinateur) |
| Dr. D. Vuillaume | (Tuteur) |

Soutenance le 5 décembre 2011

**Remerciements**

Je voudrais remercier Dominique Vuillaume, le tuteur de ce travail, pour m'avoir accueilli dans son groupe et pour toutes ces années de collaboration fructueuse qui ont permis de concrétiser ce mémoire. Un énorme merci également à mes compères expérimentateurs : Nicolas Clément et Fabien Alibart, sans lesquels rien de ce mémoire n'aurait existé, mais aussi David Guérin, Stéphane Lenfant, Kamal Lmimouni, Damien Zander, Bruno Grouiez et Romuald Ledru qui y ont tous contribué. Enfin, merci à tous les membres du groupe NCM pour cette ambiance de bonne camaraderie mais, toujours, studieuse.

# Sommaire

Ce mémoire repose sur les articles suivants qui seront référencés dans le texte par le nombre romain correspondant.

I **The electrostatic potential profile along a biased molecular wire : A model quantum-mechanical calculation**,
S. Pleutin, H. Grabert, G-L. Ingold, et A. Nitzan,
J. Chem Phys. 118, 3756 (2003).

II **1/ $f^{\gamma}$ tunnel current noise through Si-bound alkyl monolayers**,
N. Clément, S. Pleutin, O. Seitz, S. Lenfant, et D. Vuillaume,
Phys. Rev. B 76, 205407 (2007).

III **Relaxation dynamics in covalently bounded organic monolayers on silicon**,
N. Clément, S. Pleutin, D. Guérin, et D. Vuillaume,
Phys. Rev. B 82, 035404 (2010).

IV **Molecular relaxation dynamics in organic monolayer junctions**,
S. Pleutin, N. Clément, D. Guérin, et D. Vuillaume,
Phys. Rev. B 82, 125436 (2010).

V **Low frequency dielectric loss of metal/insulator/organic semiconductor junctions in ambient conditions**,
R. Ledru, S. Pleutin, B. Grouiez, D. Zander, H. Bejbouji, K. Lmimouni, et D. Vuillaume,
Org. Electron. (2012) accepté pour publication.

VI **An organic nanoparticle transistor behaving as a biological synapse**,
F. Alibart, S. Pleutin, D. Guérin, C. Novembre, S. Lenfant, K. Lmimouni, C. Gamrat, et D. Vuillaume,
Adv. Funct. Mater. 20, 330 (2009).

VII **A memristive nanoparticle/organic hybrid synapstor for neuro-inspired computing**,
F. Alibart, S. Pleutin, O. Bichler, C. Gamrat, T. Serrano-Gotarredona, B. Linares-Barranco, et D. Vuillaume,
Adv. Funct. Mater. 22, 609 (2012).

## 1. Introduction.

Les travaux présentés dans ce mémoire concernent certains aspects de l'électronique moléculaire et de l'électronique organique. Ces domaines diffèrent, tout d'abord, par l'échelle spatiale des composants - moléculaire voire atomique pour le premier, macroscopique pour le deuxième – et surtout par leurs thématiques. Le but de l'électronique moléculaire est de réaliser des fonctions en façonnant les molécules ou en les assemblant de façon adéquate. Celui de l'électronique organique est de réaliser des composants traditionnels (transistors, diodes, diodes électroluminescentes,…) mais en bénéficiant des propriétés particulières des matériaux organiques, plastiques, par exemple.

Par contre, ils ont en commun certains désavantages : les composants organiques présentent de grandes dispersions dans leurs caractéristiques qui, de plus, peuvent ne pas être stables au cours du temps. D'un côté, nous cherchons à identifier les origines physiques ou chimiques de ces fluctuations dans les performances afin de pouvoir y remédier. Pour cela nous utilisons diverses techniques peu communes dans ces domaines comme l'étude du bruit de courant, de l'admittance complexe et des mesures de relaxation de courants et de capacités en temps réel. Une grande partie de notre travail consiste à développer des méthodes et concepts afin d'analyser les résultats de ces expériences. D'un autre côté, nous cherchons à pallier les effets néfastes de ces défauts en considérant un domaine d'application directement inspiré de la biologie, celui des composants neuromorphiques. Dans les réseaux de neurones, pourvu que les connections entre composants soient nombreuses, le dispositif s'adapte de façon dynamique pour corriger les éventuelles défections.

Ce mémoire est divisé en trois parties Dans la première partie nous analysons un système idéal : une jonction où une molécule unique est contactée à deux électrodes métalliques. Nous étudions la façon dont le potentiel électrostatique y est écranté. La deuxième partie est le cœur de ce mémoire. Des modèles y sont proposés pour analyser des expériences de courant électrique, de bruit de courant électrique et de spectroscopie d'admittance. Deux types de jonctions capacitives y sont étudiés. Dans la première, le diélectrique est une monocouche de molécules alcanes. Dans la deuxième un film mince organique (pentacène) est inséré dans une structure classique Métal/Isolant/Métal. Dans la dernière partie nous abordons le domaine des composants neuromorphiques. Nous y analysons un composant élaboré dans notre groupe (le NOMFET) en insistant sur des analogies avec certaines synapses biologiques.

# Partie I :

# Dispositifs organiques idéaux.

## 2. Jonction métal/molécule/métal : aspects électrostatique.

Ce travail se réfère à une situation idéale où une molécule unique est contactée à deux électrodes métalliques. Elle pose des problèmes conceptuels importants notamment lorsque nous voulons calculer le courant électrique au travers d'une telle jonction.[1] De multiples réalisations expérimentales correspondent à cette situation utilisant des techniques variées comme celles des jonctions brisées[2-4] ou l'utilisation d'un microscope à force atomique.[5]

*Motivation*.
Calculer le courant électrique au travers d'un objet nanométrique tel qu'une molécule est un problème théorique d'une très grande complexité. Nous n'avons pas cherché à aborder ce problème mais nous nous sommes plutôt concentrés sur l'écrantage du potentiel électrostatique, imposé par les électrodes métalliques, au travers du système moléculaire. Est-il ou non fortement écranté ? C'est une question cruciale car l'intensité du courant en découle en grande partie. Ceci a été montré, par exemple, à l'aide d'un modèle semi-empirique par le groupe de Supriyo Datta.[6,7]

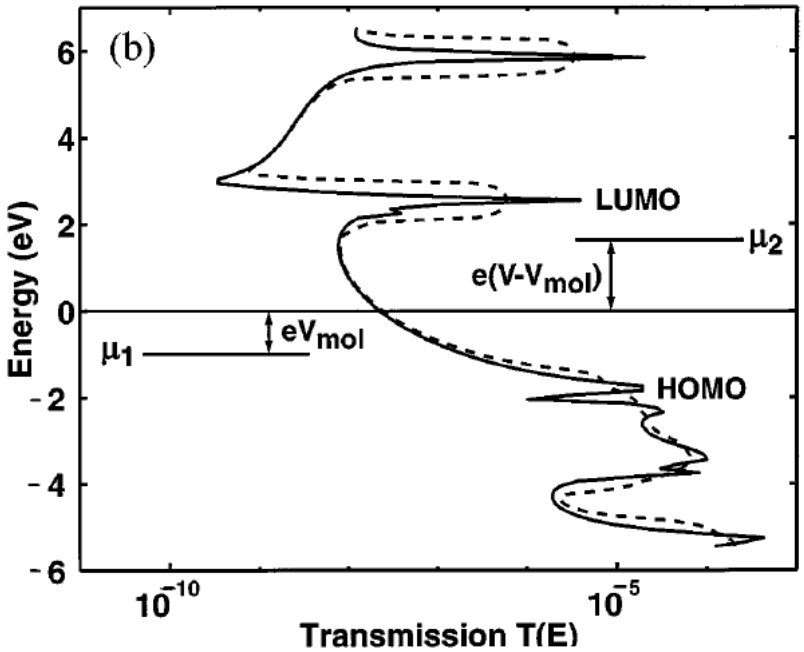


**Figure 1** : Exemple de coefficient de transmission moléculaire calculé à partir des fonctions d'onde de la molécule obtenues à l'aide d'une méthode semi-empirique. Les potentiels chimiques des électrodes délimitent la zone de $T$(E) contribuant au courant. Figure extraite de la Ref. (6).

Une molécule est considérée entre deux électrodes métalliques, *1* et *2*. Le courant est calculé à l'aide d'une expression de type Landauer – supposant un transport de charges purement cohérent à travers tout le dispositif

$$I = \frac{2e}{h}\int_{-\infty}^{+\infty} dE\, T(E)\left[f(E-\mu_1) - f(E-\mu_2)\right]. \qquad (1)$$

Dans cette expression, $T(E)$ est le coefficient de transmission d'un électron d'énergie $E$ d'une électrode à l'autre, calculé à partir de la fonction d'onde de la molécule obtenue à l'aide de la méthode semi-empirique de Hückel étendue. Un exemple de tel coefficient (extrait de la Ref. (6)) est donné dans la figure 1. $f$ est la fonction de Fermi-Dirac qui contrôle la probabilité d'occupation des états électroniques d'énergie $E$ dans les électrodes *1* et *2*, de part et d'autre de la molécule, de potentiel chimique $\mu_1$ et $\mu_2$. Avec l'expression (1) le courant est donné essentiellement (rigoureusement à température nulle) par l'intégrale de $T(E)$ entre $\mu_1$ et $\mu_2$.

Lorsqu'une tension, $V$, est appliquée au dispositif, le potentiel électrostatique au travers de la molécule est modifié ce qui perturbe, en principe, les fonctions de distribution des électrodes et le coefficient de transmission. Ce problème complexe est modélisé simplement dans ce travail[6,7] : (i) le coefficient de transmission est conservé identique et (ii) les changements du potentiel électrostatique sont entièrement répercutés sur les potentiels chimiques en introduisant un paramètre effectif, $\eta$, supposant qu'il est écranté essentiellement aux interfaces,

$$\mu_1 = E_F - \eta eV \text{ et } \mu_2 = E_F + (1-\eta)eV \ . \qquad (2)$$

$E_F$ est l'énergie de Fermi à l'équilibre thermodynamique. Avec cette modélisation, le courant $I$ est fortement influencé par le paramètre $\eta$ qui contrôle la façon dont le potentiel est écranté.

Pour connaitre les détails des modifications du potentiel électrostatique induites par une tension, il est nécessaire de considérer l'interaction électron-électron. Au moment où nous avons entrepris ce travail, cette question était controversée. Des calculs ab-initio prévoient un potentiel électrostatique très proche de la rampe linéaire qu'il y aurait dans le vide : l'écrantage du potentiel électrostatique serait donc peu efficace dans les molécules.[8,9] Au contraire, un calcul basé sur un Hamiltonien de liaisons fortes de type Hückel, couplé à l'équation de Poisson prévoit l'inverse : le potentiel électrostatique serait fortement écranté et la majorité du potentiel chuterait aux interfaces si bien que le potentiel dans la molécule serait essentiellement constant.[10] Cependant, l'équation de Poisson utilisée dans ce deuxième cas est réduite à une dimension i.e. elle est résolue sur l'axe de la molécule, nous pensons cette approximation non justifiée et à l'origine de ces différentes prédictions (Cf. Figure 2).[11] Notre motivation a été de clarifier ce problème. Le travail résumé ici est le sujet de la référence I.

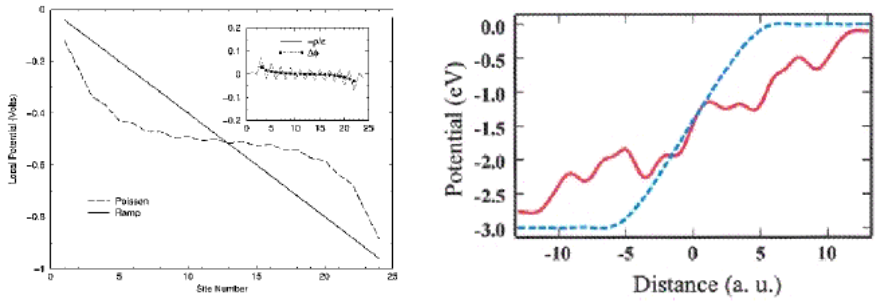


**Figure 2** : Potentiel électrostatique en fonction de la position dans la molécule. A gauche : résultat de la Ref. (10) basée sur la résolution de l'équation de Poisson 1D ; le potentiel est fortement écranté aux interfaces. A droite résultat d'un calcul ab-initio montrant un potentiel proche de la rampe linéaire (Ref. (9)).

*Modèle*.
Pour étudier ce problème nous adoptons une approche comparable à celle de la Ref. (10) mais en considérant une équation de Poisson non pas unidimensionnelle mais tridimensionnelle comme elle doit l'être.[11] Ce simple raffinement est suffisant pour modifier radicalement les conclusions. Nous considérons une molécule modélisée comme un réseau unidimensionnel (1D) à N sites entre deux électrodes métalliques macroscopiques supposées à l'équilibre thermodynamique et décrites par les potentiels chimiques $\mu_l$ et $\mu_r$ (voir Figure 3). Nous cherchons tout d'abord à écrire un Hamiltonien de type liaisons fortes pour décrire les propriétés électroniques de notre système. Pour cela une fonction d'onde électronique est attachée à chaque site $n$=1,…, $N$

$$\phi_n(r) = A_s x^s \exp\left(-\alpha\left(x^2 + y^2 + (z - z_n)^2\right)\right), \tag{3}$$

qui peut décrire une orbitale s ($s$=0) ou p ($s$=1), choisie suivant le type de molécule considérée. Le coefficient de normalisation varie $A_0=(2\alpha/\pi)^{3/4}$ et $A_1=2(2/\pi)^{3/4}\alpha^{5/4}$. Le paramètre $\alpha$ contrôle l'extension spatiale des orbitales. $z_n=d+(n-1)a$, où $d$ est la distance entre molécule et électrode supposée identique à droite et à gauche, $a$ est la distance entre sites moléculaires (cf. Figure 3).

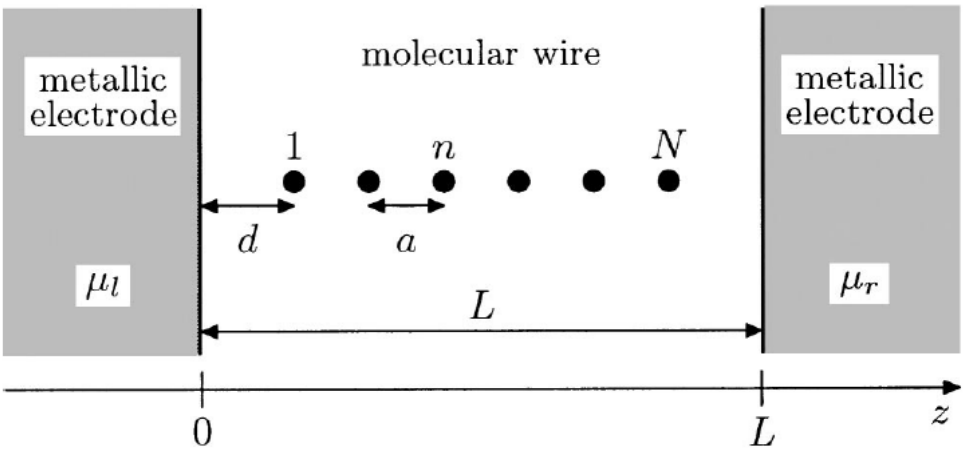


**Figure 3** : Modèle d'une molécule vue comme un réseau 1D à N sites atomiques placée entre deux électrodes métalliques, de potentiels chimiques $\mu_l$ et $\mu_r$, dont les surfaces sont supposées infinies.

Nous introduisons ensuite l'opérateur de Coulomb prenant en compte les conditions aux limites imposées par les deux électrodes métalliques

$$\varphi(\vec{r},\vec{r}') = \sum_{p=-\infty}^{+\infty}\left[\varphi_0(\vec{r} + 2pL\hat{z},\vec{r}') - \varphi_0(2pL\hat{z} - \vec{r},\vec{r}')\right], \tag{4}$$

où $L$ est la distance entre électrodes (cf. Figure 3), $\hat{z}$ est le vecteur unitaire sur l'axe de la molécule et $\varphi_0$ est l'opérateur de Coulomb

$$\varphi_0(\vec{r},\vec{r}') = \frac{U}{|\vec{r}-\vec{r}'|}, \tag{5}$$

pour lequel nous avons introduit un paramètre $U$ prenant en compte l'écrantage du potentiel coulombien par les électrons des couches internes.

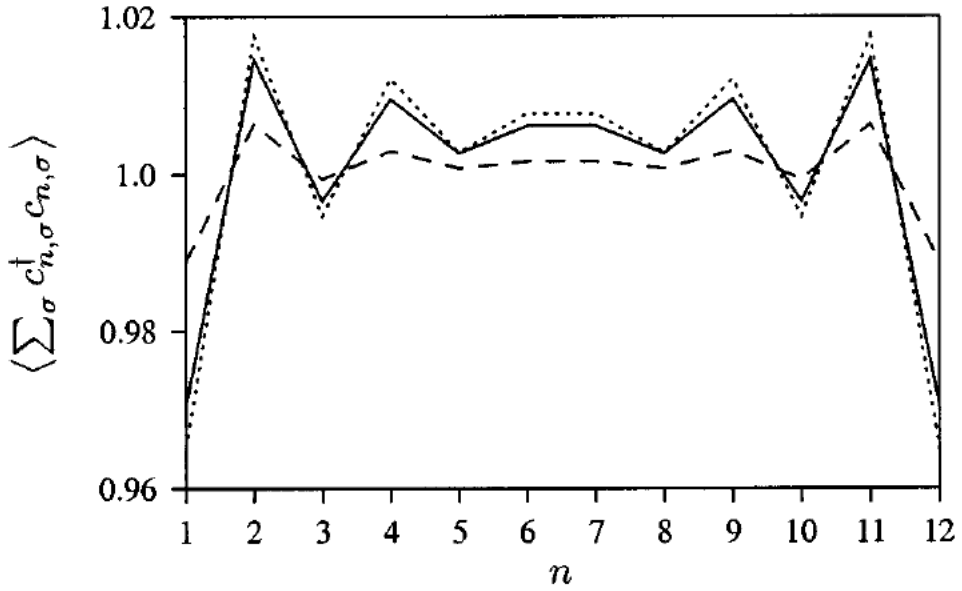


**Figure 4** : Densité électronique pour une chaîne de 12 sites pour $s$=1, $\alpha$ = 4.5/$a^2$ et $U = t$ ($t$=1). La courbe en trait plein est le résultat exact et la courbe en pointillée le résultat de l'approximation HF pour le cas $d$=2$a$. La courbe hachurée est le résultat exact pour le cas sans électrode métallique, $d \rightarrow +\infty$.

Les différents termes de l'Hamiltonien de liaisons fortes nécessaires pour décrire la molécule sont ensuite générés en considérant une approximation classique dite ZDO (pour « Zero Differential Overlap ») qui ne consiste à conserver, au plus, que les intégrales à deux centres.[12] L'Hamitonien s'écrit en seconde quantification

$$H = \sum_{n,\sigma}(\varepsilon_n + V_n)C^+_{n,\sigma}C_{n,\sigma} + \sum_{n,\sigma} t\left(C^+_{n+1,\sigma}C_{n,\sigma} + h.c.\right) + \frac{1}{2}\sum_{n,n',\sigma,\sigma'} U_{n,n'}C^+_{n,\sigma}C^+_{n',\sigma'}C_{n',\sigma'}C_{n,\sigma}\ , \tag{6}$$

$C^+_{n,\sigma}$ ($C_{n,\sigma}$) sont les opérateurs de création (d'annihilation) d'un électron avec un spin $\sigma$ dans l'orbital $\phi_n$.

$$V_n = \mu_l + \frac{\mu_r - \mu_l}{L} z_n \quad , \tag{7}$$

est le potentiel électrostatique au site $n$,

$$\varepsilon_n = -\sum_{m=1}^{N} \int d^3\vec{r} \left|\phi_n(\vec{r})\right|^2 \varphi(\vec{r}, z_m\hat{z}) \quad , \tag{8}$$

est le terme d'attraction dû aux noyaux atomiques situé en (0, 0, $z_m$) et

$$U_{n,n'} = \sum_{m=1}^{N} \int d^3\vec{r} \int d^3\vec{r}' \left|\phi_n(\vec{r})\right|^2 \varphi(\vec{r},\vec{r}') \left|\phi_{n'}(\vec{r}')\right|^2 \quad , \tag{9}$$

est le terme de répulsion coulombienne entre deux électrons localisés sur les orbitales $\phi_n$ et $\phi_{n'}$. $t$ est l'intégrale de transfert plus proches voisins qui ne peut pas être directement évaluée avec nos approximations (approximation ZDO). Pour les molécules conjuguées nous pouvons considérer $t \approx$ -2.5eV et U/t ≈ 1,…, 4.[13] Nous déterminons ensuite la structure électronique de la molécule, avec ou sans potentiel appliqué, à l'aide de diagonalisations exactes ou dans l'approximation de Hartree-Fock (HF).[12]

Dans cette dernière approximation nous remplaçons l'Hamiltonien exact (Eq. (6)) par un Hamiltonien effectif à une particule en résolvant de façon auto-cohérente les équations traditionnelles de Hartree-Fock.[12,14] Nous obtenons formellement

$$H_{eff} = \sum_{n,\sigma} \varepsilon_n(V) C^+_{n,\sigma} C_{n,\sigma} + \sum_{n,n',\sigma} t_{n,n'}(V) \left(C^+_{n,\sigma} C_{n',\sigma} + h.c.\right). \tag{10}$$

Le premier terme, $\varepsilon_n(V)$, est le potentiel effectif sur le site $n$, le deuxième terme, $t_{n,n'}$, l'intégrale de transfert du site $n$ vers le site $n'$, transfert qui peut être de longue portée.

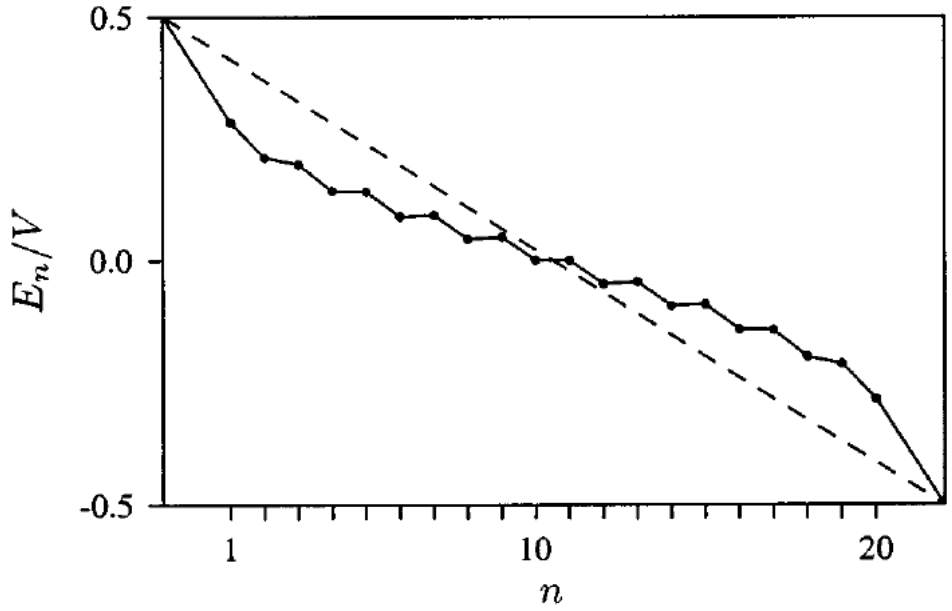


**Figure 5** : Potentiel électrostatique pour une chaîne de 20 sites pour $s$=1, $\alpha$ = 4.5/$a^2$, $U = t$ ($t$=1) et $d$=2$a$ dans l'approximation HF. La courbe hachurée est le potentiel non écranté.

*Densité électronique. Cas V = 0.*

Nous considérons une molécule de 12 sites à demi-remplissage i.e. avec un électron par site. Dans ce cas sans potentiel, nous analysons la densité électronique à l'équilibre. Des exemples sont montrés sur la Figure 4. Nous remarquons que la densité n'est pas uniforme mais que les

électrons ont tendance à se concentrer au centre de la chaîne. Cette densité est accompagnée d'importantes oscillations de Friedel. D'autre part, nous pouvons remarquer que les charges images ont un impact sur l'amplitude des oscillations. Finalement, l'approximation de Hartree Fock constitue une bonne approximation pour décrire la densité ; nous avons testé cette approximation jusqu'à de relativement fortes interactions ($U$=4$t$).

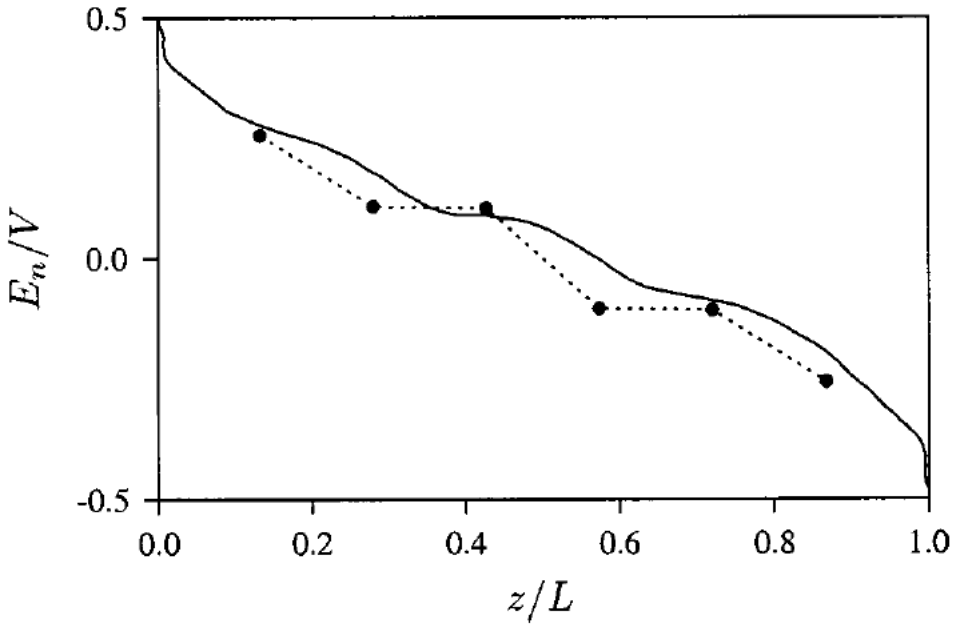


**Figure 6** : Potentiel électrostatique pour une chaîne de 6 sites pour $s$=0, $\alpha$ = 4.5/$a^2$, $U = t$ ($t$=1eV) et $d$=0.9$a$ dans l'approximation HF (points). La courbe en trait plein est le résultat obtenu à l'aide de calculs ab-initio (ref. (9)).

*Potentiel électrostatique. Cas $V \neq 0$.*
Nous considérons une chaîne plus longue, N = 20, tout comme dans la référence (10). Nous utilisons l'approximation de Hartree-Fock et nous nous intéressons au potentiel électrostatique écranté, $E_n(V)$, défini comme

$$E_n(V) = \varepsilon_n(V) - \varepsilon_n(0). \qquad (11)$$

Un exemple est montré sur la Figure 5. Nous pouvons souligner (i) que le potentiel électrostatique est pauvrement écranté et reste très proche de la rampe linéaire (potentiel sans molécule), (ii) que d'importantes oscillations de Friedel accompagnent ce potentiel électrostatique.

Nous avons d'autre part comparé les résultats de notre modèle avec les calculs ab-inito de la référence (9) pour une chaîne de six atomes d'or. Nous n'avons pas recherché à reproduire ces résultats ; nous nous sommes contentés d'utiliser des paramètres raisonnables pour ce système. L'accord trouvé est néanmoins bon (cf. figure 6).

Malgré que notre modèle soit très proche de celui employé dans la Réf. (10), nos conclusions différent radicalement et sont en accord avec les résultats de calculs ab-initio. La seule différence notable avec cette référence réside dans le traitement de l'équation de Poisson : l'approximation utilisée dans la Ref (10) ne peut se justifier que dans le cas où les dimensions

de la molécule perpendiculairement à son axe seraient très grandes devant la longueur caractéristique d'écrantage.[11] Hors, dans ces directions les molécules sont de taille atomique rendant l'approximation douteuse.

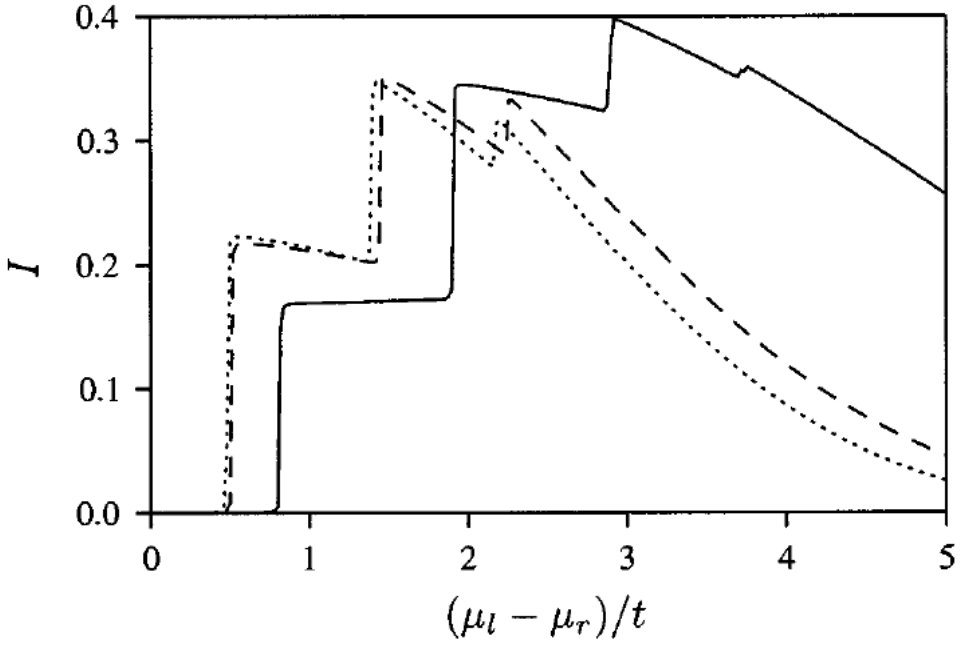


**Figure 7** : Caractéristiques *I-V* pour une chaîne de 12 sites pour *s*=1, $\alpha = 4.5/a^2$ et *d*=2*a* pour U/t = 0 (courbe pointillée), 0.1 (courbe hachurée) et 1 (courbe pleine). Le courant est donné en unité de $(2e/\pi\hbar)\ \Delta^2_0/t$.

*Courant électrique. Cas de très mauvais contacts.*
Dans le cas où la molécule est très mal contactée aux électrodes, le courant peut s'écrire très simplement

$$I = \frac{2e}{\pi\hbar}\Delta_0^2 \int_{\mu_r}^{\mu_l} dE \left| G_{1N}^0(E,V) \right|^2 \quad , \tag{12}$$

où $G_{1N}^0(E,V)$ est l'élément de matrice de la fonction de Green de la molécule non contactée telle que nous l'avons considérée dans ce travail, $\Delta_0$ est la densité d'état au niveau de fermi en l'absence de potentiel. Les caractéristiques *I-V* obtenues avec l'équation (12) montrent une structure en escalier qui témoigne simplement du spectre discret de la molécule : à chaque nouvelle marche, un niveau moléculaire supplémentaire entre dans la fenêtre d'intégration de l'équation (12). D'autre part, nous observons d'importantes zones de résistances négatives qui s'expliquent naturellement dans le cadre de nos approximations par la localisation des charges à un bout de la chaîne provoquée par un fort champ électrique : l'interaction coulombienne s'oppose à cette localisation et réduit cet effet (cf. Figure 7).

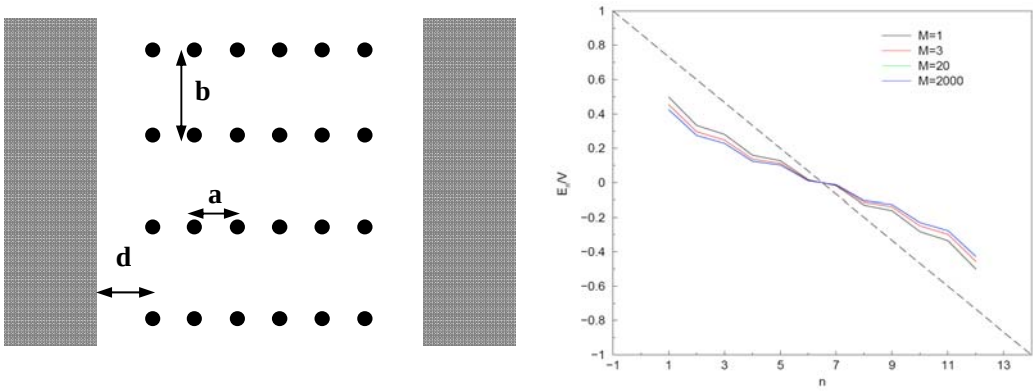


**Figure 8** : A gauche, modèle d'un film mince à $M$ molécules identiques espacées de $b$. A droite, potentiel électrostatique, dans l'approximation HF, pour une chaîne de 12 sites au sein de ce film pour différents nombres de molécules : $M$=1, 3, 20, 2000. Les paramètres de l'Hamiltonien sont $s$=1, $\alpha = 4.5/a^2$, $U = 0.5t$ ($t$=1), $d$=2$a$ et $b$=3$a$.

*Potentiel électrostatique. Cas d'un film.*
Il est des situations où les molécules ne peuvent pas à-priori être considérées comme isolées. C'est le cas, par exemple, des monocouches moléculaires. Nous cherchons à mesurer ici l'influence des interactions coulombiennes intermoléculaires sur les propriétés d'écrantage des molécules. Dans l'approximation HF, nous pouvons étendre nos calculs au cas à plusieurs molécules en introduisant quelques approximations supplémentaires.

Nous considérons un ensemble de $M$ molécules distantes de $b$ (cf. Figure 8). Nous supposons ces molécules suffisamment espacées pour pouvoir négliger les transferts de charges intermoléculaires. Cette approximation est très représentative des situations rencontrées dans la majorité des expériences. La charge dans chaque molécule est ainsi conservée tout au long du calcul. Nous supposons ensuite que chaque molécule de l'ensemble est identique à toutes les autres, c'est-à-dire que la densité électronique est la même dans toutes les molécules, et ceci à chaque étape du calcul. Cette approximation simule la situation rencontrée dans un cristal infini où il est impossible de distinguer une molécule parmi les autres. Cette approximation simplifie grandement les calculs.

Pour mesurer l'impact des interactions intermoléculaires, nous faisons varier le nombre $M$ de molécules et calculons le potentiel électrostatique. Un exemple est montré sur la figure 8 où nous avons fait varier $M$ entre 1 et 2000. Nous constatons (i) que le potentiel reste toujours faiblement écranté et (ii) le potentiel converge très vite avec $M$ vers une forme finale : à partir de $M$=20, les courbes de potentiel se superposent.

Dans le cadre de ces approximations, les molécules du film peuvent être considérées comme isolées.

# Partie II:

# Dispositifs organiques non-idéaux.

## A Monocouches organiques.

Le but de l'électronique moléculaire est de pouvoir façonner des fonctions électroniques à l'aide de la chimie, c'est-à-dire en synthétisant des molécules appropriées ou en assemblant plusieurs molécules de façon adéquate. Les perspectives semblent infinies, permettant les rêves les plus fous depuis le premier exemple théorique de la diode d'Aviram et Ratner.[15] Nous pouvons penser par exemple à des systèmes relativement simples, de type interrupteur en utilisant des molécules capables de changer de conformation sous l'action d'un courant de charges ou de la lumière,[16-20] chaque conformation étant associée à une résistance électrique différente. De tels projets ont déjà été réalisés et de multiples études sont actuellement en cours avec la perspective de réaliser de nouveaux types de mémoires, par exemple.[17-20] Nous pouvons aller au-delà et imaginer des projets plus ambitieux, où des opérations logiques seraient effectuées au sein d'une même molécule synthétisée à cet effet.[21] Nous pouvons aussi envisager d'agencer différentes molécules, de propriétés diverses, en un réseau capable de fonctions intelligentes à l'image du cerveau humain.

Cependant, maitriser un système à l'échelle moléculaire est complexe, l'analyser l'est tout autant. Des problèmes se posent, par exemple, pour contacter les molécules : bien les greffer sur un substrat de façon bien ordonnée, prendre contact avec une électrode métallique sans générer de court-circuit,… Il est difficile ensuite d'avoir une image claire du résultat de ces étapes importantes. Enfin, il est difficile d'identifier avec certitude l'origine des effets observés. Ainsi, des molécules capables de changer de conformation en solution sous l'effet d'une force extérieure, ne le feront pas forcément – ou pas dans les mêmes conditions – lorsqu'elles seront déposées sur une surface. Les raisons pour cela sont multiples : les plus évidentes proviennent des contraintes imposées par l'environnement (les molécules voisines, le substrat, les électrodes,…). Ainsi, le fonctionnement des premiers interrupteurs moléculaires[16] a été finalement identifié comme étant dû à la formation de filaments d'or. Pour pouvoir progresser, il convient de développer des méthodes d'analyse autres que les simples caractéristiques *I-V* communément réalisées.

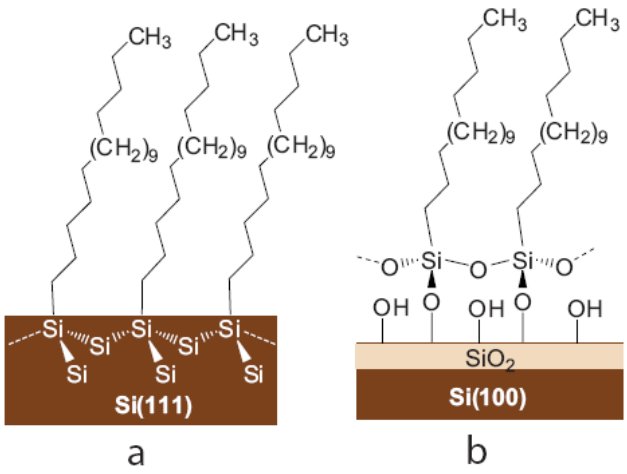


**Figure 9** : Représentations schématiques des monocouches considérées, a) OD sur substrat de silicium dopé et b) OTS sur une fine couche (~ 6 Å) d'oxyde thermique.

Pour cela nous nous concentrons sur des systèmes simples qui sont des monocouches de molécules saturées. D'un point de vue électrique, ce sont des isolants mais elles trouvent un certain nombre d'applications en tant que nanodiélectrique[22-24] ou comme couche d'accroche pour des matériaux plus complexes, en vue, par exemple, d'élaborer des capteurs.[25] Nous considérons deux types de molécules qui diffèrent par leur terminaison : des alcènes que nous greffons directement sur un substrat silicium dopé, et des silanes qui se déposent sur une surface de silicium recouverte d'une faible épaisseur d'oxyde thermique. Nous avons considéré des chaînes de longueur variant entre 12 et 20 atomes de carbone mais nous ne présentons ici que des résultats pour des chaînes de 18 atomes de carbone appelées Octadécènes (OD) et Octadecyltrichlorocilane (OTS). L'axe des molécules fait un angle avec la normale au substrat estimé à 15° pour l'OTS et 30° pour l'OD. Elles sont schématisées sur la Figure 9. Nous avons utilisé des substrats de différents dopages mais seuls des résultats pour des substrats fortement dopés (résistivité ~ 0.01 à 0.5 Ω cm) sont présentés ici. Les protocoles pour obtenir ces différentes monocouches sont bien documentés (Références II et III).

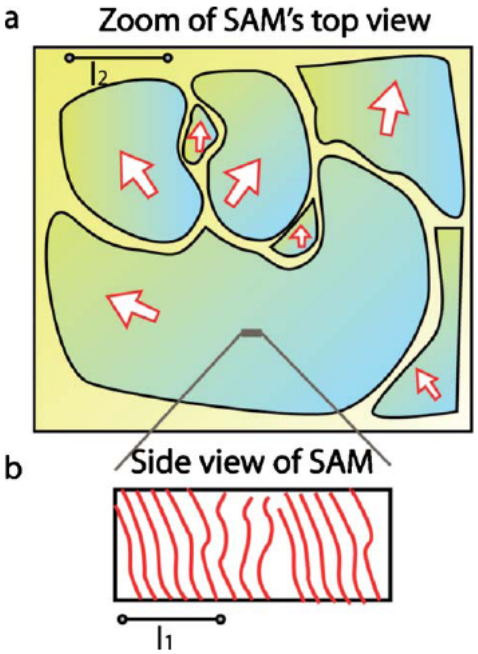


**Figure 10** :a) Structure polycristalline des monocouches où les grains ont une taille caractéristique $l_2$ ~ 1µ. Les flèches représentent la projection du vecteur bout à bout joignant les deux extrémités des molécules sur le plan du substrat. b) Organisation locale de la monocouche avec une longueur de cohérence $l_1$ ~ 45 Å.

Ces différentes monocouches ont été analysées par des expériences de diffraction X qui révèlent qu'elles sont compactes : des volumes moyens par molécule de 20 Å$^2$ pour l'OTS et 25 Å$^2$ pour l'OD sont estimés. Cependant, la longueur de cohérence, $l_1$, dans le plan des monocouches est très faible, de l'ordre de 45 Å, ce qui suggère une organisation locale comparable à celle trouvée dans les liquides.[26,27] D'autre part, les monocouches se forment simultanément à partir de différentes zones du substrat. Du fait de l'invariance par rotation autour de l'axe perpendiculaire au substrat, les molécules seront orientées différemment dans

chacune de ces zones : il en résulte une structure polycristalline présentant des grains d'une taille, $l_2$, de l'ordre du micron. Un schéma de cette organisation est présenté sur la Figure 10.

Les jonctions capacitives sont réalisées à partir de ces monocouches en prenant des contacts métalliques sur le dessus, le plus souvent en évaporant des électrodes d'aluminium à travers un masque mécanique où en déposant une goutte de mercure. Lorsque nous mesurons, sous atmosphère contrôlée, le courant tunnel et la capacité d'un ensemble de jonctions obtenues sur le même substrat, nous mettons en évidence une grande dispersion. Ceci est illustré sur la figure 11. Le courant tunnel varie sur quatre ordres de grandeur ! Nous notons cependant une corrélation entre capacité et courant : plus la valeur de la capacité est grande plus le courant tunnel est intense. L'ensemble des études présentées ici, courant tunnel, bruit de courant tunnel et admittance, ont été entreprises en vue de trouver une origine à ces dispersions.

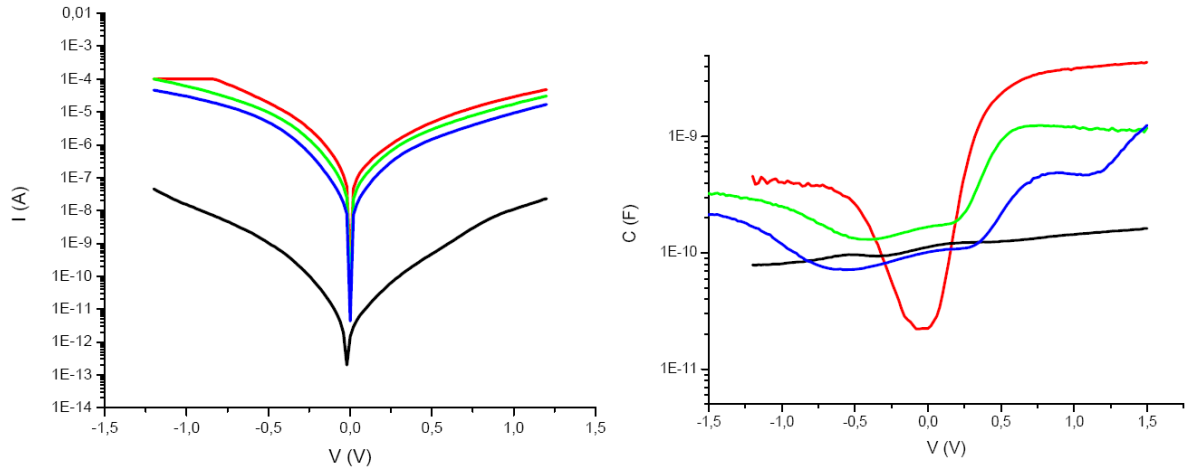


**Figure 11** : Exemples de caractéristiques *I-V* (à gauche) et de capacités (à droite) de différentes jonctions (OD) de même taille, obtenues sur une même plaquette.

## 3. Courant tunnel. Effets de défauts localisés aux interfaces et effets Electrostatiques.

Calculer le courant électronique dans des nanostructures est un problème d'une grande complexité. Nous n'avons qu'effleuré ce problème dans le chapitre précédent où nous nous sommes essentiellement concentrés sur le problème de l'écrantage du champ électrique au travers d'une molécule unique (Référence I). Le courant électrique n'a été calculé que dans une limite très simple. Aller au-delà nécessiterait de très gros investissements (utilisation du formalisme des fonctions de Green hors équilibre par exemple) d'autant plus que, concernant les jonctions à base de molécules saturées, peu d'effort ont été entrepris dans ce sens simplement parce que ces molécules n'offrent que peu d'intérêt concernant le transport électronique : ce sont de simples jonctions tunnel.[28] D'autre part, notre motivation première est de comprendre l'origine de la dispersion en courant (Figure 11). Dans ce contexte, il semble préférable, dans un premier temps, de se restreindre à des modèles et méthodes élémentaires.

*Modèle de Simmons*.
La plupart des courbes expérimentales sont interprétées à l'aide de modèles de courant tunnel simples, le plus populaire étant celui de J.G. Simmons (1963)[29] qui donne pourtant, dans la majorité des cas, un accord pauvre avec l'expérience. Ce modèle est basé sur une approche semi-classique (WKB) du courant tunnel avec l'ambition de considérer des potentiels de forme très générale. Son principal mérite est certainement de proposer une expression analytique du courant. Dans le cas d'une barrière rectangulaire et une tension appliquée $V$ la densité de courant s'écrit

$$J_{Simmons}(V)=\frac{e}{4\pi^2\hbar l^2}\left[\left(W-\frac{eV}{2}\right)\exp\left(-\alpha\sqrt{W-\frac{eV}{2}}\right)-\left(W+\frac{eV}{2}\right)\exp\left(-\alpha\sqrt{W+\frac{eV}{2}}\right)\right] \quad (13)$$

avec $\alpha = 2l\sqrt{2m}/\hbar$, $l$ l'épaisseur de barrière, $W$ sa hauteur, $m$ la masse effective des charges et $e$ la charge électronique. Dans nos cas, l'épaisseur de barrière est fixée par la longueur des molécules pour l'OD, l'épaisseur d'oxyde doit être rajoutée dans le cas de l'OTS. La hauteur de barrière est fixée par la différence entre l'énergie de la première orbitale moléculaire accessible (LUMO) et l'énergie de Fermi des électrodes à l'équilibre. Cette expression est dans la grande majorité des cas incapable de reproduire les résultats expérimentaux sur la gamme complète de tension explorée (0-1V). Il n'existe pas de consensus sur la valeur des paramètres et en particulier sur la hauteur de barrière, $W$, qui peut varier suivant les auteurs entre 1.5 eV et 4.5 eV, environ.[30,31]

On peut noter un changement de comportement dans l'expression (13) suivant la gamme de tension considérée : dans la limite où $V \rightarrow 0$, la densité de courant se réduit à une relation linéaire en $V$

$$J_{Simmons}(V) \propto V\exp\left(-\alpha\sqrt{W}\right), \quad (14)$$

alors que dans la limite où $eV > W$, nous entrons dans le régime de Fowler-Nordheim où nous pouvons écrire

$$J_{Simmons}(V) \propto V^2 \exp\left(-\frac{2\alpha}{3eV} W^{3/2}\right). \qquad (15)$$

Si nous traçons $\ln(J/V^2)$ en fonction de $1/V$ nous obtenons une droite dans le régime de Fowler-Nordheim et une loi en $\ln(1/V)$ dans le régime linéaire. Il a été suggéré récemment d'appliquer cette analyse afin de déterminer la hauteur de barrière.[32,33] Un exemple est donné sur la Figure 12. La hauteur de barrière est déterminée par le minimum de cette courbe. Dans le cas de nos jonctions alcanes, en appliquant cette analyse nous trouvons toujours un minimum mais correspondant à une hauteur de barrière beaucoup trop faible – en désaccord avec le niveau de courant observé. Nous reviendrons brièvement sur cette observation dans la suite.

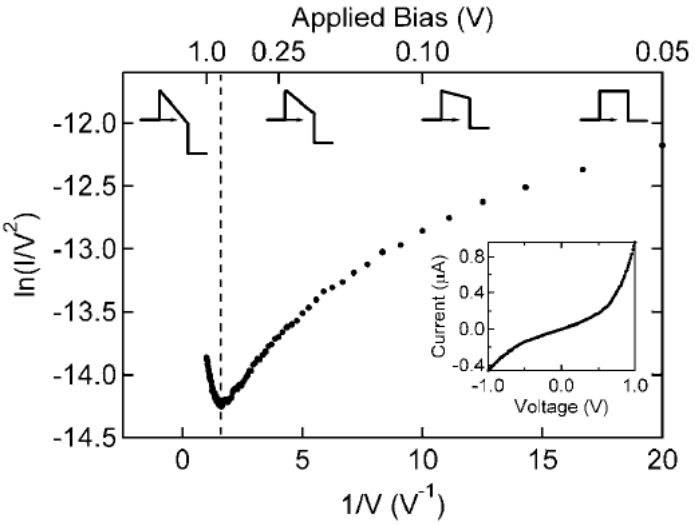


**Figure 12** : Exemple de caractéristique *I-V* issue de la Ref. (32), (moyenne de 100 mesures), d'une jonction Au/Anthracène-thiol/Au. La forme de la courbe est supposée refléter les changements de forme de la barrière. La position du minimum permettrait alors de déterminer la hauteur de barrière.

*Modèle de Tsu-Esaki*.

Le modèle de Simmons est insatisfaisant et il est difficile d'aller au-delà tout en le conservant comme point de départ. Aussi, nous nous sommes tournés vers un autre modèle simple, plus malléable i.e. qui permette certaines améliorations. Nous considérons un modèle purement quantique, souvent reconnu comme le modèle de Tsu-Esaki bien qu'il soit apparu avant 1973.[34] C'est un modèle qui entre dans la catégorie des Hamiltoniens tunnel apparus dans les années 1950 et utilisés massivement avec succès.[35] Dans ces approches les électrodes sont considérées comme des réservoirs de charges – ou quasi-particules – définies par leur masse effective. Ces réservoirs sont supposés être à l'équilibre thermodynamique, décrit chacun par un potentiel chimique $\mu_D$, pour le réservoir de droite, $\mu_G$ pour celui de gauche. On écrira dans la suite $\mu_G = \mu$ et $\mu_D = \mu$ + eV, ce qui correspond à la situation expérimentale où nous maintenons une des électrodes à la masse. L'énergie des quasi-particules, ainsi que leur moment, peut s'écrire comme une somme d'une composante transverse et longitudinale caractérisant, l'une les mouvements parallèles aux surfaces des électrodes et l'autre ceux perpendiculairement à ces surfaces. On écrit l'énergie totale $E_T = E_t + E_l$ et le vecteur d'onde

totale $\boldsymbol{k}_T = \boldsymbol{k}_t + \boldsymbol{k}_l$ (les caractères gras signifient que ce sont des vecteurs). Le transfert de charges d'un côté à l'autre de la barrière est supposé élastique : l'énergie est conservée ainsi que la composante transverse du moment. Cette deuxième restriction implique que l'énergie transverse, $E_t$, est aussi conservée durant le processus tunnel. Avec ces hypothèses, le coefficient de transfert d'un électron ne dépend que de son énergie longitudinale et nous pouvons écrire la densité de courant

$$J(V) = \frac{em}{2\pi^2\hbar^3}\int_0^{+\infty} dE_l \int_0^{+\infty} dE_t T(E_l)\left[f_D(E_T) - f_G(E_T)\right]. \qquad (16)$$

$f_{D/G}$ sont les fonctions de Fermi Dirac des réservoirs droite et gauche. L'intégration en $E_t$ peut s'effectuer et on obtient l'équation de Tsu-Esaki (TE), où nous avons omis, pour soulager l'écriture, l'indice $l$

$$J(V) = \frac{emk_B\theta}{2\pi^2\hbar^3}\int_0^{+\infty} dE T(E) \ln\left[\frac{1+e^{\beta(\mu-E)}}{1+e^{\beta(\mu-eV-E)}}\right]. \qquad (17)$$

$\theta$ est la température et $\beta = 1/k_B\theta$ ($k_B$ la constante de Boltzmann). Dans cette formulation, le transfert de charge est cohérent : un électron préserve sa cohérence de phase dans la barrière. Par contre, il la perd instantanément dans les réservoirs qui absorbent son énergie au travers de collisions avec les quasi-particules les constituant. Les réservoirs ne préservent aucun souvenir des électrons transférés.

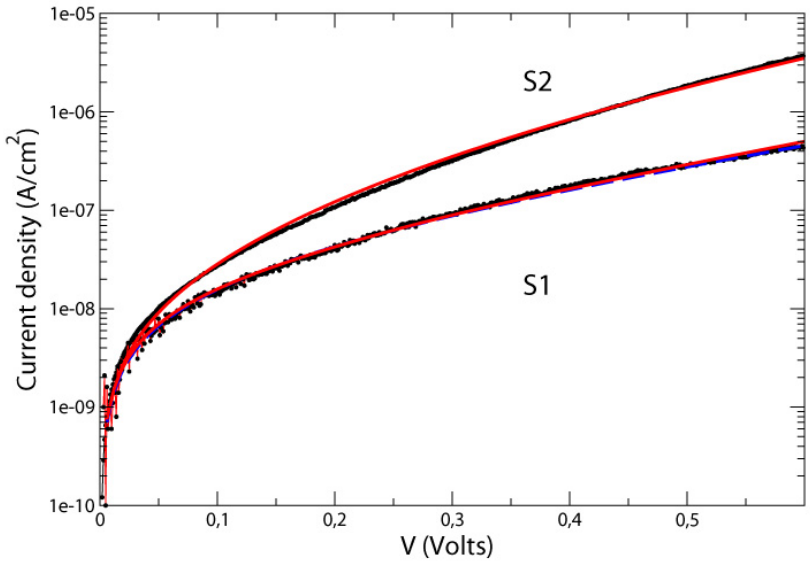


**Figure 13** : Caractéristiques *J-V* de deux jonctions tunnel avec OTS (S1) et OD (S2). Les points sont les résultats expérimentaux, les courbes rouges les résultats obtenus avec le modèle TE. Les paramètres sont pourS1, $W$-$\mu$ = 5.78 eV, $l$=20 nm et $m$=0.131$m_e$ ($m_e$, la masse de l'électron), pour S2, $W$-$\mu$ = 4.7 eV, $l$=26 nm et $m$=0.614$m_e$. La courbe bleue est obtenue avec un modèle incluant des défauts d'interface.

Nous considérons une barrière rectangulaire de hauteur $W$ et de largeur $l$. Nous négligeons les déformations dues au potentiel électrique appliqué ce qui se justifie, à posteriori, par les hauteurs de barrières que nous obtenons, toujours telles que $W >> eV$. Dans l'approche de TE le coefficient de transmission est déterminé en considérant une particule unique, cohérente au travers de toute la structure comme dans l'approche de Simmons. Pour le potentiel choisi, il peut être calculé exactement. Dans le cas où l'énergie longitudinale des électrons est telle que $E < W$, il s'écrit

$$T(E)=\left[1+\left(\frac{k^2+K^2}{2Kk}\right)^2 \sinh^2 Kl\right]^{-1} \text{ où } k=\frac{\sqrt{2mE}}{\hbar} \text{ et } K=\frac{\sqrt{2m(W-E)}}{\hbar}. \tag{18}$$

L'équation de TE (Eq. (17)) avec le coefficient de transmission (18) donne souvent un bon accord avec nos expériences. Deux exemples sont montrés dans la Figure 13, les paramètres obtenus sont donnés dans la légende. Il convient de remarquer que les hauteurs de barrière trouvées sont relativement hautes : celle de l'échantillon S2 est compatible avec des valeurs déjà suggérées, celle de l'échantillon S1 parait trop haute. Nous verrons qu'il est possible d'abaisser cette valeur en employant un modèle introduisant l'effet tunnel assisté par défauts. En utilisant cette expression du courant, nous pouvons à priori traduire les dispersions en courant, telles que celles montrées sur la Figure 11, en distribution de $m$ et $W$, ce qui offrirait un intérêt plutôt limité.

Compte tenu des barrières très hautes que nous obtenons pour nos systèmes, nous pouvons simplifier les expressions (17) et (18) sans changer les résultats. (i) Nous considérons l'équation de Tsu-Esaki à température nulle ($W >> k_B\theta$)

$$J(V)\approx\frac{em}{2\pi^2\hbar^3}\left(\int_0^{\mu+eV} dET(E)(\mu+eV-E)-\int_0^{\mu} dET(E)(\mu-E)\right), \tag{19}$$

(ii) nous simplifions le coefficient de transmission ($W > eV$)

$$T(E)\cong\left(\frac{4Kk}{k^2+K^2}\right)^2 \exp(-2Kl). \tag{20}$$

Avec cette approximation supplémentaire, les intégrales de l'équation (19) peuvent être effectuées pour donner

$$J(V)=\frac{em}{2\pi^2\hbar^3}\{P_2(\mu+eV)-P_2(\mu)-eVP_1(0)\} \tag{21}$$

avec

$$P_1(E)=\frac{-32}{W^2}\{a_5x^5+a_4x^4+a_3x^3+a_2x^2+a_1x^1+a_0\}\exp(-\alpha x)$$

$$a_5=\frac{1}{\alpha},\ a_4=\frac{5}{\alpha^2},\ a_3=\frac{20}{\alpha^3}-\frac{W}{\alpha},\ a_2=\frac{60}{\alpha^4}-\frac{3W}{\alpha^2},\ a_1=\frac{120}{\alpha^5}-\frac{6W}{\alpha^3},\ a_0=\frac{120}{\alpha^6}-\frac{6W}{\alpha^4}$$

et

$$P_2(E) = \frac{-64}{W^2}\left\{b_6 x^6 + b_5 x^5 + b_4 x^4 + b_3 x^3 + b_2 x^2 + b_1 x^1 + b_0\right\}\exp(-\alpha x)$$

$$b_6 = \frac{1}{\alpha^2},\ b_5 = \frac{11}{\alpha^3},\ b_4 = \frac{75}{\alpha^4} - \frac{W}{\alpha^2},\ b_3 = \frac{360}{\alpha^5} - \frac{7W}{\alpha^3},\ b_2 = \frac{1200}{\alpha^6} - \frac{27W}{\alpha^4},$$

$$b_1 = \frac{2520}{\alpha^7} - \frac{60W}{\alpha^5},\ b_0 = \frac{2520}{\alpha^8} - \frac{60W}{\alpha^6}$$

où $x = \sqrt{W - E}$ et $\alpha = 2\sqrt{2ml}/\hbar$. Des différences entre les courants obtenus avec les équations (21) et ((17) et (18)) apparaissent seulement lorsque ($\mu$+$eV$) ~ $W$, très loin de nos conditions expérimentales.

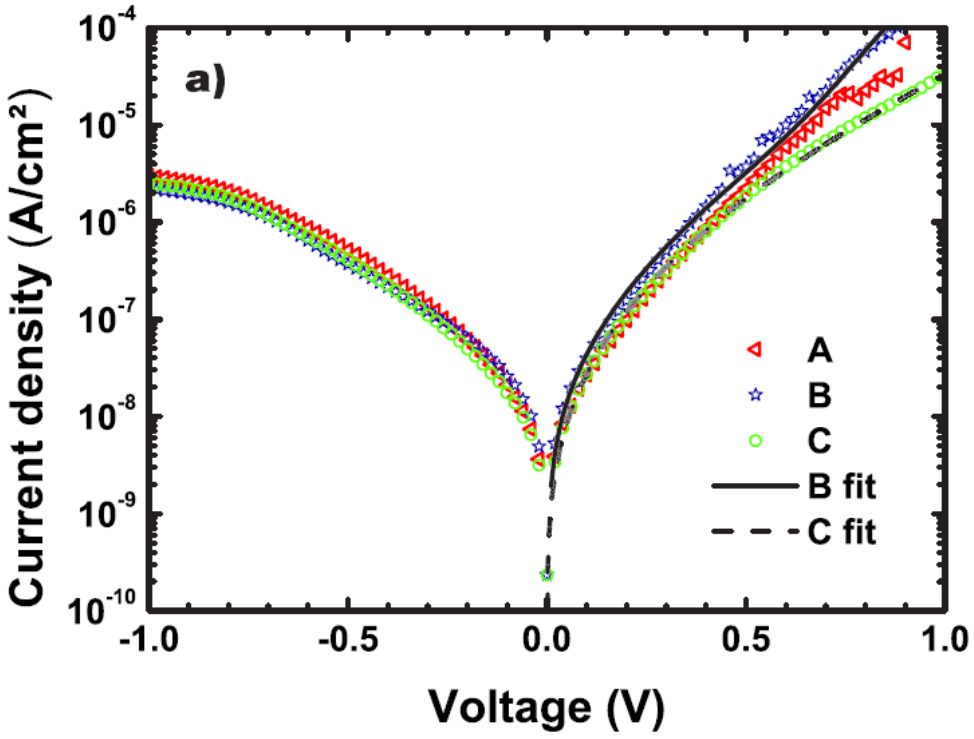


**Figure 14** : Exemples de caractéristiques *J-V* (référence II) obtenues pour trois jonctions OD (échantillons A, B et C). Les échantillons B et C montrent un accroissement de courant pour $V_{dc} > 0.4$V.

Finalement, il convient de remarquer qu'avec l'expression TE du courant tunnel, nous trouvons toujours un minimum tel que celui pointé sur la Figure 12. Il provient des non-linéarités de la densité de courant particulièrement apparentes dans l'équation (21) où le courant s'exprime comme un polynôme en $V$, et n'est pas dû à une transition vers un régime d'émission de champ : pour illustration, pour une barrière $W$ ~ 4 eV, nous trouvons un minimum à ~ 0.2 eV. Positionner le minimum ne suffit pas dans cette analyse pour situer le haut de la barrière tunnel : il convient aussi de bien identifier les comportements

asymptotiques tels que ceux soulignés par les équations (14) et (15) dans le cadre du modèle de Simmons.

Le modèle TE permet souvent de bien reproduire nos résultats expérimentaux, pour les deux types de monocouches explorés comme nous l'avons illustré avec la Figure 13. Cependant, dans la référence II nous présentons des caractéristiques *J-V* montrant un accroissement de courant pour V > 0.4V que nous attribuons à des défauts d'interface. Le modèle TE peut décrire de façon satisfaisante les caractéristiques sans défaut, pour les autres il est nécessaire d'aller au-delà. Pour cela nous commençons par dériver l'équation (17) à l'aide d'un formalisme qui nous permette d'aller au-delà en incluant des défauts, par exemple.

*Modèle de Appelbaum-Brinkmann-Zawadowski*.
Il est possible de retrouver l'équation de TE dans la limite où $W > eV$, à partir d'une formulation due à Appelbaum, Brinkmann[36] et, indépendamment, Zawadowski (ABZ)[37] utilisant l'arsenal du problème à N corps. A la différence de TE, ces auteurs déterminent le coefficient de transmission à l'aide d'une approche à N particules et non plus en considérant une quasi-particule unique. Les effets des interactions sur le gaz d'électrons constituant l'électrode peuvent alors être incorporés de façon systématique. Autrement dit, les approches à une particule, telles que celles dues à Simmons ou à Tsu-Esaki, considèrent des quasi-particules où les effets des interactions sont supposés pris en compte dans les paramètres effectifs. L'approche à N-corps peut permettre de considérer de réelles particules qui interagissent entre elles et avec leur environnement (phonons, défauts, …) – ou au moins, se réserver la possibilité de le faire.

La barrière de potentiel est supposée haute i.e. tel que $W > eV$ et $W > k_B\theta$. Le problème initial est alors séparé en deux. Cette approximation est illustrée sur la Figure 15. Un problème gauche pour lequel nous considérons le potentiel, $U(x)$, suivant

$$U(x) = \begin{cases} 0, -\infty > x > -l/2 \\ W, -l/2 < x < +\infty \end{cases}. \qquad (22)$$

Nous associons ce problème au substrat de Silicium et notons $G^{Si}$ la fonction de Green correspondante. Un problème droit pour lequel nous considérons

$$U(x) = \begin{cases} W, -\infty > x > +l/2 \\ 0, +l/2 < x < +\infty \end{cases}. \qquad (23)$$

Nous associons ce problème à l'électrode métallique qui, dans la majorité des cas est faite d'aluminium, pour cela nous notons sa fonction de Green $G^{Al}$. Des impuretés sont supposées proches de la surface de silicium à une énergie $U_i$. Elles n'apparaissent alors que dans le problème gauche, lié au silicium. Le coefficient de transmission s'écrit d'après ABZ

$$T(E) = \int d\vec{r} \int d\vec{r}\,' \Delta \,\mathrm{Im}\, G^{Si}(\vec{r},\vec{r}\,';E) \hat{D}\, \mathrm{Im}\, G^{Al}(\vec{r},\vec{r}\,';E), \qquad (24)$$

avec

$$\hat{D} = \left(\vec{\partial}_x - \vec{\partial}_x\right)\left(\vec{\partial}_{x'} - \vec{\partial}_{x'}\right)$$
$$\Delta = \delta(x - \bar{x})\delta(x' - \bar{x}) \qquad (25)$$

La flèche au-dessus des opérateurs de dérivé partielle indique la fonction sur laquelle il s'opère (à droite ou à gauche de l'opérateur), $\bar{x}$ est un point quelconque à l'intérieur de la barrière, le résultat final étant indépendant de celui-ci.

Dans le cas d'une jonction tunnel idéale telle que celles que nous avons considérées jusqu'à présent, nous pouvons évaluer les fonctions de Green que nous notons $G_0^{Si}$ et $G_0^{Al}$. Du fait de l'invariance par translation dans les directions transverses, nous pouvons écrire

$$G_0^{Si/Al}(\vec{r},\vec{r}';E_T) = \frac{1}{(2\pi)^2}\int d\vec{k}_t e^{i\vec{k}_t\left(\vec{r}_t - \vec{r}_t'\right)} G_0^{Si/Al}(x,x';E) \qquad (26)$$

avec

$$G_0^{Al}(x,x';E) = \frac{1}{2K}\left[e^{-K|x-x'|} + \frac{K+ik}{K-ik}e^{K(x+x'-d)}\right]$$
$$G_0^{Si}(x,x';E) = -\frac{1}{2K}\left[e^{-K|x-x'|} + \frac{K+ik}{K-ik}e^{-K(x+x'+d)}\right] \qquad (27)$$

Les deux vecteurs d'onde sont donnés dans l'expression (18). En appliquant l'équation (24) nous retrouvons le coefficient de transmission (20) et donc l'expression du courant de TE dans le cas d'une barrière tunnel haute. Ce résultat est naturel puisque dans le cas sans aucune interaction nous retrouvons une description en terme de quasi-particules libres, implicite dans la formulation de TE. Le formalisme ABZ nous permet d'inclure diverses sortes d'interaction. Nous ne considérerons ici que les changements apportés par une impureté localisée près d'une interface (voir Figure 15)

*Transfert assisté par défauts.*
Nous considérons des défauts proches de l'interface substrat/molécules. D'après des études récentes, ces défauts pourraient être des molécules d'eau adsorbées à la surface du silicium ou de l'oxyde, suivant les cas considérés. Ce sont des défauts polaires qui peuvent avoir une grande influence sur les propriétés électrostatiques d'une jonction et donc sur l'amplitude du courant tunnel. Nous reviendrons sur ce point un peu plus tard. D'autre part, les électrons vont entrer en collision avec ces impuretés ce qui va contribuer également à modifier le courant tunnel. Nous nous intéressons ici à ce deuxième mécanisme.

La densité de défauts est supposée suffisamment faible pour pouvoir les considérer comme indépendants. Nous pouvons alors nous concentrer sur le problème à un seul défaut, *i*, modélisé par un potentiel local $U_i$ situé en $\vec{r}_i$

$$V_i(\vec{r}) = a^3 U_i \delta(\vec{r} - \vec{r}_i), \qquad (28)$$

où *a* est la portée effective du potentiel d'impureté. Cette approche très qualitative vise seulement à souligner de possibles effets de défauts présents dans la barrière sans en préciser la nature. La fonction de Green de l'électrode Si en présence du défaut peut être déterminée avec le modèle (28) en résolvant l'équation de Dyson

$$G^{Si}(\vec{r},\vec{r}') = G_0^{Si}(\vec{r},\vec{r}') + G_0^{Si}(\vec{r},\vec{r}'')V_i(\vec{r}'')G^{Si}(\vec{r}'',\vec{r}'), \tag{29}$$

ce qui donne

$$G^{Si}(\vec{r},\vec{r}') = G_0^{Si}(\vec{r},\vec{r}') + V_i(\vec{r})\frac{G_0^{Si}(\vec{r},\vec{r}_i)G_0^{Si}(\vec{r}_i,\vec{r}')}{1-V_i(\vec{r})G_0^{Si}(\vec{r}_i,\vec{r}_i)}. \tag{30}$$

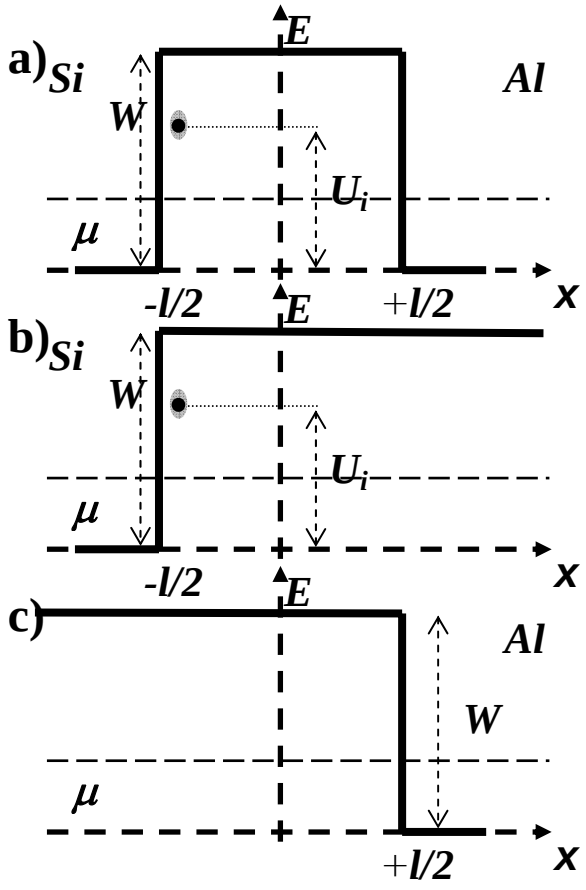


**Figure 15** : a) Potentiel rectangulaire de hauteur *W* et largeur *l*. $\mu$ est le potentiel chimique à l'équilibre. Une impureté d'énergie $U_i$ est localisée proche de l'interface Si. Ce problème initial est décomposé en deux pour pouvoir calculer le coefficient de transfert b) un problème gauche et c) un problème droit.

A l'aide de cette fonction de Green nous pouvons évaluer le coefficient de transmission en présence de défauts à partir de l'équation (24). Avec nos approximations, il s'écrit dans le cas où nous avons $N_{imp}$ défauts

$$T(E) = T_1(E) + T_2(E) = T_1(E) + \sum_{i=1}^{N_{imp}} T_2(E, U_i). \quad (31)$$

Le premier terme correspond à celui déjà calculé, il contrôle l'effet tunnel direct où les électrons transitent sans collision au travers de la barrière. Le second terme prend en compte les collisions avec les impuretés, il contrôle l'effet tunnel indirect assisté par défauts. Les impuretés sont vues comme indépendantes les unes des autres, chacune donnant une contribution au coefficient de transfert.

Le calcul du terme $T_2(E,U_i)$ pose un problème de convergence provenant du fait que nous considérons les impuretés avec un potentiel de portée nulle i.e réduit à une fonction de Dirac (équation (28)), ce qui n'est pas réaliste. En effet, le terme $G_0^{Si}(\vec{r}_i, \vec{r}_i)$ qui apparaît dans l'équation (30) n'est pas convergent : nous devons par conséquent introduire une coupure, $E_C$, dans l'intégration qui est naturellement identifiée à l'énergie de Fermi des réservoirs à l'équilibre,

$$G_0^{Si}(\vec{r}_i, \vec{r}_i) \propto \int_0^{+\infty} dE_t \rightarrow \int_0^{E_C} dE_t G_0^{Si}(x_i, x_i; E_T - E_t). \quad (32)$$

Nous vérifions ensuite que l'essentiel des résultats n'est pas dépendant de cette coupure.

Le terme de transmission assistée par défauts est contrôlé par

$$\frac{a^3 U_i}{1 - a^3 U_i G_0^{Si}(\vec{r}_i, \vec{r}_i)}. \quad (33)$$

Ce terme montre des quasi-résonances lorsque $a^3 U_i \,\mathrm{Re}\, G_0^{Si}(\vec{r}_i, \vec{r}_i) = 1$. Les défauts dont les caractéristiques permettent de respecter cette dernière égalité peuvent contribuer de façon significative au courant tunnel. Dans la référence II, nous présentons des jonctions OD dont certaines montrent un accroissement de courant conséquent pour V > 0.4V : des exemples sont donnés sur la Figure 14. En sélectionnant $10^{13}$ défauts/cm$^2$ d'énergie distribuée suivant une gaussienne centrée à 3eV i.e. nous avons sélectionné un maximum de défauts produisant cette quasi-résonnance, nous pouvons reproduire les résultats expérimentaux. Cependant, il est nécessaire de souligner que ce mécanisme seul ne peut expliquer les variations de courant de quatre ordres de grandeur illustrées sur la Figure 11 sans avoir recours à une densité de défauts totalement irréalistes.

Avec ce modèle simple nous voulons également souligner une conséquence importante due aux défauts. Elle est illustrée sur un exemple de caractéristique tunnel particulièrement résistive (Figure 13, courbe S1) que nous pouvons reproduire aussi bien avec que sans défauts. Cependant, en incluant les mécanismes d'effet tunnel assistés par défauts nous changeons, de façon notable, le jeu de paramètres nécessaire pour avoir un bon accord avec l'expérience. Ainsi, en considérant une densité de $2.10^{13}$ défauts/cm$^2$, uniformément répartis en énergie, nous obtenons une valeur légèrement différente pour la masse effective, $m$ = $0.177 m_e$, ($0.131\ m_e$ sans défaut) mais, surtout, une hauteur de barrière, $W$-$\mu$ = 4.5 eV (5.78 eV sans défaut), davantage en accord avec celles escomptées.

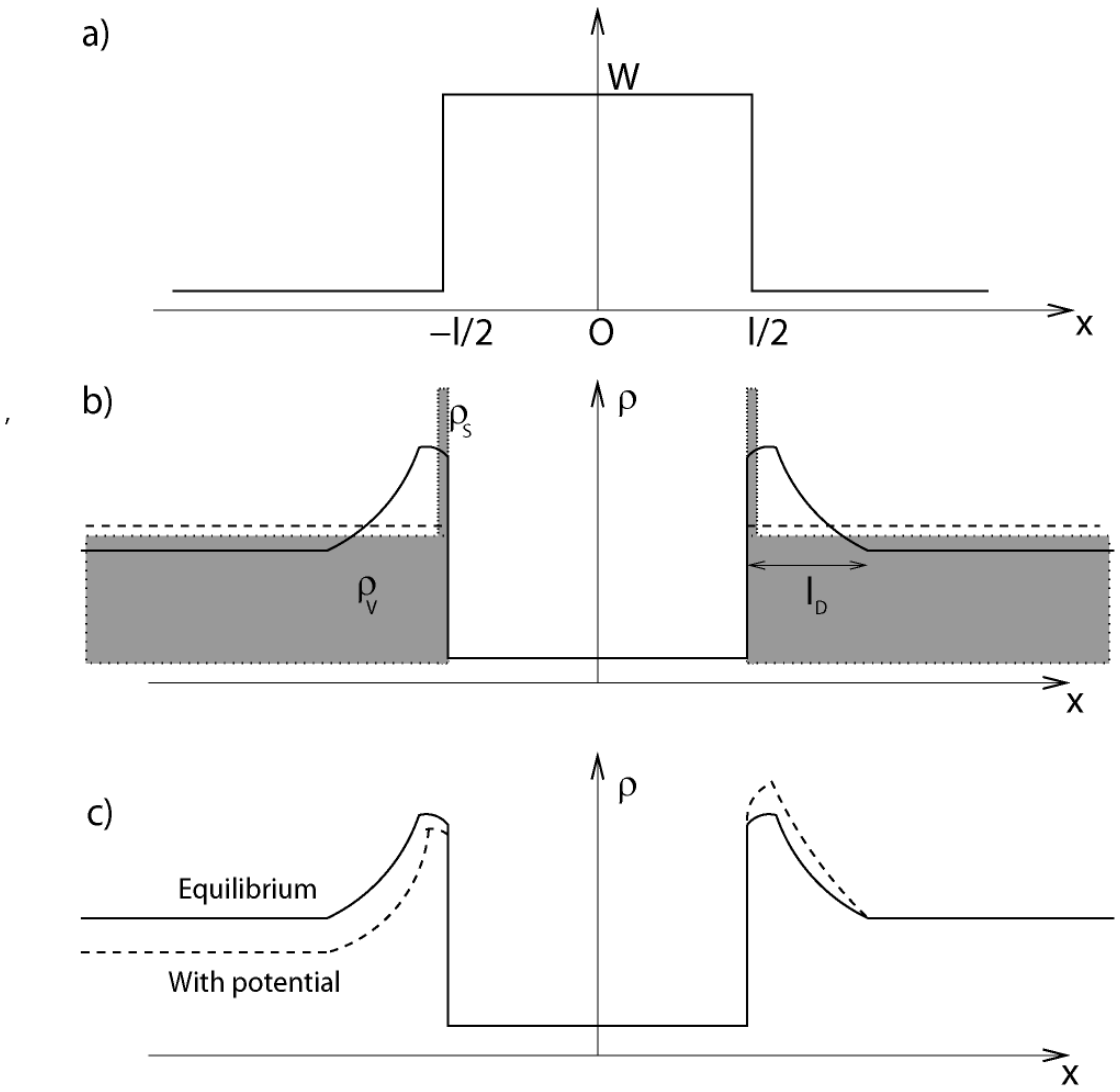


**Figure 16** : a) Potentiel électrostatique à travers la jonction. x est la direction perpendiculaire à l'interface métal/oxyde. b) Vue schématique de la densité de charge à travers la jonction à l'équilibre (trait plein) : les charges s'accumulent aux interfaces et la densité est une fonction de x sur une longueur de taille $l_D$, la longueur de Debye ; densité uniforme considérée dans le modèle de Tsu-Esaki (ligne hachurée) ; densité modèle utilisée (surface grisée) : la densité de charge est une somme d'une composante volumique, $\rho_V$, et surfacique, $\rho_S$. c) Schéma du changement de densité lorsqu'un potentiel est appliqué à l'électrode de gauche, l'électrode de droite étant à la masse (ligne hachurée).

*Modèle de Tsu-Esaki. Relation avec la capacité*.

Sur la Figure 11 nous avons souligné l'apparition de fluctuations importantes, aussi bien en courant qu'en capacité. Ces deux grandeurs sont cependant corrélées : nous constatons que plus la capacité est grande plus le courant tunnel est élevé. Cette observation semble naturelle car plus la capacité est forte plus le nombre de charges accumulées à l'interface, $Q$, à une tension donnée sera grand. Or, ce sont précisément ces charges qui sont susceptibles de traverser la barrière tunnel : le courant tunnel doit être une fonction croissante de la capacité. Nous tentons ici d'établir un lien simple entre ces deux quantités.

Nous l'avons déjà souligné, le modèle de Tsu-Esaki est très simplifié. En particulier, il considère une densité de charge spatialement uniforme dans chacune des électrodes (voir Figure 16) et néglige la formation de charges d'espace : dû à la barrière tunnel des charges s'accumulent sur chacune des interfaces. La densité de charges est une fonction de la coordonnée perpendiculaire aux interfaces, x, à proximité de celles-ci sur une distance de l'ordre de la longueur caractéristique d'écrantage (la longueur de Debye, $l_d$, dans le cas d'un semiconducteur dopé). Un profil de densité est schématisé sur la Figure 16.b. Il doit être plus précisément considéré comme une enveloppe contenant de possibles oscillations de Friedel. Nous simplifions cette densité de charges par le modèle représenté par les surfaces grisées contenant deux composantes : (i) une composante surfacique, $\rho_s$, répartie sur une zone de largeur $l_d$ que nous simplifions ici en considérant la limite $l_d \to 0$ de sorte que les charges de surface sont supposées être sur un même plan ; (ii) une composante volumique ; $\rho_V$. Nous obtenons pour les deux électrodes

$$\rho_{G/D} = \rho_V + \rho_S = \int_{-\infty}^{+\infty} \frac{D_{3D}(\varepsilon)}{1+\exp\left(\beta^*\left(\varepsilon-\mu_{G/D}\right)\right)} d\varepsilon + \int_{-\infty}^{+\infty} \frac{D_{2D}(\varepsilon)}{1+\exp\left(\beta^*\left(\varepsilon-\mu_{G/D}\right)\right)} d\varepsilon \qquad (34)$$

où $D_{3D}$ et $D_{2D}$ sont les densités d'états à deux et trois dimensions. $\mu_{G/D}$ est le potentiel chimique de l'électrode droite (gauche), que nous supposons fixé à la valeur prise dans le modèle initial de Tsu-Esaki. Le nombre d'électrons donnés en intégrant la densité supposée dans le modèle TE et notre densité doit être identique i.e. l'intégration de la courbe hachurée doit donner la surface grisée. Cette contrainte permet de fixer le paramètre $\beta^*$ de l'équation (34) qui peut être interprété comme l'inverse d'une température effective.

En plus d'être des jonctions tunnel nos systèmes sont avant tout des capacités. Elles vérifient la relation bien connue

$$Q=C(V)V \qquad (35)$$

entre les charges stockées sur les interfaces et la tension appliquée. Quand un potentiel est appliqué à l'une des électrodes, l'autre étant à la masse, la densité de charge est modifiée de la façon représentée sur la Figure 16.c : la charge totale de l'électrode sous tension est modifiée, seule la composante surfacique est changée pour l'autre électrode. La différence du nombre de charges surfaciques avec et sans tension définit la charge, $Q$, stockée par la capacité. Dans le cas idéal, la valeur absolue de cette différence est la même à droite et à gauche, seul le signe change. Pour l'électrode à la masse, on peut écrire

$$Q = \int_{l/2}^{l/2+l_D} dx \int dA\left[\rho(x,V) - \rho(x,0)\right] \qquad (36)$$

où $\rho(x,V)$ est la densité électronique à la tension $V$, $dA$ l'élément infinitésimal de surface pour l'intégration. Avec le modèle (34) la charge stockée peut se réécrire (nous omettons l'indice $D$ afin de simplifier l'écriture)

$$Q \approx A \int_0^{+\infty} D_{2D}(\varepsilon)\left[\frac{1}{1+e^{\beta^*(\varepsilon-\mu(V))}} - \frac{1}{1+e^{\beta^*(\varepsilon-\mu(0))}}\right] d\varepsilon \,. \qquad (37)$$

$A$ est l'aire de la capacité. Le potentiel chimique, $\mu$, est considéré comme une fonction de $V$. Nous supposons $\exp(\beta^*(\varepsilon-\mu(V))) >> 1$ et remplaçons la distribution de Fermi-Dirac par celle de Maxwell-Boltzmann

$$Q \approx A\int_0^{+\infty} D_{2D}(\varepsilon)\left[e^{-\beta^*(\varepsilon-\mu(V))} - e^{-\beta^*(\varepsilon-\mu(0))}\right]d\varepsilon \approx \beta^* \left.\frac{\partial\mu}{\partial V}\right|_V VA\int_0^{+\infty} D_{2D}(\varepsilon)e^{-\beta^*(\varepsilon-\mu(V))}d\varepsilon\,. \qquad (38)$$

Pour obtenir la deuxième égalité, nous avons décomposé $\mu(0)$ en série de Taylor autour du point $V$. En supposant la densité d'état constante, $D_{2D}$, ce qui est le cas pour un gaz d'électrons en deux dimensions, nous obtenons à partir des équations (35) et (38) la relation suivante

$$\mu(V) = \frac{1}{\beta^*}\log\left(\frac{C(V)}{A\,D_{2D}\,\partial\mu/\partial V\big|_V}\right) = a\log(bC(V))\,. \qquad (39)$$

Nous avons introduit deux paramètres, $a$ et $b$.

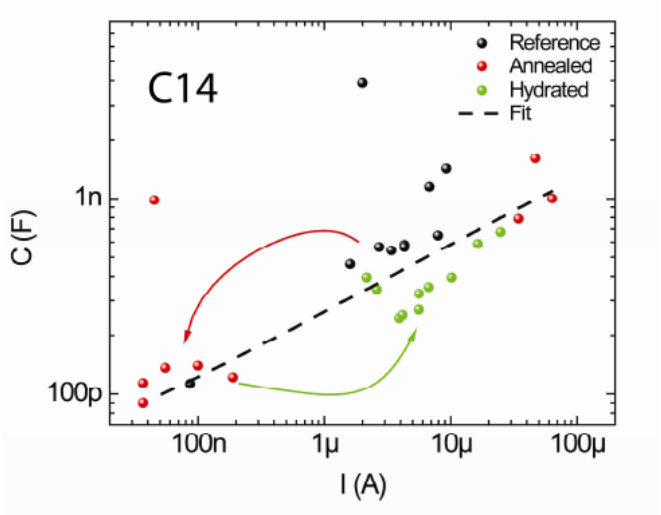


**Figure 17** : Mesures de capacités de jonctions à base d'alcènes de 14 atomes de carbone à tension, $V$ = 1V, et fréquence fixe, $f$ = 1kHz. Différentes préparations des monocouches sont considérées (cf texte). La courbe hachurée présente le résultat obtenu avec l'équation (39).

Dans la référence (38) nous avons étudié un grand nombre de jonctions. Pour chacune d'elles, nous avons effectué diverses mesures dont celles de courant et de capacité dans trois différentes situations : (i) directement après les avoir élaborées, (ii) après un recuit de 120° C pendant 1 heure sous atmosphère contrôlée ($N_2$) et, enfin, (iii) après les avoir hydratées en y déposant une goutte d'eau pendant 20s. Nous mettons ainsi en évidence que la présence d'eau provoque une augmentation importante de capacité et de courant tunnel. Les molécules d'eau doivent vraisemblablement s'adsorber sur la surface du substrat (oxyde ou silicium, suivante les cas). Etant fortement polaires, elles ajoutent alors d'importantes contributions à la

polarisation. Cependant, ces molécules ne doivent pas s'adsorber de façon uniforme sur la surface mais doivent plutôt se concentrer dans les zones défectueuses des monocouches, leurs laissant davantage de place pour former une fine couche. Cette image donne une origine possible aux dispersions montrées sur la Figure 11.

Sur la Figure 17, nous représentons une courbe *C-I* obtenue à $V$ = 1V et $f$ = 1kHz, issue de cette étude, pour des chaînes plus courtes de 14 atomes de carbone. Différentes mesures, correspondant aux trois situations décrites ci-dessus, y sont reportées ainsi que les résultats donnés par l'équation (39) qui donne un bon accord avec l'expérience. Pour obtenir cette courbe, nous imposons d'avoir $\mu$=0.05eV pour $C$=$10^{-10}$ F qui correspondrait à des jonctions peu hydratées, et $\mu$=1.5eV pour $C$=$10^{-9}$ F qui correspondrait à des jonctions très hydratées. Ces valeurs permettent de fixer les paramètres *a* et *b* de l'équation (39). Ces valeurs limites du potentiel chimique semblent indiquer qu'une fine couche d'eau est susceptible de provoquer une diminution du travail de sortie du métal (Al ou Hg) d'environ 1.5 eV. Cette valeur surprenante est en accord avec d'anciennes mesures.[39]

Il est difficile d'extraire des informations sur les propriétés de la monocouche par les mesures du seul courant tunnel. Les mesures dynamiques – mesures de bruit de courant et, surtout, d'admittance complexe - sont nécessaires pour identifier des mécanismes à l'aide de leur signatures temporelles. Ce sont ces études que nous présentons dans la suite.

## 4. Bruit basses fréquences de courant tunnel. Interprétation standard.

Nous nous sommes intéressés, dans la référence II, aux fluctuations du courant tunnel autour de la valeur moyenne, $J$, seule grandeur considérée jusqu'ici

$$\delta J(t) = J(t) - J \,. \tag{40}$$

Seules les fluctuations aux temps longs sont considérées. Les fonctions de corrélation de ces fluctuations permettent de caractériser ces phénomènes stochastiques. En particulier, dans le cas d'un processus stationnaire, comme nous supposons que c'est bien le cas ici, la variance est directement liée à la densité spectrale de bruit, $S_J$, auquel nous avons directement accès par l'expérience :[40]

$$\overline{\delta J(t)^2} = \lim_{t_E \to +\infty} \frac{1}{\tau} \int_{-t_E}^{+t_E} dt \delta J(t)^2 = \int_0^{+\infty} df S_J(f). \tag{41}$$

Dans cette définition, $2t_E$ est le temps durant laquelle la mesure est effectuée, $f$ est la fréquence. Il est observé dans des systèmes extrêmement divers, électriques ou autres, que la densité spectrale de bruit augmente à basses fréquences comme $1/f^{\gamma}$ ($\gamma > 1$).[40] C'est un phénomène qui semble universel et qui apparaît aussi dans nos systèmes comme l'illustre la Figure 18. Ce sont des résultats obtenus pour des OD et présentés dans la référence II. L'indice $\gamma$ change très légèrement lorsque nous augmentons la tension, passant de 1 à 1.2.

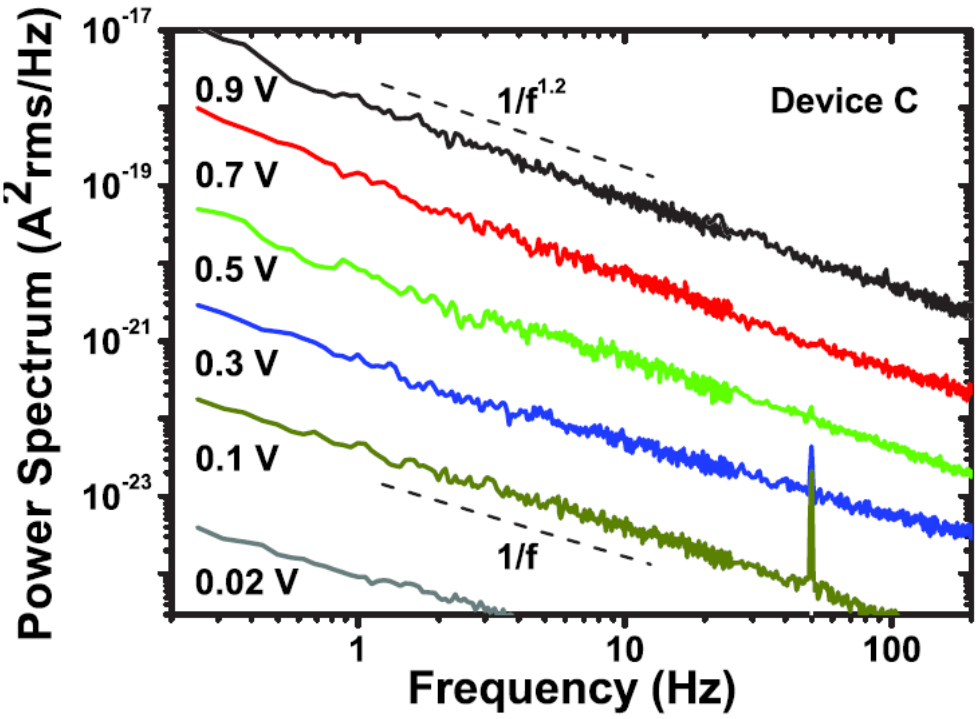


**Figure 18** : Densité spectrale de bruit d'une jonction à base d'OD pour plusieurs tensions appliquées, V. Les mesures sont effectuée sous atmosphère contrôlée ($N_2$) et à température ambiante.

Ce bruit est notamment observé dans les structures Métal/Oxyde/Semiconducteur inorganique. Il est en général associé à un autre bruit dit bruit télégraphique (Random Telegraph Noise, RTS).[40,41] Dans les jonctions sous-micrométriques, il est possible d'observer des variations du courant électrique en fonction du temps entre deux niveaux bien définis, $I_1$ et $I_2$. Ces fluctuations sont attribuées à un défaut dont l'état interne oscille avec un certain temps caractéristique, $\tau$, entre deux niveaux, chacun étant associé à un niveau de courant. Le bruit en $1/f$ est vu comme une somme de telles fluctuations avec une très large distribution de temps caractéristiques.[40,41] Nous adoptons, ici, ce point de vue. Il faut noter que bien que nos jonctions soient de tailles macroscopiques, nous avons observé l'apparition de bruits RTS favorisant cette interprétation.

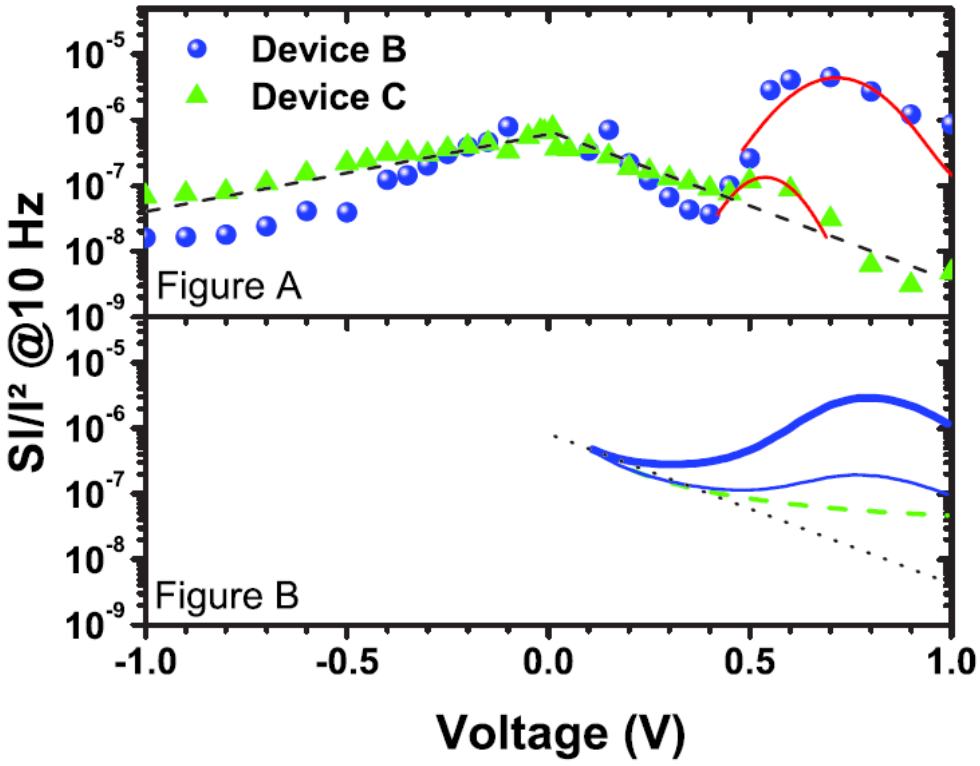


**Figure 19** : A) Densité spectrale de bruit de deux jonctions à base d'OD normalisée par $I^2$ à 10 Hz, en fonction de $V$. Une des jonctions montre un accroissement important de densité spectrale pour $V > 0.4$ V. B) Résultats du modèle (Eqs. (44) et (45). Un facteur multiplicatif a été appliqué.

Ainsi, nous supposons que certaines des impuretés considérées précédemment (Eq. (28)) peuvent capturer des charges que nous modélisons comme des systèmes à deux niveaux[40] : leurs minima sont séparés d'une énergie $2\varepsilon_i$ et on note $\Delta_i$ la probabilité de passer d'un minimum à l'autre. Après diagonalisation, nous associons l'état d'énergie $E_i^- = -E_i = -\sqrt{\varepsilon_i^2 + \Delta_i^2}$ , à l'état neutre, celui d'énergie $E_i^+ = E_i$ à l'état chargé. A chaque état est associé une densité de courant $J_{i-}$ et $J_{i+}$. Nous introduisons enfin un temps de résidence moyen dans ces états, $\tau_i$. La densité spectrale associée à ce défaut a été calculée[40,42]

$$S_J^i(f,\tau_i,E_i) = (J_{i-} - J_{i+})^2 \frac{\tau_i}{1+\omega^2\tau_i^2} \mathrm{Cosh}^{-2} \frac{E_i}{2k_B\theta}. \quad (42)$$

Le bruit en 1/*f* est compris comme une superposition de tels signaux. Nous écrivons

$$S_J = \sum_i \int dU_i P_1(U_i) \iint d\tau_i dE_i P_2(\tau_i, E_i) S_J^i(f,\tau_i,E_i). \quad (43)$$

$P_1$ est la distribution de ces défauts en énergie, $P_2$ la distribution des caractéristiques internes de ces défauts. $P_1$ est la distribution que nous avons déjà utilisée, sans le mentionner, pour reproduire les caractéristiques *J-V* montrant des signes d'effet tunnel assisté par défauts (cf. Eq. (31)). Pour obtenir une loi en 1/*f* il est nécessaire de considérer une distribution $P_2$ uniforme. A titre d'exemple nous considérons le cas où $k_B\theta >> E_i$ ; le terme en $\mathrm{Cosh}^{-2}$ se réduit alors à une constante et en considérant $P_2 \sim 1/\tau$, nous obtenons bien une loi en 1/*f*

$$S_J \propto \sum_i \int dU_i P_1(U_i) (J_{i-} - J_{i+})^2 \frac{1}{f}. \quad (44)$$

Nous traçons, comme il est usuel de le faire, $S_J/J^2$ à 10 Hz. Un exemple est donné sur la Figure 19. Nous remarquons (i) une contribution principale qui est proportionnelle non pas à $J^2$, comme il est commun de l'observer dans les systèmes MOS classiques où le courant est mesuré dans le canal, mais en $(\partial I/\partial V)^2$ ; (ii) un accroissement de densité spectrale local à certaines tensions qui correspondent aux accroissements de courant observés dans les courbes *J-V* (voir Figure 14).

La densité de courant est modifiée lorsque le défaut change d'état. Nous identifions deux causes à ces changements. Le premier effet est capacitif : lorsque le piège est chargé il modifie par interaction coulombienne la densité de charges accumulées aux interfaces ce qui introduit un changement de tension aux bornes de la capacité. Le deuxième est de type résistif : lorsque le défaut passe d'un état à l'autre, son énergie est modifiée ce qui va affecter le coefficient de transmission $T_2$. Nous écrivons en conclusion (cf. Eqs. (17) et (31))

$$J_{i+}(V) \cong J_{i-}(V+\delta V) + \frac{emk_B\theta}{2\pi^2\hbar^3} \sum_{i=1}^{N_{imp}} \int_0^{+\infty} dE \left. \frac{\partial T_2(E,U_i)}{\partial U_i} \right|_{U_i} E_i \ln\left( \frac{1+e^{\beta(\mu-E)}}{1+e^{\beta(\mu-eV-\delta V-E)}} \right). \quad (45)$$

En ne conservant que le premier terme nous obtenons

$$S_I \propto E^* \frac{1}{\mathrm{A}} N_{imp}^* \left( \frac{\partial I}{\partial V} \right)^2 \frac{e^2}{C^2} \frac{1}{f} \quad . \quad (46)$$

Cette expression est qualitativement en accord avec nos observations reportées sur la Figure 19. Le deuxième terme de l'équation (45) permet d'expliquer, aussi qualitativement, l'accroissement de bruit observé pour certaines tensions en sélectionnant une densité $P_1$, centrée sur une énergie particulière. De la même façon nous avons reproduit les accroissements en courant observés sur certaines *J-V*. Il est important de souligner qu'il y a une correspondance entre augmentation locale de courant et augmentation locale de bruit. Elles sont toutes deux reproduites en utilisant la même distribution $P_1$. Cependant, pour

obtenir un bon accord avec l'expérience dans le cas du bruit de courant, un facteur multiplicatif arbitraire doit être ajouté, dans tous les cas (i.e avec ou sans contribution résistive), pour reproduire la bonne amplitude : ce facteur correspond à des densités de défauts irréalistes. Dans certains cas nous obtenons un nombre de défauts supérieur au nombre d'atomes dans la jonction. Une autre interprétation possible serait de supposer qu'un défaut ne piège pas une unique charge mais un nombre macroscopique de charges, ~ $10^6$. Dans le paragraphe VI, nous proposerons une autre interprétation du bruit de courant tunnel.

**5. Spectroscopie d'admittance des jonctions moléculaires. Relaxation moléculaire et défauts d'interface.**

Nous avons étudié la réponse dynamique de nos jonctions en appliquant, superposé à la tension $V_{dc}$, un faible signal ac de fréquence comprise entre 20Hz et $10^5$Hz (cf. Figure 20). C'est le sujet des références III et IV. Cette technique est très sensible et permet de différentier, et donc d'identifier les différents mécanismes participant à la polarisation, en fonction de la fréquence. Ceci est illustré sur le schéma de la Figure 20. Dans la gamme de fréquences que nous étudions nous sondons, aux plus basses fréquences, les défauts lents d'interface qui peuvent être certains systèmes à deux niveaux invoqués pour décrire le bruit en 1/*f*. A plus hautes fréquences, nous sondons les moments dipolaires permanents présents dans la structure. Ce type de spectroscopie n'a été appliqué que récemment à des systèmes comparables au nôtre mais pour des géométries différentes qui rend l'interprétation des résultats difficile.[43,44] Pour des jonctions capacitives, qui sont déjà de réels dispositifs électroniques, nos mesures constituent une première.

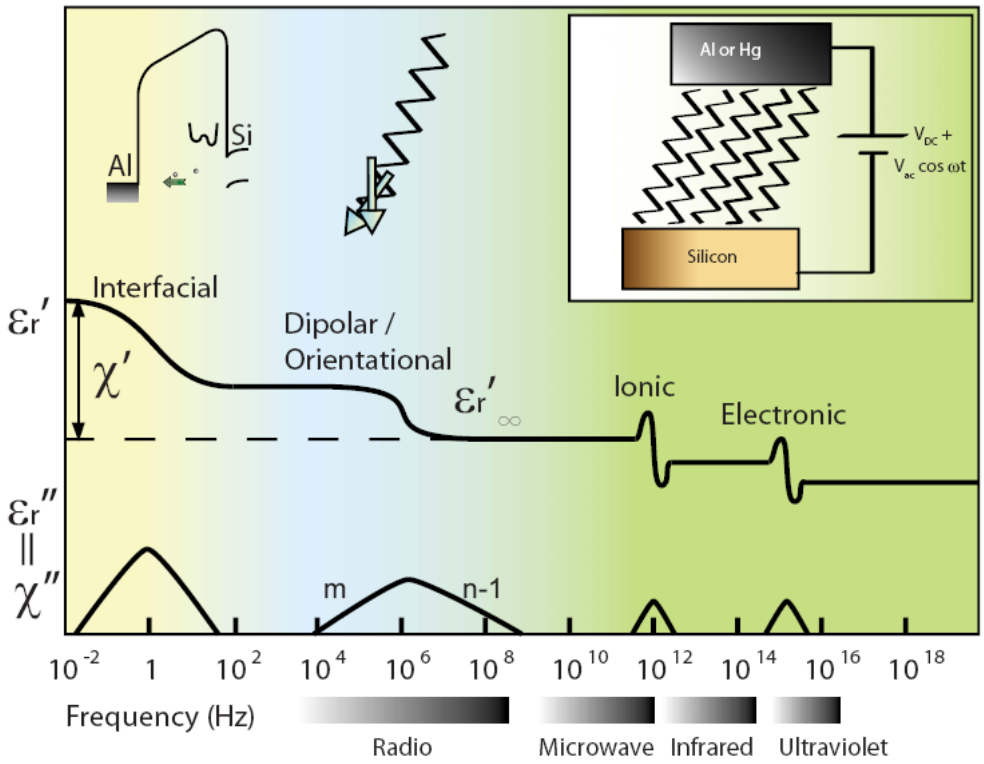


**Figure 20** : Dépendance en fréquences des parties réelles et imaginaires de la constante, $\varepsilon_r$, et susceptibilité, $\chi$, diélectrique. Les différents mécanismes participants à la polarisation répondent à des fréquences très différentes qu'il est possible d'identifier. Encarts : à gauche, défaut d'interface vu comme un système à 2 niveaux localisé près du substrat de Si ; au centre, les moments dipolaires portés par les molécules donnent la contribution dipolaire de nos jonctions ; à droite, schéma de l'expérience.

Les molécules alcanes (OD et OTS) sont faiblement polaires (cf. Figure 21). Elles possèdent de faibles moments dipolaires sur chacune des liaisons CH, de l'ordre de 0.1D et surtout des

moments dipolaires plus intenses au niveau de leur attache avec le substrat. Ce moment est de l'ordre de 0.5 à 1D, valeur estimée à l'aide de calculs simples (programme MOPAC, Référence IV) qui néglige notamment les effets d'écrantage, dus aux électrodes métalliques. La valeur de ce dipôle dans la jonction doit, très certainement, être inférieure à cette estimation. En réponse à un champ électrique, ces dipôles vont se réorienter suivant une dynamique déterminée par leur interaction avec leur environnement et du champ électrique local.

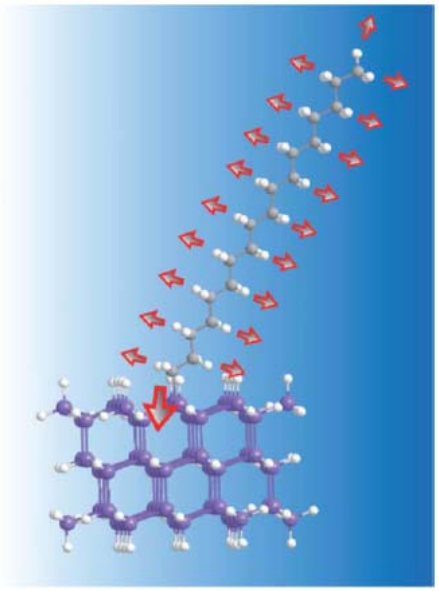

**Figure 21** : Les deux molécules étudiées ont des dipôles (~ 0.1 D) perpendiculaires à leur axe et un dipôle (~ 1 D) plus important au pied. Ces valeurs ont été estimées à l'aide du logiciel MOPAC

L'admittance complexe, $Y(\omega)$, s'exprime en fonction de la conductance tunnel, $G_T$, et de la susceptibilité diélectrique, $\chi(\omega)$, qui prend en compte les phénomènes de polarisation dont la fréquence caractéristique de relaxation est comprise dans la gamme explorée (cf. Figure 20). Elle s'écrit

$$\begin{aligned} \mathrm{Re}\,Y(\omega)/\omega &= G_T/\omega + \frac{\varepsilon_0}{d}\chi''(\omega) = G_T/\omega + C''(\omega), \\ \mathrm{Im}\,Y(\omega)/\omega - C_\infty &= \frac{\varepsilon_0}{d}\chi'(\omega) = C'(\omega) \end{aligned} \quad . \qquad (47)$$

où nous ne considérons que des grandeurs normalisées par la surface des jonctions. $d$ est l'épaisseur de la jonction. $C_\infty$ contient les processus de polarisation rapides devant les fréquences considérées, typiquement, ces processus sont dus aux électrons et aux ions du réseau formé par les molécules (cf. Figure 20). La composante $C'$ rend compte des phénomènes de polarisation, $C''$ de la perte d'énergie électrique dans le milieu environnant les moments dipolaires. Nos mesures mettent en évidence deux contributions à la polarisation : une contribution d'interface et une contribution dipolaire. Nous notons

$$\chi(\omega) = \chi_{\text{int}}(\omega) + \chi_{dip}(\omega). \qquad (48)$$

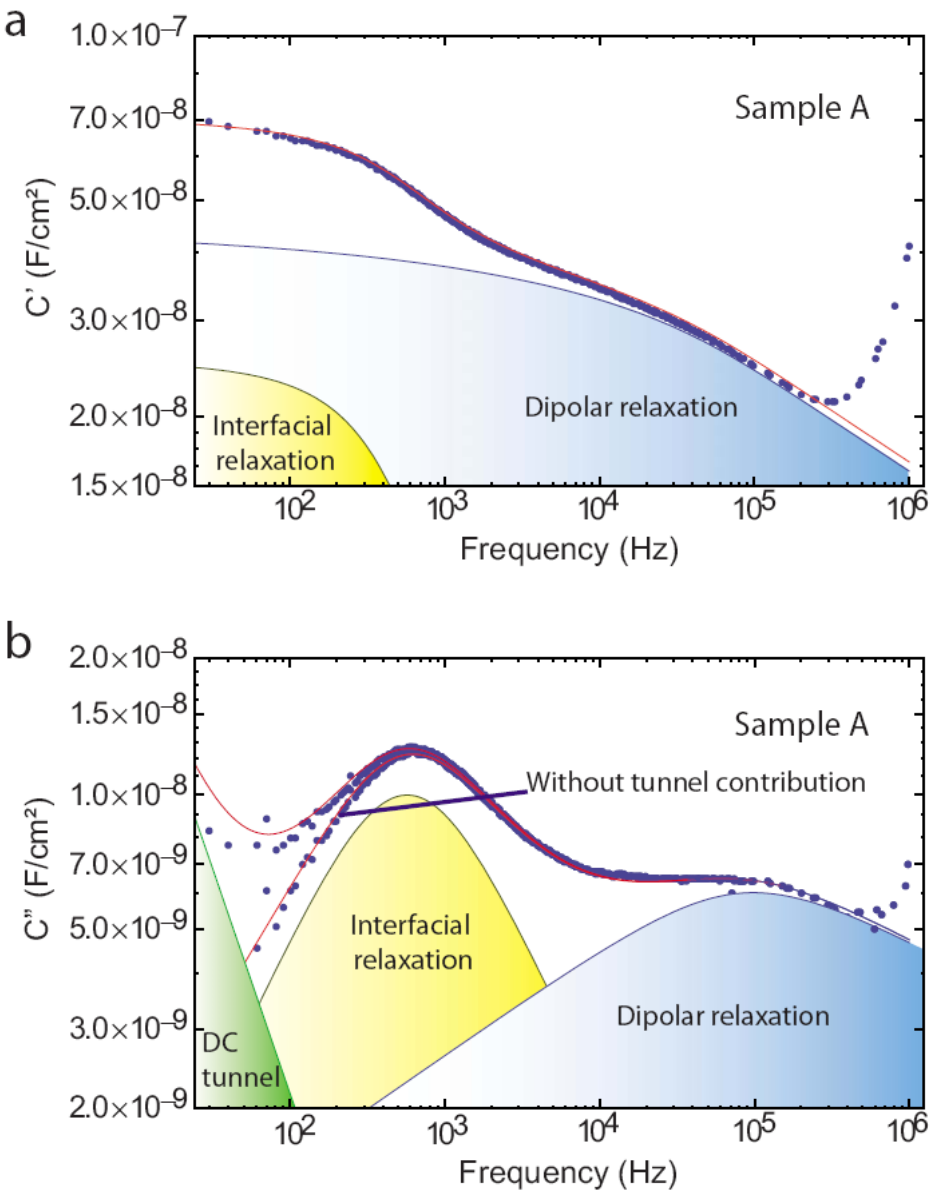


**Figure 22** : Admittance complexe d'une jonction à base d'OD à $V_{dc}$=0.1 V décomposé en a) sa partie imaginaire et b) sa partie réelle. Les points bleus sont les données expérimentales. Les traits rouges, la modélisation obtenue en décomposant la réponse en trois composantes : le courant tunnel (en vert), les défauts d'interface de type debye (en jaune) et la relaxation dipolaire de type Dissado-Hill (en bleu). Cette courbe est issue de la référence IV.

Différentes expressions, plus ou moins empiriques, sont répertoriées pour les susceptibilités diélectriques.[45-49] Nous trouvons que la composante d'interface est bien reproduite par l'expression de Debye,[45]

$$\chi_{Debye}(\omega) = \chi_0 \frac{1 + j\omega\tau}{1 + \omega^2\tau^2}, \tag{49}$$

la composante dipolaire par celle, plus complexe, due à Dissado et Hill[49]

$$\chi_{DH}(\omega) = \chi_0 \frac{\Gamma(1+m-n)}{\Gamma(m)\Gamma(2-n)}(1 - j\omega\tau)^{n-1}\,{}_2F_1\left(1-n, 1-m; 2-n; (1-j\omega\tau)^{-1}\right), \tag{50}$$

où $n$ et $m$ sont des paramètres tels que $0 \leq n \leq 1$ et $0 \leq m \leq 1$, $\Gamma$ est la fonction Gamma et ${}_2F_1$ est la fonction hypergéométrique de Gauss. Pour $n = 0$ et $m = 1$, la susceptibilité de Dissado-Hill se réduit à celle de Debye. Dans les deux cas, $\tau$ est le temps caractéristique de relaxation de l'espèce considérée (défauts d'interface ou moments dipolaires permanents), $\chi_0$ détermine l'amplitude de la réponse. Ces susceptibilités présentent un pic dans leur partie imaginaire en $\omega_P$ qui se confond avec $1/\tau$ pour le modèle de Debye seulement. Dans les zones pre- et post-pic les comportements asymptotiques de ces réponses sont

$$\begin{aligned} &\chi(\omega) \propto (j\omega)^{n-1} \text{ pour } \omega >> \omega_P \\ &\chi(0) - \chi(\omega) \propto (j\omega)^m \text{ pour } \omega << \omega_P \end{aligned}. \tag{51}$$

Le modèle de Debye pour la susceptibilité possède une assise théorique : il repose sur le mouvement Brownien de rotation d'une particule porteuse d'un moment dipolaire.[45] Ce n'est pas le cas de la susceptibilité de Dissado-Hill : bien que des tentatives aient été faites dans ce sens, nous devons la considérer essentiellement comme purement empirique.[49]

En utilisant les équations (48-50), l'accord avec l'expérience est remarquable. Un exemple est donné sur la Figure 22. D'autres exemples peuvent être trouvés dans la référence (III). Nous remarquons que nous vérifions toujours $m \approx 1 - n$, avec $m \approx 0.2$ et $n \approx 0.8$ ; davantage de détails peuvent être trouvés dans la référence (IV). Avec cette relation entre paramètres, la fonction de réponse de la contribution dipolaire est très proche de l'expression Cole-Cole[46] pour laquelle une assise théorique existe, généralisant l'approche de Debye à un mouvement Brownien fractionnaire[50]

$$\chi_{ColeCole}(\omega) = \frac{\chi_0}{1 + (j\omega\tau)^{1-n}}. \tag{52}$$

Cette expression offre également l'avantage d'être plus facile à manipuler.

Nous avons récemment mis en évidence que la contribution d'interface était liée à la présence de molécules d'eau, probablement adsorbées sur la surface de l'oxyde.[38] Nous l'avons déjà évoqué précédemment. Pour cela nous avons effectué des séries de mesures sur une cinquantaine de jonctions, du courant tunnel et de l'admittance (i) directement après avoir élaboré les échantillons, (ii) après des recuits d'une heure à 110°C sous atmosphère contrôlée ($N_2$) et (iii) après avoir déposé une goutte d'eau sur la surface de la monocouche pendant 20s avant de la retirer. Les différentes étapes (i), (ii) et (iii) sont successivement effectuées sur chacune des cinquante jonctions explorées. Les conclusions sont claires : le recuit tend à faire diminuer l'amplitude du pic, l'ajout d'eau tend à le faire augmenter. D'autre part, comme nous l'avons déjà vu, les valeurs du courant tunnel et de la capacité sont étroitement corrélées : la valeur de la capacité peut augmenter considérablement en présence d'eau – la

constante diélectrique effective pouvant alors atteindre 80 – ce qui induit une augmentation de courant tunnel. La dispersion en courant s'étend sur plusieurs ordres de grandeur.

La réponse dynamique d'une espèce polarisable est déterminée en grande partie par son interaction avec son environnement. Nous avons illustré ce point (référence IV) en adaptant un modèle dû à I. Goyshuk à l'étude de la contribution dipolaire de nos jonctions.[51] Nous considérons une monocouche comme un ensemble de dipôles permanents $\mu_i$ faisant un angle $\phi_i^0$ avec la normale au plan. Ces dipôles peuvent être réorientés, en particulier, lorsqu'une perturbation sinusoïdale est appliquée $\phi_i(t)=\phi_i^0+\delta\phi_i(t)$. Les dipôles sont supposés à l'équilibre au minimum d'un potentiel harmonique $H_{trap}=k_i\delta\phi_i(t)^2/2$, $k_i$ étant la constante élastique. Ils interagissent avec le champ électrique ; l'interaction avec la composante ac, $E_{ac}(t)=E_{ac}\cos(\omega t)$, s'écrit $H_{int}=\mu_i\cos\phi_i(t)E_{ac}(t)$. Nous notons $\mu_{i\parallel} = \mu_i \cos\phi^0$ et $\mu_{i\perp}=\mu_i \sin\phi^0$ les composantes parallèle et perpendiculaire au champ électrique. Jusqu'à présent les dipôles sont vus comme des oscillateurs harmoniques dans un champ extérieur. Leur mouvement va être amorti du fait de leur interaction avec leur environnement matérialisé par un nombre infini d'oscillateurs harmoniques. Ces modes pourraient être par exemple les modes de vibration ou de rotation propres de la monocouche. Nous négligeons les interactions entre dipôles si bien que nous pouvons considérer l'Hamiltonien pour un dipôle isolé

$$H = \frac{J\delta\dot{\phi}(t)^2 + k\delta\phi(t)^2}{2} - \mu_\perp\delta\phi(t)E_{AC}(t) + \frac{1}{2}\sum_{\alpha=1}^{N} J_\alpha\delta\dot{\phi}_\alpha(t)^2 + k_\alpha\left(\delta\phi_\alpha(t) - \frac{c_\alpha}{k_\alpha}\delta\phi(t)\right)^2 \qquad (53)$$

Nous avons omis l'indice *i* pour alléger les notations. Seul le terme linéaire en $\delta\phi$ est conservé dans le terme d'interaction avec le champ électrique. $J$ est le moment d'inertie du dipôle. Le dernier terme de l'équation (53) caractérise le bain d'oscillateurs harmoniques ($N$ est le nombre de modes supposé « infini »). $J_\alpha$ et $k_\alpha$ sont les moments d'inertie et les constantes élastiques du mode $\alpha$, $c_\alpha$ est le terme de couplage linéaire entre le dipôle et ce mode. C'est un Hamiltonien de type Caldeira-Leggett dont l'ingrédient principal est le produit de la densité de modes avec le carré du terme d'interaction[52]

$$\gamma(\omega) = \sum_{\alpha=1}^{N} \frac{c_\alpha^2}{J_\alpha\omega_\alpha}\delta(\omega - \omega_\alpha) \qquad (54)$$

où $\omega_\alpha = \sqrt{k_\alpha / J_\alpha}$ .

A priori, un modèle similaire devrait aussi pouvoir être dérivé pour la contribution d'interface. Il conviendrait pour cela d'identifier le mécanisme de polarisation des défauts d'interface, les variables dynamiques correspondantes et de caractériser le bain dans lequel une partie de l'énergie électrique est dissipée. L'analyse détaillée ici pour la composante dipolaire devrait pouvoir s'étendre à celle des défauts d'interface avec des conclusions différentes puisque la fonction de réponse diffère.

A partir de l'Hamiltonien (53), nous pouvons écrire les équations du mouvement pour finalement obtenir, après élimination des variables du bain, une équation du type Langevin généralisé.[50]

$$J\delta\ddot{\phi}(t)+\int_0^t \eta(t-t')\delta\dot{\phi}(t')dt'+k\delta\phi(t)=\xi(t)+\mu_\perp E_{AC}(t) \tag{55}$$

où le terme de friction s'exprime à partir des caractéristiques du bain d'oscillateurs.[53]

$$\eta(t)=\sum_\alpha \frac{c_\alpha^2}{J_\alpha\omega_\alpha^2}\cos\omega_\alpha t=\int_0^{+\infty} d\omega\,\frac{\gamma(\omega)}{\omega}\cos\omega t=\eta_S f(t). \tag{56}$$

$f$ est une fonction sans dimension, $\eta_S$ le coefficient de friction (ou de Stoke). $\xi$ est une force aléatoire dont la fonction de corrélation est liée au terme de friction par le théorème fluctuation-dissipation

$$\langle\xi(t)\xi(t')\rangle=k_B T\eta(|t-t'|). \tag{57}$$

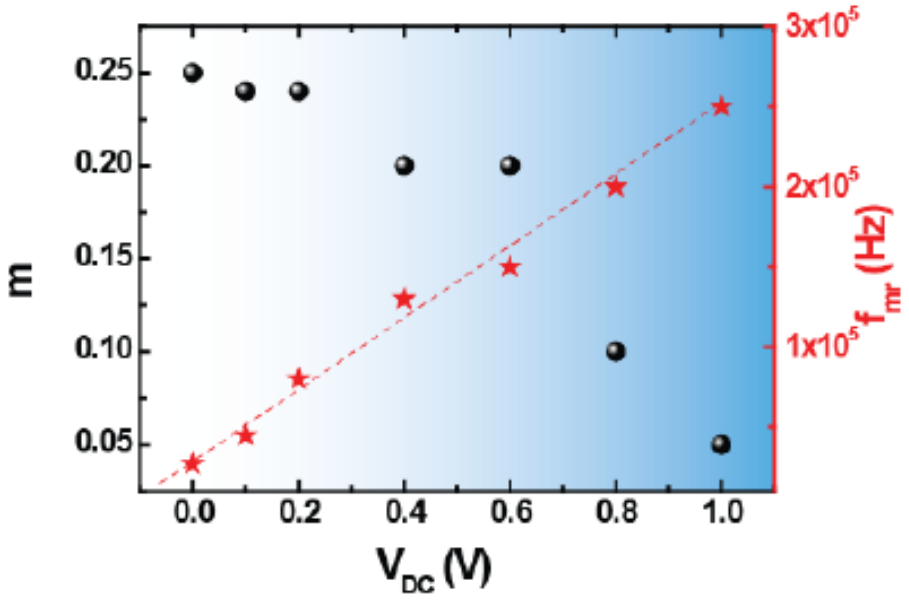


**Figure 23** : Evolution typique du paramètre $m$ de la susceptibilité dipolaire (Eq. (50)) et de $f_m=1/\tau$ en fonction de $V_{dc}$. La fréquence caractéristique suit la loi linéaire (60).

Ce formalisme permet de déterminer la susceptibilité, $\chi$, la réponse linéaire de l'oscillateur au champ électrique à partir des caractéristiques de l'environnement

$$\chi(\omega)=\frac{1}{k-j\omega\tilde{\eta}(-j\omega)} \tag{58}$$

où $\tilde{\eta}$ est la transformée de Laplace du terme de friction (Eq. (56)). L'amplitude et le temps caractéristique apparaissant dans les différentes expressions des susceptibilités s'expriment à l'aide des paramètres de l'équation du mouvement (55)

$$\chi_0=1/k \text{ et } \tau=\eta_S/k. \tag{59}$$

La composante continue du champ électrique est absorbée dans l'équation (55) en redéfinissant une nouvelle constante élastique $k \to k + \mu_{//} E_{dc}$ et une nouvelle variable dynamique $\delta\phi \to \delta\phi + \frac{\mu_{\perp}}{k + \mu_{//} E_{dc}}$. Ces transformations débouchent sur une relation linéaire entre la fréquence caractéristique du système et le champ électrique que nous avons vérifié expérimentalement (cf. Figure 23)

$$\frac{1}{\tau} = \frac{k + \mu_{//} E_{dc}}{\eta_A}. \tag{60}$$

La constante diélectrique des monocouches étant peu élevée nous avons négligé les corrections de champ local et avons donc identifié le champ vu par les moments dipolaires avec le champ appliqué. Avec cette approximation, la susceptibilité (50) est simplement liée à la réponse dipolaire que nous mesurons

$$\chi_{dip}(\omega) = \frac{\mathbf{M}\mu_{\perp}^{\,2}}{\varepsilon_{\mathbf{0}}} \chi(\omega). \tag{61}$$

M est le nombre de dipôles présents dans la monocouche.

A partir de l'équation (55), nous pouvons également montrer que cette susceptibilité est liée à la densité spectrale, $S(\omega)$, de la force aléatoire $\xi$

$$S(\omega) = 4k_B T \frac{\mathrm{Im}\,\chi(\omega)}{\omega|\chi(\omega)|^2}. \tag{62}$$

Cette expression souligne le fait qu'à partir des mesures d'admittance nous obtenons des informations sur l'environnement des dipôles. La force $\xi$ a pour origine les modes de vibration et/ou de rotation de la monocouche. Analyser cette densité spectrale devrait nous permettre d'obtenir des informations sur la structure de la monocouche. Dans le cas d'une réponse de type Cole-Cole dont nous sommes très proche, la densité spectrale peut se calculer pour donner

$$S(\omega) = S_{ColeCole}(\omega) = \frac{4k_B T}{\chi_0} \tau(\omega\tau)^{-n} \mathrm{Sin}(1-n)\frac{\pi}{2}. \tag{63}$$

Les molécules de la monocouche forment un réseau triangulaire. Calculer le spectre des modes de vibration et de rotation de la monocouche moléculaire est une tâche complexe. Cependant nous n'explorons dans nos expériences que les modes de faibles énergies et donc de grandes longueurs d'onde comparées à l'espacement entre molécules. Nous pouvons en principe, dans ces conditions, négliger les détails du réseau et décrire les propriétés mécaniques de la monocouche à l'aide d'une théorie élastique continue. Pour un réseau triangulaire, la théorie continue correspondante est bidimensionnelle avec un champ de déplacement qui est la somme de deux contributions indépendantes, longitudinale et transverse.[54] Pour chacune de ces composantes, nous pouvons écrire l'équation d'onde suivante

$$\left(\Delta + \frac{\omega^2}{v^2}\right) u(\vec{r}) = 0. \tag{64}$$

où $v$ est la vitesse du son appropriée. La densité d'état est alors une fonction linéaire de la fréquence

$$\rho(\omega) = \frac{1}{2\pi v^2}\omega\,. \tag{65}$$

En supposant que $c_\alpha = \bar{c}$ et $J_\alpha = \bar{J}$, nous pouvons simplifier l'équation (56) et obtenir une relation simple entre la densité de modes harmoniques et la densité spectrale de la force aléatoire de Langevin

$$\rho(\omega) = \frac{1}{L^2}\sum_n \delta(\omega - \omega_n) \approx \frac{\bar{J}}{L^2\vec{c}^{\,2}}\omega\gamma(\omega) = \frac{\bar{J}}{k_B T L^2 \vec{c}^{\,2}}\omega^2 S(\omega)\,. \tag{66}$$

A partir des résultats expérimentaux nous pouvons à l'aide de cette équation déterminer une densité de modes harmoniques. Deux exemples sont représentés sur la Figure 24 et comparés à l'expression (65) valable pour une monocouche idéale. Il est suggéré, basé sur des résultats connus,[55] que l'écart entre densités réelles et idéales est dû à la présence de désordre, important dans la structure de la monocouche organique.

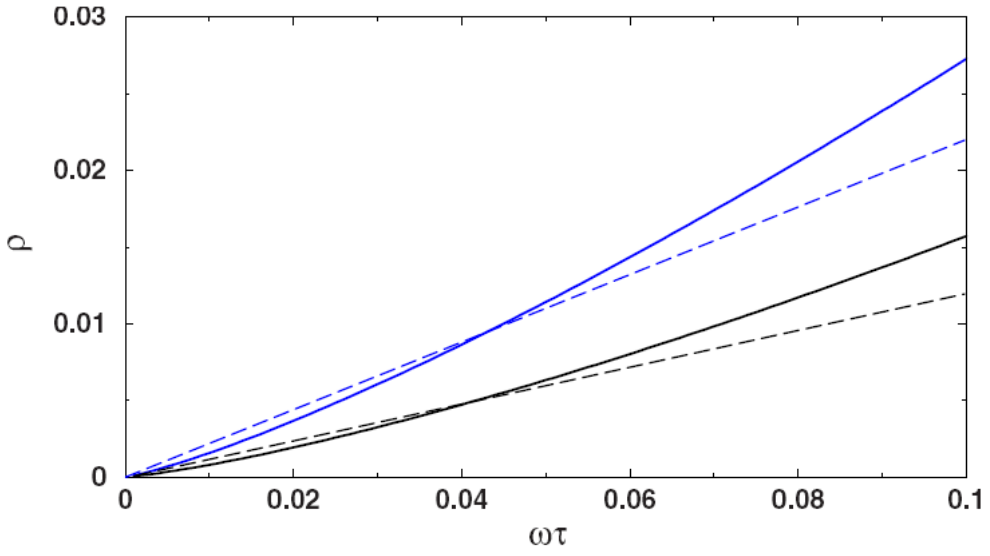


**Figure 24** : Densités de modes harmoniques obtenues à partir de l'équation (66) pour une jonction OD (courbe bleue) et une jonction OTS (courbe noire) à champ électrique nul. Les courbes hachurées sont les densités dans le cas de monocouches idéales (Eq. (65)).

D'autre part, à partir de l'équation (66) nous pouvons définir la densité de modes harmoniques correspondant à une réponse dipolaire de type Cole-Cole (Eq. (63)). Nous obtenons

$$\rho(\omega) = \rho_{ColeCole}(\omega) = \frac{4\bar{J}\tau^{1-n}}{L^2\vec{c}^{\,2}\chi_0}\omega^{2-n}\,\mathrm{Sin}(1-n)\frac{\pi}{2}\,. \qquad (67)$$

La réponse que nous obtiendrions dans le cas d'une monocouche idéale s'obtient en posant n=1 dans les équations (63) et (67), ce qui donnerait une densité spectrale nulle. Dans le cadre de nos approximations, nous pouvons suggérer que la dissipation d'énergie électrique, mesurée dans nos expériences de spectroscopie d'admittance, serait due à la présence de désordre dans la monocouche organique.

Ces différentes observations montrent qu'il pourrait être instructif de considérer parallèlement à l'admittance complexe, des mesures purement mécaniques du module d'Young ou de la vitesse du son des monocouches, par exemple.

## 6. Bruits basses fréquences de courant tunnel. Bruit de polarisation.

Précédemment nous avons adopté une interprétation standard du bruit de courant tunnel basses fréquences comme étant la somme de fluctuations de systèmes à deux niveaux répartis suivant une distribution large de fréquences caractéristiques. Cette interprétation parait insatisfaisante pour plusieurs raisons. (i) La nature physique de ces systèmes à deux niveaux demeure inconnue. (ii) Des hypothèses arbitraires sur leur distribution en temps caractéristiques et en énergie sont nécessaires. (iii) Plus important, pour reproduire la large amplitude du signal observé, une densité totalement irréaliste de défauts doit être considérée : pour certains résultats nous avons recours à un nombre de défauts supérieur au nombre d'atomes constituants la monocouche ! Nous devons chercher une autre origine pour ce bruit.

Nous considérons une jonction hypothétique débarrassée de ses défauts d'interface, c'est-à-dire que nous ne considérons que la partie dipolaire de la susceptibilité ; en pratique, nous avons montré récemment que des recuits sous atmosphère contrôlée pouvait réduire de façon conséquente la densité de défauts et qu'il ne parait donc pas irréaliste de se rapprocher de cette limite.

La densité spectrale des fluctuations de potentiel aux bornes d'une capacité macroscopique est donnée par la formule de Nyquist[56]

$$S_V(\omega) = 4k_B T \frac{\mathrm{Im}\, C(\omega)}{\omega |C(\omega)|^2}. \tag{68}$$

Dans ce cas, les fluctuations de tension sont dues uniquement à des fluctuations de polarisation causées par les mouvements thermiques des molécules. Ces fluctuations de tension ont deux effets : (i) elles produisent des fluctuations de courant de déplacement aux bornes de la capacité représentées par la densité spectrale suivante[56]

$$S_I^P(\omega) = 4k_B T \omega\, \mathrm{Im}\, C(\omega), \tag{69}$$

(ii) elles produisent également des fluctuations du courant tunnel qui traverse la jonction. En supposant, par simplicité, la résistance tunnel constante, une relation simple peut être écrite entre les fonctions de corrélation de fluctuations de courant et de tension

$$\langle \delta I(t) \delta I(t') \rangle = \left( \frac{\partial I}{\partial V} \right)^2 \langle \delta V(t) \delta V(t') \rangle \tag{70}$$

où $\delta O(t) = O(t) - \langle O \rangle$. Il en découle une relation simple entre les densités spectrales de courant tunnel et de tension

$$S_I(\omega) = \left( \frac{\partial I}{\partial V} \right)^2 S_V(\omega). \tag{71}$$

Nous considérons la somme des deux contributions et la comparons à des résultats typiques (cf Figure 25). Nous pouvons observer que (i) la loi de puissance est bien reproduite mais pas l'amplitude : un facteur d'environ $10^3$ est manquant. (ii) Les fluctuations de courant de

déplacement ne sont observables qu'à hautes fréquences. Afin d'améliorer l'accord il conviendrait (i) de considérer les défauts d'interface qui peuvent contribuer à augmenter le bruit comme nous l'avons vu précédemment, (ii) d'aller au-delà de l'équation (70) qui néglige les fluctuations de résistance qui très certainement accompagnent les fluctuations de polarisation.

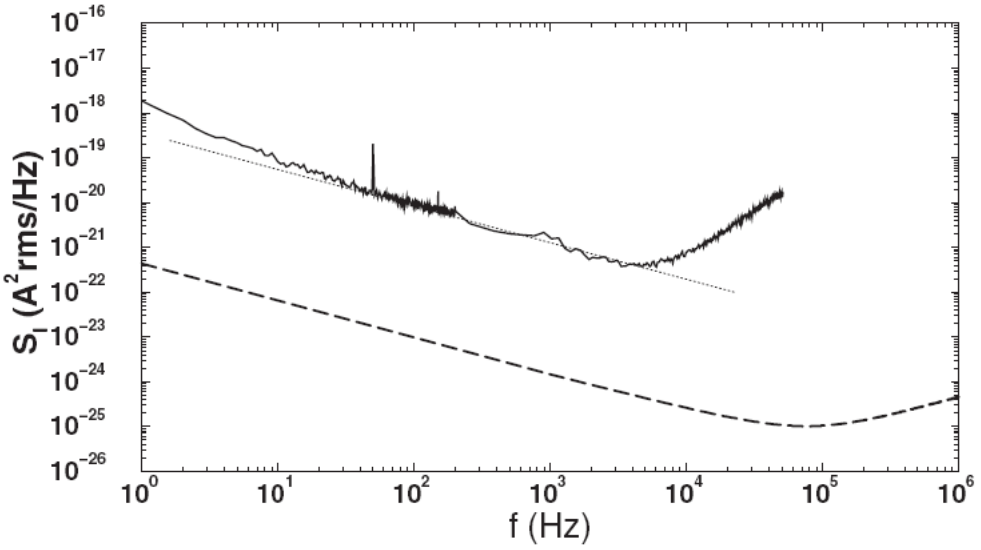


**Figure 25** : Densité spectrale du bruit de courant tunnel pour une jonction à base d'OD à $V_{dc}$ = 0.8 V. Les résultats expérimentaux sont en trait plein, l'estimation basée sur les équations (68) et (71) en trait hachuré.

## B Jonctions Métal/Oxyde/Semiconducteur Organique.

Nous considérons dans ce chapitre et, dans toute la suite, des composants différents basés sur des films minces de pentacène, qui est un des matériaux les plus utilisés dans le domaine de l'électronique organique. Il est relativement aisé à déposer et les performances obtenues par les transistors à effet de champ (OFET, Organic Field Effect Transistor) sont parmi les meilleures, comparables à celles obtenues avec des transistors basés sur du silicium amorphe.[57] La structure du film mince est complexe et est encore étudiée aujourd'hui : elle dépend du substrat utilisé et des conditions de dépôt. Dans tous les cas, le film mince est polycristallin avec des domaines de quelques centaines de nanomètres (Cf. Figure 26).

Les OFETs témoignent d'une bonne mobilité (jusqu'à ~ 1 $cm^2$ $V^{-1}$ $s^{-1}$) mais les mécanismes de transport restent mal compris. Le pentacène étant fortement polarisable, les porteurs de charge sont très probablement des polarons. Cependant, au vue de la structure granulaire des films minces il est probable que les mécanismes de transport soient dominés par le transfert de charges d'un domaine à l'autre.[58] Aussi, beaucoup d'approches théoriques se basent sur du transport par sauts assistés thermiquement dans un milieu désordonné ; la distribution en énergie des états localisés sur les grains est alors la quantité la plus importante. [58,59]

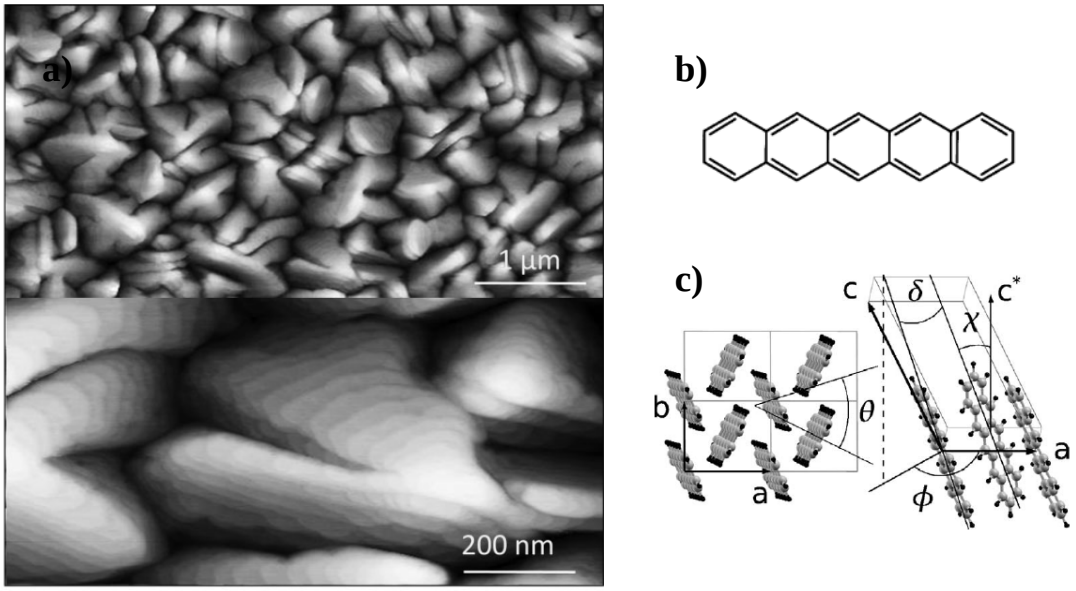


**Figure 26** : Illustrations de la structure des films minces de pentacène : a) images de microscopie à force atomique pour deux résolutions différentes montrant la structure polycristalline, b) schéma d'une molécule de pentacène et c) possibles caractéristiques structurelles du film mince (les détails sont donnés dans la référence (60)).

Les transistors organiques à effet de champ témoignent en général d'une grande variabilité dans leurs performances à la manière des monocouches organiques présentées ci-dessus. De plus, les caractéristiques de ces transistors ne sont pas stables dans le temps. Par exemple, lorsqu'on maintient la tension de grille constante pendant un certain temps les caractéristiques des composants, telle que la tension de seuil, évoluent. Ces effets sont connus sous l'appellation « bias stress effects » et sont actuellement très étudiés car il convient de

comprendre l'origine de ces instabilités pour pouvoir envisager des applications. Plusieurs origines possibles ont été avancées.[61] Certaines d'entre elles sont intrinsèques, invoquant des piégeages de charges dans des défauts à l'interface oxyde/organique[62] ou dans l'organique au niveau des joints de grains (cf. Figure 26) ou dans sa structure même qui est très désordonnée,[63-65] ou des scénarios plus exotiques telle que la transformation de deux polarons libres en un bipolaron localisé dans l'espace.[66] D'autres sont extrinsèques invoquant, par exemple, la formation de protons au cours de réactions chimiques entre porteurs libres et molécules d'eau adsorbées sur la surface de l'oxyde suivies d'une diffusion de ces ions dans l'oxyde.[67,68]

Dans ce contexte, nous effectuons diverses mesures dynamiques sur des transistors ou des jonctions capacitives à base de films minces de pentacène. Ces différentes expériences consistent à (i) mesurer la relaxation de charges créées dans le canal d'un transistor à l'aide de pulses appliqués sur la grille, (ii) mesurer la capacité en fonction du temps en maintenant une tension constante aux bornes d'une jonction capacitive et, (iii) à mesurer l'admittance complexe de ces mêmes jonctions. Au niveau théorique, l'analyse de ces données expérimentales s'oriente vers la description de mécanismes de diffusion fractionnaire, propres aux matériaux amorphes.[69,70]

L'ensemble constitue le thème de la thèse de Romuald Ledru dont la soutenance est prévue fin 2012. Dans ce chapitre nous présentons uniquement les mesures d'admittance de jonctions Métal/Oxyde/semiconducteur organique, jonctions capacitives, qui font l'objet de la Référence V.

## 7. Spectroscopie d'admittance de jonctions organiques MOS. Courant de diffusion fractionnaire et réponses dipolaires.

Nous considérons des jonctions schématisées sur la Figure 27, avec ~ 70 nm d'oxyde et ~ 40 nm de pentacène, et mesurons leur admittance complexe en faisant varier la tension $V_{dc}$ entre -20 et +20V. L'ensemble des mesures est effectué à l'ambiante. Un exemple typique est représenté sur la Figure 27. Nous avons systématiquement effectué les mêmes mesures sur des jonctions, dites « de référence », $Si^{+}$/Oxyde/Au, obtenues sur les mêmes plaquettes en protégeant l'oxyde lors du dépôt de pentacène. Le résultat obtenu pour la jonction de référence correspondant à la jonction organique étudiée est également reporté sur la même figure. L'admittance s'écrit comme précédemment, avec les mêmes conventions

$$\frac{Y(\omega)}{\omega} = j\left(C'(\omega) - jC''(\omega)\right) = j\left(\chi'(\omega) + C_{\infty}\right) + \chi''(\omega). \qquad (72)$$

Comparé à l'expression pour les monocouches (Eq. (47)), nous avons ici $G_T$=0 : la couche d'oxyde est trop épaisse pour qu'il y ait du courant tunnel. Nous trouvons que la susceptibilité diélectrique comprend trois composantes indépendantes

$$\chi(\omega) = \chi_{SiO_2}(\omega) + \chi_{organic}(\omega) + \chi_{Ion}(\omega). \qquad (73)$$

Les deux premières composantes sont de type dipolaire. Leur dépendance avec $V_{\mathrm{dc}}$ nous permet de les localiser spatialement dans la jonction.

- En régime d'accumulation, $V_{\mathrm{dc}} \gtrsim 5$ V, (Figures 27, 28.a et 28.b), seul le volume de l'oxyde est sondé, le reste étant écranté par les charges libres accumulées à l'interface. Nous n'observons que la composante, $\chi_{SiO_2}$ de l'équation (73). Pour les jonctions références, c'est également la seule contribution dipolaire observée mais pour toute la gamme de tension. Les caractéristiques dynamiques sont les mêmes dans les deux cas avec toutefois un léger déplacement de la fréquence de coupure vers les basses fréquences pour les jonctions organiques, ce qui est normal d'après l'équation (60) puisque le champ électrique vu par ces défauts n'est pas identique dans les deux cas. Par contre, pour chaque type de jonctions, aucune dépendance en tension de la fréquence de coupure n'est observée. Toujours d'après l'équation (60), nous pouvons en conclure que les dipôles portés par les défauts sondés ne sont pas alignés selon une direction préférentielle. En conclusion, cette contribution est donc identifiée comme étant due à des défauts de type dipolaire situés dans le volume de l'oxyde sans qu'aucune direction particulière ne soit privilégiée. Leur susceptibilité est de type Debye

$$\chi_{SiO_2}(\omega) = A_{SiO_2}\left(1 - j\omega\tau_{SiO_2}\right)^{-1}. \qquad (74)$$

  avec une fréquence caractéristique difficile à évaluer dans nos expériences mais telle que $1/\tau_{Organic} \gtrsim 10^6$ Hz ; l'amplitude est très variable.

- Lorsque nous diminuons la tension appliquée, nous diminuons le nombre de porteurs accumulés à l'interface organique/oxyde et entrons progressivement dans le régime de

déplétion : nous sondons alors aussi l'interface organique/oxyde et le volume de l'organique. La deuxième composante dipolaire devient alors sensible (Figures 27, 28.c et 28.d). Contrairement à la composante dipolaire précédente nous notons une dépendance en tension de la fréquence de coupure : elle se déplace vers les basses fréquences lorsqu'on diminue la tension d'où nous pouvons conclure, d'après l'équation (60), que les dipôles de ces défauts sont préférentiellement orientés vers la surface d'or. Leur susceptibilité est de type Cole-Cole

$$\chi_{Organic}(\omega) = A_{Organic}\left(1+\left(-j\omega\tau_{Organic}\right)^{\alpha}\right)^{-1}, \qquad (75)$$

avec $\alpha$ variant entre 0.5 et 0.6, la fréquence caractéristique, $1/\tau_{Organic}$, étant de l'ordre de $10^3$-$10^4$ Hz. $A_{Organic}$ est très variable d'un échantillon à l'autre.

La dernière composante est de nature différente : elle se comporte en loi de puissance $(j\omega)^{-\sigma}$ (avec $0 \leq \sigma \leq ½$). Ce genre de comportement se rencontre le plus souvent dans les systèmes où la polarisation est due à des courants de charges lentes.[71] De plus, il a été observé dans des hétérostructures que ce type de réponse était lié à la présence d'une fine couche d'eau adsorbée à l'une des interfaces.[71] Les systèmes que nous étudions présentent ces caractéristiques. Ce sont des hétérostructures et nos expériences sont toutes faites à atmosphère ambiante : des molécules d'eau de l'environnement peuvent alors diffuser au travers du film organique pour finalement réagir avec les liaisons Si-H de la surface d'oxyde pour s'y adsorber. Ces processus d'oxydation ont été étudiés et décrits dans la Réf. (68). En présence de charges libres positives (h), des protons $H^+$ peuvent être alors produits au niveau de cette fine couche d'eau par le système de deux réactions couplées suivant $2H_2O + 4h \rightarrow 4H^+ + O_2(g)$ et $2H^+ \rightarrow 2h + H_2(g)$, proposé dans la Réf. (68). Les protons alors créés vont diffuser au travers de l'oxyde et modifier la capacité de la jonction qui devient une fonction du temps $C(t)$. Ce scénario a été proposé comme origine possible à l'évolution de la tension de seuil des transistors organiques lorsqu'une tension de grille est maintenue constante. Il est compatible avec nos résultats mais à condition de considérer des mécanismes de diffusion pour les protons dans l'oxyde, fractionnaires et non pas normaux comme dans la référence (68). Ces mécanismes sont en effet clairement mis en évidence dans nos mesures.

Nous définissons $p(x,t)$ la densité volumique de protons dans l'oxyde à une distance $x$ de l'interface organique/oxyde. Les protons sont supposés suivre à travers l'oxyde une marche au hasard avec un temps de résidence sur un site, après chaque saut effectué, distribué selon une loi de puissance. Autrement dit, la particule peut éventuellement rester piégée sur le même site infiniment longtemps. Ce type de marche au hasard est caractéristique des matériaux amorphes. Elle peut-être décrite – dans la limite des temps longs – à l'aide de l'équation de diffusion fractionnaire[70,72]

$$\frac{\partial p(x,t)}{\partial t} = {}_0D_t^{1-\beta} K_\beta \frac{\partial^2 p(x,t)}{\partial x^2} = \frac{K_\beta}{\Gamma(\beta)} \frac{\partial}{\partial t} \int_0^t dt' \frac{1}{(t-t')^{1-\beta}} \frac{\partial^2 p(x,t')}{\partial x^2}. \qquad (76)$$

${}_0D_t^{1-\beta}$ est l'opérateur fractionnaire de Riemann-Liouville dont la définition est donnée avec la seconde égalité. $\beta$ est une constante telle que $0 \leq \beta \leq 1$, $\Gamma$ est la fonction Gamma et $K_\beta$, de dimension $cm^2.s^{-\beta}$, généralise le coefficient de diffusion au cas anormale, ou fractionnaire. Le

paramètre $\beta$ contrôle la dynamique des ions, le cas $\beta = 1$ correspondant à la diffusion normale. Nos expériences permettent de le mesurer.

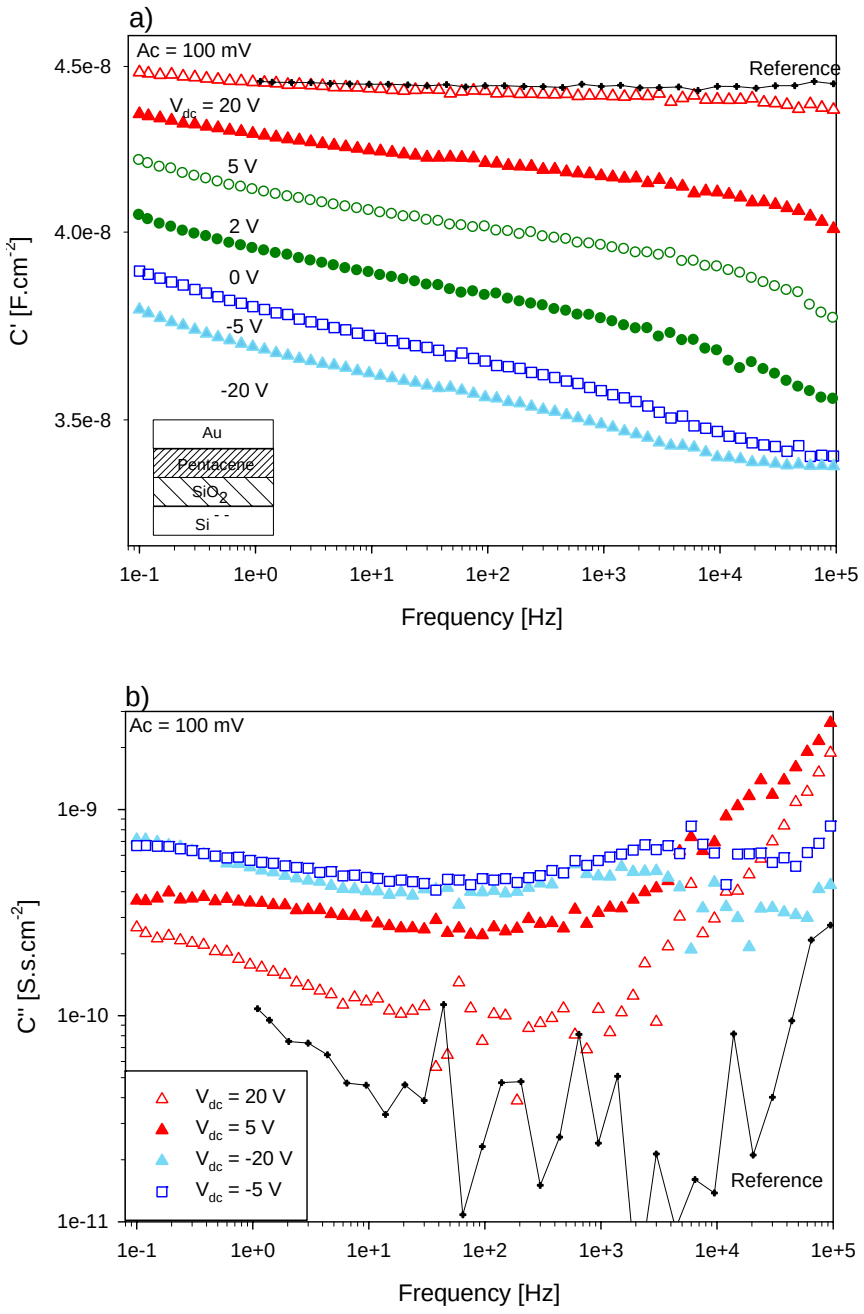


**Figure 27** : Partie réelle et imaginaire de la capacitance d'une jonction organique représentée en encart, pour plusieurs tensions $V_{dc}$. L'amplitude du signal ac est de 100 mV. La réponse de la jonction de référence (voir texte) est aussi représentée : elle est indépendante de $V_{dc}$. En régime d'accumulation la capacité de la jonction organique coïncide avec celle de la référence comme il se doit.

La densité volumique doit aussi respecter la loi de conservation de charges

$$\frac{\partial p(x,t)}{\partial t} = -\frac{\partial J_\beta(x,t)}{\partial x}. \tag{77}$$

$J_\beta$ est le courant de diffusion généralisé au cas anormal.

Le temps nécessaire pour un proton pour traverser une épaisseur d'oxyde, $L$, de 70 nm peut être estimé en utilisant la valeur du coefficient de diffusion donnée dans la Réf. (68) à environ $10^7$s. Par conséquent, durant toute la durée des expériences les protons restent très proches de l'interface organique/oxyde. Dans ces conditions, nous pouvons écrire une relation simple en supposant que les changements de capacité sont proportionnels au nombre de protons contenus dans l'oxyde

$$C(t) = C(0) - A_C \int_0^L dx\, p(x,t). \tag{78}$$

$A_c$ est une constante mesurant cet effet. Cette approximation est équivalente à celle employée dans la Réf. (68) pour décrire l'évolution de la tension de seuil des OFETs lorsqu'une tension de grille est maintenue constante. En prenant la dérivée temporelle de l'expression (78), nous obtenons, en utilisant la loi de conservation de charges (77),

$$\dot{C}(t) = -A_C J_\beta(0,t), \tag{79}$$

où le courant de diffusion ionique est considéré à l'interface organique/oxyde (x=0). Pour dériver l'équation (79) nous avons supposé $J_\beta(L,t) = 0$ puisque les ions demeurent proche de l'autre interface.

Les ions diffusent continuellement à travers l'oxyde. Appliquer un faible potentiel ac introduit une perturbation à la contribution principale. Nous écrivons donc

$$p(x,t) = p_0(x,t) + p_1(x,t). \tag{80}$$

$p_0$ est la composante dc, $p_1$ la perturbation ac. Le potentiel électrique à l'interface organique/oxyde, $\psi$, peut être décomposé de la même façon

$$\psi(t) = \psi_0(t) + \psi_1(t). \tag{81}$$

Pour déterminer l'admittance associée au courant ionique nous n'avons à prendre en compte que les termes ac, $p_0(x,t)$ et $\Psi_0(t)$ peuvent en effet être considérés comme constants durant le temps des expériences. Prenant la transformée de Laplace de l'équation (79) donne

$$\chi_{Ion}(s) = -\frac{A_C}{s} Y_{Ion}(s) \tag{82}$$

où l'admittance associée au courant ionique est définie par

$$Y_{Ion}(s) = \frac{\tilde{J}_\beta(0,s)}{\tilde{\psi}_1(s)}. \tag{83}$$

$\tilde{J}_\beta(0,s)$ et $\tilde{\psi}_1$ sont les transformées de Laplace du courant de diffusion, $J_\beta$, considéré en $x = 0$ et de $\Psi_1$. L'équation (83) a été résolue dans la référence (73) en supposant une relation linéaire entre $p_1(x,t)$ considéré en $x = 0$ et $\psi_1(t)$. Dans le cas d'une réaction électrochimique idéale il est possible d'écrire[74]

$$\psi_1(t) = \frac{k_B\theta}{p_0(0,0)} p_1(0,t). \tag{84}$$

Différentes conditions aux limites ont été considérées sur l'autre interface. Cependant, elles n'influent pas les résultats dans le domaine de fréquences que nous étudions. Dans le cas d'une condition aux bords absorbante $p_1(L,t)=0$, le résultat est

$$\chi_{Ion}(\omega) = -\frac{A_c}{j\omega} Y_{Ion}(\omega) = \frac{qk_B\theta K_\beta}{L} \frac{\omega_d^{1-\beta}}{p_0(0,0)} \left(\frac{-j\omega}{\omega_d}\right)^{-\beta/2} \frac{1}{\tanh\left((-j\omega/\omega_d)^{\beta/2}\right)}. \tag{85}$$

où $\omega_d = \left(K_\beta / L^2\right)^{1/\beta} \approx 10^{-7}$ Hz. Dans la limite où $\omega/\omega_d \to +\infty$

$$\chi_{Ion}(\omega) \approx q \frac{k_B T K_\beta}{L} \frac{\omega_d^{1-\beta}}{p_0(0,0)} \left(\frac{-j\omega}{\omega_d}\right)^{-\beta/2} = A_{Ion}(-j\omega)^{-\beta/2}, \tag{86}$$

équation que nous aurions obtenue avec d'autres conditions aux bords.

L'équation (86) permet de reproduire avec un bon accord l'ensemble de nos résultats expérimentaux. Nous obtenons différents comportements suivant l'interface considérée. (i) Pour les jonctions de référence nous obtenons $\beta = 1$, ce qui correspond à un terme de diffusion normal. (ii) Pour les jonctions organiques nous obtenons $\beta = 0.4$, soit une diffusion anormale, valeur reproductible, à peu près identique sur l'ensemble des jonctions étudiées. D'autre part, nous constatons que l'amplitude $A_{Ion}$ augmente lorsque $V_{dc}$ diminue (Cf. Figure 28.f). Cette variation peut s'expliquer avec l'équation (86) où $A_{Ion}$ est inversement proportionnelle à $p_0(0,0)$, la densité initiale de protons à l'interface. Or, d'après les réactions chimiques supposées permettant la production de protons, la densité $p_0(0,0)$ doit être proportionnelle à la densité de porteurs libres qui est contrôlée par $V_{dc}$. $A_{Ion}$ est donc inversement proportionnel à la concentration de charges à l'interface et doit décroître lorsque $V_{dc}$ diminue.

La réponse diélectrique des différentes espèces participant à la polarisation dépend d'une façon cruciale de leur environnement et de leur interaction avec lui. Suivant les caractéristiques de ce bain, la réponse sera modifiée. Ainsi dans le cas d'un bain 'sans mémoire' (markovien) où les effets des perturbations sont instantanément absorbés et oubliés pour retourner à l'équilibre, les réponses dipolaires sont de type Debye et les courants ioniques suivent une loi de diffusion normale. Dans le cas contraire d'un bain 'avec mémoire' (non-markovien) où l'état du système à un instant $t$ dépend de toute son histoire, les réponses seront plus complexes. Nous en avons vu des exemples dans le cas où les espèces polarisantes

sont localisées dans l'organique ou à l'interface avec celui-ci : les réponses dipolaires sont de type Cole-Cole et la diffusion ionique devient fractionnaire. La raison de ces changements de comportements entre les films minces de pentacène et l'oxyde de silicium restent à comprendre.

Finalement, nous obtenons les caractéristiques $C_\infty$-$V_{dc}$ (Cf. eq. (72)) qui contiennent la réponse diélectrique d'une jonction idéale, sans défauts dipolaires d'aucune sorte et sans courants ioniques dont les contributions ont été extraites au terme de notre analyse. Un exemple est donné sur la Figure 28.e. Nous obtenons ainsi des courbes modèles d'un système où les propriétés électrostatiques sont contrôlées par des particules complexes, les polarons. Par exemple, nous notons que la zone de transition entre le régime d'accumulation et de déplétion est bien plus douce que celles observées dans les capacités MOS classiques où les charges libres sont des quasi-électrons ou des quasi-trous.

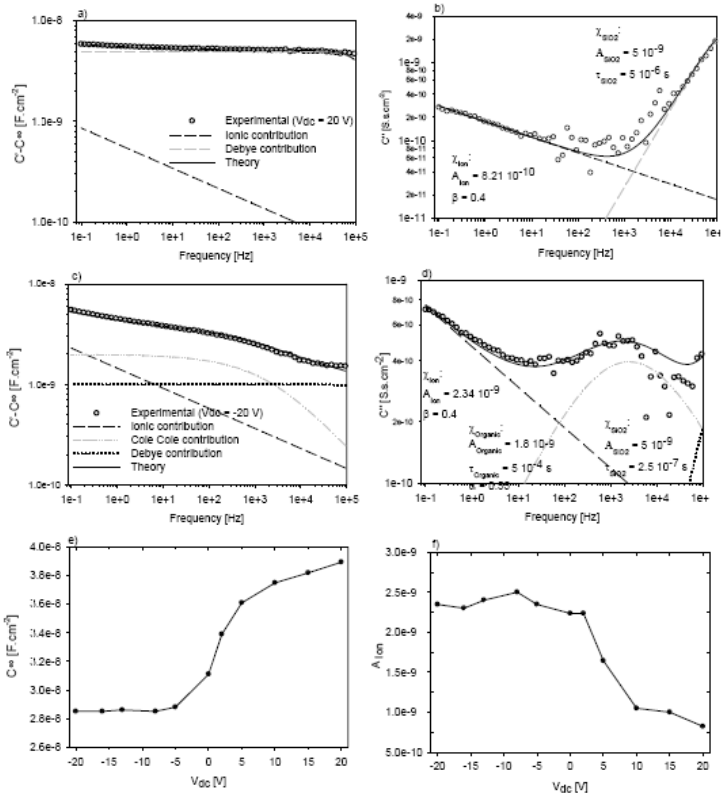


**Figure 28** : Parties réelles et imaginaires de la capacitance a) et b) dans le régime d'accumulation ($V_{dc}$=20 V), c) et d) dans le régime de déplétion ($V_{dc}$=-20 V). Dans les deux cas, la réponse est décomposée en trois contributions (voir texte) ; les paramètres de ces contributions sont inclus directement sur les figures. e) Courbe $C_\infty$-$V_{dc}$ contient la réponse des espèces rapides (polarons,…). f) Evolution de l'amplitude du courant ionique qui est inversement proportionnelle à la densité de porteurs libres.

# Partie III :

# Dispositifs neuromorphiques.

Est-il possible de concevoir une nouvelle électronique inspirée du monde du vivant où nous savons que les entités, prises séparément (synapses, neurones,…) sont infiniment lentes devant les composants silicium mais qui, assemblées, peuvent résoudre des tâches très complexes infiniment rapidement ? Le secret réside dans les connections multiples et les interactions dynamiques entre les différents éléments. La tentation est grande avec les composants organiques de s'orienter dans cette direction car ils sont beaucoup plus lents que les composants inorganiques et, d'autre part, souffrent d'un manque de reproductibilité d'un système à l'autre qui rend les applications classiques difficiles. Dans un réseau de neurones, les déficiences de certains éléments sont, en quelque sorte, absorbées dans la dynamique de l'ensemble. D'autre part, les composants organiques ont des avantages, surtout au niveau de leur conception, comme nous le montrons dans ce travail qui fait l'objet des références VI et VII.

En effet, il est possible de réaliser des synapses artificielles à l'aide de la technologie CMOS mais cela requiert au minimum sept transistors, ce qui pose un problème pour réaliser des circuits neuromorphiques où les synapses seront les composants les plus nombreux. Nous avons élaboré un composant (Figure 29) qui se comporte à lui seul comme une synapse biologique. Sa structure de base est un OFET classique à base de pentacène (la longueur de canal $L$ varie de 200 nm à 20 µm, la largeur de canal est de l'ordre de 100 µm). Au préalable des nanoparticules (NP) d'or, de diamètres allant de 5 à 20 nm, ont été déposées et fixées sur la surface de l'oxyde (par chimie de surface). Ces nanoparticules vont jouer le rôle de nano capacitances. Des charges peuvent y être piégées et dé-piégées suivant les potentiels appliqués aux électrodes. Les charges stockées vont modifier la résistance du canal par effet capacitif. D'autre part, le nombre de charges à l'intérieur des nanoparticules à un certain instant dépend de l'historique des perturbations électriques qu'a subi le composant : les nanoparticules agissent comme une mémoire. Dans un même élément, nous avons allié une unité de mémoire, les nanoparticules, et une unité de calcul, le transistor. Ce schéma est différent des machines usuelles où ces unités sont physiquement séparées. Nous avons baptisé notre composant Nanoparticle Organic Memory Field Effect Transistor (NOMFET).

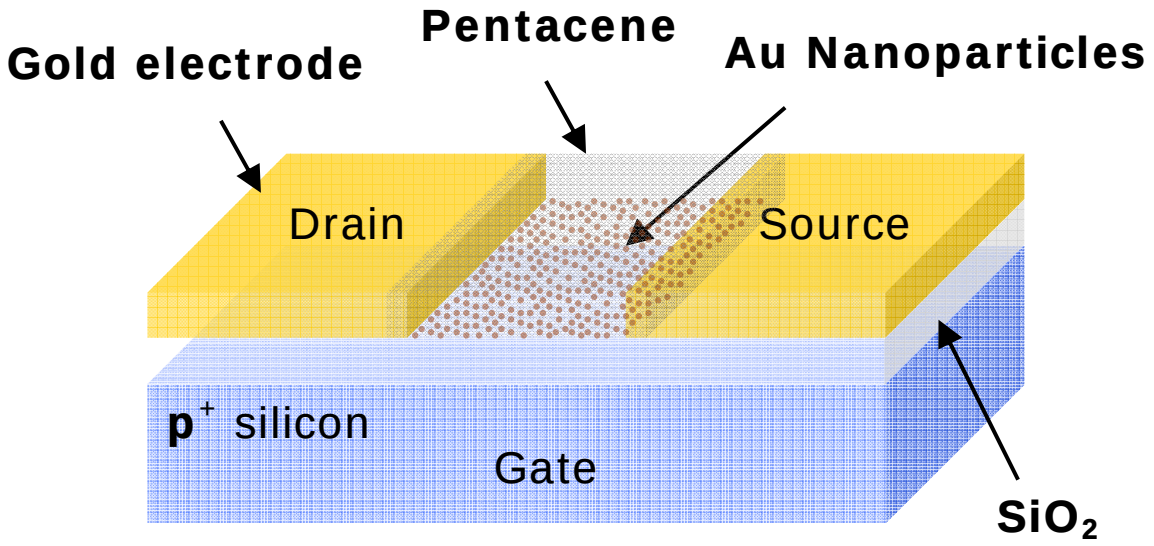


**Figure 29** : Schéma du NOMFET. C'est un transistor à effet de champ organique à base de pentacène (OFET) mais où des nanoparticules d'or identiques, d'un diamètre entre 5 et 20 nm, encapsulées ont été auto-assemblées sur la surface de l'oxyde.

Nous avons étudié son comportement en soulignant des analogies avec certaines synapses biologiques.

Dans ce travail nous ne nous sommes pas focalisés sur l'aspect 'matériaux' du NOMFET pour nous concentrer sur l'aspect dynamique afin de démontrer avant tout sa pertinence en tant que composant de base pour élaborer des dispositifs neuromorphiques. Nous avons voulu faire des démonstrations de principe en prenant soin toutefois de proposer différentes pistes que nous avons testé pour améliorer les performances du NOMFET ou modifier ses caractéristiques. Ainsi, les résultats présentés ici sont basés sur des dispositifs macroscopiques (canal de ~ 1 à 10 μm) mais nous avons pris soin de démontrer son fonctionnement avec un canal de quelques centaines de nanomètres. D'un point de vue théorique, un effort particulier a été fait pour simuler nos expériences de mesures à l'aide de modèles – calqués sur ceux utilisés en biologie – suffisamment simples pour pouvoir être adaptés à des programmes simulateurs de circuits.

## 8. Comportements synaptiques du NOMFET. Plasticité à courts termes.

Une synapse biologique transmet un potentiel d'action d'un neurone, N1, vers un autre, N2. L'état interne de la synapse va évoluer en fonction des signaux reçus de N1 et N2 ce qui va déterminer la façon dont elle va traiter l'information. Un exemple relativement simple de comportements synaptiques correspond au fonctionnement du NOMFET. En réponse à un pulse de potentiel d'action de N1, la synapse transmet un flux de neurotransmetteurs qui va être transformé en un nouveau pulse par N2. L'intensité du flux transmis à un instant $t$ va dépendre de la quantité de neurotransmetteurs disponibles à cet instant dans la synapse. Or, il lui faut un certain temps $\tau_r$ pour reformer sa population initiale après une décharge. La réponse de la synapse à un train de pulse va donc dépendre de l'intervalle, $T$, entre deux pulses. Si $T \ll \tau_r$, après chaque pulse la synapse n'a pas le temps de reconstituer sa population initiale de neurotransmetteurs avant l'arrivée du deuxième pulse. La population de neurotransmetteurs va continuellement décroitre ainsi que l'amplitude du signal transmis : on dit que la synapse a un comportement dépressif. Au contraire, si $T \gg \tau_r$, la population de neurotransmetteurs va augmenter entre chaque pulse et le signal sera de plus en plus intense : on dit alors que la synapse a un comportement facilitateur.[75-77] Ces propriétés définissent la plasticité à court terme des synapses. Nous avons montré que le NOMFET pouvait avoir le même type de comportements, les charges piégées dans les nanoparticules jouant le rôle des neurotransmetteurs.

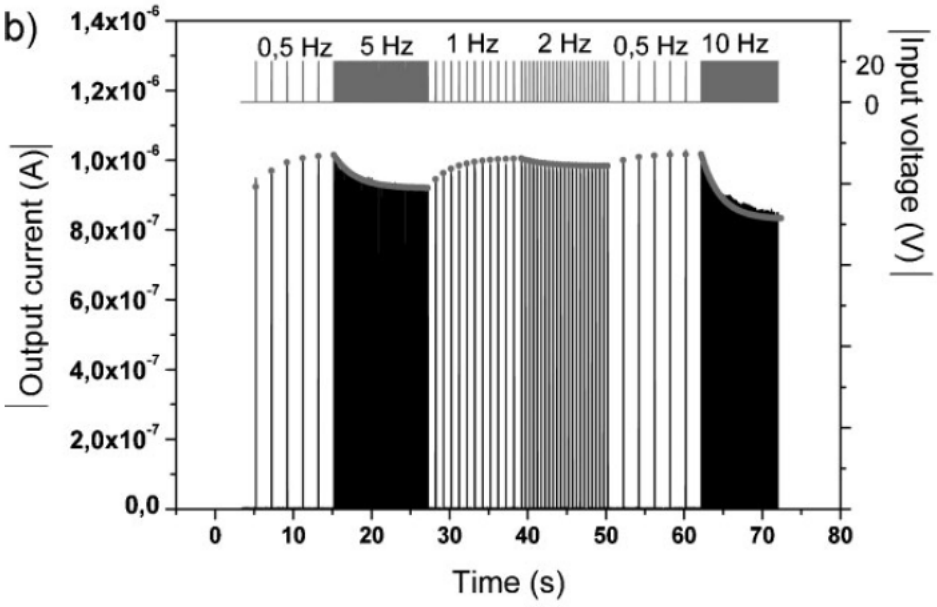


**Figure 30** : En haut, exemple de train de pulses envoyé sur la grille et la source d'un NOMFET ($L/W$ = 12 µm/113 µm, NP de 5 nm de diamètre), ici des séquences successives de fréquences variables notées sur le schéma et d'amplitude $V_P$= -30 V. En bas, le courant source-drain correspondant. Nous notons des zones de dépression où le courant chute, et des zones facilitatrices où le courant augmente dépendant de la fréquence du train de pulses.

Pour démontrer cette propriété, le NOMFET est utilisé comme un composant à deux terminaux : la source et la grille reçoivent le même signal, un train de pulses de fréquences $1/T$ et d'amplitude $V_P$ (Cf. Figure 30). Nous mesurons le courant source-drain, l'équivalent du flux de neurotransmetteurs. Un exemple est montré sur la Figure 30 où le signal envoyé est une succession de trains de pulses de même amplitude, $V_P$= -30 V, mais de fréquences différentes (0.5 Hz, 5 Hz, 1 Hz, 2 Hz, 0.5 Hz et 10 Hz). Le courant mesuré montre un comportement qui dépend de la fréquence de l'excitation : à hautes fréquences (2 Hz, 5 Hz et 10 Hz) nous observons des zones de dépression où le courant diminue et à basses fréquences (0.5 Hz et 1 Hz) des zones facilitatrices où le courant augmente. Nous avons développé un modèle inspiré de ceux trouvés en biologie pour comprendre nos résultats.[77]

*Modèle de Vissenberg et Matters. Effets des charges piégées dans les nanoparticules.*
Pour décrire les propriétés de transport de notre composant, nous utilisons la théorie de percolation développée par Vissenberg et Matters[59] (VM) pour modéliser les OFETS. Nous ne cherchons pas à décrire avec précision ces propriétés mais plutôt les changements de résistance apportés par les charges contenues dans les nanoparticules. La théorie VM propose des développements analytiques que nous pouvons étendre pour inclure ces effets.

Les films minces sont très désordonnés. Les états quantiques importants pour le transport sont spatialement localisés et distribués en énergie suivant (cf. Figure 31)[59]

$$D(\varepsilon) = \frac{N_t}{k_B\theta_0}\exp\left(\frac{\varepsilon}{k_B\theta_0}\right), \tag{87}$$

où $N_t$ est le nombre par unité de volume de ces états disponibles, $k_B\theta_0$ mesure la largeur de la distribution. Les charges sautent d'un état à l'autre avec une probabilité qui dépend de la distance entre états localisés et de leurs énergies. Dans la limite où la tension appliquée est faible, domaine linéaire, ce problème est équivalent à celui d'un réseau électrique dans lequel entre chaque nœud $i$ et $j$ distant de $R_{ij}$, une conductance est définie par $G_{ij} = G_0 e^{-s_{ij}}$ avec[78]

$$S_{ij} = 2\alpha R_{ij} + \frac{\left|\varepsilon_i - \varepsilon_F\right| + \left|\varepsilon_j - \varepsilon_F\right| + \left|\varepsilon_i - \varepsilon_j\right|}{2k_B\theta}. \tag{88}$$

Le premier terme prend en compte l'effet tunnel avec un paramètre $\alpha$ qui modélise le recouvrement des fonctions d'onde. Le deuxième terme est un terme de saut assisté thermiquement, $\varepsilon_i$ et $\varepsilon_j$ sont les énergies des états concernés, $\varepsilon_F$ l'énergie de Fermi.

VM se ramènent à un problème de percolation qu'ils résolvent pour finalement trouver la conductance du film[59]

$$G = A_0\exp(\beta\varepsilon_F), \tag{89}$$

$A_0$ est une fonction sans dimension de $N_t$, $\theta_0$, $\theta$ et $\alpha$. Quand les particules d'or sont chargées positivement, il apparait un terme d'interaction coulombien entre les charges piégées et les trous créés dans le film de pentacène par le potentiel de grille. Chaque état localisé, $i$, ressent alors un terme répulsif supplémentaire

$$\delta_i = \frac{e^2}{4\pi\varepsilon_O\varepsilon_r}\sum_\alpha \frac{n_\alpha}{|\vec{r}_\alpha - \vec{r}_i|}. \qquad (90)$$

Les NPs sont repérées par l'indice $\alpha$. $n_\alpha$ est le nombre de trous occupant la NP $\alpha$ ($n_\alpha$=0, 1, 2,…). $\varepsilon_0$ et $\varepsilon_r$ sont les permittivités du vide et du pentacène. $\vec{r}_\alpha$ et $\vec{r}_i$ sont les vecteurs positions de la NP $\alpha$ et de l'état quantique $i$. $\delta_i$ est une variable stochastique. Nous devons en principe résoudre un nouveau problème de percolation où les énergies sont toutes déplacées $\varepsilon_i \rightarrow \varepsilon_i+\delta_i$. Quand les NPs sont chargées positivement, la conductance du film décroit. C'est une conséquence de la distribution exponentielle (87). Notons que les mêmes conclusions pourraient découler d'autres choix, l'essentiel étant d'avoir une densité d'état croissante avec l'énergie. Le niveau de Fermi est fixé par les électrodes. Les énergies de site sont toutes déplacées vers les énergies positives par le terme (90) (cf. Figure 31.a). La densité d'état est alors modifiée : en particulier, le nombre d'états au niveau de Fermi est réduit. Puisque nous nous intéressons uniquement à la conductance, c'est le seul effet qui nous importe en première approximation. Nous pouvons alors modéliser la décroissance de la conductance en conservant la même densité d'état (Eq. (87)) et en déplaçant le niveau de Fermi vers les énergies négatives par une constante $-\Delta$ (cf. Figure 31.b). Pour une distribution donnée d'énergie, il est toujours possible de trouver une telle constante en imposant de retrouver la conductance du système. Cette constante dépend du nombre de charges piégées dans les NPs et donc du potentiel de grille. Nous pouvons finalement écrire la conductance du système à une tension fixe $V_G$ incluant les effets 'capacitifs' des NPs

$$G = A_0 \exp(\beta\varepsilon_F - \beta\Delta). \qquad (91)$$

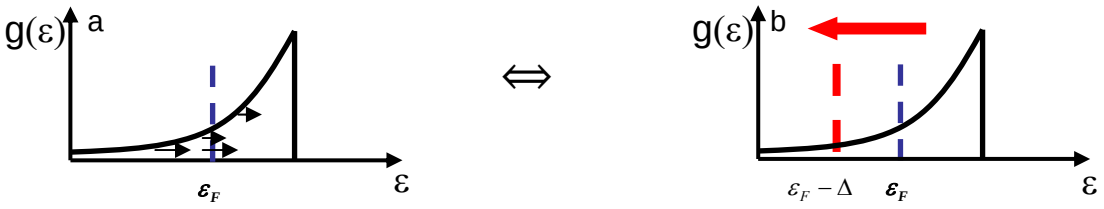


**Figure 31** : a) Schéma de la densité d'état considérée par VM. L'énergie de Fermi est fixée par les réservoirs. Avec les charges piégées dans les NPs, les énergies des états localisés sont déplacées aléatoirement vers les énergies positives, déplacements modélisés par les flèches. b) Modèle utilisé : dû aux shifts des énergies des états localisés, le nombre d'états au niveau de Fermi est réduit ce qui peut-être modélisé en conservant la même densité mais en déplaçant le niveau de Fermi par $-\Delta$ ($\Delta > 0$).

Le courant, $I=GV_{sd}$, $V_{sd}$ la tension source-drain, est bien réduit par les charges positives piégées dans les NPs. Remarquons qu'avec des charges négatives l'inverse est trouvée : les énergies de site sont déplacées vers les énergies négatives par un terme attractif ce qui sera modélisé par un shift positif du niveau de Fermi. Nous avons observé ces différents comportements expérimentalement (cf. référence VI).

*Modèle itératif et plasticité à courts termes.*

Basé sur l'équation (91) nous avons développé un modèle itératif, très similaire à des approches développées pour décrire le comportement de synapses biologiques,[77] pour

déterminer l'évolution du courant dans des expériences telles que celle résumée sur la Figure 30. Dans ces expériences, des séquences de pulses sont appliquées ; l'amplitude des pulses, $V_P$, et leur largeur, $W$, sont toujours maintenues constantes, seule la fréquence des séquences peut varier (Cf. Figure 30). Nous notons $I_n$ le courant à la fin du $n^{\text{ième}}$ pulse.

Durant un pulse, les nanoparticules vont se charger avec une certaine dynamique. Nous supposons que la quantité de charges injectée dans les NPs ne dépend que de $V_P$ et de $W$ : il en résulte, d'après l'équation (91), que dans nos séquences après chaque pulse le courant sera réduit par un facteur multiplicatif $K < 1$.

Entre les pulses, les NPs se déchargent. La fonction de relaxation a été étudiée dans la référence VI : elle varie très lentement avec un comportement en loi de puissance mais, dans la gamme de fréquences qui nous intéresse ici, nous pouvons la simplifier et la considérer comme une simple exponentielle décroissante avec un temps caractéristique, $\tau_d \sim 10$ s. Avec ces hypothèses nous pouvons écrire la relation de récurrence suivante

$$I_{n+1} = I_n K e^{-(T-W)/\tau_d} + \tilde{I}\left(1 - e^{-(T-W)/\tau_d}\right)K . \qquad (92)$$

$\tilde{I}$ est le courant 'intrinsèque' du dispositif : il serait le courant mesuré en l'absence de NPs. Le premier terme de l'itération $I_0$ dépend de l'état de charges du NOMFET à l'instant considéré ; il doit être considéré comme un paramètre qui dépend de l'historique des expériences subies par le dispositif. Il y a un comportement dépressif lorsque $I_{n+1} < I_n$ et facilitateur lorsque $I_{n+1} > I_n$. Davantage de détails sur la dérivation de l'équation (92) peuvent être trouvés dans la référence VI et la Réf. (79).

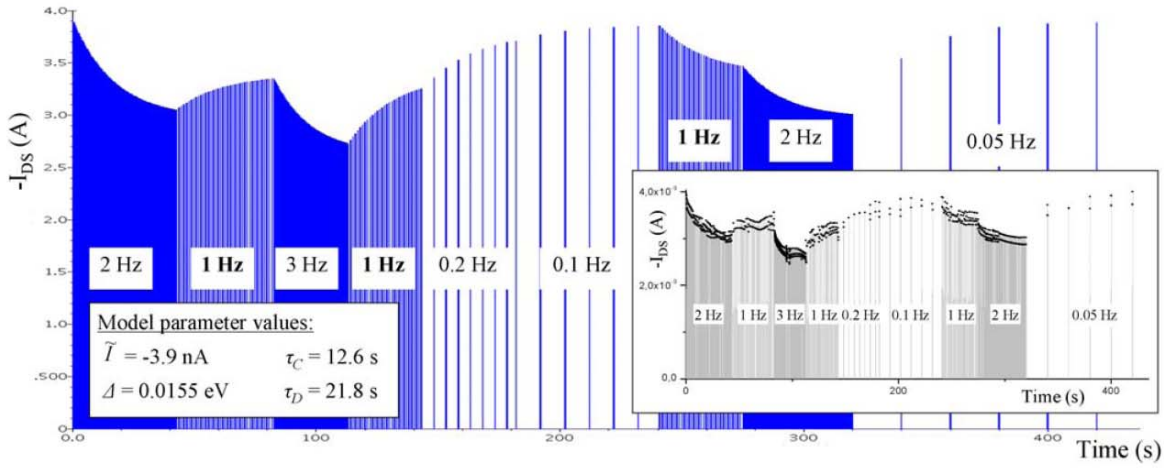


**Figure 32** : Expérience (encart) et modélisation avec le même NOMFET que pour la Figure (30). Nous observons que, dépendant de l'histoire du NOMFET, nous pouvons observer en réponse à la même fréquence (1 Hz) un comportement facilitateur ou dépressif.

Ce modèle donne un bon accord avec l'expérience (Figures 30 et 32). Il a également été implémenté dans un simulateur de circuit qui nous a permis de tester diverses propositions ; un exemple est donné dans la Réf. (79).

## 9. Propriétés de 'Spike Timing Dependent Plasticity' (STDP).

Une synapse fait le lien entre deux neurones, N1 et N2. Son état va être modifié selon l'activité de ces neurones ce qui va contribuer à faire évoluer sa façon de traiter l'information qu'elle reçoit. La propriété de 'spike timing dependent plasticity' (STDP) a été mise en évidence récemment dans des synapses biologiques.[80-82] Elle est résumée dans ce qui est communément appelé la fonction STDP qui détermine les changements d'états de la synapse en fonction de l'intervalle de temps entre un pulse provenant de N1 et un pulse provenant de N2. Un exemple fameux, dû à Bi et Poo, est donné dans la Figure 33.[82] Cette propriété est reconnue aujourd'hui comme étant probablement l'un des mécanismes fondamentaux de l'apprentissage non supervisé des réseaux de neurones biologiques. Inspirés par la biologie, de nombreux composants montrant des comportements STDP fleurissent aujourd'hui ;[83-86] nous allons montrer que le NOMFET possède aussi cette propriété. D'autre part, contrairement aux systèmes biologiques, nous avons la possibilité supplémentaire de modeler la forme des pulses appliqués à notre système. Il a été prédit récemment qu'en modifiant la forme des pulses il était possible de modifier la forme de la fonction STDP.[87,88] La fonction STDP est une sorte de caractéristique dynamique du système ; cette prédiction nous offre donc la possibilité de modeler cette caractéristique et donc, éventuellement, les propriétés du composant au sein d'un réseau de neurones.

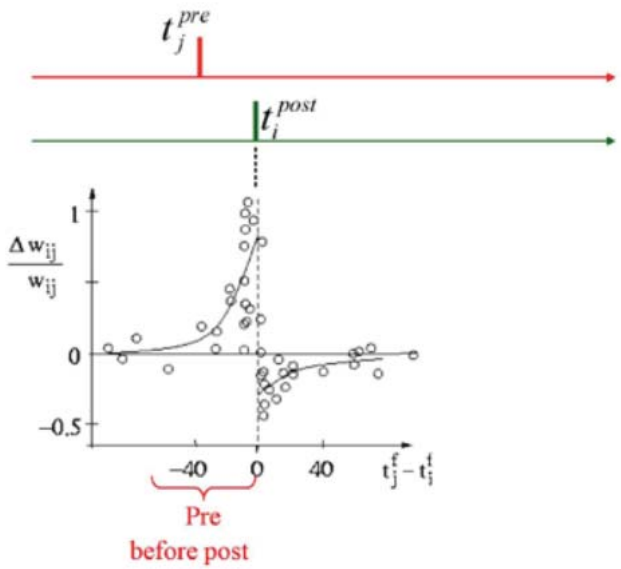


**Figure 33** : Exemple de fonction STDP pour une synapse biologique. $w_{ij}$ est le poids synaptique qui caractérise l'état de la synapse, $t_j$ et $t_i$ sont les temps d'arrivé des pulses pre- et post- synaptiques. Les ronds sont les données expérimentales. Cette courbe est issue de la Ref. (82).

Le NOMFET est un composant memristif au sens de Chua,[89] dont la variable interne, susceptible de changer avec le temps, est la charge contenue dans les nanoparticules d'or que nous notons $Q_{NP}(t)$. Nous réécrivons l'équation (91) en faisant apparaître explicitement les dépendances temporelles et en remplaçant le paramètre $\Delta$, qui quantifie la façon dont les

charges stockées dans les NPs déplacent le niveau de Fermi, par une relation, que nous supposons linéaire, avec $Q_{NP}(t)$.

$$G(Q_{NP}(t),V_{DS}(t),t) = \sigma_0(V_{DS}(t))e^{-\gamma Q_{NP}(t)}. \quad (93)$$

$\sigma_0$ est la conductance du NOMFET incluant l'effet de champ. $\gamma$ est un paramètre lié aux interactions entre charges dans les NPs et dans le film mince de pentacène. Nous mesurons les changements du paramètre interne $\delta Q_{NP}$ en appliquant un large pulse, de façon à optimiser la charge des NPs, d'amplitude variable et en mesurant le courant avant, $I_{initial}$, et après, $I_{after}$, le pulse. Nous obtenons

$$\frac{I_{after} - I_{initial}}{I_{initial}} = e^{-\gamma\delta Q_{NP}} - 1 \approx -\gamma\delta Q_{NP}. \quad (94)$$

où $\delta Q_{NP} = Q_{NP}^{After} - Q_{NP}^{Initial}$. Nous avons supposé dans le terme de droite que les charges piégées étaient telles que $\gamma\delta Q_{NP} << 1$. Nous représentons les résultats de cette mesure en fonction de l'amplitude du pulse (Figure 34).

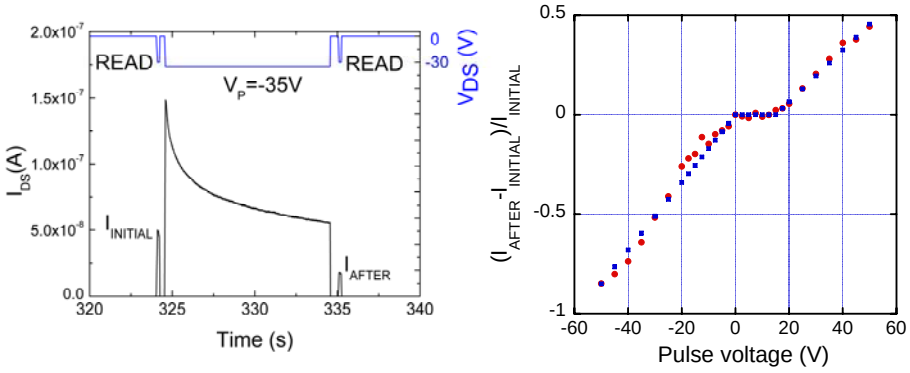


**Figure 34** : Nous appliquons un large pulse au NOMFET d'amplitude $V_P$ variable et traçons $(I_{after}\text{-}I_{initial})/I_{intial}$ en fonction de $V_P$ (à droite).

Nous distinguons trois régions dans la fonction obtenue qui caractérise les changements de la variable interne du NOMFET en fonction de la tension. Elle nous aide à façonner les pulses que nous avons appliqués au NOMFET. Nous reprenons ensuite l'expérience de Bi et Poo[82] (Figure 33) avec des pulses triangulaires et des pulses rectangulaires (davantage de détails sont donnés dans la référence VII). Les résultats obtenus sont montrés sur la Figure 35. Ils démontrent (i) que le NOMFET a des comportements de STDP, (ii) qu'il est possible de modeler la fonction STDP en modifiant la forme des pulses.[87,88] Dans le cas de pulses triangulaires, notre réponse est très similaire à celles des synapses biologiques de la Figure 33.

Pour reproduire les données expérimentales nous avons dérivé une équation contrôlant l'évolution temporelle de $Q_{NP}$ (voir référence VII)

$$\dot{Q}_{NP}(t) = -\frac{Q_{NP}(t) - Q_{NP}^0}{\tau(V_{DS})} - \eta(V_{DS}(t))V_{DS}(t). \quad (95)$$

où le premier terme de droite correspond à la décharge des NPs et le second terme, à la charge des NPs. En faisant des hypothèses raisonnables sur le comportement des fonctions $\tau(V_{ds})$ et $\eta(V_{ds})$ nous arrivons aux résultats présentés dans la Figure 35.

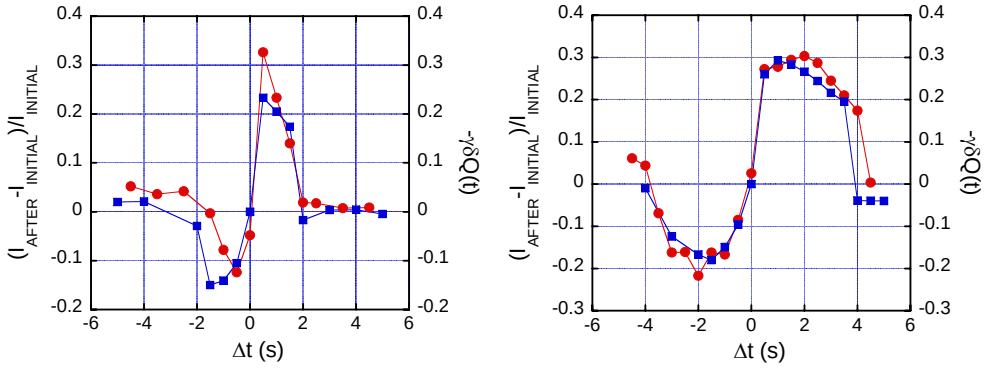


**Figure 35** : Exemples de fonctions STDP du NOMFET, à gauche pour des pulses de forme triangulaire, à droite pour des pulses de formes rectangulaire. Les ronds rouges sont les données expérimentales, les carrés bleus les résultats de la modélisation.

Pour finir, deux NOMFETs ont été inclus dans un circuit CMOS (détails dans la référence VII). Leurs fonctions STDP ont été ainsi mesurées simultanément dans une réelle configuration de circuit (Figure 36). Bien que les deux NOMFETs aient des caractéristiques *I-V* totalement différentes (elles différent par un ordre de grandeur en courant) leurs fonctions STDP, elles, sont identiques.

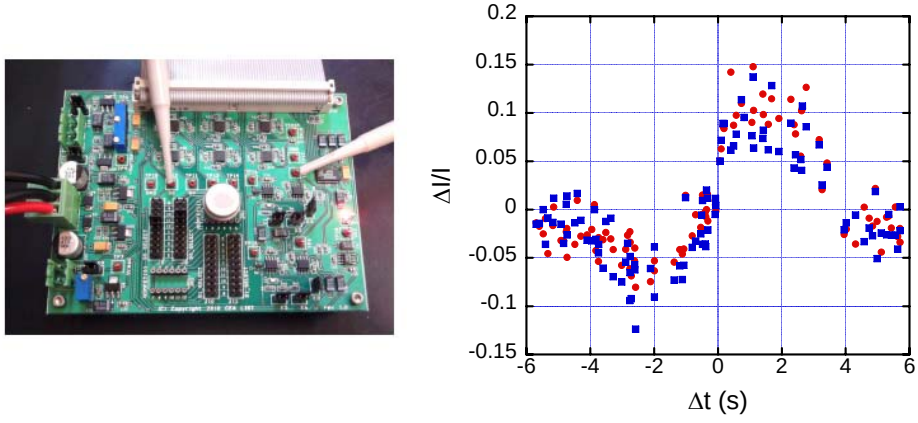


**Figure 36** : Plaquette électronique développée pour caractériser les NOMFETs (à gauche). Fonctions STDP de deux NOMFETs mesurées simultanément. Les NOMFETs ont des caractéristiques dc très différentes mais leurs fonctions STDP sont identiques.

## 10. Conclusion.

En conclusion, dans ce mémoire nous avons présenté essentiellement nos premières avancées dans deux directions nouvelles ou peu empruntées dans les domaines de l'électronique moléculaire et organique. Au fur et à mesure de nos expériences de spectroscopie d'admittance et de bruit de courant, nous avons développé des méthodes et concepts qui nous permettent, aujourd'hui, d'avoir une meilleure compréhension de certains phénomènes de relaxation et de l'origine des dispersions observées dans les caractéristiques de nos composants. Cependant, beaucoup d'efforts sont encore nécessaires pour parfaire ces avancées ; le travail entrepris aujourd'hui sur les jonctions à base de films minces de pentacène va dans cette direction. En ce qui concerne les dispositifs neuromorphiques, nous nous sommes efforcés, jusqu'à présent, de reproduire des comportements synaptiques, riches (STDP), sur un composant unique. Aujourd'hui nous souhaitons nous orienter vers l'étude de véritables réseaux de neurones : pour ouvrir de nouvelles possibilités dans ce domaine, l'étude d'un composant unique n'est d'aucun recours, il faut se tourner vers l'étude d'une assemblée de composants en interaction, la plus large possible.

# Bibliographie


1. A. Nitzan, Annu. Rev. Phys. Chem. 52, 681 (2001).
2. M.A. Reed, C. Zhou, C.J. Muller, T.P. Burgin, et J.M. Tour, Science 278, 252 (1997).
3. C. Kergueris, J.P. Bourgoin, S. Palacin, D. Estève, C. Urbina, M.Magoga, et C. Joachim, Phys. Rev. B 59, 12505 (1999).
4. J. reichert, R. Ochs, D. Beckmann, H.B. Weber, M. Mayor, et H. v. Löhneysen, Phys. Rev. Lett. 88, 176804 (2002).
5. X.D. Cui, A. Primak, X. Zarate, J. Tomfohr, O.F. Sankey, A.L. Moore, T.A. Moore, D. Gust, G. Harris, et S.M. Lindsay, Science 294, 571 (2001).
6. S. Datta, W. Tian, S. Hong, R. Reifenberger, J.I. Henderson, et C.P. Kubiak, Phys. Rev. Lett. 79, 2530 (1997).
7. W. Tian, S. Datta, S. Hong, R. Reifenberger, J.I. Henderson, et C. P. Kubiak, J. Chem. Phys. 109, 2874 (1998).
8. N.D. Lang et P. Avouris, Phys. Rev. Lett. 84, 358 (2000).
9. P.S. Damle, A.W. Ghosh, et S. Datta, Phys. Rev. B 64, 201403 (2001)
10. V. Mujica, E.E. Roitberg, et M.A. Ratner, J. Chem. Phys. 112, 6834 (2000).
11. A. Nitzan, M. Galperin, G.-L. Ingold, et H. Grabert, J. Chem. Phys. 117, 10837 (2002).
12. L. Salem, *Molecular Orbital Theory of Conjugated Systems* (Benjamin, London, 1966).
13 D. Baeriswyl, D.K. Campbell, et S. Mazumdar, in *Conjugated Conducting Polymers*, edited by H. Kiess (Springer, Heidelberg, 1992),pp 7-133.
14. P. Fulde, *Electron Correlations in Molecules and Solids* (Springer, Berlin, Heidelberg, New York, 1995).
15. A. Aviram et M.A. ratner, Chem. Phys. Lett. 29, 277 (1974).
16. M.A. Reed, J. Chen, A.M. Rawlett, D.W. Price, et J.M. Tour. Appl. Phys. Lett. 78, 3735 (2001).
17. Ferri, V. *et al.*, Angew. Chem. Int. Ed. Engl. 47, 3407-3409 (2008).
18. N. Katsonis, et al, Adv. Mater 18, 1397 (2006).
19. J.M. Mativetsky et al, J. Am. Chem. Soc. 130, 9192 (2008).
20. K. Smaali, S. lenfant, S. Karpe, M. Ocafrain, P. Blanchard, D. Deresmes, S. Godey, A. Rochefort, J. Roncali, et D. Vuillaume, ACS Nano 4, 2411 (2010).
21. C. Joachim, J.K. Gimzewski, et A. Aviram, Nature (London) 408, 541 (2000).
22. J. Collet et al, Appl. Phys. Lett. 76, 1941 (2000).
23. M. Halik et al, Nature (London) 431, 963 (2004).
24. A. Facchetti et al., Adv. Mater. 17, 1705 (2005).
25. E. Stern et al., Nature (London) 445, 519 (2007).
26. I.M. Tidswell, et al., Phys. Rev. B 41, 1111 (1990).
27. I.M. Tidswell,et al., J. Chem. Phys. 95, 2854 (1991).
28 W. Wang, T. lee, et M.A. Reed, Phys. Rev. B 68 035416 (2003).
29. J.G. Simmons, J. Appl. Phys. 34, 1793 (1963).
30. A. Salomon et al., Phys. Rev. Lett. 95, 266807 (2005)
31.D. Vuillaume et al, Phys. Rev. B 5_, 016491 (1998).
32. J. M. Beebe et al, Phys. Rev. Lett. 97, 026801 (2006).
33. F. Mirjani et al, Phys. Rev. B 84, 115402 (2011).
34. R. Tsu et L. Esaki, Appl. Phys. Lett. 22, 562 (1973).
35. G.D. Mahan, *Many-Particle Physics*, 3rd ed. (Kluwer Academic/Plenum Publishers, New York 2000).
36.J.A. Appelbaum et W.F. Brinckman, Phys. Rev. B 2, 907 (1970).
37. A. Zawadowski, Phys. Rev. 163, 341 (1967).

38. N. Clément, S. Pleutin, D. Guérin, S. Godey, et D. Vuillaume, J. Phys. Chem. C (soumis).
39. E.E. Huber et C.T. Kirk, Surf. Sci. 5, 447 (1966).
40 S.M. Kogan, *Electronic Noise and Fluctuations in Solids* (Cambridge University Press, Cambridge, 1996).
41 C.T. Rogers et R.A. Buhrman, Phys. Rev. Lett. 53, 1272 (1984)
42. S. Machlup, J. Appl. Phys. 25, 341 (1954).
43. Q. Zhang, Q. Zhang, and L. A. Archer, J. Phys. Chem. B 110, 4924 (2006).
44. M. C. Scott, et al., Acs Nano 2, 2392 (2008).
45 P. Debye, '*Polar Molecules*', Dover (1965).
46. K. S. Cole and R. H. Cole, J. Chem. Phys. 9, 341 (1941).
47. D. W. Davidson and R. H. Cole, J. Chem. Phys. 19, 1484 (1951).
48. S. Havriliak and S. Negami, Polymer 8, 161 (1967).
49. L. A. Dissado and R. M. Hill, Nature 279, 685 (1979); Proc. R. Soc. London 390, 131 (1983).
50. W.T. Coffey, Yu.P. Kalmykov, et J.T. Waldron, *The Langevin Equation*, 2nd Ed. (World Scientific, Singapore, 2004).
51. I. Goychuk, Phys. Rev. E 76, 040102(R) (2007).
52. A. O. Caldeira and A. J. Leggett, Ann. Phys. (USA) 149, 374 (1983).
53. U. Weiss, '*Quantum dissipative systems*', 3rd Ed. (World Scientific, Singapore, 2008).
54. L. D. Landau and E. M. Lifshitz, *Theory of Elasticity* (Pergamon, New York, 1970).
55. V. Gurarie and A. Altland, Phys. Rev. Lett. 94, 245502 (2005).
56. N. E. Israeloff, Phys. Rev. B 53, R11913 (1996).
57 C.D. Dimitrakopoulos et P.R.L. Malenfant, Adv. Mater. 14, 99 (2002).
58. N. Tessler, Y. Preezant, N. Rappaport, and Y. Roichman, *Adv. Mater.* **2009**, 21, 2741.
59. M.C.J.M. Vissenberg et M. Matters, Phys. Rev. V. 57, 12964 (1998).
60. D. Nabok et al., Phys. Rev. B 76, 235322 (2007)
61. H. Sirringhaus, *Adv. Mater*. **2009**, 21, 3859.
62. R.A. Street, M.L. Chaninyc, F. Endicott, and B. Ong, *J. Appl. Phys.* **2006**, 100, 114518.
63. J.B. Chang and V. Subramanian, *Appl. Phys. Lett.* **2006**, 88, 233513.
64. A. Salleo, F. Endicott, and R.A. Street, *Appl. Phys. Lett.* **2005**, 86, 263505.
65. M. Tello, M. Chiesa, C.M. Duffy, and H. Sirringhaus, *Adv. Funct. Mater.* **2008**, 18, 3907.
66. R.A. Street, A. Salleo, and M.L. Chaninye, *Phys. Rev. B* **2003**, 68, 085316.
67. A. Sharma, S.G.J. Mathijssen, M. Kemerink, D.M. de Leeuw, and P.A. Bobbert, *Appl. Phys. Lett.* **2009**, 95, 253305.
68. A. Sharma, S.G.J. Mathijssen, E.C.P. Smits, M. Kemerink, D.M. de Leeuw, and P.A. Bobbert, *Phys. Rev. B.* **2010**, 82, 075322.
69. H. Scher and E.W. Montroll, *Phys. Rev.B* **1975**, 12, 2455.
70. R. Metzler and J. Klafter, *Phys. Rep.* **2000**, 339, 1.
71. L.A. Dissado and R.M. Hill, *J. Chem. Soc. Faraday Trans. 2* **1984**, 80, 291.
72. A. Compte, *Phys. Rev. E* **1996**, 53, 4191.
73. J. Bisquert and A. Compte, *J. Electroanal. Chem.* **2001**, 499, 112.
74. J. Bisquert, G. Garcia-Belmonte, F. Fabregat-Santiago, and P.R. Bueno, *J. Electroanal. Chem.* **1999**, 475, 152.
75. M. Tsodyks et al., Neural Computation **1998**, 10, 821
76. M.V. Tsodyks, et al., Proc. Natl. Acad. Sci. USA **1997**, 80, 613.
77. J.A. Varela et al., J. Neurosci. **1997**, 17, 7926.
78. V. Ambegaokar, B.I. Halperin, et J.S. Langer, Phys. Rev. B **1971**, 4, 2612
79. O. Bichler, W.S. Zhao, F. Alibart, S. Pleutin, D. Vuillaume, et C. Gamrat, IEEE Trans. Electron. Devices. **2010**, 99, 1.
80. K. Gant, C. Bell, et V. Han, J. Physiol. Paris **1996**, 90, 233.

81. H. Markram, J. Lubke, M. Frotscher, et B. Sakmann, Science **1997**, 275, 213.
82. G.Q. Bi et M.M. Poo, J. Neurosci. **1998**, 18 10464.
83. S.H. Jo, T. Chang, I. Ebong, B.B. Bhadviya, P. Mazumder, et W. Lu, Nano Lett. **2010**, 10, 1297
84. Q. Lai, L. Zhang, Z. Li, W.F. Stickle, R.S. Williams, et Y. Chane Adv. Matter. **2010**, 22, 2448.
85. K. Seo, I. Kim, S. Jung, M. Jo, S. Park, J. Park, J. Shin, K.P. Biju, J. Kong, K. Lee, B. Lee, et H. Hwang, Naotehnology **2011**, 22, 254023.
86. D. Kuzum, R.G.D. Jeyasingh, B. Lee, et H.-S P. Wong, Nano Lett. **2011**
87. B. Linares-Barranco, T. Serrano-Gottarredona, IEEE Nano2009, **2009**, 601.
88. C. Zamarreno-Ramos, L. Camunas-Mesa, J. Perez-Carrasco, T. Masquelier, T. Serrano-Gottarredona, B. Linares-Barranco, Frontiers in Neuroscience **2011**, 5, 26.
89. L.O. Chua, IEEE Trans. on Circuit Theory **1971**, 18, 507.

# The electrostatic potential profile along a biased molecular wire: A model quantum-mechanical calculation

Stéphane Pleutin and Hermann Grabert
*Physikalisches Institut, Albert-Ludwigs-Universität, Hermann-Herder-Straße 3, D-79104 Freiburg, Germany*

Gert-Ludwig Ingold
*Institut für Physik, Universität Augsburg, Universitätsstraße 1, D-86135 Augsburg, Germany*

Abraham Nitzan
*School of Chemistry, The Sackler Faculty of Science, Tel Aviv University, 69978 Tel Aviv, Israel*

(Received 4 October 2002; accepted 27 November 2002)

We study the electrostatic potential of a molecular wire bridging two metallic electrodes in the limit of weak contacts. With the use of a tight-binding model including a fully three-dimensional treatment of the electrostatics of the molecular junction, the potential is shown to be poorly screened, dropping mostly along the entire molecule. In addition, we observe pronounced Friedel oscillations that can be related to the breaking of electron–hole symmetry. Our results are in semiquantitative agreement with recent state-of-the-art *ab initio* calculations and point to the need of a three-dimensional treatment to properly capture the behavior of the electrostatic potential. Based on these results, current-voltage curves are calculated within the Landauer formalism. It is shown that Coulomb interaction partially compensates the localization of the charges induced by the electric field and consequently tends to suppress zones of negative differential resistance. © *2003 American Institute of Physics.* [DOI: 10.1063/1.1539863]

## I. INTRODUCTION

Due to important technical progress, the field of molecular electronics, born in the mid-70s with the proposal of Aviram and Ratner to use single organic molecules as rectifiers,[1] receives rapidly growing interest.[2–4] Indeed, new fabrication methods and probes now enable individual molecules or small numbers of them to be connected to macroscopic electrodes.[2,5–8] Among these methods, one may cite, for instance, the break-junction technique[5,6,8] and the use of a conducting atomic-force microscope (AFM) to contact molecules absorbed on a metallic surface.[7]

On the theoretical side, the problem posed by these experimental works is highly challenging. We are facing a nonequilibrium many-body problem where, moreover, the coupling to a phonon bath may also be of importance. Up to now, most of the studies have focused on the coherent regime and the Landauer approach has been employed to obtain the conductance from *ab initio* or semiempirical models.[3] Important inelastic processes were included only within simple models[9–13] and much further progress is needed before one may hope to reach a satisfactory understanding of the problem.

The exact number of molecules contacted by the leads remains for a large part uncontrolled in the experimental setups cited above.[2,8] In theoretical modeling it is convenient to assume that a single organic molecule bridges two semiinfinite metallic electrodes (cf. Fig. 1). Another important experimental aspect is the fact that current-voltage characteristics are measured with applied voltages up to a few volts, values which bring us well away from the linear regime.

In this context, a central question concerns the electrostatic potential profile of a biased molecular wire. The importance of this issue was first demonstrated by Datta and co-workers.[14,15] Using semiempirical models, they have shown that different choices of the electrostatic profile have a profound effect on the current-voltage characteristics of a molecular junction. For instance, the transport properties are strongly modified depending on whether the potential drop occurs at the interface between molecule and electrode or along the molecular wire. In fact, it is natural to assume that even the details of the potential shape have a considerable effect on molecular conductance.

Recently, a few works along that line have been reported.[16–18] They give us a rather ambiguous view of this fundamental problem. Model calculations involving self-consistent solutions of the coupled Poisson and Schrödinger equations suggest that the potential drop occurs mainly at the interface between the molecule and the electrodes.[16] Within the molecule, the electrostatic potential is then found to be essentially flat. Screening appears to be very efficient within this approach, and the final conclusions are in agreement with some previous investigations.[14,15] However, these model calculations involve a drastic approximation: instead of solving the full Poisson equation, the authors of Ref. 16 have used a one-dimensional version of it. Implicitly, it is then assumed that the lateral dimensions of the molecule are much larger than the screening length. For quasi-one-dimensional systems with lateral dimensions of the order of a few angstroms, such as the organic molecules used in recent experimental work, this approximation is clearly questionable.[19] Indeed, recent state-of-the-art *ab initio* calculations on carbon and gold chains show a quite different picture.[17,18] In these works, the potential drop occurs not

 

only at the interface but rather along the entire molecule. Moreover, the local potential is found to display pronounced Friedel oscillations. Contrary to previous results, screening appears to be rather inefficient, even for metallic wires.

We are then left with two different pictures, and it becomes clear that a full understanding of the electrostatic potential profile in biased molecular wires or metallic constrictions is still lacking. In this work, we readdress the problem following the approach by Mujica *et al.*[16] We perform model calculations and solve the coupled set of two equations: the Poisson equation for the electrostatics and the Schrödinger equation for the electronic structure. In this respect, our work is similar to that of Mujica *et al.*[16] However, the calculation is modified in ways that we believe to be essential. In particular, we treat the real three-dimensional Poisson equation. As recently discussed by us,[19] we expect that this proper handling of the electrostatic problem changes the qualitative behavior: The potential is poorly screened and falls off substantially along the molecule. Indeed, the electrostatic potential profile of the model calculations presented here is in semiquantitative agreement with the *ab initio* results reported in Refs. 17 and 18. However, while *ab initio* calculations are involved and intricate enough to leave the underlying physics essentially obscure, our model includes only the ingredients necessary to capture the correct screening effects, and consequently our calculations are rather economic in time. We thus believe that our approach may help to gain further insight into the difficult problem of understanding transport through molecules, i.e., at a scale where quantum effects are prominent. A forthcoming work by Ghosh *et al.*[20] reaches conclusions similar to those presented here.

In Sec. II, our model Hamiltonian is introduced. The electronic density in the absence of a bias potential is then studied in Sec. III, using exact diagonalization and Hartree–Fock calculations that are shown to agree reasonably well with each other. The electrostatic profile is then calculated in Sec. IV at the Hartree-Fock level. Finally, the current-voltage characteristics are discussed in Sec. V.

## II. MODEL HAMILTONIAN

### A. Coulomb interaction including image charges

The physical problem posed by a molecular wire between two infinite metallic reservoirs is far too complicated to be solved exactly and, to proceed, several approximations are necessary. First, we assume that the surfaces of the two electrodes are infinite planes (cf. Fig. 1). Second, the molecule is assumed to be weakly connected to the metallic electrodes so that their chemical constitution is unimportant. This is certainly not fulfilled for some of the wires examined experimentally, with covalent bonds between molecule and electrode. Finally, we assume the characteristic time scale for electronic processes in the electrodes to be much shorter than the transit time of electrons in the wire. The electrodes can then be treated as equipotential surfaces, and the Schrödinger equation is solved under these potential boundary conditions. We are then within the same framework used in Ref. 16, but proceed differently. We first determine the Coulomb interaction potential which includes the image charges due to the metallic leads, keeping its three-dimensional character. Then, we solve the electronic wire problem.

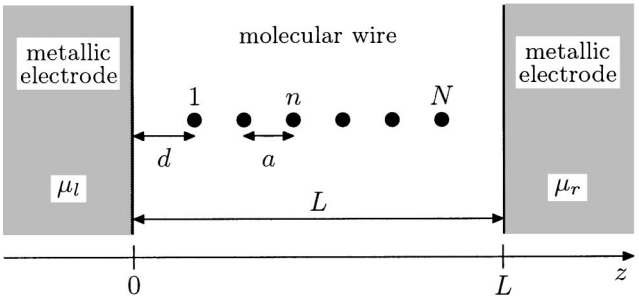


FIG. 1. Idealized molecular junction. A molecular wire, modeled by a finite one-dimensional lattice, bridges two metallic electrodes with surfaces assumed to be infinite planes. The tunneling contacts, effective only at the two molecular end sites indicated by 1 and *N*, are assumed to be weak. The chemical potentials in the left and right electrode are denoted by $\mu_l$ and $\mu_r$, respectively.

The Coulomb interaction energy reads

$$W=\tfrac{1}{2}\int d^3\mathbf{r}\int d^3\mathbf{r}'\rho(\mathbf{r})\rho(\mathbf{r}')\varphi(\mathbf{r},\mathbf{r}'), \tag{1}$$

where $\rho(\mathbf{r})$ is the charge density in the wire and $\varphi(\mathbf{r},\mathbf{r}')$ is the potential at point $\mathbf{r}=(x,y,z)$ produced by the charge located at point $\mathbf{r}'=(x',y',z')$. The Coulomb potential is the solution of the Poisson equation

$$\Delta_{\mathbf{r}}\varphi(\mathbf{r},\mathbf{r}')=-4\pi U\delta(\mathbf{r}-\mathbf{r}'), \tag{2}$$

where for convenience we have introduced a factor $U$ measuring the strength of the electron–electron interaction. In the absence of the metallic electrodes the solution of (2) is given by the standard Coulomb potential

$$\varphi_0(\mathbf{r},\mathbf{r}')=\frac{U}{|\mathbf{r}-\mathbf{r}'|}. \tag{3}$$

In the setup depicted in Fig. 1, we require the potential in the absence of an external bias to vanish on the surfaces of the metallic electrodes, i.e., at $z=0$ and $z=L$. A solution of the Poisson equation with these particular boundary conditions is found using the standard method of image charges

$$\varphi(\mathbf{r},\mathbf{r}')=\sum_{p=-\infty}^{+\infty}[\varphi_0(\mathbf{r}+2pL\hat{\mathbf{z}},\mathbf{r}')-\varphi_0(2pL\hat{\mathbf{z}}-\mathbf{r},\mathbf{r}')], \tag{4}$$

where $L$ is the distance between the two electrodes (cf. Fig. 1) and $\hat{\mathbf{z}}$ the unit vector along the molecular axis.

$\varphi(\mathbf{r},\mathbf{r}')$ is a genuine three-dimensional Coulomb potential including the effects of the two semi-infinite metallic electrodes. The electrostatics of the molecular junction is then governed by this potential. It remains to construct and solve the Schrödinger equation for the molecular wire.

### B. Tight-binding model including image charges

In the following, we will mainly be concerned with conjugated molecules and, in particular, with their low-energy properties. An appropriate description can then be given by

an effective tight-binding Hamiltonian for the $\pi$ electrons only.[21,22] In addition, since there exist *ab initio* results for short chains of gold atoms,[18] it is also of interest to study systems with electrons in *s* orbitals.

We therefore attach Gaussian-type orbitals of the form

$$\phi_n(\mathbf{r}) = A_s x^s \exp[-\alpha[x^2+y^2+(z-z_n)^2]], \tag{5}$$

to each atomic site *n*. This allows us to model both *s* orbitals with $s=0$ and *p* orbitals with $s=1$. The center of the orbital, $z_n = d+(n-1)a$, depends on the distance *d* between each electrode and the molecule as well as the lattice constant *a* in the molecule (cf. Fig. 1). The parameter $\alpha$ determines the spread of the state and gives an estimate of the electronic density. Finally, the normalization constants for *s*- and *p* orbitals are given by $A_0=(2\alpha/\pi)^{3/4}$ and $A_1=2(2/\pi)^{3/4}\alpha^{5/4}$, respectively.

The explicit form (5) of the orbitals allows us to determine the effective parameters entering the tight-binding model. In the following, we adopt the ''zero differential overlap'' (ZDO) approximation[21–23]

$$\phi_n^*(\mathbf{r})\phi_m(\mathbf{r}) = |\phi_n(\mathbf{r})|^2 \delta_{n,m}, \tag{6}$$

which remains valid as long as the orbitals $\phi_n$ are strongly localized on the atomic sites *n*. It implies orthogonality between the Gaussian orbitals on different sites and, most importantly, leads to a drastic reduction of nonvanishing matrix elements of the Coulomb operator since only the two center integrals are retained in the final model. In particular, no exchange integrals will appear. These integrals, involving a differential overlap, are usually negligibly small compared to the Coulomb integrals. Moreover, we approximate the positive cores by point charges localized at the atomic sites *m* with coordinates $(0,0,z_m)$. Then, the energy of an electron localized at site *n* due to all positive core charges and their images becomes

$$\epsilon_n = -U\sum_{m=1}^{N} \int d^3\mathbf{r} |\phi_n(\mathbf{r})|^2 \varphi(\mathbf{r}, z_m\hat{\mathbf{z}}). \tag{7}$$

Within the ZDO approximation the only finite Coulomb matrix elements are related to the interaction energy between electrons localized at sites *n* and *n'*

$$U_{n,n'} = U\int d^3\mathbf{r}\int d^3\mathbf{r}' |\phi_n(\mathbf{r})|^2 \varphi(\mathbf{r},\mathbf{r}') |\phi_{n'}(\mathbf{r}')|^2. \tag{8}$$

It is worthwhile to notice that the interaction terms (7) and (8) depend on the position *n* along the chain due to the image charges but also because of the finite size of the molecular wire.

Within the ZDO approximation kinetic energy contributions vanish as a consequence of (6). To lowest order, the overlap leads to a constant shift of the on-site energy $\epsilon_n$ that may be disregarded and to nearest-neighbor hopping. The hopping matrix element *t* cannot be evaluated directly within the ZDO and, therefore, has to be treated as a parameter of the model.[21–23] However, it is possible to relax the approximation[23] and estimate the hopping matrix elements from (5). Doing so, we have found that their dependences on *n* are not pronounced, and, moreover, this kind of more sophisticated treatment would not change qualitatively our final conclusions. Therefore, we assume the hopping matrix elements, *t*, to be constant along the chain, and use the ratio $U/t$ as a parameter to examine the importance of electron–electron interaction.

With the parameters just discussed, we obtain a description of the electrons in terms of an effective tight-binding model which includes long-range Coulomb interaction[21,22]

$$H = \sum_{n,\sigma} (\epsilon_n + v_n) c^\dagger_{n,\sigma} c_{n,\sigma} + \sum_{n,\sigma} t(c^\dagger_{n+1,\sigma} c_{n,\sigma} + \text{h.c.}) + \frac{1}{2}\sum_{n,n',\sigma,\sigma'} U_{n,n'} c^\dagger_{n,\sigma} c^\dagger_{n',\sigma'} c_{n',\sigma'} c_{n,\sigma}. \tag{9}$$

$c^\dagger_{n,\sigma}(c_{n,\sigma})$ are the usual creation (annihilation) operators for an electron with spin $\sigma$ in the local state $\phi_n$. In the first term, we have accounted for an additional shift of the local potential due to an external bias. With the chemical potentials $\mu_l$ and $\mu_r$ in the left and right electrode, respectively, the shift at site *n* is given by

$$v_n = \mu_l + \frac{\mu_r - \mu_l}{L} z_n. \tag{10}$$

The resulting tight-binding model (9) is mostly defined by the geometry of the molecular junction. The only other parameters are the energies *t* and *U*, which determine the strength of the kinetic and Coulomb energies, respectively. It is usually believed that conjugated molecules lie in an intermediate regime where $U/t=1,...,4$.[21,22]

## III. ELECTRON DENSITY WITHOUT BIAS POTENTIAL

Consider first the situation without bias potential, $\mu_l = \mu_r$ or $v_n=0$. We analyze for this case the electron density at equilibrium in the absence of electron transfer between the molecule and the leads. In all the calculations presented here, we assume the chains to be electrically neutral with on average one electron per site. Because of the electron spin, this corresponds to the half-filled case. Furthermore, we restrict ourselves to the ground state of the system.

We have done exact diagonalization studies for chains of up to 12 sites. Results for the charge density of a chain with 12 sites shown in Fig. 2 are typical for other cases studied. Two main features can easily be seen. (i) The electron density is nonuniform: the electrons have a tendency to shift towards the middle of the chain. (ii) Because of this nonuniformity, substantial Friedel oscillations occur across the wire. These features can be explained by invoking electron–hole symmetry as shown below.

For the case of a half-filled band it has long been known that the electron density is uniform, i.e., does not depend on the site index *n*, for models defined on bipartite lattices in such a way that electron–hole symmetry is fulfilled. This theorem was first discovered for the ground state of the free-electron (Hückel) model[24] and later extended to some interacting systems.[25] More recently, a generalization to canonical and grand canonical ensembles was proven for a large class of models.[26] Mathematically, the theorem applies to models invariant with respect to the transformation $c^\dagger_{n,\sigma} \rightarrow (-1)^n c_{n,\sigma}$.

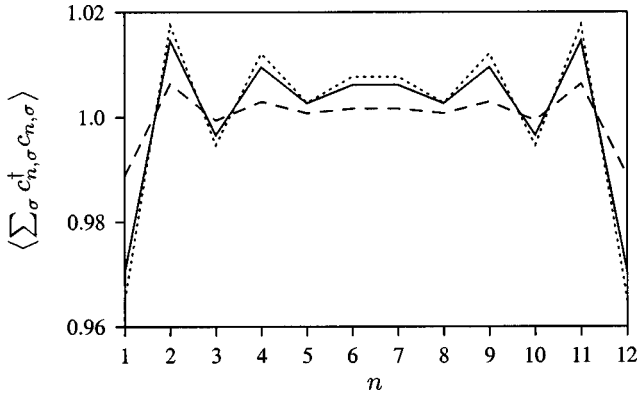


FIG. 2. Electronic density without bias potential for a molecular wire of carbon ($s=1$) with $N=12$ sites. The parameters are $\alpha=4.5/a^2$ and $U=t$. The full curve is the exact result for a molecule–electrode distance of $d=2a$. The dotted curve is for the same geometry but at Hartree–Fock level. The dashed curve is the exact result for the case without metallic electrodes, $d\to\infty$.

Applying this transformation, we find that the Hamiltonian of the molecular wire (9) is invariant only if the equality

$$\epsilon_n=-\frac{1}{2}\sum_{m=1}^{N}U_{n,m}\left(1-\frac{\delta_{n,m}}{2}\right)+K \tag{11}$$

is fulfilled, where $K$ is a constant. This implies that the electron–ion interaction is essentially compensated, up to a constant term, by the repulsive electron–electron interaction. Notice that allowing for hopping matrix elements that depend on the position in the chain would not change this equality. Indeed, a term like $\Sigma_{n,\sigma}t_{n,n+1}(c^{\dagger}_{n+1,\sigma}c_{n,\sigma}+c^{\dagger}_{n,\sigma}c_{n+1,\sigma})$ remains unchanged when the electron–hole transformation is applied. From this point of view, it is not necessary to go beyond the ZDO approximation.

The equality (11) can be satisfied only in very particular cases where at least one of the following conditions is satisfied:

(i) the chain is infinite;
(ii) there is no interaction, $U=0$;
(iii) $\alpha\to\infty$, corresponding to interactions between point charges.

None of these criteria is fulfilled in realistic cases of interest. With the exception of carbon nanotubes, experimental molecular junctions involve relatively short (<10 nm) molecular chains.[2] The Coulomb interaction is of the same order of magnitude as the kinetic terms[21,22] and certainly not negligible. Even then, the electron density would still be uniform if the electron-orbitals are reduced to points ($\alpha\to\infty$) regardless of the presence of image charges. Therefore, one may say that the nonuniformity of the density comes from the lateral extension of the electronic clouds, the *p*- or *s* states. This shows, once again, the need for a three-dimensional treatment of the electronic structure.

The exact shape of the electron density is determined by (i) the strength of the Coulomb interaction, $U/t$; (ii) the spread of the electronic orbitals, $\alpha$; and (iii) the geometry of the system, expressed in our model by the length $(n-1)a$ of the molecule and by the distance $d$ between the electrodes and the molecule.

All these factors contribute to yield, instead of the uniform density condition (11), the relation

$$\epsilon_n=-\frac{1}{2}\sum_{m=1}^{N}U_{n,m}\left(1-\frac{\delta_{n,m}}{2}\right)+f_L(n), \tag{12}$$

where $f_L(n)$ is a function of the position in the chain; its dependence on $n$ is responsible for the nonhomogeneity of the electronic density. It is of interest to understand the effects of each of these parameters separately.

*Coulomb interaction*. Starting from the noninteracting case where the electronic density is uniform, increasing $U$ results in an increase of the Friedel oscillations until the electrons start to localize. In the limit $U\to\infty$, half filling leads to a Mott insulator and one recovers a constant electron density.

*Spread of the electronic orbitals*. When the orbitals are reduced to points (point charge limit), $\alpha\to\infty$, the electronic density is uniform. Indeed, in this particular limit the electron–ion and electron–electron interactions have the same form, restoring the electron–hole symmetry of the molecular Hamiltonian. Accounting for a spread of the orbitals increases slowly the amplitude of the Friedel oscillations.

*Geometry of the molecular junction*. Two effects need to be distinguished: (i) the finite size effects and (ii) the image-charge effects. In Fig. 2, the dashed curve shows the density for the very same system used to obtain the other two curves, except that now no metallic electrodes are present. Therefore, the dashed curve contains only the finite size effects. From this particular example, one sees that both effects contribute to the Friedel oscillations and that, in order to get the correct density, image interactions should be included unless the electrode–molecule distances are large. In fact, in the example of Fig. 2, the contribution to the oscillations due to the image charges is the larger one. The Coulomb interaction with the electrodes described by the image charges is therefore crucial to estimate transport properties of molecular wires or metallic constrictions. We have observed, as expected, that finite size effects alone tend to disappear when the chain size is increased. In contrast, the effect of image charges tends to become more important: the amplitude of the Friedel oscillations increases with the system size due to the presence of the two metallic electrodes. This tendency should continue until, for long wires, which we do not consider here, the oscillations occur predominantly near the edges.

Finally, the dotted curve of Fig. 2 shows the electron density with metallic electrodes calculated within the Hartree–Fock approximation; it is in very good agreement with the exact result. We have performed calculations for different values of $U$ up to $U=4t$ and observed that, as far as the electron density is concerned, the Hartree–Fock approximation gives reasonable results. This allow us to use this mean-field approach for the study of the electrostatic profile in biased molecular wires (Sec. IV) and their transport properties (Sec. V).

## IV. ELECTROSTATIC POTENTIAL IN BIASED MOLECULAR WIRES

The application of the screened on-site electrostatic potential to calculations of conductance properties is useful only within a single electron theory, e.g., in the mean-field description of the process. This is how this concept was applied in the calculation of Mujica *et al.*[16] and in the density functional theory.[17,18] Here, our calculations are done using the Hartree–Fock approximation applied to the molecular Hamiltonian (9). In the previous section, by comparing the mean-field electron density with the exact one, we have already shown that the approximate result is reasonable in the range of parameters proper to conjugated molecules. More precisely, the Hartree–Fock density is in very good agreement with the exact results for values of $U$ up to, approximately, $2t$ (cf. Fig. 2) and remains of reasonable accuracy up to values of about $4t$. In the following we present only results for $U=t$, but the same qualitative picture arises also for larger values of $U$.

Starting from the initial tight-binding model (9), we build an effective Hamiltonian by solving self-consistently the usual Hartree–Fock equations[21] leading to

$$H_{\mathrm{eff}}=\sum_{n,\sigma}\epsilon_n(V)c^{\dagger}_{n,\sigma}c_{n,\sigma} + \sum_{n,n',\sigma} t_{n,n'}(V)(c^{\dagger}_{n',\sigma}c_{n,\sigma}+\mathrm{h.c.}), \tag{13}$$

where $V=\mu_l-\mu_r$. The chemical potentials will always be chosen such that $\mu_l=-\mu_r$. $\epsilon_n(V)$ is the effective on-site potential which includes the ionic attraction and the electron–electron repulsion incorporated within a mean-field picture as well as the on-site potential (10). $t_{n,n'}(V)$ is the effective hopping matrix element which includes the exchange terms. Note that a vanishing of exchange integrals in the ZDO approximation is not equivalent to a Hartree approximation. Indeed, a mean-field approximation of (9) still contains exchange terms of the form $-\frac{1}{2}\Sigma_{n\neq n'}U_{n,n'}\langle c^{\dagger}_{n,\sigma}c_{n',\sigma}\rangle c^{\dagger}_{n',\sigma}c_{n,\sigma}$ which, due to the long-range part of the Coulomb potential (4), include long-range hopping.

Without Coulomb interactions, the electrostatic potential is given by the ramp defined in (10), i.e., by the potential in the absence of a molecule. This linear profile has been used sometimes in the literature to study nonlinear current-voltage characteristics.[27,28]

In the presence of Coulomb interaction, the linear profile is changed and the screened electrostatic potential, $E_n(V)$, is given by the difference between the on-site term with and without bias voltage

$$E_n(V)=\epsilon_n(V)-\epsilon_n(0). \tag{14}$$

A typical example is shown in Fig. 3 for a chain with 20 sites. We see two main features: (i) screening is not very efficient and, consequently, there is only a small potential drop at the interfaces but a finite slope of the potential along the entire molecule; (ii) there are substantial Friedel oscillations along the profile.

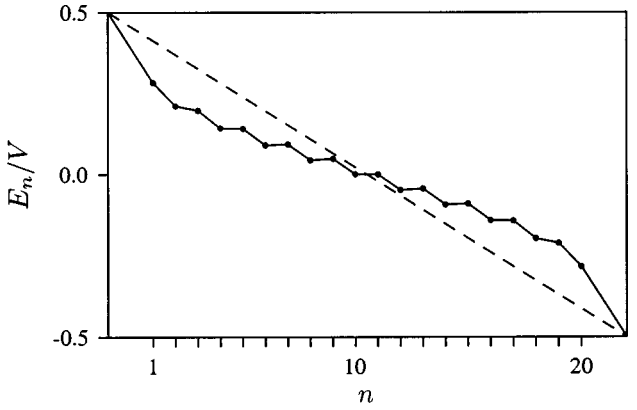


FIG. 3. Electrostatic potential profile for a carbon wire [$s=1$ in Eq. (5)] with $N=20$ sites. The parameters are $\alpha=4.5/a^2$, $U=t$, $V=\mu_l-\mu_r=t$, and $d=2a$. The dashed curve is the unscreened potential without molecule (ramp potential). The full curve is the screened potential in the presence of the molecular wire. It shows a small decrease in slope along the entire molecule with substantial Friedel oscillations.

Our results differ from those of Mujica *et al.*[16] despite the fact that the two models are closely related. These differences mostly come from the fact that we solve the Poisson equation without resorting to a one-dimensional approximation. As recently shown by us within a classical model,[19] a three-dimensional treatment of the electrostatics is necessary, and in fact leads to the identification of the lateral thickness of the molecule as a new generic attribute that determines the potential profile. In Fig. 4, we show a comparison between our results and the calculations of Damle *et al.*[18] for a chain of six gold atoms. It is important to stress that we did not try to fit the *ab initio* curve but, instead, we simply chose a reasonable set of parameters. Note, however, that we include the response of infinite leads while the *ab initio* calculations take only small metal clusters into account. Furthermore, the asymmetry in the latter case indicates that the *ab initio* calculations result in a charged molecule, while in our case the molecular wire always remains neutral. Other *ab initio* calculations[17,29,30] on similar models are also in agreement with our observations.

To conclude this section, we summarize our main results: in the relevant range of parameters, screening is not

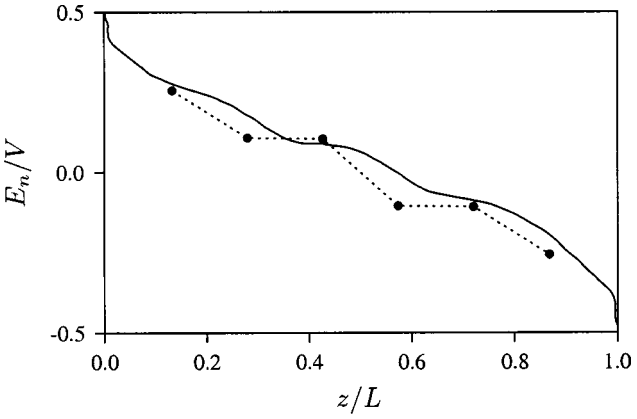


FIG. 4. The electrostatic potential profile for a gold wire [$s=0$ in Eq. (5)] with $N=6$ sites obtained from Hartree–Fock calculations is shown by the filled circles. The parameters used are $d=0.9a$, $\alpha=4.5/a^2$, and $U=t$. For comparison the full curve shows the *ab initio* results taken from Ref. 18.

very efficient in the wire and the drop of the potential occurs along the entire molecule. Additionally, substantial Friedel oscillations are present in the electrostatic profile. Our results are in good agreement with recent *ab initio* results.[17,18] When compared with the results of Ref. 16, our treatment stresses the need to study the full three-dimensional problem, as far as the electrostatics of the molecular junction is concerned.

In the next section, we discuss consequences of the screening effects for the current-voltage characteristics of molecular wires studied within the Landauer formalism.

## V. CURRENT–VOLTAGE CHARACTERISTICS OF A MOLECULAR WIRE IN THE WEAK TUNNELING CONTACT LIMIT

In a model where only the first and the last atom of a molecular chain couple to the corresponding metal leads and at $T=0$, the Landauer conduction formula yields[3,31]

$$I=\frac{2e}{\pi\hbar}\int_{\mu_r}^{\mu_l} dE|G_{1N}(E,V)|^2\Delta_l(E,V)\Delta_r(E,V), \tag{15}$$

where $V=\mu_l-\mu_r$ and $\Delta_{l/r}$ are the spectral functions for the left and right reservoirs. The molecule–lead coupling only occurs at sites 1 and $N$ and $G_{1N}$ is the matrix element of the exact Green function of the molecular junction between these sites (cf. Fig. 1).

This equation can be understood as a special case of the Landauer formula[32] adapted to the case of bad contacts, where it is possible to use second-order perturbation theory in the tunneling matrix element.[31] In the limit of ''extremely'' bad contacts of interest here, the Green function of the system in formula (15) may be replaced by the Green function of the isolated molecular wire, $G^0_{1N}$.[33] Moreover, assuming that the product of spectral densities does not significantly depend on energy in the range between $\mu_l$ and $\mu_r$, one gets

$$I=\frac{2e}{\pi\hbar}\Delta_0^2\int_{\mu_r}^{\mu_l} dE|G^0_{1N}(E,V)|^2, \tag{16}$$

where $\Delta_0$ is the spectral density at zero bias.

From this simplified equation, we can calculate the current-voltage characteristics of the molecular junction, using only the Green function of the isolated molecular wire, evaluated in the presence of the electrostatic potential created by the metallic electrodes. Examples are given in Fig. 5 for increasing Coulomb strength $U$ starting from the noninteracting case where the on-site potential is given by the ramp (10).

In all cases, the $I-V$ curves have a staircase structure which is a common feature in the weak tunneling limit[18,27,34] and simply reflects the discreteness of the molecular electronic spectrum. Indeed, an increase of the bias potential corresponds to an increase of the window of integration in formula (16). Therefore, a jump in the $I-V$ curves means that one more discrete molecular level enters this window of integration.

It is interesting to note that Fig. 5 shows also wide regions of negative differential resistance, in particular in the noninteracting case. Within our simple formulation, they can be explained by the localization of charges induced by a strong enough electric field: at sufficiently high bias voltage, charge carriers are localized at one end of the chain, resulting in a decrease of the current. This could be an artifact of our weak molecule–electrode coupling model; however, negative differential resistance has been found in recent experiments,[35] and electric field-induced localization could be a way to understand these experimental findings.

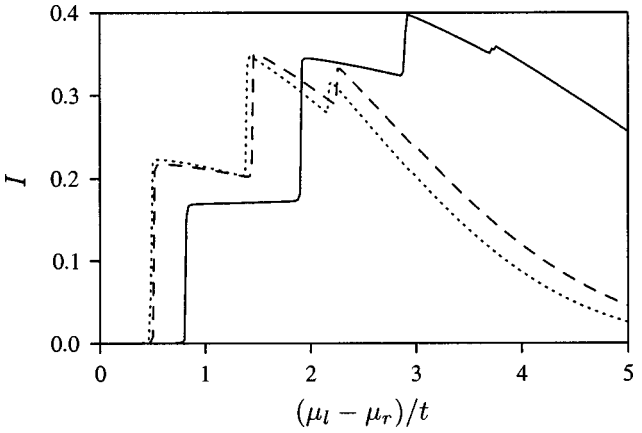


FIG. 5. Current-voltage characteristics for a carbon molecule ($s=1$) with $N=12$, $d=2a$, $\alpha=4.5/a^2$, and for different Coulomb interaction strengths $U/t=0$, 0.1, 1 are depicted by the dotted, dashed, and full line, respectively. The current is given in units of $(2e/\pi\hbar)\Delta_0^2/t$.

The Coulomb interaction has two main effects on the $I-V$ characteristics. First, the positions of the current-voltage steps are shifted to higher voltages reflecting the displacement of the molecular levels to higher energy with increasing Coulomb interaction. Second, the localization of the charges due to a strong electric field is partially compensated by the electron–electron repulsion. These screening effects attenuate the negative differential resistance effects (cf. Fig. 5). These observations are similar to those made by Mujica *et al.*,[27] where a Hubbard model was studied at the Hartree level.

## VI. CONCLUSION

We have addressed the problem of calculating transport properties of a molecular wire bridging two semi-infinite metallic electrodes. A first important part of this task is to determine the electrostatic potential profile through the biased wire.[14–18] Indeed, it is of importance to know how screening effects modify the ramp potential [Eq. (10)] existing in the absence of the organic molecule.

This work and our earlier paper[19] resolve discrepancies between answers available in the literature. On the one hand, a tight-binding model combined with a one-dimensional Poisson equation gives a strong screening version of the problem: the drop of the potential occurs at the interfaces and the potential is therefore almost flat within the molecule.[16] On the other hand, recent *ab initio* results give a weak screening version: no substantial drop at the interfaces but rather a decrease along the entire molecule together with substantial Friedel oscillations.[17,18]

In this paper, we have proposed a modified tight-binding model to address this question. It is based on three main ingredients. (i) We introduce a three-dimensional Coulomb potential [Eq. (4)] which includes the image interaction with the two metallic electrodes assumed to have planar surfaces. (ii) The electrons localized at atomic sites are modeled by Gaussian-type orbitals of finite lateral extent [Eq. (5)]. (iii) The positive background is assumed to be a set of point charges localized on the atomic sites. With these three ingredients, it is possible to evaluate the various terms of our model Hamiltonian: the on-site energy [Eq. (7)] and the electron–electron interaction [Eq. (8)]. They are all functions of the position on the chain due to the finite size of the system and the image charges induced by the electrodes. All our calculations are done in the weak tunneling limit, assuming bad contacts.

This model yields an electronic density that is nonuniform already in the absence of a bias potential—the electrons prefer to be in the center of the wire—and displays pronounced Friedel oscillations (Fig. 2). These characteristics are due to the fact that our model does not fulfill, in general, the electron–hole symmetry.[24–26] In the presence of an applied voltage the electrostatic potential profile does not drop appreciably at the interfaces but rather, in accordance with the *ab initio* results of Refs. 17 and 18, it decreases along the molecule with substantial Friedel oscillations appearing along the entire profile (Figs. 3 and 4). Our results are different from the ones of Ref. 16, where a one-dimensional Poisson equation was used. This disagreement stresses the need to perform a three-dimensional calculation, as done here, to properly describe the electrostatic properties of the molecular junction.

Finally, the current-voltage characteristics are obtained within the same Hartree–Fock calculation using the Landauer formula (i.e., neglecting electronic correlation effects and assuming coherent tunneling). It shows a staircase structure (Fig. 5), as is common in the weak tunneling limit.[18,27] Zones of negative differential resistance are found due to charge localization induced by the electric field. The main effects of the Coulomb interaction, within our approximations, are, on the one hand, a shift to higher energies of the position of the current-voltage steps and, on the other hand, a partial compensation of the localization of the electrons diminishing the negative differential resistance effects in agreement with a previous study.[27]

In closing, it is important to stress some limitations of our model. On the one hand, we consider coherent transport, assuming that the electrons are transferred from one lead to the other in a single quantum-mechanical process. This is a good approximation if the tunneling time is much less than the inelastic scattering time. For organic molecules, this transit time could be of the same order of magnitude as the intramolecular vibronic relaxation time, especially in the weak contact limit employed here.[3] In this case, part of the current could be due to sequential tunneling, where the molecular wire would be successively charged and discharged. This important issue remains to be studied further. We have neglected charging effects assuming the molecule to remain neutral. At high voltage, this approximation could fail.[27] The average charge number of the molecule could increase in analogy with Coulomb blockade phenomena observed in mesoscopic metallic double-tunnel junctions and quantum dots,[36] and, more recently, in multiwall carbon nanotubes.[37]

A proper handling of the full problem requires treating the wire as an open system dynamically coupled to the electrodes and to the vibronic degrees of freedom. This program is far beyond the scope of the present work.

## ACKNOWLEDGMENTS

The authors have benefited from useful discussions with P. Hänggi, S. Kohler, J. Lehmann, and S. Yaliraki. Three of us (H.G., G.L.I., and A.N.) would like to thank the Institute for Theoretical Physics at UCSB for hospitality during the workshop on ''Nanoscience'' where this work was started. This research was supported in part by the National Science Foundation under Grant No. PHY99-07949, by the Volkswagen-Stiftung under Grant No. I/77217, by the Israel Science Foundation and by the Israel Ministry of Science.

[1] A. Aviram and M. A. Ratner, Chem. Phys. Lett. **29**, 277 (1974).
[2] C. Joachim, J. K. Gimzewski, and A. Aviram, Nature (London) **408**, 541 (2000).
[3] A. Nitzan, Annu. Rev. Phys. Chem. **52**, 681 (2001).
[4] Special issue on *Processes in Molecular Wires*, edited by P. Hänggi, M. Ratner, and S. Yaliraki, Chem. Phys. **281**, 111–487 (2002).
[5] M. A. Reed, C. Zhou, C. J. Muller, T. P. Burgin, and J. M. Tour, Science **278**, 252 (1997).
[6] C. Kergueris, J.-P. Bourgoin, S. Palacin, D. Esteve, C. Urbina, M. Magoga, and C. Joachim, Phys. Rev. B **59**, 12505 (1999).
[7] X. D. Cui, A. Primak, X. Zarate, J. Tomfohr, O. F. Sankey, A. L. Moore, T. A. Moore, D. Gust, G. Harris, and S. M. Lindsay, Science **294**, 571 (2001).
[8] J. Reichert, R. Ochs, D. Beckmann, H. B. Weber, M. Mayor, and H. v. Löhneysen, Phys. Rev. Lett. **88**, 176804 (2002).
[9] E. G. Petrov and P. Hänggi, Phys. Rev. Lett. **86**, 2862 (2001); E. G. Petrov, V. May, and P. Hänggi, Chem. Phys. **281**, 211 (2002).
[10] J. Lehmann, G.-L. Ingold, and P. Hänggi, Chem. Phys. **281**, 199 (2002).
[11] D. Segal and A. Nitzan, Chem. Phys. **281**, 235 (2002).
[12] H. M. Pastawski, L. E. F. Foa Torres, and E. Medina, Chem. Phys. **281**, 257 (2002).
[13] H. Ness and A. J. Fisher, Chem. Phys. **281**, 279 (2002).
[14] S. Datta, W. Tian, S. Hong, R. Reifenberger, J. I. Henderson, and C. P. Kubiak, Phys. Rev. Lett. **79**, 2530 (1997).
[15] W. Tian, S. Datta, S. Hong, R. Reifenberger, J. I. Henderson, and C. P. Kubiak, J. Chem. Phys. **109**, 2874 (1998).
[16] V. Mujica, A. E. Roitberg, and M. A. Ratner, J. Chem. Phys. **112**, 6834 (2000).
[17] N. D. Lang and P. Avouris, Phys. Rev. Lett. **84**, 358 (2000).
[18] P. S. Damle, A. W. Ghosh, and S. Datta, Phys. Rev. B **64**, 201403 (2001).
[19] A. Nitzan, M. Galperin, G.-L. Ingold, and H. Grabert, J. Chem. Phys. **117**, 10837 (2002).
[20] A. W. Ghosh, private communication (2002).
[21] L. Salem, *Molecular Orbital Theory of Conjugated Systems* (Benjamin, London, 1966).
[22] D. Baeriswyl, D. K. Campbell, and S. Mazumdar, in *Conjugated Conducting Polymers*, edited by H. Kiess (Springer, Heidelberg, 1992), pp. 7–133.
[23] P. Fulde, *Electron Correlations in Molecules and Solids* (Springer, Berlin, Heidelberg, New York, 1995).
[24] C. A. Coulson and G. S. Rushbrooke, Proc. Cambridge Philos. Soc. **36**, 193 (1940).
[25] A. D. MacLachlan, Mol. Phys. **2**, 271 (1959); **4**, 49 (1961).
[26] E. H. Lieb, M. Loss, and R. J. McCann, J. Math. Phys. **34**, 891 (1993).
[27] V. Mujica, M. Kemp, A. Roitberg, and M. Ratner, J. Chem. Phys. **104**, 7296 (1996).
[28] S. Dallakyan and S. Mazumdar, arXiv:cond-mat/0209143.

[29] H. B. Weber, J. Reichert, F. Weigend, R. Ochs, D. Beckmann, M. Mayor, R. Ahlrichs, and H. v. Löhneysen, Chem. Phys. **281**, 113 (2002).
[30] P. Damle, A. W. Ghosh, and S. Datta, Chem. Phys. **281**, 171 (2002).
[31] J. Bardeen, Phys. Rev. Lett. **6**, 57 (1961).
[32] R. Landauer, IBM J. Res. Dev. **1**, 223 (1957); S. Datta, *Electronic Transport in Mesoscopic Systems* (Cambridge University Press, Cambridge, England, 1995).
[33] A. Onipko, Y. Klymenko, L. Malysheva, and S. Stafström, Solid State Commun. **108**, 555 (1998).
[34] A finite molecule-lead coupling matrix element would smoothen the sharp steps in Fig. 5.
[35] J. Chen, M. A. Reed, A. M. Rawlett, and J. M. Tour, Science **286**, 1550 (1999).
[36] *Single Charge Tunneling. Coulomb Blockade Phenomena in Nanostructures*, edited by H. Grabert and M. H. Devoret (Plenum, New York, 1992).
[37] M. R. Buitelaar, A. Bachtold, T. Nussbaumer, M. Iqbal, and C. Schönenberger, Phys. Rev. Lett. **88**, 156801 (2002).

# $1/f^{\gamma}$ tunnel current noise through Si-bound alkyl monolayers

Nicolas Clément,[1] Stéphane Pleutin,[1] Oliver Seitz,[2] Stéphane Lenfant,[1] and Dominique Vuillaume[1,*]
[1]*"Molecular Nanostructures and Devices" Group, Institute for Electronics, Microelectronics and Nanotechnology, CNRS and University of Sciences and Technologies of Lille, BP60069, Avenue Poincaré, F-59652 Cedex, Villeneuve d'Ascq, France*
[2]*Department of Materials and Interfaces, Weizmann Institute of Science, Rehovot 76100, Israel*
(Received 27 August 2007; published 8 November 2007)

We report low frequency tunnel current noise characteristics of an organic monolayer tunnel junction. The measured devices, *n*-Si/alkyl chain $(C_{18}H_{37})$/Al junctions, exhibit a clear $1/f^{\gamma}$ power spectrum noise with $1<\gamma<1.2$. We observe a slight bias-dependent background of the normalized current noise power spectrum $(S_I/I^2)$. However, a local increase is also observed over a certain bias range, mainly if $V>0.4$ V, with an amplitude varying from device to device. We attribute this effect to an energy-dependent trap-induced tunnel current. We find that the background noise, $S_I$, scales with $(\partial I/\partial V)^2$. A model is proposed showing qualitative agreements with our experimental data.

DOI: 10.1103/PhysRevB.76.205407 PACS number(s): 85.65.+h

## I. INTRODUCTION

Molecular electronics is a challenging area of research in physics and chemistry. Electronic transport in molecular junctions and devices has been widely studied from a static (dc) point of view.[1,2] More recently electron-molecular vibration interactions were investigated by inelastic electron tunneling spectroscopy.[3] In terms of the dynamics of a system, fluctuations and noise are ubiquitous physical phenomena. Noise is often composed of $1/f$ noise at low frequency and shot noise at high frequency. Although some theories about shot noise in molecular systems were proposed,[4] it is only recently that it was measured, in the case of a single $D_2$ molecule.[5] Low frequency $1/f$ noise was studied in carbon nanotube transistors,[6] but, up to now, no study of the low frequency current noise in molecular junctions (e.g., electrode/short molecules/electrode) has been reported. Low frequency noise measurements in electronic devices usually can be interpreted in terms of defects and transport mechanisms.[7] While it is obvious that $1/f$ noise will be present in molecular monolayers as in almost any system, only a detailed study can lead to insights in the transport mechanisms, defect characterization, and coupling of molecules with electrodes.

We report here the observation and detailed study of the $1/f^{\gamma}$ power spectrum of current noise through organic molecular junctions. *n*-Si/$C_{18}H_{37}$/Al junctions were chosen for these experiments because of their very high quality, which allows reproducible and reliable measurements.[8] The noise current power spectra $(S_I)$ are measured for different biases. Superimposed on the background noise, we observe noise bumps over a certain bias range and propose a model that includes trap-induced tunnel current, which satisfactorily describes the noise behavior in our tunnel molecular junctions.

## II. CURRENT-VOLTAGE EXPERIMENTS

Si-C linked alkyl monolayers were formed on Si(111) substrates (0.05–0.2 Ω cm) by thermally induced hydrosilylation of alkenes with Si:H, as detailed elsewhere.[8,9] 50 nm thick aluminum contact pads with different surface areas between $9\times10^{-4}$ and $4\times10^{-2}$ cm$^2$ were deposited at 3 Å/s on top of the alkyl chains. The studied junction, Si-*n*/$C_{18}H_{37}$/Al, is shown in Fig. 1(a) (inset). Figure 1(a) shows typical current density–voltage (*J*-*V*) curves. We measured 13 devices with different pad areas. The maximum deviation of the current density between the devices is not more than half an order of magnitude. It is interesting to notice that although devices A and C have different contact pad areas (see figure caption), their *J*-*V* curves almost overlap. This confirms the high quality of the monolayer.[9] Figure 1(b) shows a linear behavior around zero bias and we deduce a surface-normalized conductance of about $(2-3)\times10^{-7}$ S cm$^{-2}$. For most of the measured devices, the *J*-*V* curves diverge from that of device C at $V>0.4$ V, with an increase of current that can reach an order of magnitude at 1 V (device B). Taking into account the difference of work functions between *n*-Si and Al, considering the level of doping in the Si substrate (resistivity ~0.1 Ω cm), there will be an accumulation layer in the Si at $V>-0.1$ V.[10] From capacitance-voltage (*C*-*V*) and conductance-frequency (*G*-*f*) measurements (not shown here), we confirmed this threshold value (±0.1 V). As a consequence, for positive bias, we can neglect any large band bending in Si (no significant voltage drop in Si). The *J*-*V* characteristics are then calculated with the Tsu-Esaki formula[11] that can be recovered from the tunneling Hamiltonian.[12] Assuming the monolayer to be in between two reservoirs of free quasielectrons and the system to be invariant with respect to translation in the transverse directions (parallel to the electrode plates) we get

$$J(V)=\frac{emk_B\theta}{2\pi^2\hbar^3}\int_0^{+\infty}dET(E)\ln\left[\frac{1+e^{\beta(\mu-E)}}{1+e^{\beta(\mu-eV-E)}}\right], \qquad (1)$$

where $e$ is the electron charge, $m$ the effective mass of the charge carriers within the barrier, $k_B$ the Boltzmann constant, $\hbar$ the reduced Planck constant, $\mu$ the Fermi level, and $\beta=1/k_B\theta$ ($\theta$ the temperature in K). $T(E)$ is the transfer coefficient for quasielectrons flowing through the tunnel barrier with longitudinal energy $E$. The total energy, $E_T$, of quasielectrons is decomposed into a longitudinal and a trans-

 

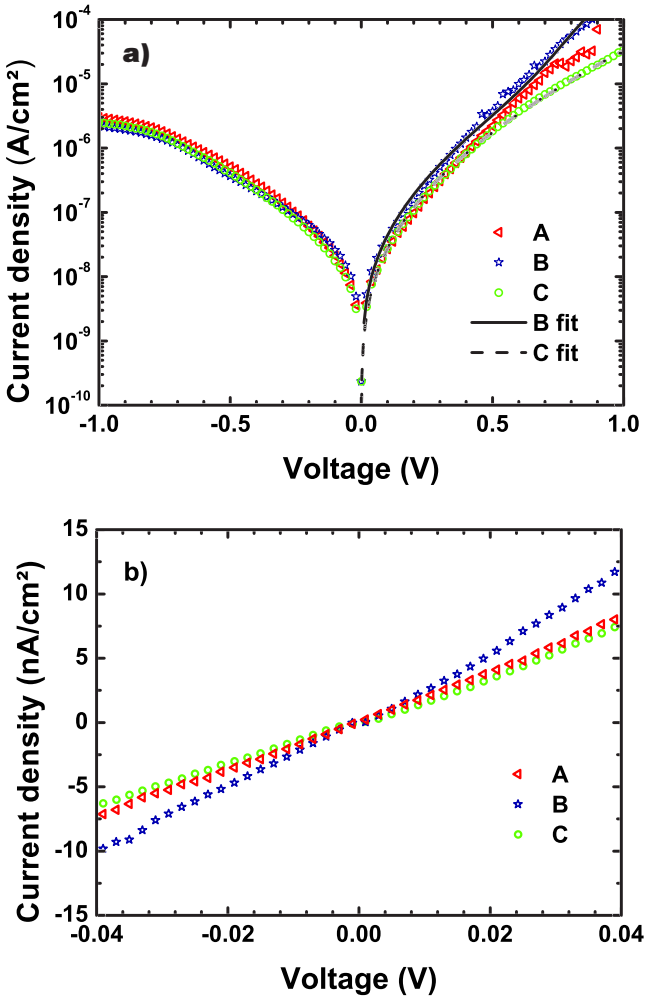


FIG. 1. (Color online) (a) Experimental *J-V* curves at room temperature for *n*-Si/$C_{18}H_{37}$/Al junctions. The contact areas are 0.36 $mm^2$ for device A and 1 $mm^2$ for devices B and C. The voltage *V* is applied to the aluminum pad and the Si is grounded, using a semiconductor signal analyzer Agilent 4155C. Each curve was acquired with a trace-retrace protocol and repeated three times with different delay times between each measurement (voltage step $\Delta V = 1$ mV) in order to check a possible hysteresis effect and confirm that no transient affects the dc characteristics. Theoretical *J-V* curves are also shown for devices B and C. (b) *J-V* curves around zero bias in a linear scale for the three samples showing the good linearity at low bias.

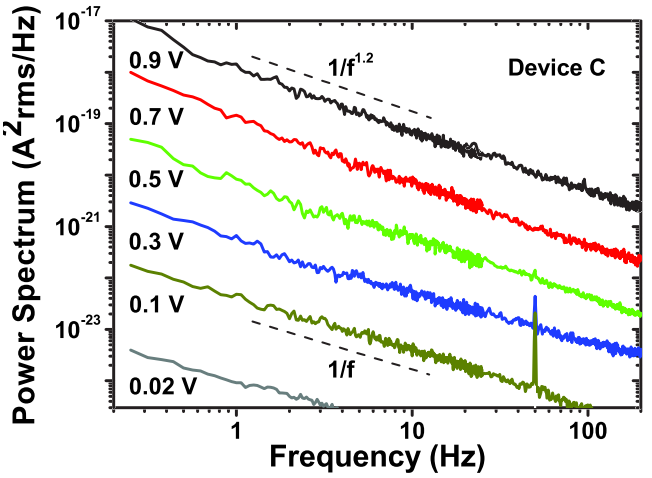


FIG. 2. (Color online) Low frequency $(1/f^{\gamma})$ power spectrum current noise for device C. Although we measured all spectra of the sequence $|V| = [0.02; 0.05; 0.1; 0.15; 0.2; 0.25; 0.3; 0.35; 0.4; 0.45; 0.5; 0.6; 0.7; 0.8; 0.9; 1$ V], we selected for this figure only spectra with $V>0$ V and a spacing of 0.2 V for clearer presentation. $\gamma$ varies from 1 at low voltages to 1.2 at 1 V. For noise measurements, the experimental setup was composed of a low noise current-voltage preamplifier (Stanford SR570), powered by batteries, and a spectrum analyzer (Agilent 35670A). All the measurements were performed under controlled atmosphere ($N_2$) at room temperature.

verse component, $E_T = E + E_t$; $E_t$ was integrated out in Eq. (1). The transfer coefficient is calculated for a given barrier height, $\phi$, and thickness, *d*, and shows two distinct parts: $T(E) = T_1(E) + T_2(E)$. $T_1(E)$ is the main contribution to $T(E)$ that describes transmission through a defect-free barrier. $T_2(E)$ contains perturbative corrections due to assisted tunneling mechanisms induced by impurities located at or near the interfaces. The density of defects is assumed to be sufficiently low to consider the defects as independent from each other, each impurity at position $\vec{r}_i$ interacting with the incoming electrons via a strongly localized potential at energy $U_i, U_i\delta(\vec{r}-\vec{r}_i)$. The value of $U_i$ is random. We write $T_2(E) = \Sigma_{i=1}^{N_{imp}} T_2(E, U_i)$, with $N_{imp}$ being the number of impurities and $T_2(E, U_i)$ the part of the transmission coefficient due to the impurity *i*. The two contributions of $T(E)$ are calculated following the method of Appelbaum and Brinkman.[13] Using Eq. (1), we obtain a good agreement with experiments. The theoretical *J-V* characteristic for devices C and B are shown in Fig. 1(a). The best fits are obtained with $\phi = 4.7$ eV, $m = 0.614 m_e$ ($m_e$ is the electron mass), $10^{10}$ traps/$cm^2$ uniformly distributed in energy for device C, and additional $10^{13}$ traps/$cm^2$ for device B distributed according to a Gaussian peaked at 3 eV. The transfer coefficients $T_2(E, U_i)$ show pronounced quasiresonances at energies depending on $U_i$ that explain the important increase of current. The thickness is kept fixed, $d = 2$ nm (measured by ellipsometry).[8]

## III. NOISE BEHAVIOR

The differences observed in the *J-V* curves are well correlated with specific behaviors observed in the low frequency noise. Figure 2 shows the low frequency current noise power spectrum $S_I$ for different bias voltages from 0.02 to 0.9 V. All curves are almost parallel and follow a perfect $1/f^{\gamma}$ law with $\gamma = 1$ at low voltages, increasing up to 1.2 at 1 V. We could not observe the shot noise because the high gains necessary for the amplification of the low currents induce a cutoff frequency of our current preamplifier lower than the frequency of the $1/f$-shot noise transition. At high currents, $1/f^{\gamma}$ noise was observed up to 10 kHz.

The low frequency $1/f$ current noise usually scales as $I^2$, where *I* is the dc tunnel current,[14] as proposed, for example, by the standard phenomenological equation of Hooge[15] $S_I = \alpha_H I^2 / N_c f$ where $N_c$ is the number of free carriers in the

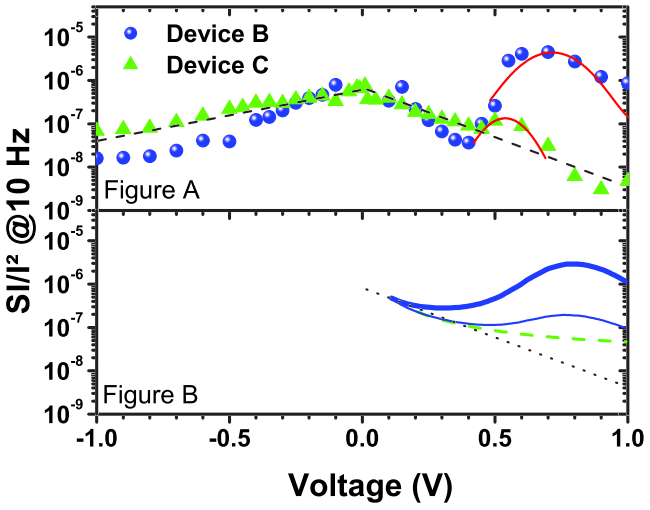


FIG. 3. (Color online) (A) Normalized power spectrum current noise $S_I/I^2$ as a function of bias $V$ for devices B and C. The curve for device C follows asymptotes (black dashed lines) which are used as a reference for other devices. A local increase of noise over the asymptotes with a Gaussian shape (solid lines) is shown. (B) Theoretical estimates are shown for $V>0$, based on Eq. (4) with a uniform defect distribution (dashed line), with adding a Gaussian energy-localized distribution of defects (thin solid line), and keeping the two terms of Eq. (3) with $E^*=5e\delta V$ (bold solid line). An *ad hoc* multiplicative factor has been applied to the theoretical results.

sample and $\alpha_H$ is a dimensionless constant frequently found to be $2\times10^{-3}$. This expression was used with relative success for homogeneous bulk metals[14,15] and more recently also for carbon nanotubes.[6] Similar relations were also derived for $1/f$ noise in variable range hopping conduction.[16] In Fig. 3(a) we present the normalized current noise power spectrum ($S_I/I^2$) at 10 Hz (it is customary to compare noise spectra at 10 Hz) as a function of the bias $V$ for devices B and C. Device C has a basic characteristic with the points following the dashed line asymptote. We use it as a reference for comparison with our other devices. We basically observed that $S_I/I^2$ decreases with $|V|$. For most of our samples, in addition to the background normalized noise, we observe a local (Gaussian with $V$) increase of noise at $V>0.4$ V. The amplitude of the local increase varies from device to device. This local increase of noise is correlated with the increase of current seen in the $J$-$V$ curves. The $J$-$V$ characteristics [Fig. 1(a)] of device B diverge from those of device C at $V>0.4$ V and this is consistent with the local increase of noise observed in Fig. 3. The observed excess noise bump is likely attributed to this Gaussian distribution of traps centered at 3 eV responsible for the current increase. Although the microscopic mechanisms associated with conductance fluctuations are not clearly identified, it is believed that the underlying mechanism involves the trapping of charge carriers in localized states.[17] The nature and origin of these traps are, however, not known. We can hypothesize that the low density of traps uniformly distributed in energy may be due to Si-alkyl interface defects or traps in the monolayer, while the high density, peaked in energy, may be due to metal-induced gap states[18] or residual aluminum oxide at the metal-alkyl interface. The difference in the noise behaviors of samples B and C simply results from inhomogeneities of the metal deposition, i.e., of the chemical reactivity between the metal and the monolayer, or is due to the formation of a residual aluminum oxide due to the presence of residual oxygen in the evaporation chamber. More $1/f$ noise experiments on samples with various physical and chemical natures of the interfaces are in progress to figure out how the noise behavior depends on specific conditions such as the sample geometry, the metal or monolayer quality, the method used for the metal deposition, and so forth.

## IV. TUNNEL CURRENT NOISE MODEL

To model the tunnel current noise in the monolayers, we assume that some of the impurities may trap charge carriers. Since we do not know the microscopic details of the trapping mechanisms and the exact nature of these defects, we use a qualitative description that associates to each of them an effective two-level tunneling system (TLTS) characterized by an asymmetric double well potential with the two minima separated in energy by $2\varepsilon_i$. We denote as $\Delta_i$ the term allowing tunneling from one well to the other, and get, after diagonalization, two levels that are separated in energy by $E_i=\sqrt{\varepsilon_i^2+\Delta_i^2}$. Since we are interested in low frequency noise, we focus on defects with very long trapping times, i.e., defects for which $\Delta_i \ll \varepsilon_i$. The lower state (with energy $E_i^-$) corresponds to an empty trap, and the upper state (with energy $E_i^+$) to a charged one. The relaxation rate from the upper to the lower state is determined by the coupling with the phonons and/or with the quasielectrons giving $\tau^{-1}\propto E_i\Delta_i^2\coth(E_i/2k_B\theta)$ and $\tau^{-1}\propto(\Delta_i^2/\hbar E_i)\coth(E_i/2k_B\theta)$, respectively. In all cases, the time scale of the relaxation, $\tau$, is very long compared to the duration of a scattering event. This allows us to consider the TLTS with a definite value at any instant of time. We then consider the following spectral density of noise for each TLTS:[19]

$$S_I^i(f)=\overline{(I_- - I_+)^2}\frac{\tau}{1+\varpi^2\tau^2}\cosh^{-2}\frac{E_i}{2k_B\theta}, \tag{2}$$

where $\varpi=2\pi f$ and $I_{-(+)}$ is the tunnel current for the empty (charged) impurity state. In this equation, we consider the average of $(I_- - I_+)$ over the TLTSs, having similar $\varepsilon_i$ and $\Delta_i$. The difference between the two levels of current has two different origins. The first one is the change in energy of the impurity level that directly affects $T_2(E)$. The second one is the change in the charge density at the interfaces of the molecular junction induced by the trapped quasielectron that produces a shift in the applied bias, $\delta V$. We write

$$I_+(V)\cong I_-(V+\delta V)+\mathsf{A}\frac{emk_B\theta}{2\pi^2\hbar^3}\int_0^{+\infty}dE\left.\frac{\partial T_2(E,U_i)}{\partial U_i}\right|_{E_i^-}E_i \times\ln\left[\frac{1+e^{\beta(\mu-E)}}{1+e^{\beta(\mu-eV-\delta V-E)}}\right], \tag{3}$$

where $\mathsf{A}$ is the junction (metal electrode) area. The first term in the right hand side is due to the fluctuating applied bias, and the second to the change in the impurity energy. Since $T_2(E)$ is already a perturbation, the second contribution is in

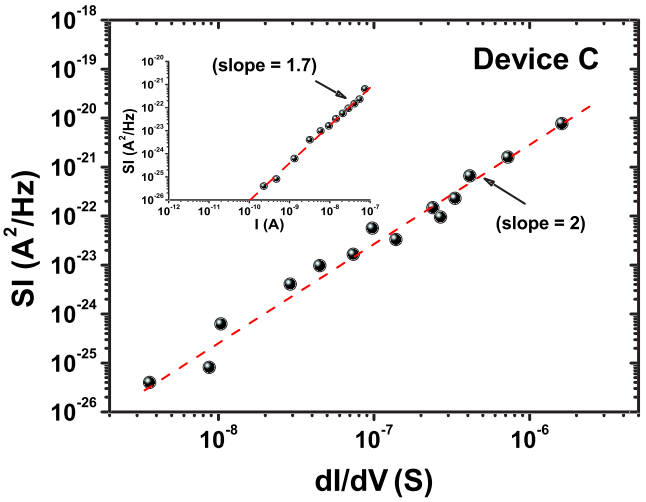


FIG. 4. (Color online) $S_I$-$(\partial I/\partial V)$ curve for device C on a log-log scale. The dashed line represents the slope of 2. In the inset, the $S_I$-$I$ curve is also presented on a log-log scale with a slope of 1.7.

general negligible but becomes important to explain the excess noise. We focus first on the background noise and therefore we keep only the first term of Eq. (3). We assume for simplicity that all the charged impurities give the same shift of bias $\delta V = e/C_{TJ}A$, where $C_{TJ}$ is the capacitance of the tunnel junction per unit surface. Capacitance-voltage measurements (not shown) indicate that $C_{TJ}$ is constant for positive bias. By using usual approximations regarding the distribution in relaxation times, $\tau$, and energies, $E_i$,[19] we get

$$S_I \propto E^* \frac{1}{A} N^*_{imp} \left( \left. \frac{\partial I}{\partial V} \right|_{-} \right)^2 \frac{e^2}{C_{TJ}^2} \frac{1}{f}. \tag{4}$$

We assume that the distribution function of $\varepsilon_i$ and $\Delta_i$, $P(\varepsilon_i, \Delta_i)$, is uniform to get the $1/f$ dependence. In this last expression, the derivative of the current is evaluated for the lower impurity state; $N^*_{imp}$ is the impurity density per unit energy and surface area. We have $E^* = E_{\max}$, the maximum of $E_i$, if $E_{\max} \ll k_B\theta$ and $E^* = k_B\theta$ if $E_{\max} \gg k_B\theta$. $N^*_{imp}$ cannot be determined accurately from the last equation because of lack of information concerning the microscopic nature of the traps.

This predicted dependence of $S_I$ on $(\partial I/\partial V)^2$ is experimentally verified in Fig. 4, where $S_I$ vs $(\partial I/\partial V)$ for device C is plotted on a log-log scale, showing a slope of 2. At the same time (see inset), we show that $S_I$-$I$ follows a power law with a slope of 1.7 and not 2 as usually assumed. The value 1.7 explains why the normalized noise $S_I/I^2$ shown in Fig. 3 decreases with $V$. The appropriate normalization factor to obtain flat background noise is $S_I/I^{1.7}$. These two features imply that $(\partial I/\partial V)^2$ scales with $I^{1.7}$ which has been experimentally verified from the $I$-$V$ curves (not shown). The calculated noise, using Eq. (4), is shown in Fig. 3(b). Qualitative agreements with the experimental data are obtained. With few defects uniformly distributed (device C), $S_I/I^2$ follows (green solid line) at low voltages the dashed line asymptote. With additional defects with a Gaussian distribution (device B), a local increase is found at the correct position but with much too small amplitude (dot blue line). To get a better estimate it is essential to take into account the second term of Eq. (3). Results are shown in Fig. 3(b) (blue solid line) taking $E^* = 5e\delta V$. The quasiresonances of $T_2(E)$ are at the origin of the local increase. The Gaussian distribution selects defects for which $T_2(E, U_i)$ shows quasiresonance in the appropriate range of energy. These traps may be associated with a nonuniform contribution to the distribution function $P(\varepsilon_i, \Delta_i)$ that would break the $1/f$ dependence of $S_I$ above a certain bias. This is what is observed in Fig. 2, with $\gamma$ changing from 1 to 1.2.

## V. CONCLUSION

In summary, we have reported the study of low frequency $(1/f^\gamma)$ current noise in molecular junctions. We have correlated the small dispersion observed in dc $J$-$V$ characteristics and the local increase of normalized noise at certain biases (mainly at $V > 0.4$ V). A theoretical model qualitatively explains this effect as due to the presence of an energy-localized distribution of traps. The model predicts that the power spectrum of the background current noise is proportional to $(\partial I/\partial V)^2$ as observed in our experiments.[20] We also show that the power spectrum of the current noise should be normalized as $S_I/I^{1.7}$. The background noise is associated with a low density of traps uniformly distributed in energy that may be due to Si-alkyl interface defects or traps in the monolayer. The local increase of noise for bias $V > 0.4$ V is ascribed to a high density of traps, peaked in energy, probably induced by the metal deposition on the monolayer.

## ACKNOWLEDGMENTS

We thank David Cahen for many valuable discussions. N.C. and S.P. acknowledge support from the "ACI Nanosciences" program and IRCICA. We thank Hiroshi Inokawa and Frederic Martinez for helpful comments.

*Author to whom correspondence should be addressed; dominique.vuillaume@iemn.univ-lille1.fr

[1] A. Nitzan and M. A. Ratner, Science **300**, 1384 (2003).

[2] A. Salomon, D. Cahen, S. Lindsay, J. Tomfohr, V. B. Engelkes, and C. D. Frisbie, Adv. Mater. (Weinheim, Ger.) **25**, 1881 (2003).

[3] W. Wang, T. Lee, and I. Krestchmar, Nano Lett. **4**, 643 (2004); J. G. Kushmerick, J. Lazorcik, and C. H. Patterson, *ibid.* **4**, 643 (2004); A. Troisi and M. A. Ratner, Phys. Rev. B **72**, 033408 (2005); D. K. Aswal, C. Petit, and G. Salace, Phys. Status Solidi A **203**, 1464 (2006); C. Petit, G. Salace, and S. Lenfant, Microelectron. Eng. **80**, 398 (2005).

[4] M. Galperin, A. Nitzan, and M. A. Ratner, Phys. Rev. B **74**, 075326 (2006); A. Thielmann, M. H. Hettler, J. König, and G. Schön, *ibid.* **68**, 115105 (2003); Phys. Rev. Lett. **95**, 146806 (2005); R. Guyon, T. Jonckheere, V. Mujica, A. Crépieux, and T. Martin, J. Chem. Phys. **122**, 144703 (2005).

[5] D. Djukic and J. M. van Ruitenbeek, Nano Lett. **6**, 789 (2006).

[6] P. G. Collins, M. S. Fuhrer, and A. Zettl, Appl. Phys. Lett. **76**, 894 (2000); Y.-M. Lin, J. Appenzeller, J. Knoch, Z. Chen, and P. Avouris, Nano Lett. **6**, 930 (2006).

[7] M. J. Kirton and M. J. Uren, Adv. Phys. **38**, 367 (1989).

[8] A. Salomon, T. Boecking, C. K. Chan, F. Amy, O. Girshevitz, D. Cahen, and A. Kahn, Phys. Rev. Lett. **95**, 266807 (2005).

[9] O. Seitz, T. Böcking, A. Salomon, J. J. Gooding, and D. Cahen, Langmuir **22**, 6915 (2006).

[10] S. M. Sze, *Physics of Semiconductor Devices* (Wiley, New York, 1981).

[11] R. Tsu and L. Esaki, Appl. Phys. Lett. **22**, 562 (1973).

[12] G. D. Mahan, *Many-Particle Physics*, 3rd ed. (Plenum, New York, 2000).

[13] J. A. Appelbaum and W. F. Brinkman, Phys. Rev. B **2**, 907 (1970).

[14] P. Dutta and P. M. Horn, Rev. Mod. Phys. **53**, 497 (1981); M. B. Weissman, *ibid.* **60**, 537 (1988).

[15] F. N. Hooge, Physica B & C **83**, 14 (1976); F. N. Hooge, T. G. M. Kleinpenning, and L. K. J. Vandamme, Rep. Prog. Phys. **44**, 479 (1981).

[16] B. I. Shklovskii, Phys. Rev. B **67**, 045201 (2003); A. L. Burin, B. I. Shklovskii, V. I. Kozub, Y. M. Galperin, and V. Vinokur, *ibid.* **74**, 075205 (2006).

[17] S. Machlup, J. Appl. Phys. **25**, 341 (1954); C. T. Rogers and R. A. Buhrman, Phys. Rev. Lett. **53**, 1272 (1984).

[18] M. Kiguchi, R. Arita, G. Yoshikawa, Y. Tanida, S. Ikeda, S. Entani, I. Nakai, H. Kondoh, T. Ohta, K. Saiki, and H. Aoki, Phys. Rev. B **72**, 075446 (2005); H. Vasquez *et al.*, Europhys. Lett. **65**, 802 (2004).

[19] S. M. Kogan, *Electronic Noise and Fluctuations in Solids* (Cambridge University Press, Cambridge, 1996).

[20] A similar behavior has been some time observed in $SiO_2$ tunnel devices, see G. B. Alers, K. S. Krisch, D. Monroe, B. E. Weir, and A. M. Chang, Appl. Phys. Lett. **69**, 2885 (1996); F. Martinez, S. Soliveres, C. Leyris, and M. Valenza, IEEE ICMTS Proceedings, 2006 (unpublished), p. 193.

# Relaxation dynamics in covalently bonded organic monolayers on silicon

Nicolas Clément,* Stéphane Pleutin, David Guérin, and Dominique Vuillaume†
*Institute for Electronics Microelectronics and Nanotechnology (IEMN), CNRS, University of Lille, BP 60069, Avenue Poincaré, Villeneuve d'Ascq, F-59652 Cedex, France*

(Received 28 January 2010; revised manuscript received 19 April 2010; published 6 July 2010)

We study the dynamic electrical response of a silicon-molecular monolayer-metal junctions and we observe two contributions in the admittance spectroscopy data. These contributions are related to dipolar relaxation and molecular organization in the monolayer in one hand, and the presence of defects at the silicon/molecule interface in the other hand. We propose a small signal equivalent circuit suitable for the simulations of these molecular devices in commercial device simulators. Our results concern monolayers of alkyl chains considered as a model system but can be extended to other molecular monolayers. These results open door to a better control and optimization of molecular devices.

DOI: 10.1103/PhysRevB.82.035404 PACS number(s): 85.65.+h, 73.61.Le, 77.22.Gm, 77.55.Bh

## I. INTRODUCTION

Molecule-based devices are envisioned to complement silicon devices by providing new functions or already existing functions at a simpler process level and at a lower cost by virtue of their self-organization capabilities. Molecular monolayers represent a widely used systems covering a large range of applications such as molecular memories,[1] switches,[2–5] nanodielectrics for organic and carbon nanotube transistors,[6–8] or biosensors.[9] The physics and engineering of the molecule/electrode contact has long been recognized as a key issue, and this has been mainly studied through the impact on the static (dc) characteristics of these molecular devices.[10,11] Here we use admittance spectroscopy to study quantitatively the dielectric response of highly ordered monolayers grafted on silicon in a parallel-plate-capacitor structure with different interfaces and electrodes. We study both the contribution of dipolar relaxation, molecular reorganization in the monolayer, and the contribution of defects at the silicon/molecule interface. We propose a small signal equivalent circuit suitable for the simulations of these molecular devices in commercial device simulators. Our results concern monolayers of alkyl chains considered as a model system but can be extended to other molecular monolayers. These results open door to a better control and optimization of molecular devices.

Dielectric properties of organic monolayers sandwiched between two contact electrodes in a parallel-plate structure are a key issue for a complete understanding of the electronic properties of any nanodevices using functional molecules. Up to now, only dc characteristics (e.g., current-voltage curves) were used to access electron transport through the monolayers and especially to emphasize the role of the molecule-electrode interface.[12–14] The dynamic electron-transport properties in molecular junctions have only been studied by inelastic electron spectroscopy to characterize the interaction between electrons and the molecular vibrations in the infrared region ($>10^{12}$ Hz).[15–17] However, other relaxation phenomena in the intermediate frequency range ($1-10^6$ Hz) are also important to assess the molecular organization and the presence of defect in the monolayers. Permanent molecular dipoles tend to relax to be oriented with the electric field direction.[18] Their dynamics is expected to depend on the molecular packing and organization (e.g., presence of domains and clusters) in the monolayers. We note that dynamic relaxations were previously characterized for alkyl monolayers grafted on porous glass[19] and on thick oxide using a lateral electrode configurations.[20] These authors were able to distinguish the dipole relaxation coming from the bottom and top of the organic monolayers[19] and to follow the dependence of these dipole relaxation as a function of the monolayer density.[20] At lower frequency ($<1$ kHz), other phenomena regrouped under the name "interfacial polarization" have to be considered. For instance, we recently showed that electrically active defects can be observed in monolayer through the measurement of the low-frequency noise ($<100$ Hz) of the tunneling current,[21] and we showed how they can modify the tunnel current in the molecular junction.

## II. EXPERIMENTAL SECTION

The electric polarization of a solid has several contributions that may be termed intrinsic, e.g., electronic, ionic or dipolar polarization, or extrinsic e.g., polarization caused by defects or traps. Those contributions act in different frequency regions and show particular signatures in the dielectric constant or susceptibility (Fig. 1) as shown in many textbooks.[22] The real part of the response function describes polarization while their imaginary part takes account for dissipation. Here, we used admittance spectroscopy[23] which is a very sensitive measurement technique for probing molecular relaxation processes on a wide range of time scales. This method characterizes molecular scale dynamics through its relationship to transient changes in the dielectric properties of a macroscopic sample. The method is sensitive enough to measure the ac admittance $Y_m = G_m + jC_m\omega$ of a molecular monolayer junction (containing less than $10^{11}$ molecules) in the range $20-10^6$ Hz (see Sec. II B) and as function of a superimposed static potential in the range 0–1 V. $G_m$ and $C_m$ are the measured parallel conductance and capacitance.

### A. Sample manufacturing

We prepared high-quality alkyl chain monolayers on both oxide-free silicon wafers and on ultrathin (0.6-nm-thick)

 

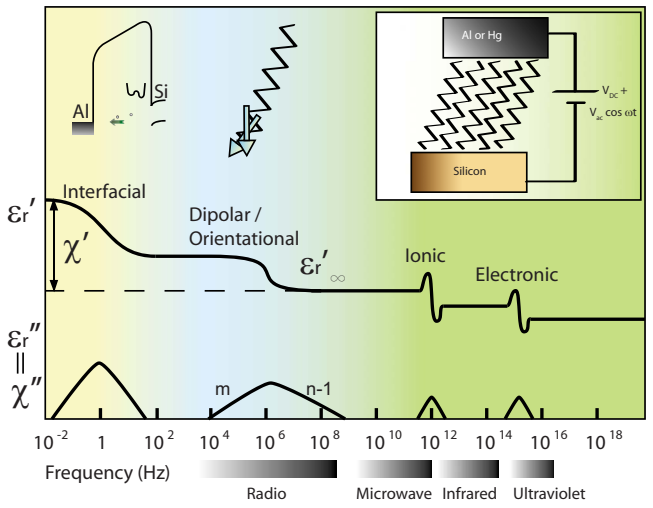


FIG. 1. (Color online) Frequency dependence of real, $\varepsilon_r'$ (or $\chi'$), and imaginary, $\varepsilon_r''$ (or $\chi''$), parts of the permittivity in the presence of interfacial, orientational, ionic, and electronic polarization mechanisms. Inset: left: a band diagram with a two-level tunneling system illustrate the interfacial polarization mechanism and middle: the small dipole linked to each alkyl chain tends to orient with the electric field. It creates a dipolar polarization; right: schematic view of the experimental setup, parallel-plate-capacitor structure, on Si-*n*/alkyl chain monolayer/Al or Hg molecular tunnel junction.

thermal oxides. This allowed us to compare two types of silicon/molecule interfaces. On both cases, we used an 18-carbon atom chain (octadecene, OD, on silicon, and octadecyltrichlorosilane, OTS, on oxidized silicon). The chemical structures of the molecules are shown in Fig. 2. Samples A and B: Si-C linked alkyl monolayers were formed by thermally induced hydrosilylation of alkenes (octadecene, see Fig. 2) with hydrogen-terminated Si surfaces, adapting a procedure described elsewhere.[24] We used *n*-type doped (0.02–0.5 Ω cm) Si(111). Two categories of devices, referred to as A and B, with different dc tunnel conductance $G_T$ (low and high, respectively) are selected with the aim to evaluate its impact on the dielectric response. These two types of samples are selected (after dc current-voltage measurements) from the same batch as a result of the inherent dispersion already observed with such a chemical approach. Sample C: a 2-nm-thick oxide was thermally grown on

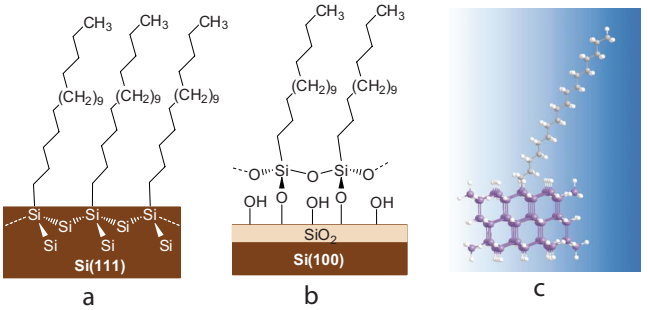


FIG. 2. (Color online) Schematic representation of (a) OD molecules grafted on Si substrate, (b) OTS on oxydized silicon substrate, and (c) stick and bowl model of the molecule and a Si cluster.

TABLE I. Water contact angle ($\theta_{H20}$), measured thickness ($d$), and theoretical, expected thickness for a monolayer with molecules in the all-trans conformation tilted by an angle $\theta$ with respect to surface normal [$\theta < 15°$ and 30° for OTS on slightly oxidized Si (sample C) and OD on Si:H (samples A and B), respectively].

| Samples | $\theta_{H20}$ (deg) | $d$ (nm) | $d_0 \cos(\theta)$ (nm) |
|---|---|---|---|
| A and B | 111 (±1) | 2.18 (±0.15) | 2.2 |
| C | 109 (±1) | 2.50 (±0.15) | 2.6 |

*n*-type doped ($1-3\times10^{-3}$ Ω cm) Si(100) in dry $O_2$ at 720 °C and chemically thinned to 0.6 nm at 0.64 Å/min by a HF(0.1%)/HCl(2.5%) solution. A monolayer of OTS—see Fig. 2—was formed by reacting in solution the freshly prepared oxide surface with $10^{-3}$ M of OTS in a mixture of hexadecane/$CCl_4$ as reported elsewhere.[25,26] In that case the alkyl chain is bonded to the substrate through siloxane (Si-O-Si) bonds. The quality of the monolayers was assessed by spectroscopic ellipsometry and water contact angle measurements (Table I). We selected only monolayers with a water contact angle larger than 110° and a thickness close to $d_0 \cos\theta$ (within ±3 Å) where $d_0$ is the expected length of the molecule in its all-trans conformation and $\theta$ is the tilt angle between the long axe of the molecule and the normal to the surface (<15° and <30° for OTS on oxidized Si and OD on Si:H, respectively).[27,28] We also prepared a control experiment sample (no organic monolayer) with a 3-nm-thick thermal oxide using the same oxidation process as for sample C (dry $O_2$ at 720 °C). A 50-nm-thick aluminum contact pads with different surface areas between $9\times10^{-4}$ and $4\times10^{-2}$ $cm^2$ were vacuum ($10^{-7}$ Torr) evaporated at 3 Å/s on top of the alkyl chains or they were contacted with a hanging Hg drop. In case of evaporated metal electrodes, the devices were contacted with a micromanipulator probe station (Süss Microtec PM-5) placed inside a glove box (MBRAUN) with a strictly controlled nitrogen ambient (less than 1 ppm of water vapor and oxygen). The hanging naked Hg drop was formed using a controlled growth mercury electrode system (BASi) in a glove box, the sample was placed on an elevator stage and put into contact by moving it upward. The junction size was estimated by measuring the Hg drop profile by a calibrated USB webcam. The Hg drop contact method has been demonstrated to be shortage free and reproducible.[11,29,30] All electrical measurements were conducted in dark. Some OTS samples were submitted to a thermal annealing at 200 °C in $N_2$ for 1 h. We measured about 20 samples of each type to assess the dispersion of the junction parameters, the curves shown in the figures are representative of the average behavior.

### B. Admittance spectroscopy measurements

The dc voltage bias (0–1 V) superimposed with a small ac signal (10 $mV_{eff}$) was applied on the metallic electrode, the Si substrate was grounded, and the complex admittance was measured using an impedance-meter Agilent 4284A in the range 20–$10^6$ Hz. Measured conductances and capacitances

are corrected from a small series resistance $R_S$ (typically in the range 5–70 Ω for our experimental setup) according to standard procedures.[31]

The Agilent 4284A provides directly the parallel conductance and capacitance values, $G_m$ and $C_m$, which are normalized by the contact surface area. To remove the series resistance, $R_S$, contribution and extract intrinsic dielectric properties, $G_m$ and $C_m$ are corrected using Eqs. (1) and (2) to give the corrected conductance and capacitance at each measurement pulsation

$$G_c(\omega) = G_m - R_S C_m^2 (1 - R_S G_m)\omega^2, \tag{1}$$

$$C_c(\omega) = \frac{1 - \sqrt{1 - (2C_m R_S \omega)^2}}{2C_m (R_S \omega)^2}. \tag{2}$$

We get a corrected admittance per surface unit $Y_c = G_c + jC_c\omega$, from which we deduced two quantities $C'$ and $C''$ related to the real and imaginary parts of the dielectric susceptibility of the monolayer $\chi = \chi'(\omega) + j\chi''(\omega)$, by

$$C' = C_c - C_\infty = \frac{\varepsilon_0 \chi'}{d} \quad \text{and} \quad C'' = \frac{\varepsilon_0 \chi''}{d} = \frac{G_c - G_T}{\omega}, \tag{3}$$

where $C_\infty$ is the high-frequency part of capacitance due to ionic and electronic contributions (Fig. 1), $G_T$ is the tunneling conductance per surface area [measured from dc current-voltage curves or from $\lim_{\omega \to 0} G_c(\omega)$], $d$ is the monolayer thickness, $\varepsilon_0$ is the vacuum permittivity, and $\omega$ is the measurement pulsation. There is still a small parasitic effect (increase in $C'$ and $C''$ at high frequencies) which is due to the sample environment (cables). It is a known effect[32] but since it only affects the highest frequency part of the curves, we let it as it is.

## III. THEORY

In the limit of a response that is linear in the applied electric field (weak ac field), the complex dielectric susceptibility is related to the relaxation function, $\phi$, which is the response function of the system after the abrupt removal of a constant electric field

$$\chi(\omega) = \chi'(\omega) + j\chi''(\omega) = \varepsilon_r(\omega) - \varepsilon_r(\infty) = (\chi_0 - \chi_\infty)\left[1 + \int_0^{+\infty} \phi(t) e^{j\omega t} dt\right]. \tag{4}$$

We are interested in the low frequencies part of the dielectric susceptibility attributed to defect or dipolar relaxation (see Fig. 1). $\chi_0$ is the value at zero frequency and $\chi_\infty = 0$ since at high enough frequencies the mobile dipoles cannot follow the field anymore and do not contribute to the polarization. $\varepsilon_r(\infty)$ is the part of the relative dielectric constant due to ionic and electronic contributions; more precisely, it is defined for intermediate frequencies large enough for the dipoles to be "frozen" and not contributing to the polarization but small enough not to consider dissipation from the ionic and electronic degrees of freedom.

In the simplest case, considered long ago by Debye,[33] the relaxation function is given by a single exponential

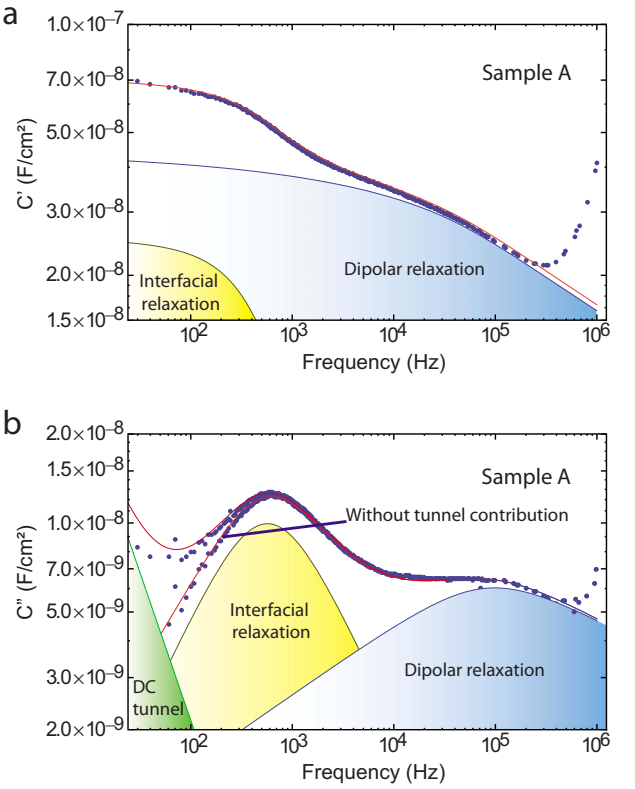


FIG. 3. (Color online) [(a) and (b)] $C' \propto \chi'$ and $C'' \propto \chi''$ graphs with frequency dependence for samples A (alkene monolayer with low density of interfacial defects). Experimental data are the dots, with and without the dc tunnel contribution. Fits (lines) include a contribution from interfacial relaxation and dipolar relaxation as indicated. The dc tunnel conductance contribution [plotted as $G_T/\omega$, see Eq. (3)] is also represented in $C''$ graphs. The dc bias voltage is $V_{dc} = 0.2$ V.

$$\phi_{Debye}(t) = e^{-t/\tau}, \tag{5}$$

where $\tau$ is the characteristic time of relaxation. This is for instance the relaxation function of a rigid polar molecule in a viscous isotropic fluid. Such simple response yields

$$\chi_{Debye}(\omega) = \chi_0 \frac{1 + j\omega\tau}{1 - \omega^2\tau^2}. \tag{6}$$

The real part of Debye's susceptibility shows a plateau at low frequencies below $1/\tau$ and decreases as $\omega^{-2}$ above $1/\tau$. Its imaginary part shows a peak at $1/\tau$: it increases as $\omega$ in the prepeak region and decreases as $\omega^{-1}$ in the postpeak region. However, this type of response is not usual in condensed matter. Instead, fractional power laws are most often observed,

$$\chi(\omega) \propto (j\omega)^{n-1} \quad \text{for} \quad \omega \gg \omega_p,$$

$$\chi(0) - \chi(\omega) \propto (j\omega)^m \quad \text{for} \quad \omega \ll \omega_p, \tag{7}$$

$\omega_p$ being the peak of maximum loss. This is the well-known "universal" dielectric response pointed out by Jonscher.[18] Our data clearly show two contributions (Figs. 3–5). We write

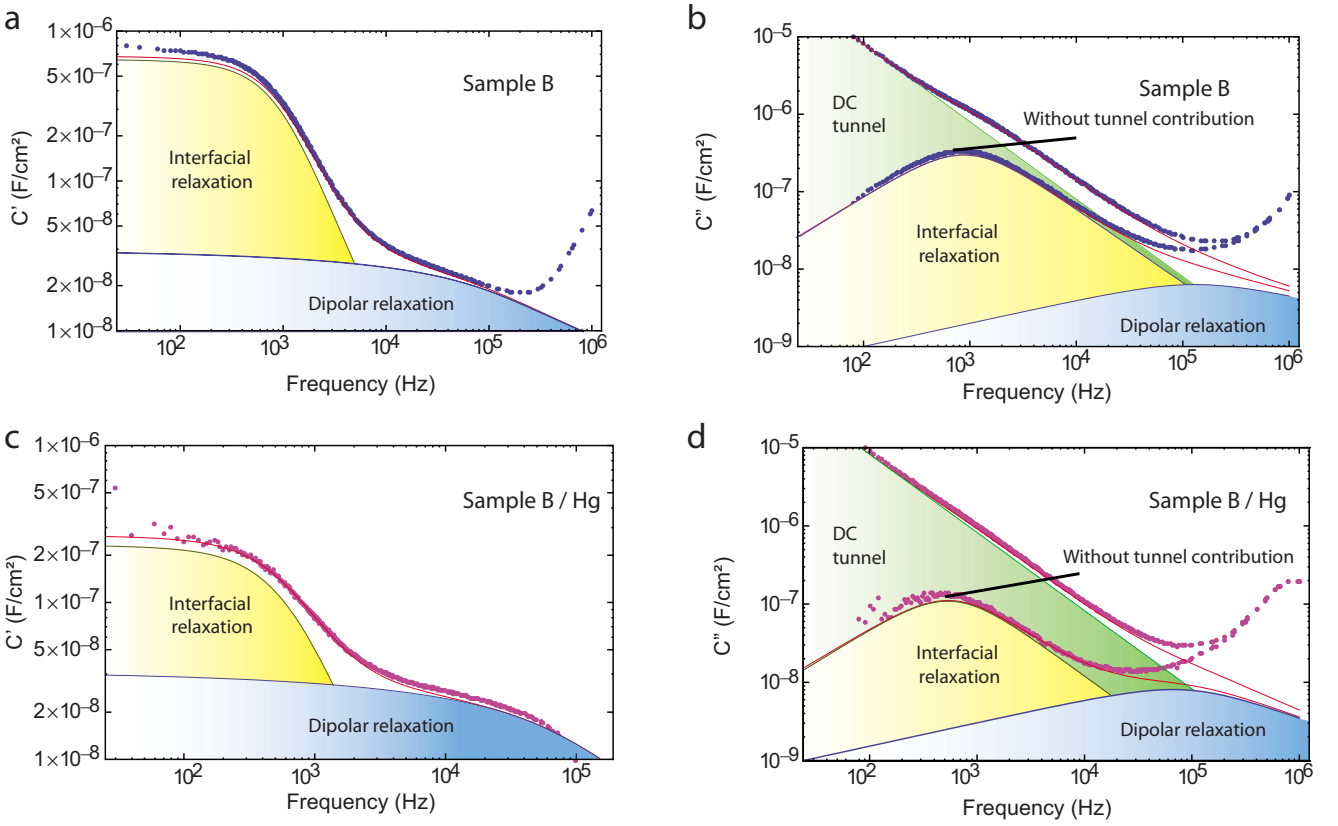


FIG. 4. (Color online) [(a) and (b)] Same as Fig. 3 for sample B (alkene monolayer with a large density of interfacial defects contacted by an Al electrode) and [(c) and (d)] sample B contacted by a Hg drop. The dc bias voltage is $V_{dc}=0.2$ V.

$$\chi(\omega) = \chi_1(\omega) + \chi_2(\omega), \tag{8}$$

where 1 and 2 refer to the first and second (at higher frequencies) peaks as shown in Figs. 3–5 and are discussed below.

### A. Peak 1, interfacial contribution

The first peak in the dielectric response (Fig. 1) is usually attributed to interface defects.[31] The internal dynamics of such defects, modeled by two level systems, results in a Debye contribution to the dielectric susceptibility[31]

$$\chi_1(\omega) = \frac{q^2 N_T}{k_B T} \frac{1}{1 - j\omega\tau_1}, \tag{9}$$

where $N_T$ is the defect density, $1/2\pi f_1 = \tau_1$ with $f_1$ the frequency of the peak 1 maximum, $k_B$ the Boltzmann constant, $T$ the temperature, and $q$ the electron charge. The characteristic time $\tau_1$ of relaxation may be due to thermal excitation or interaction with the phonons of the bath, for instance.

### B. Peak 2, molecular contribution

This contribution usually follows the universal behavior of Jonscher.[34] The response is then characterized by three parameters: the prepeak and postpeak exponents, $m$ and $n$, respectively, and the peak position, $f_2$ (as shown in Fig. 1). Several phenomenological expressions have been proposed to mimic the universal dielectric response.[22] A suitable expression that models remarkably well our data is the Dissado-Hill dielectric susceptibility.[35] It reads

$$\chi_2(\omega) = \chi_0 \frac{\Gamma(1+m-n)}{\Gamma(m)\Gamma(2-n)} (1 - j\omega\tau_2)^{n-1} \times {}_2F_1[1-n, 1-m, 2-n, (1-j\omega\tau_2)^{-1}] \tag{10}$$

with $1/2\pi f_2 = \tau_2$, $f_2$ being the frequency of the peak 2 maximum, and $\Gamma$ the gamma function ($n$ and $m$ are defined above). Equation (10) follows the asymptotic limits given by Eq. (7). ${}_2F_1$ is the Gauss hypergeometric function with $0 \leq m \leq 1$ and $0 \leq n \leq 1$. Dissado and Hill have proposed this function based on some qualitative arguments. Their function has proven to model successfully numerous data of very different systems. Moreover they have tentatively related the $n$ and $m$ exponents to structural characteristics. Derived from the generic arguments they have developed we propose below a qualitative model to understand dissipation in our device.

## IV. RESULTS

Figures 3 and 4 show $C'$ and $C''$ for two representative samples hereafter denoted as samples A and B. They are both made of OD on Si but differ by their level of measured dc tunnel current (see above, Sec. II A). We distinguish three contributions corresponding to peaks in the dielectric loss $C''$ and steps and plateaus in the capacitance $C'$. The first peak in $C''$ (filled in yellow) corresponds to interfacial relaxations

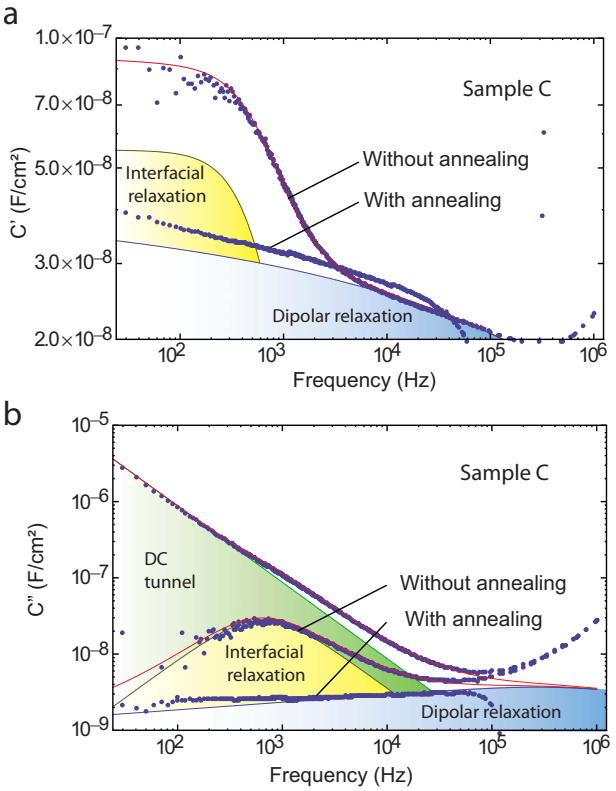


FIG. 5. (Color online) Same as Figs. 3 and 4 for and sample C (OTS monolayer with/without annealing). The dc bias voltage is $V_{dc}=0.2$ V.

and the second peak (in blue) to molecular relaxations. The contribution of the dc tunnel conductance is filled in green [it follows a $1/f$ behavior, $G_T/\omega$ contribution in Eq. (3)]. In all curves, we observe in the high-frequency part an increase in both $C'$ and $C''$, which is due to a parasitic inductance (see Sec. II B). The first peak is well fitted with the Debye model[33] describing a set of identical noninteracting defects whose dynamics is reduced to tunneling between two minimal configurations (see Sec. III on theory). It can be linked to the bias dependent $1/f$ noise increase due to a peaked density of defect previously reported for this device.[21] The amplitude of this peak varies from device to device: the interfacial relaxation contribution is relatively weak for sample A and strong for sample B. We note an increase in the $C''$ peak and the $C'$ plateau by about 30 times. This increase is strongly related with an increase in the dc tunnel conductance $G_T$ by three orders of magnitude. Device B was selected (see Sec. II A) to illustrate this point. The second peak was fitted with a Dissado-Hill expression[35] (see Sec. III). The imaginary part of this phenomenological expression shows fractional power laws, $\omega^m$ and $\omega^{n-1}$, in the prepeak and postpeak regions, respectively. Such behaviors are the signature of strongly constrained dynamic of relaxation due to interaction between the relaxing quantities and their environment. The $n$ and $m$ exponents have been related by Dissado and Hill to structural characteristics. The dipolar relaxation contributions to $C'$ and $C''$ are similar for samples A and B, which means that they have a similar molecular organization and packing. Since the nature and technology used to form the top contact on the monolayer can strongly influence and even degrade the electronic properties of the molecular junction,[11,36] we also tested samples A and B using a hanging Hg drop. The results (Fig. 4) are almost similar as for the evaporated Al electrode. The dipolar relaxation contributions to $C'$ and $C''$ have almost the same amplitude, however, the interfacial peak position is shifted by the difference in work function between Al and Hg (see later, discussion section).

The interface with the Si is also playing an important role. The presence of an ultrathin oxide layer (0.6 nm) between the molecule and the Si electrode electronically decouples the molecule from the Si while a stronger electronic coupling is obtained without the oxide. These features induce changes in the dc current-voltage characteristics.[37] Figure 5 shows the measured $C'$ and $C''$ for sample C (OTS on a slightly oxidized Si, see Sec. II A). The interfacial relaxation is still observed with almost the same amplitude as for sample A. This means that this contribution comes from the molecule and is not strongly related to the nature of the substrate (no peak from oxide as checked on a reference $Si/SiO_2$ sample, see Sec. V A). Finally, the sample C was annealed at 200 °C under $N_2$ atmosphere. We observed a strong decrease in the interfacial relaxation peak (Fig. 5).

## V. DISCUSSIONS

### A. Peak 1, interfacial contribution

According to the above considerations and previous literature on other semiconductor-insulator-metal results,[31] we assign the interfacial relaxation contribution (peak 1) to defects, traps, localized at, or near, the interface between the monolayer and the substrate. This hypothesis can be considered for several reasons: (i) we have already pointed out the link between interface-trap assisted tunneling current and low-frequency noise in these molecular junctions,[21] considering traps energetically localized in the highest occupied molecular orbital-lowest unoccupied molecular orbital gap of the alkyl monolayers and (ii) interface traps in other inorganic tunnel barrier usually respond in this frequency range.[31] We note, however, that we did not observe (Fig. 6) a significant interfacial relaxation peak in this frequency range for a reference sample (i.e., a 3-nm-thick thermal oxide without any molecular monolayer, see Sec. II A), which means that the observed peaks are due to some defects related to the organic monolayer and not at the $Si/SiO_2$ interface nor buried in the $SiO_2$ layer. The nature, origin, of which remains to be discovered. One possible origin should be interface defects at the molecule-substrate interface (e.g., dangling or distorted bonds).[38,39] Because covalently bonded organic monolayers are organized in domains with grain boundaries and they present also pinholes, another possible origin could be surface states coming from substrate surface atoms belonging to these regions where molecules are absent. It has been previously observed and calculated that these pinholes can play an important role to determine the overall electrical behavior of the monolayer devices.[40,41] We can note that the fact that the first contribution is very close to a Debye response is attributed to a distribution of defects with a time constant response strongly peaked around the frequency $f_1$:

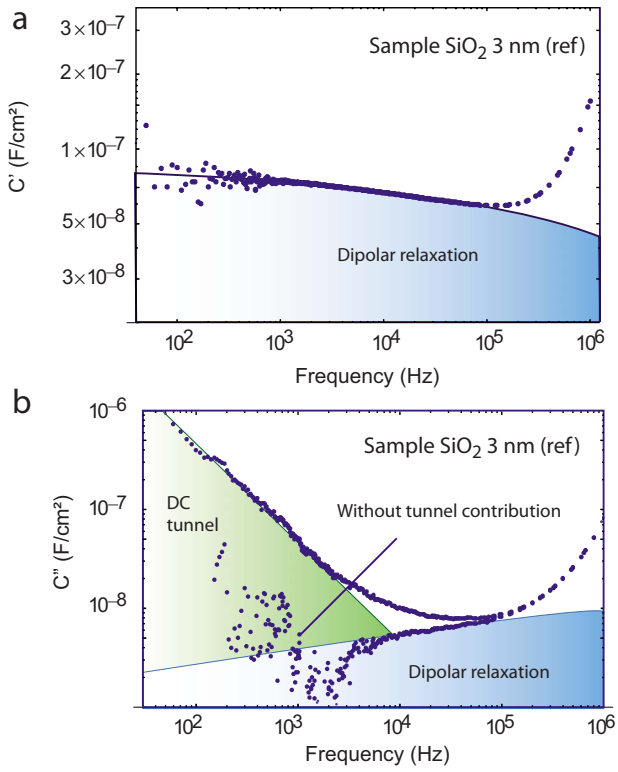


FIG. 6. (Color online) Same Figs. 3–5 for the reference samples (3-nm-thick $SiO_2$, no monolayer). No interfacial relaxation (peak 1) can be detected. The dc bias voltage is $V_{dc}=0.2$ V.

one type of defects seems to dominate the dielectric response in this frequency range. We can deduce the trap density, $N_T$, from the following equation:[23]

$$C' = C_\infty + \frac{C_D}{(1-j\omega\tau_1)} = C_\infty + \frac{q^2 N_T}{k_B T}\frac{1}{(1-j\omega/2\pi f_1)}, \quad (11)$$

where $C_\infty$ is the high-frequency limit of $C'$, $C_D$ is the capacitance associated to charges trapped on defects, $\tau_1$ is a characteristic time constant of these traps, $T$ is the temperature, $k_B$ is the Boltzmann constant, $q$ is the electron charge, and $f_1$ is the frequency at the maximum of the peak 1. By doing the above measurements at various dc bias, the Fermi energy of the Si is swept along the energy distribution of the traps. Figure 7 plots the corresponding trap density distribution for the samples A and B (with Al and Hg drop contacts). Sample A (with both Al and Hg electrodes) displays a remarkably low density (in the range $1.2\times10^9-10^{10}$ $cm^{-2}$) for a room-temperature process, almost on a par with the state-of-the-art $Si/SiO_2$ interface, but, in this latter case, obtained after a high-temperature postoxidation annealing. Samples B (both Al and Hg electrodes) have a higher density of traps ($2\times10^{10}-10^{12}$ $cm^{-2}$), and we clearly observed a shift in the $N_T$-$V_{dc}$ characteristics due to the difference in work functions between the Al and Hg electrodes. This means that the defects are located near the alkly/Si interface since they are sensitive to the Si surface potential.[31] For $V_{dc}>0$, the probed traps are located at energy close or slightly higher than the Si conduction band since the Si is in accumulation regime.

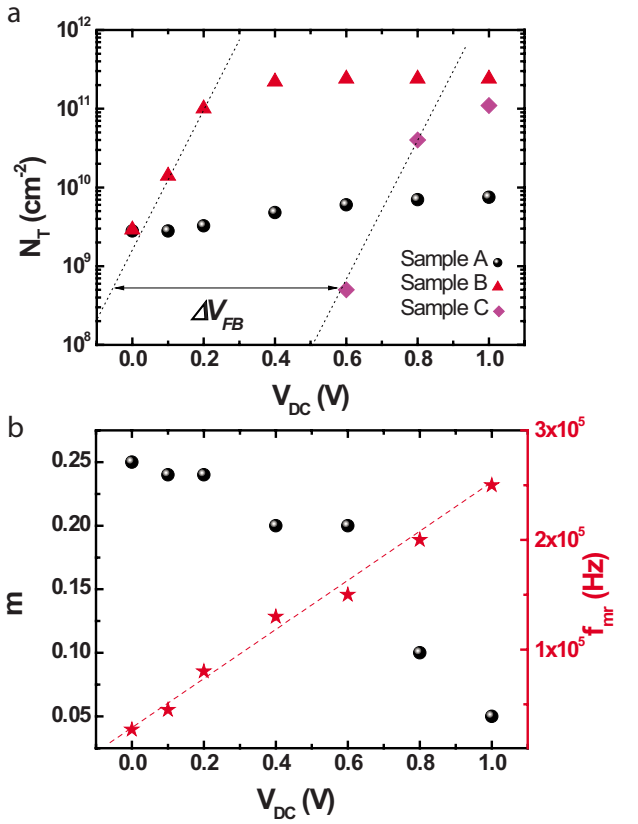


FIG. 7. (Color online) (a) The density of defects $N_T$, [Eq. (11)] as a function of $V_{dc}$ for alkene monolayer (sample A with Al and Hg electrodes, and B with Al electrode and Hg electrodes). Curves A(Hg) and B(Hg) are shifted by $V_{FB}$ corresponding to the difference of metal work function between Al and Hg. (b) Parameters (sample A/Al) for molecular relaxation m (slope before peak) and $f_2$ (frequency of molecular relaxation peak) are plotted as a function of $V_{dc}$.

### B. Peak 2, molecular contribution

The second peak can be linked to molecular relaxation. We found that the Dissado-Hill function [see above, Eq. (10)] is appropriate to fit both $C'$ and $C''$. It is characterized by three parameters: the prepeak and postpeak exponents, $m$ and $n$, respectively, and the peak position (see Fig. 1). Table II summarizes these parameters (at $V_{dc}=0.2$ V), and the maximum peak 2 frequency, $f_2$, deduced from the fits for the three devices shown in Figs. 3–5. According to Ref. 35, $n$ is ascribed to reflect the order within clusters ($n=1$ representing a perfectly ordered cluster) and $m$ is ascribed to characterize cluster size fluctuations ($m=0$ representing a completely frozen—no fluctuation—structure). The alkyl chains have two small permanent dipoles localized at both ends but most of the molecules are strongly constraint since they are sandwiched between the substrate and the top electrode. The amplitudes of the two local permanent dipoles may be roughly estimated by semiempirical calculations between 0.5 and 1 D (MOPAC software).[42] We did the calculation by considering a single molecule attached to a silicon cluster [88 Si atoms, see Fig. 2(c)]. These values are clearly an overestimation since screening effects from the metallic electrodes

TABLE II. Fitted parameters [Eq. (12)] $m$, $n$, and $C_{mr}$ (data measured at low bias, $V_{dc}=0.2$ V) and frequency $f_2$ of the dipolar relaxation peak. Parameters $C_D$ for peak 1 [Eq. (11)] and $C_\infty$ [Eqs. (3) and (11)]. Sample A: alkene on Si (low density of interfacial defects), B: alkene on Si (high density of interfacial defects), and C: OTS on $Si/SiO_2$ (6 Å of $SiO_2$). We did not see any significant variation whether the top electrode is evaporated Al or hanging Hg drop, so parameter range given in the table takes both cases into account. n.a. stands for nonapplicable. ( $^*$) This value may be underestimated due to the upper limit (1 MHz) of our apparatus.

| Device | A | B | C | Reference $SiO_2$ |
|---|---|---|---|---|
| $m$ | 0.2–0.3 | 0.2–0.45 | 0.1–0.2 | 0.15 |
| $n$ | 0.7–0.8 | 0.7–0.8 | 0.8–0.9 | n.a. |
| $f_2$ (kHz) | 80–200 | 60–200 | 370 | $10^3$ ( $^*$) |
| $C_{mr}$ ($F/cm^2$) | $5-6\times10^{-9}$ | $5-6\times10^{-9}$ | $3-4\times10^{-9}$ | $9.4\times10^{-9}$ |
| $C_D$ ($F/cm^2$) | $0.6-4.5\times10^{-8}$ | $0.2-1.5\times10^{-6}$ | $0.3-2.5\times10^{-7}$ | n.a. |
| $C_\infty$ ($F/cm^2$) | $4-6\times10^{-7}$ | $3-4\times10^{-7}$ | $3-4\times10^{-7}$ | $5\times10^{-7}$ |

and interactions between molecules have not been considered. In the case of OTS on oxidized silicon, the dipole is a little bit larger (1.5–2 D) since the Si-O bond is more polar than the Si-C bond. The presence of these permanent dipoles, even small dipoles, should be sufficient to give sizable dielectric polarization but, in our case, a thin electrode is deposited on top of the monolayer. As a result most of the molecules are strongly constraint and can hardly react to an electric field: they can be considered as inactive during the polarization process. However, we assume that some molecules—or at least segments of some molecules—are more free. They may be preferentially located at (or near) some structural defects of the monolayer. The local permanent dipoles of those molecules are then mobile, or partially mobile, and are consequently able to follow the applied electric field. They give the most important contribution to the dipolar polarization. Moreover, when they are reoriented by the applied field they affect also the rest of the monolayer due to the van der Waals type of interaction that exist between molecules. The reorientation of the mobile dipoles and the disturbance that these motions induce in the surrounding of the mobile dipoles are both responsible for the observed dielectric susceptibility. In this picture, the details of the dielectric relaxation are due to the interaction of the active dipole with the harmonic modes of the monolayer. They should be sensitive to the way the monolayer mechanically reacts to the local constraints caused by the reorientation of the active dipoles. The measured response is a system average which contains elements both from the active dipoles and from the mechanical interaction of these dipoles with the rest of the structure. The basic case is OTS monolayers (sample C). $m=0.1-0.2$ and $n=0.8-0.9$ exponents are close to the flat loss limit ($m=0$ and $n=1$). These are typical values for imperfectly crystallized materials and it is well known that OTS monolayers are polycrystalline with a short-range order (coherence length of 70 Å from x-ray grazing angle diffraction).[43] We estimate (MOPAC software)[42] the small dipole at the foot of the molecule in the range 0.5–2 D (depending on the OD or OTS samples, see above) when the alkyl chain is in all-trans conformation and a little higher, if we include a gauche defect somewhere in the chain conformation. Such a local dipole has been also suggested to explain the dielectric loss measurements done on alkyl chains grafted on porous glass[19] and thick oxide.[20] A more quantitative comparison of the peak amplitude and frequency remains difficult given the wide differences in the experimental conditions (low temperatures and disordered, low packing, monolayers in their cases, room temperature and highly packed, better-ordered, monolayer in our case) and differences in the sample geometries (porous glass and planar electrodes for the quoted works, vertical structure with a sandwiched monolayer here).

For OD monolayers (samples A and B), the $m$ exponent is found to be more than two times larger ($m=0.2-0.45$) at low electric field. The molecular packing (the density of molecules is two times higher for OTS than OD) and the molecular organization (e.g., the tilt angles of the long hydrocarbon chain with respect to the surface normal, $\theta_{OTS}=15°$ and $\theta_{OD}=34°$) differ for the two types of monolayers.[27,28] Therefore, we expect changes in the interaction between the active dipoles and the inactive part of the monolayers that should result in different exponents. These variations in $m$ seem in agreement with the statement of Dissado and Hill mentioning that the more the structure of the system is mechanically rigid the more $m$ approaches 0. This is corroborated by the behavior of $m$ versus the application of a constant electric field (Fig. 7 for sample A with Al electrodes). The dipole fluctuations are reduced (frozen) by increasing a dc field and therefore $m$ should be reduced as observed in Fig. 7. The peak frequency is also shown to be linearly shifted to high frequencies. This can be explained in simple terms assuming the dynamics of the mobile dipoles described by a damped harmonic oscillator (see the Appendix).

To summarize: (i) $m$ depends on the nature of the monolayer. Since the density of molecules is larger for OTS than OD monolayer, we expect the OTS monolayer to be more rigid and therefore $m_{OTS}<m_{OD}$. This is indeed what we have observed (Table II and Figs. 3–5). (ii) $m$ is changed when a dc electric field is applied perpendicularly to the electrode surface. We expect the continuous field to rigidify the structure and therefore $m_{E\neq0}<m_{E=0}$. This is the behavior that we have observed [Fig. 7(b)].

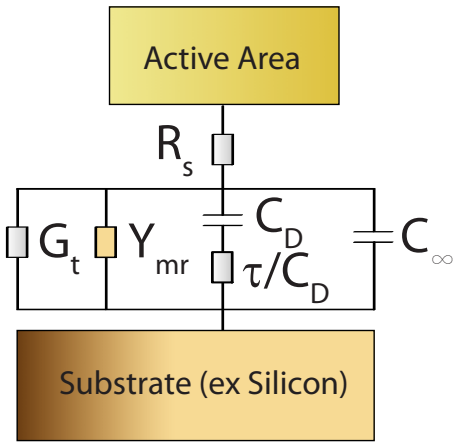


FIG. 8. (Color online) Small signal equivalent circuit for Si/alkyl chain self-assembled monolayers/metal junctions.

## VI. ELECTRICAL EQUIVALENT CIRCUIT

We deduced a small signal equivalent circuit for these Si-monolayer-metal junctions (Fig. 8). A perfect molecular tunnel junction would be modeled with a tunnel conductance $G_T$ in parallel with the capacitance $C_\infty$. The admittance for the Debye peak (interfacial relaxation, peak 1) is $Y_D = jC_D\omega/(1+j\omega\tau_1)$, which corresponds to a capacitance $C_D$ in series with a resistance $\tau_1/C_D$, where $\tau_1$ and $C_D$ are defined and given by Eq. (11). The specific admittance for the molecular relaxation (peak 2) is deduced from the Dissado-Hill function as

$$Y_{mr} = \frac{jC_{mr}(V)\omega}{(1-j\omega\tau_2)^{1-n}} {}_2F_1\left(1-n, 1-m, 2-n, \frac{1}{1-j\omega\tau_2}\right), \tag{12}$$

where ${}_2F_1$ is the Gauss hypergeometric function [see also Eq. (10)], and the parameters $n$, $m$, $C_{mr}$, and $\tau_2=(2\pi f_2)^{-1}$ are given from the fits of the molecular relaxation peak (Table II). The quantitative contribution of each of these loss mechanisms on the total capacitance $C'$ is obtained by comparison of $C_D$ and $C_{mr}$ with $C_\infty$. It is clear that the contribution of $C_D$ to $C'$ is weak for device A [$<10\%$ of $C_\infty$, Fig. 3(a), Table II] but very large for device B [up to 300% of $C_\infty$ at $f<100$ Hz, Fig. 4(a), Table II]. Preliminary studies on technological issue (thermal annealing, assembly process) let us think that it can be reduced by thermal annealing (see Fig. 5). The contribution of molecular relaxation $C_{mr}$ to the total capacitance is weak but non-negligible ($\sim 10\%$ $C_\infty$ at 10 Hz, low $V_{dc}$). It is the dominant mechanism of loss for high-quality junctions (low $C_D$), as observed for device A at low $V_{dc}$. However this contribution would dominate in the case of high-$k$ nanodielectrics[8] using push-pull molecules with a larger dipole.

## VII. CONCLUSIONS

In summary, we have shown how to distinguish between the relaxation dynamics of molecules and the dynamics of molecule/electrode interface by admittance spectroscopy. The interfacial relaxation is related to defects found in Si/monolayer or $Si/SiO_2$/monolayer molecular junctions (not in $Si/SiO_2$). They are located at the bottom of the monolayer and at energy close to the conduction-band edge of the silicon. Depending on their density, dc electrical characteristics are more or less affected. Preliminary studies on technological issues, such as thermal annealing, let us think that this interfacial relaxation peak can be strongly reduced. These results also open the way for a better tuning of the dielectric response of molecular junctions by choosing and designing appropriate selection of molecules.

## ACKNOWLEDGMENTS

D.G. thanks David Cahen and Oliver Seitz for their welcome during his stay at the Weizmann Institute. We thank David Cahen and Oliver Seitz for sample preparations (alkene on Si), advice on making a high-quality alkene monolayer on Si-H surfaces and discussions. We thank Stéphane Lenfant for a careful reading of the manuscript. This work was partly supported by the ANR under Contract No. 05-NANO-001-01.

## APPENDIX

When a dc electric field is applied, a linear shift of the maximum loss frequency is observed [$f_2$ in Fig. 6(b)]. This can be explained in simple terms. We consider a mobile dipole, $\mu$, with disordered orientation, $\phi_0$, that can be dynamically reoriented $\phi(t)=\phi_0+\delta\phi(t)$. The dipole is trapped in a potential assumed to be harmonic $H_{trap}=k\delta\phi(t)^2/2$, with $k$ the elastic constant. It interacts with the electric field, $E_{ac}$ and $E_{dc}$, the ac and dc components, $H_{int}=-\mu\cos\phi(t)[E_{ac}(t)+E_{dc}]$. The dissipation is introduced in the simplest way via a constant friction coefficient, $\eta$, that models the interaction with the bath $H_{dis}=\eta\delta\dot{\phi}(t)$. After an expansion of the interaction with the field in $\delta\phi(t)$, the equation of motion reads

$$J\delta\ddot{\phi}(t) + \eta\delta\dot{\phi}(t) + (k + \mu\cos\phi_0 E_{dc})\delta\phi(t) = \xi(t) + \gamma E_{ac}(t), \tag{A1}$$

where $J$ is the inertial moment of the dipole, $\gamma=\mu\sin\phi_0$, $\xi(t)$ is a random field related to the frictional coefficient by $\langle\xi(t)\xi(t')\rangle=k_BT\eta$ ($\langle\,\rangle$ represents the mean over thermal noise), $T$ is the temperature, and $k_B$ is the Boltzmann constant. In this equation we have replaced the initial dynamical variable by a shifted variable

$$\delta\phi \to \delta\phi + \frac{\gamma}{k + \mu E_{dc}\cos\phi_0}. \tag{A2}$$

Equation (A1) is the usual classical Langevin equation that can be solved by Laplace's transform. Assuming the dipole dynamics to be overdamped ($J\to 0$), the susceptibility is readily found to be of the Debye type with a characteristic frequency increasing with $E_{dc}$,

$$f = \frac{1}{\tau} = \frac{k + \mu\cos\phi_0 E_{dc}}{\eta}. \tag{A3}$$

To get a more general susceptibility of the Jonscher type it is necessary to consider more complex friction that depends on time instead of the simple memory less constant taken here.[44] However, with more general friction term the characteristic frequency of the mobile dipole remains unchanged [Eq. (A3)].

*nicolas.clement@iemn.univ-lille1.fr
†dominique.vuillaume@iemn.univ-lille1.fr

[1] Z. Liu, A. A. Yasseri, J. S. Lindsey, and D. F. Bocian, Science **302**, 1543 (2003).
[2] V. Ferri, M. Elbing, G. Pace, M. D. Dickey, M. Zharnikov, P. Samori, M. Mayor, and M. A. Rampi, Angew. Chem., Int. Ed. **47**, 3407 (2008).
[3] C. Dri, M. Peters, J. Schwarz, S. Hecht, and L. Grill, Nat. Nanotechnol. **3**, 649 (2008).
[4] N. Katsonis, T. Kudernac, M. Walko, S. Van der Molen, B. Van Wees, and B. Feringa, Adv. Mater. **18**, 1397 (2006).
[5] J. M. Mativetsky, G. Pace, M. Elbing, M. A. Rampi, M. Mayor, and P. Samori, J. Am. Chem. Soc. **130**, 9192 (2008).
[6] J. Collet, O. Tharaud, A. Chapoton, and D. Vuillaume, Appl. Phys. Lett. **76**, 1941 (2000).
[7] M. Halik, H. Klauk, U. Zschieschang, G. Schmid, C. Dehm, M. Schütz, S. Maisch, F. Effenberger, M. Brunnbauer, and F. Stellacci, Nature (London) **431**, 963 (2004).
[8] A. Facchetti, M.-H. Yoon, and T. J. Marks, Adv. Mater. **17**, 1705 (2005).
[9] E. Stern, J. F. Klemic, D. A. Routenberg, P. N. Wyrembak, D. B. Turner-Evans, A. D. Hamilton, D. A. LaVan, T. M. Fahmy, and M. A. Reed, Nature (London) **445**, 519 (2007).
[10] A. Salomon, D. Cahen, S. M. Lindsay, J. Tomfohr, V. B. Engelkes, and C. D. Frisbie, Adv. Mater. **15**, 1881 (2003).
[11] H. Haick and D. Cahen, Prog. Surf. Sci. **83**, 217 (2008).
[12] S. Wu, M. T. Gonzalez, R. Huber, S. Grunder, M. Mayor, C. Schönenberger, and M. Calame, Nat. Nanotechnol. **3**, 569 (2008).
[13] A. Nitzan and M. A. Ratner, Science **300**, 1384 (2003).
[14] C. Joachim and M. A. Ratner, Proc. Natl. Acad. Sci. U.S.A. **102**, 8801 (2005).
[15] J. G. Kushmerick, J. Lazorcik, C. H. Patterson, R. Shashidhar, D. S. Seferos, and G. Bazan, Nano Lett. **4**, 639 (2004).
[16] W. Wang, T. Lee, I. Krestchmar, and M. A. Reed, Nano Lett. **4**, 643 (2004).
[17] A. Troisi, J. M. Beebe, L. B. Picraux, R. D. van Zee, D. R. Stewart, M. A. Ratner, and J. G. Kushmerick, Proc. Natl. Acad. Sci. U.S.A. **104**, 14255 (2007).
[18] A. K. Jonscher, Nature (London) **267**, 673 (1977).
[19] Q. Zhang, Q. Zhang, and L. A. Archer, J. Phys. Chem. B **110**, 4924 (2006).
[20] M. C. Scott, D. R. Stevens, J. R. Bochinski, and L. I. Clarke, ACS Nano **2**, 2392 (2008).
[21] N. Clément, S. Pleutin, O. Seitz, S. Lenfant, and D. Vuillaume, Phys. Rev. B **76**, 205407 (2007).
[22] G. G. Raju, *Dielectrics in Electric Fields* (Marcel Dekker, New York, 2003).
[23] E. H. Nicollian and A. Goetzberger, Bell Syst. Tech. J. **46**, 1055 (1967).
[24] A. Salomon, M. Boecking, C. K. Chan, F. Amy, O. Girshevitz, D. Cahen, and A. Kahn, Phys. Rev. Lett. **95**, 266807 (2005).
[25] J. B. Brzoska, N. Shahidzadeh, and F. Rondelez, Nature (London) **360**, 719 (1992).
[26] C. Boulas, J. V. Davidovits, F. Rondelez, and D. Vuillaume, Phys. Rev. Lett. **76**, 4797 (1996).
[27] A. Ulman, *An Introduction to Ultrathin Organic Films: From Langmuir-Blodgett to Self-Assembly* (Academic Press, Boston, 1991).
[28] A. B. Sieval, B. van den Hout, H. Zuilhof, and E. J. R. Sudhölter, Langmuir **17**, 2172 (2001).
[29] B. Mann and H. Kuhn, J. Appl. Phys. **42**, 4398 (1971).
[30] R. E. Holmlin, R. Haag, M. L. Chabinyc, R. F. Ismagilov, A. E. Cohen, A. Terfort, M. A. Rampi, and G. M. Whitesides, J. Am. Chem. Soc. **123**, 5075 (2001).
[31] E. H. Nicollian and J. R. Brews, *MOS (Metal Oxide Semiconductor) Physics and Technology* (Wiley, New York, 1982).
[32] Y. Wang, Rev. Sci. Instrum. **74**, 4212 (2003).
[33] P. Debye, *Polar Molecules* (Dover, New York, 1945).
[34] A. K. Jonscher, *Dielectric Relaxation in Solids* (Chelsea Dielectrics Press, London, 1983).
[35] L. A. Dissado and R. M. Hill, Nature (London) **279**, 685 (1979).
[36] C. A. Richter, C. A. Hacker, and L. J. Richter, J. Phys. Chem. B **109**, 21836 (2005).
[37] Y. Selzer, A. Salomon, and D. Cahen, J. Phys. Chem. B **106**, 10432 (2002).
[38] R. B. Laughlin, J. D. Joannopoulos, and D. J. Chadi, in *The Physics of $SiO_2$ and Its Interfaces*, edited by S. T. Pantelides (Pergamon Press, New York, 1978), pp. 321–327.
[39] T. Sakurai and T. Sugano, J. Appl. Phys. **52**, 2889 (1981).
[40] H. Haick, M. Ambrico, T. Ligonzo, and D. Cahen, Adv. Mater. **16**, 2145 (2004).
[41] A. Natan, L. Kronik, H. Haick, and R. T. Tung, Adv. Mater. **19**, 4103 (2007).
[42] CambridgeSoft Corporation, Cambridge, 1996.
[43] R. Maoz, J. Sagiv, D. Degenhardt, H. Möhwald, and P. Quint, Supramol. Sci. **2**, 9 (1995).
[44] I. Goychuk, Phys. Rev. E **76**, 040102(R) (2007).

# Molecular relaxation dynamics in organic monolayer junctions

Stéphane Pleutin, Nicolas Clément, David Guérin, and Dominique Vuillaume
*"Molecular Nanostructures and Devices" Group, Institute for Electronics, Microelectronics and Nanotechnology, CNRS and University of Sciences and Technologies of Lille, BP 690069, Avenue Poincaré, F-59652 Villeneuve d'Ascq, France*
(Received 26 March 2010; revised manuscript received 25 June 2010; published 20 September 2010)

The complex admittance of various molecular junctions based on long alkyl chains (C18) has been measured and resolved into different components. The dipolar contribution of the response function has been analyzed in terms of the generalized Langevin equation. This formalism allows us to extract from experimental data the spectral density of polarization noise and to characterize the fluctuation dynamics of the molecules around their equilibrium positions. This spectral density is of $1/f$ type, characteristic of fractional Gaussian noise. It is suggested that the structural disorder of the junctions is at the origin of these polarization fluctuations. Possible relation between the $1/f$ tunnel current and polarization noises is also discussed.

DOI: 10.1103/PhysRevB.82.125436 PACS number(s): 77.22.Gm, 05.40.−a, 85.65.+h

## I. INTRODUCTION

Self-assembled monolayers (SAMs) composed of hydrocarbon chains and small molecules are widely used nowadays. This is motivated by their relative ease of preparation and their chemical flexibility that allows controls at molecular level of the structure and chemistry of surfaces.[1] The range of applicability is large: they commonly serve as nanodielectric[2–5] and prototypes for molecular memories[6] or switches,[7–10] to name a few. In this context, to understand their electric properties is an important issue. However, most of the characterizations are done by dc electric measurements[11,12] or inelastic electron spectroscopies[13,14] that give limited information about the electric current (tunneling, resonant tunneling, etc.) and the molecular vibration modes excited by the current. More recently, electric noise in the low-frequency limit ($1/f$ noise) has been investigated giving additional information.[15] Increase in both electric current and electric noise for certain bias have been evidenced and explained by invoking interfacial traps and trap-assisted tunneling mechanisms associated to them.[15] In this work we discuss admittance spectroscopy which is a powerful technique to analyze relaxation mechanisms in a wide range of time scale. For many of the applications listed above it is essential to understand the response of the monolayer to ac signals.

The motion of single or ensemble of molecules are believed to influence significantly the thermal,[16] the mechanical,[17] and the transport properties[18] of the SAMs. They can be of large amplitude despite the close packing of the alkyl chains and the chemical links between the substrate and the molecules.[19,20] The low signal levels produced by SAMs coatings on planar surface prevent the application of standard techniques such as nuclear magnetic resonance that are conventionally used to detect such motions in materials.[16] However, admittance spectroscopy proves, in two recent works,[21,22] to be sensible enough to probe molecular relaxation associated to these motions. A first set of measurements have been performed on SAMs with varying coating densities and different substituent polar groups but using nanoporous substrates to scale up the surface area in order to increase the response signals.[21] The main drawback of this method is to consider complex geometry very different from what is commonly used in applications and that makes interpretation more difficult. In a second work, planar geometries have been considered with molecule densities varying from 10% of surface coverage to multilayer coverage. The excitation has been applied parallel to the surface of the substrate. The temperature has been varied but the range of frequencies centered about 1 kHz was very limited.[22]

We have done complex admittance measurements for usual planar geometry:[23] the alkyl chains are grafted on planar surfaces and contacted on top with metallic electrodes. A small ac signal (10 mV), with frequency ranging between 20 and $10^6$ Hz, plus a dc bias varying from 0 to 1 V are applied perpendicular to the surface electrodes. The complex admittance shows three independent contributions due to tunnel current, interfacial defects, and molecular relaxation.[23] Here we focus on the theoretical analysis of the last contribution. As suggested also in Ref. 21, it is interpreted as due to small permanent dipoles present in the monolayer. With applied fields, these dipoles are displaced contributing to the polarization and dissipating energy by interactions with the environment. This dipolar contribution is shown to follow the universal behavior pointed out by Jonsher.[23,24] The imaginary part of the susceptibility vs frequency shows a peak with two power laws in the prepeak and postpeak regions. The exponents depend on the nature of the SAM and on the metallic electrodes (Al or Hg). In all cases the exponents and the peak position are very similar to the ones found in bulk amorphous organic polymers such as the polyethylene in the glass phase. However the dissipated energy is more important by one order of magnitude in our systems.

We analyze the data in terms of a Caldeira and Leggett type of model[25,26] that describes the dynamics of independent permanent dipoles trapped in harmonic potential and interacting with the harmonic modes of the SAMs (vibration, rotation) playing the role of a bath where the energy is dissipated. We choose this model for dissipation among several other possibilities[27] because, to our opinion, it is the simplest that fits our present understanding of the structure of the monolayer and mechanisms of dipolar polarization. Since the experiments are done at room temperature we neglect quantum fluctuations. This model is then equivalent to a classical generalized Langevin equation (GLE) where the friction

 

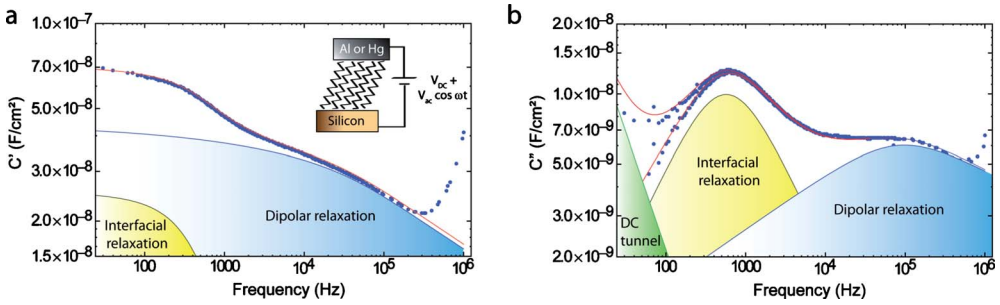


FIG. 1. (Color online) Typical complex admittance obtained for an OD junction with Al top electrode at $V_{dc}=0.1$ V, decomposed in (a) imaginary and (b) real parts. The experimental data (dots) are fitted (red lines) assuming three independent components (see text): a tunnel current contribution (filled in green), an interfacial contribution attributed to interface defects (filled in yellow), and a dipolar contribution attributed to the permanent dipoles of the monolayer (filled in blue). Note in the real part two sets of data: the top data corresponds to $\Re Y(\omega)/\omega$, the down data to $\Re Y(\omega)/\omega - G_T/\omega$ (see text). Inset of (a): schematic of the experiment.

term is non-Markovian.[28] In the framework of the GLE, the admittance spectroscopy is seen as a noise spectroscopy. A relation between the complex admittance that we measure and the spectral density of the bath fluctuations is naturally derived. These fluctuations entirely control the dynamics of the permanent dipoles participating to the polarization. In particular, it is shown that the dynamics of the dipoles is well described in terms of damped harmonic oscillator with fractional Gaussian noise.[29] This type of dynamics is rather widespread in nature being observed in very different systems; a recent appealing example concerns the distance separating the donor and acceptor sites of single protein complex.[30] From the power spectrum of the bath fluctuations we obtain the spectral density of dielectric—or polarization—noise. It is then suggested that the $1/f$ current noise observed in the very same systems[15] could be caused, at least partly, by the voltage fluctuation induced by the polarization noise. The generalized Langevin theory gives us a useful way to interpret our results and explain successfully part of our data such as the linear variation in the inverse of the characteristic time of relaxation of the permanent dipoles, $1/\tau$, with the applied dc voltage. However, to understand the physical mechanisms at the origin of the power laws observed in the complex admittance, more microscopic analysis of the mechanical properties of the SAMs are required. A first effort in this direction is proposed in this work relating the spectral density of polarization noise to the density of states of the harmonic modes of the SAMs.

The paper is organized as follows. In Sec. II some details about the devices and experiments are given. A model structure of our monolayer based on experimental observations is proposed in Sec. III; possible origins of the permanent dipoles are also discussed. Experimental data for the dipolar contribution of the susceptibility are shown and discussed in Sec. IV. In Sec. V the generalized Langevin equation used to interpret our data is presented and analyzed. The spectral densities of the fluctuations of the bath and of the polarization noise are obtained from the experimental susceptibility. Last a direct relation between the polarization noise and the $1/f$ current noise observed in a previous work[15] is suggested and discussed. In Sec. VI the effects of the dc field are included in our model and the variations in the characteristic time of relaxation are well reproduced. To conclude, qualitative arguments are developed in Sec. VII showing relation between the spectral density of the bath and the density of its harmonic modes (vibration and rotation of the SAM).

## II. SAMPLES AND EXPERIMENTS

Two different types of monolayers were prepared, based on similar alkyl chains of 18 carbon atoms but with different terminal groups. The two alkyl monolayers are grafted on different silicon substrates following well-defined recipes described elsewhere.[31,32] In the first type, octadecyltrichlorosilane (OTS) molecules are grafted on 0.6-nm-thick oxide thermally grown on *n*-type doped (resistivity $\sim 10^{-3}$ $\Omega$ cm) Si(100).[31] In the second type, octadecene (OD) molecules are directly grafted on *n*-type doped (0.02–0.5 $\Omega$ cm) Si(111).[32] The quality of the monolayers was assessed by spectroscopic ellipsometry and water contact angle measurements. We selected only monolayers with a water contact angle larger than 110° and a thickness close (within 3 Å) to the theoretical expectation for a SAM with the molecules in their all-trans conformation. The monolayers were contacted by 50-nm-thick aluminum contact pads with different surface area between $9\times10^{-4}$ cm$^2$ and $4\times10^{-2}$ cm$^2$ or by a mercury drop. At the end, we have a set of similar molecular junctions that allows us to compare two types of silicon/molecule interfaces and two types of top metal contacts (see details in Ref. 23).

We have performed ac admittance spectroscopy.[23] All the measurements were done in dark, under controlled atmosphere ($N_2$) and at room temperature. A small ac signal (10 mV) superimposed to a dc voltage bias (0–1 V) was applied to the metallic electrodes, the Si was grounded and the complex admittance was measured using an impedance-meter Agilent 4284 A in the range 20–$10^6$ Hz [see inset of Fig. 1(a)]. Measured conductance and capacitance were corrected from small series resistances (typically in the range 5–70 $\Omega$) according to a standard procedure.[33] There is still a small parasitic effect due to the sample environment (cables) that causes increase in the response at high frequencies. It is a known effect[34] but since it only affects the highest frequency part of the curves, we let it as it is (see Fig. 1). More details about the experimental procedure can be found elsewhere.[23]

The complex admittance $Y(\omega)$ can be expressed in terms of the tunnel conductance, $G_T$, and the macroscopic dielectric susceptibility, $\chi_M(\omega)=\chi'_M(\omega)+j\chi''_M(\omega)$, which is the response of the whole system to oppose to the local susceptibility which is the response of an individual dipole (Secs. IV and V). The tunnel conductance is assumed frequency independent. The real part of the susceptibility describes polarization phenomena while its imaginary part takes account for dissipation. We plot

$$\Re Y(\omega)/\omega = G_T/\omega + \frac{A\epsilon_0}{d}\chi''_M(\omega) = G_T/\omega + C''(\omega),$$

$$\Im Y(\omega)/\omega - C_\infty = \frac{A\epsilon_0}{d}\chi'_M(\omega) = C'(\omega), \quad (1)$$

where $A$ is the surface area of the junction, $\epsilon_0$ the permittivity of the vacuum, and $d$ the interelectrode spacing. We have approximately $d_{\mathrm{OTS}}=2.5$ nm and $d_{\mathrm{OD}}=2$ nm (ellipsometry measurements). In the frequency range that we consider we probe the slow polarization mechanisms caused by permanent dipoles. $C_\infty$ is the part of the capacitance due to ionic and electronic contribution. More precisely, it is defined for intermediate frequencies large enough for the dipoles to be frozen and not contributing to the polarization but small enough to not consider dissipation from the ionic and electronic degrees of freedom. $C(\omega)=C'(\omega)+jC''(\omega)$ is the part of the capacitance due to permanent dipoles.

Typical results are given in Fig. 1 for an OD junction with Al electrode at $V_{\mathrm{dc}}=0.1$ V. All the results that we have obtained—with different junctions and different dc potential—are qualitatively similar to this example.[23] The admittance shows three contributions that can be well identified in the real component—Fig. 1(b): a $G_T/\omega$ contribution due to tunnel current (filled in green) and two peaks at low frequencies (filled in yellow) and higher frequencies (filled in blue). The peaks correspond in the imaginary part of the admittance to plateaulike contributions [Fig. 1(a)]. The low-frequency peak is attributed to interfacial defects. Its amplitude strongly varies from device to device and these variations are related to changes by orders of magnitude in the dc conductance.[23] On the opposite the precise shape of the second peak at higher frequency depends only on the nature of the junction, OD or OTS, and of the top electrode, Al or Hg, but is very reproducible from device to device of the same set.[23] In particular, it is not affected by the amplitudes of the first peak and of the tunnel current. This contribution is interpreted as being the intrinsic susceptibility of the junction. In fact, the susceptibility contains two parts (interfacial and dipolar) and we write

$$\chi_M(\omega) = \chi_{int}(\omega) + \chi_{dip}(\omega). \quad (2)$$

The two parts are assumed to be independent as confirmed by experimental observations.[23] The interface part gives rise to the low-frequency peak and is due to some defects as briefly discussed above and that we have found to be located near the Si interface.[23] In this work we focus on the dipolar—or molecular—part of the relaxation.

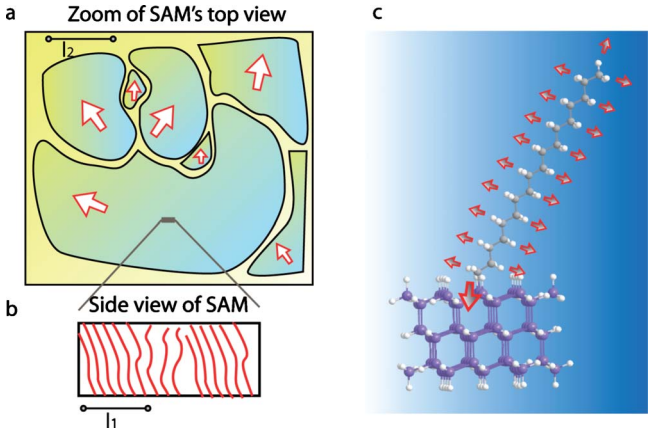


FIG. 2. (Color online) (a) Schematic top view of the monolayer. Each molecule is represented by a vector joining its two ends. The arrows are the projection of those vectors to the surface of the substrate. The monolayer appears as a collection of clusters, with characteristic size $l_2$ ($\sim 1$ $\mu$m), defined by a certain direction separated from each other by grain boundaries. (b) Zoom of a cut in a particular cluster. The translational order appears to be very short with correlation length $l_1$ ($\sim 50$ nm). (c) The two molecules studied in this work show weak permanent dipoles ($\sim 0.1$ D) perpendicular to their backbone and two stronger dipoles at both ends ($\sim 1$ D) more or less parallel to their axes. They both show a tilt angle [15° (30°) for OTS (OD)] with respect to the normal at the interfaces. The permanent dipoles are estimated (MOPAC software) using a model structure with small clusters of Si atoms.

At the frequencies considered in this work ($\leq 1$ MHz), we probe the relaxation mechanisms of permanent dipoles present in our system. Studies of the response should provide us information concerning the permanent dipoles themselves (amplitude, density) but also on structural aspects of their surrounding where the relaxation takes place. This is a crucial point. For instance, it is well known that the relaxation of permanent dipoles is considerably slowed down in glassy systems because of their amorphous structures.[35] First questions concern those two aspects. Where are the permanent dipoles located in our molecules? What is their magnitude? What is the kind of typical structure expected for the SAMs? Are they crystals or amorphous systems? In the next section structure models are proposed based on experimental evidences.

## III. ORIGIN OF THE PERMANENT DIPOLES AND STRUCTURE OF THE SAMs

The two types of monolayers that we have investigated in this work are based on saturated molecules with 18 carbon atoms. These molecules are known to be weakly polar. Each CH bond perpendicular to the backbone of the molecules carries a small dipole of about 0.1 D. Such dipoles, even if they are weak are probably at the origin of the $\beta$ relaxation observed for saturated polymers in amorphous phases.[35] In addition, in our systems, two stronger residual permanent dipoles are located at both ends of the molecules [see Fig. 2(c)]. One of these dipoles—the strongest—is induced by the substrate and is carried by the chemical bonds with the mol-

ecules [see Fig. 2(c)]. The magnitudes of those two local permanent dipoles may be roughly estimated by semiempirical calculations between 0.5 and 1 D (MOPAC software). In these simulations we have included clusters of Si atoms to accurately model the interfacial dipoles [see Fig. 2(c)]. Note that all these values are certainly overestimated since the Coulomb interaction between dipoles and with the metallic surrounding have not been included in the calculations. Strong dipolar effects cannot be expected here. However, we see in these interfacial dipoles, all more or less aligned in the same direction, a possible origin for the difference in amplitude of the peak of maximum loss observed in our systems and in bulk polymers.[35]

van der Waals interaction force the molecules to be packed together and aligned in the same direction at a tilt angle, $\theta$, with respect to the normal to the substrate.[1] We estimate $\theta_{\mathrm{OTS}} \approx 15°$ and $\theta_{\mathrm{OD}} \approx 30°$ from ellipsometry measurements. In both cases the molecules are organized in a triangular lattice[1] with a nearest-neighbor distance of about 4.8 Å for OTS and slightly more, 5.1 Å, for OD.[36] The SAMs could, in principle, form well-ordered phases. However because of rotational invariance there is no preferred plan for tilting. During the formation of a monolayer, clusters grow up simultaneously from different positions on the substrate, having each a particular orientation. As a consequence the SAMs form polycrystals at the micrometer scale [$l_2$ in Fig. 2(a)], where organized clusters with a particular molecular orientation are separated by grain boundaries. This large-scale structure is expected for all types of SAM and was clearly observed for OTS and alkanethiols monolayers by atomic force microscopy.[37] The organization inside the clusters has been investigated by x-ray grazing diffraction incidence[38] and specular reflections[39] for OTS and other SAMs. Because of similarities between the different SAMs it is reasonable to expect the same qualitative characteristics for OD systems. The molecules appear to be packed with a volume per molecule of about 20 $\mathrm{Å}^2$ for OTS (and slightly more for OD, approximately 25 $\mathrm{Å}^2$) but with a very short in plane correlation length of 45 Å [$l_1$ in Fig. 2(b)]. This suggests a liquidlike organization within the plane. A schematic side view inspired by Ref. 39 is shown in Fig. 2(b). In addition, a thin electrode is in our case deposited on top of the monolayer: the SAM is sandwiched between the substrate and the top electrode. The molecules are therefore strongly constraint due to the large packing density within the monolayer and the electrodes to which they are linked either chemically or physically. As a consequence they can react only weakly to an electric field.

Because of their peculiar structural organization we expect the dielectric response of the SAMs to be nonuniform: most of the molecules may be quasi-inactive under the action of an external electric field while some of them—or at least segments of some molecules—may have more space to move and, as a consequence, may be more flexible. These "mobile" molecules are likely to be located at the grain boundaries or at some other structural defects inside the clusters where the molecule density is reduced and the constraints are somehow relaxed (see Fig. 2). The local permanent dipoles of those molecules are then mobile, or partially mobile, and are consequently able to follow more easily the applied electric field: in this picture only part of the SAM contributes significantly to the total dipolar polarization. The average induced displacement of the permanent dipoles, of amplitude $\delta\mu$, determines the magnitude of the dipole contribution to the capacitance. It should depend on the chain density and on the nature of the electrodes. The OTS samples are denser than the OD samples. We expect therefore $\delta\mu$ to be more intense for OD. We can estimate this quantity from the low-frequency capacitance. After subtracting $C_\infty$ and the part due to the interface traps we are left with a pure dipolar contribution $C_{dip}$. We write using the same kind of qualitative arguments developed in Ref. 40,

$$\tilde{C}_{dip} = \frac{\delta\mu}{AdV_{\mathrm{dc}}}, \tag{3}$$

where $d$ is the SAM thickness and $V_{\mathrm{dc}}$ is small (in practice we have taken $V_{\mathrm{dc}}=0.1$ V). $\tilde{C}_{dip}$ is the dipolar capacitance per unit surface; we have from typical experimental values $3\times10^{-8}$ F cm$^{-2}$ and $4\times10^{-8}$ F cm$^{-2}$,[23] for OTS and OD, respectively. From the volume per molecule estimated by x-ray experiments there is approximately $5\times10^{13}$ molecules of OTS and approximately 1.25 time less of OD, for a sample with a surface $A=10^{-2}$ cm$^2$. From these values we extract $\delta\tilde{\mu}=\delta\mu$/molecule. We find $4.5\times10^{-3}$ D and $6\times10^{-3}$ D for OTS- and OD-based junctions, respectively. This difference may reflect the different molecular density of the molecular junctions, as stressed above. The amplitude of the peak of maximum loss should depend on the magnitude of the relaxing dipoles and of their faculty to fluctuate around their equilibrium position. The amplitude of these fluctuations should be related to the density of molecules of the SAMs. Indeed, the loss peak is more pronounced for OD than OTS type of junctions.[23]

When the dipoles are reoriented by the applied field they affect also the rest of the monolayer due to the interaction that exist between molecules. The reorientation of the dipoles and the disturbance that these motions induce in the surrounding of the dipoles are both responsible for the observed dielectric susceptibility.

## IV. ELECTRIC SUSCEPTIBILITY AND RELAXATION FUNCTION—DEBYE VS UNIVERSAL BEHAVIOR

The dipoles are considered as independent or, in other words, their mutual interaction is assumed to be taken in a mean-field manner. We focus now on a single dipole and hence to the local susceptibility, $\chi$, associated to it. The macroscopic susceptibility of Eq. (1), $\chi_M$, is simply proportional to $\chi$ as will be seen in more details in Sec. V. Moreover, as already stressed in Sec. II, we consider throughout this work that the dipolar contribution can be treated independently of the tunnel current and of the interfacial part of the admittance. This assumption seems in agreements with our experimental observations.[23]

In linear-response theory (weak ac field), the complex dielectric susceptibility is related to the relaxation function, $\varphi$, which is the response function of the system after the abrupt removal of a constant electric field at $t=0$.[41] In our case, the

relaxation function describes the way the dipoles relax toward a stable equilibrium once the perturbation has been removed,

$$\chi(\omega) = \chi'(\omega) + j\chi''(\omega) = (\chi_0 - \chi_\infty)\left[1 + j\omega\int_0^{+\infty} dt\varphi(t)e^{j\omega t}\right], \tag{4}$$

where $\chi_0$ is the value at zero frequency. We take $\chi_\infty=0$, meaning that at high enough frequencies the dipole cannot follow the field anymore and do not contribute to the polarization. Equation (4) is well defined in the context of equilibrium statistical mechanics: this is the fluctuation dissipation theorem (FDT).[41] We observe anomalous relaxation following power laws, as it will be clear below, that make transient dynamics very slow. This type of relaxation is known to add complication to Eq. (4).[42,43] However it was shown in Ref. 26 that the FDT is recovered by adding an additional averaging over the initial condition of the relaxation. We will come back to this point in Sec. V with a little more details and the proper definition of the relaxation function $\varphi$.

In the simplest case, considered long ago by Debye, the relaxation function is given by a single exponential[44]

$$\varphi_{Debye}(t) = e^{-t/\tau}. \tag{5}$$

$\tau$ is the characteristic time of relaxation. The exponential law may be obtained by using a variety of microscopic models for relaxation process. This equation was first derived by Debye by considering the rotational Brownian motion (excluding the inertial effects) of an assembly of noninteracting dipoles.[44] His treatment is appropriate for a dilute solution of polar molecules with axial symmetry in an isotropic and nonpolar liquid. Such simple response yields[44]

$$\chi_{Debye}(\omega) = \chi_0\frac{1 + j\omega\tau}{1 + \omega^2\tau^2}. \tag{6}$$

The real part of Debye's susceptibility shows a plateau at low frequencies below $1/\tau$ and decreases as $\omega^{-2}$ above $1/\tau$. Its imaginary part shows a peak at $1/\tau$: it increases as $\omega$ in the prepeak region and decreases as $\omega^{-1}$ in the postpeak region. However, this type of response is hardly seen in condensed matter. Instead, fractional power laws are most often observed[24]

$$\chi(\omega) \propto (j\omega)^{n-1} \quad \text{for} \quad \omega \gg \omega_P,$$

$$\chi_0 - \chi(\omega) \propto (j\omega)^m \quad \text{for} \quad \omega \ll \omega_P. \tag{7}$$

$\omega_p$ being the frequency of maximum loss which is equal to $1/\tau$ in the Debye case but is a function of $\tau$ and of the two exponents, $n$ and $m$, for more general cases. This is the famous "universal" dielectric response pointed out by Jonscher[24] but observed long before by many authors in very different systems (amorphous systems, van der Waals crystals, ionic solids, etc.). Several phenomenological expressions have been proposed over the years to mimic this behavior such as the Cole-Cole,[45] Cole-Davidson,[46] or Havriliak-Negami[47] (HN) dielectric susceptibilities. A suitable expression that models remarkably well our data is the Dissado-Hill[48] (DH) dielectric susceptibility. It reads

$$\chi_{DH}(\omega) = \chi_0\frac{\Gamma(1+m-n)}{\Gamma(m)\Gamma(2-n)}(1-j\omega\tau)^{n-1}{}_2F_1[1-n,1-m;2-n;(1-j\omega\tau)^{-1}], \tag{8}$$

where ${}_2F_1$ is the Gauss hypergeometric function,[49] $0 \le m \le 1$ and $0 \le n \le 1$. Dissado and Hill have proposed this function based on some handling arguments. The details of their derivation are difficult to follow and some of their assumptions seem even hard to justify.[48] Nevertheless their function has proven to model successfully numerous data of very different systems. As the HN model, the DH function shows asymptotic fractional power laws both in the prepeak and postpeak region [Eq. (7)]. However, the two models differ noticeably in a frequency interval around the peak that can be a few decades large.[50] The particular shape of the HN function is not appropriate to our cases (see Figs. 4 and 6 of Ref. 50). The DH expression gives much better agreements with our data.

TABLE I. Parameters of the Dissado-Hill susceptibility obtained by fitting our data and averaging over six or eight samples depending on cases. Three cases are considered: OD junctions at $V_{dc}=0.1$ V and $V_{dc}=1$ V, and OTS junction at $V_{dc}=0.1$ V. The top electrode in these three cases is made of Al.

| | OD (0.1 V) | OD (1 V) | OTS (0.1 V) |
|---|---|---|---|
| $m$ | 0.22 | 0.1 | 0.13 |
| $n$ | 0.8 | 0.85 | 0.85 |
| $1/\tau$ (kHz) | 150 | 330 | 370 |

To match our data, together with a tunnel contribution a linear combination of two DH dielectric susceptibilities has been considered (see Fig. 1). This point was already discussed in Sec. II [see Eqs. (1) and (2)]. If we omit the high frequency, increases known to be a parasitic effect caused by the environment of the junction,[23,34] our fitting procedure gives good agreements with our data (see Fig. 1). It turns out that the interface part is well fitted by considering $n=0$ and $m=1$, which corresponds to a Debye type of response. The dipole part follows the universal behavior of Jonscher.[24] Table I gives experimental results for the dipolar part. We choose to quote the values of $n$, $m$, and $\tau$ for OD systems at 0.1 and 1 V (dc voltage) and for OTS systems at 0.1 V. The parameter values are obtained after averaging over six or eight samples depending on cases. Note that the observed dispersions for each parameter are rather small. This set of values is representative and sufficient to point out some important information. (i) The parameters of relaxation depend on the nature of the molecules in the SAM, OD, or OTS. (ii) The parameter values change by applying a dc electric field perpendicular to the surface electrodes. Interestingly, we can notice that the parameter values for OD with constant electric field (at 1 V) are close to the ones of OTS almost without field (at 0.1 V). Changes in the DH parameters with the nature of the electrodes is also observed and commented elsewhere.[23] Note that with the parameters of Table I, the

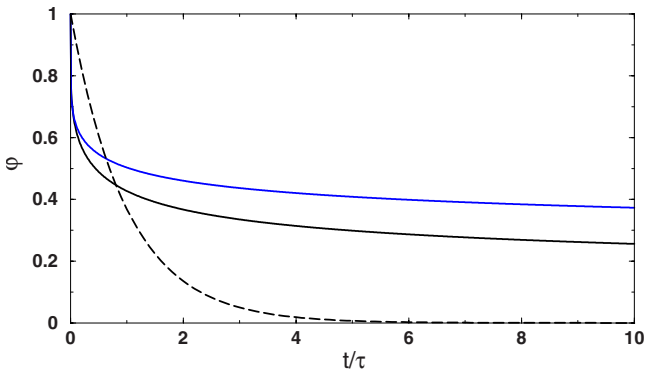


FIG. 3. (Color online) Relaxation functions related to the Debye (dashed line) and to the DH (full line)—with $n=0.85$ and $m=0.2$ (the down curve in black), and $n=0.85$ and $m=0.1$ (the top curve in blue)—susceptibilities.

asymptotic behaviors of the DH susceptibility are very close to the ones of the Cole-Cole model,[45] $\chi_{Cole\text{-}Cole}(\omega) \propto (j\omega)^{\alpha}$, for $\omega \ll \omega_P$, and $\chi_{Cole\text{-}Cole}(\omega) \propto (j\omega)^{-\alpha}$, for $\omega \gg \omega_P$, with $\alpha = n-1$: in our case, we obtain $\alpha \simeq 0.2$ for OD at 0.1 V and $\alpha \simeq 0.1$ for OD at 1 V and OTS at 0.1 V. As a final remark on this table we may notice that all the values reported here are typical for imperfectly crystallized materials such as glasses or vitreous polymer systems.[35] Typical examples concern nonpolar polymers such as poly-$\gamma$-benzyl-L-glutamate on NaCl plates,[48] epoxy resin at temperatures below the glass transition[51] and perhaps, the most interesting for us, the polyethylene—the polymer counterpart of our molecules—in the glass phase.[35] All of these examples show DH parameters very similar to those measured for our SAMs. X-ray diffraction studies on OTS (Refs. 38 and 39) favor the analogy between our systems and the nonpolar polymers cited above which show very poor translational order.

The relaxation function corresponding to the DH susceptibility can be derived from Eq. (4). One gets

$$\varphi_{\mathrm{DH}}(t) = 1 - \frac{\Gamma(1+m-n)}{\Gamma(2-n)^2\Gamma(m)}(t/\tau)^{1-n}{}_2F_2(1-n,1+m-n;2-n,2-n;-t/\tau), \tag{9}$$

where ${}_2F_2$ is a hypergeometric function.[49] In Fig. 3, as a matter of illustration, $\varphi_{Debye}$ and $\varphi_{\mathrm{DH}}$ are shown in units of $\tau$ for typical parameters ($n=0.85$, $m=0.2$) and ($n=0.85$, $m=0.1$). One can notice that the dynamics of relaxation in our systems is dramatically slowed down compared to Debye's relaxation as usually observed for glassy systems. $\varphi_{\mathrm{DH}}$ reduces asymptotically (at short, $t<\tau$, and large, $t>\tau$, time) to power laws. This is typical of fractional Brownian motion.[26,29,30] The slowing down of the relaxation is usually understood as the result of interaction between the relaxing quantities—here the permanent dipoles—and low-energy excitations present in the system. This type of complex relaxation is described in terms of system plus reservoir models such as the one due to Caldeira and Leggett.[25,28] In the next section such model is used to establish a relation between the measured dielectric susceptibility and the spectral density of polarization noise. The reader not interested by technical details may switch directly to Eq. (24) relating the spectral density of the fluctuating bath to the measured complex susceptibility.

## V. GENERALIZED LANGEVIN EQUATION—NOISE CHARACTERISTICS

Following closely Ref. 26, we consider a monolayer as an ensemble of dipoles $\mu_i$ with disordered orientation $\phi_i^0$, that can be dynamically reoriented $\phi_i(t)=\phi_i^0+\delta\phi_i(t)$. These are the mobile dipoles of Sec. III. They are trapped in a potential assumed to be harmonic, $H_{trap}=k_i\delta\phi_i(t)^2/2$, and interact with the electric field, the dc and ac components; we first consider only the ac component $E_{\mathrm{ac}}(t)=E_{\mathrm{ac}}\cos(\omega t)$. The interaction between the dipoles and the applied field reads, as usual, $H_{int}=\mu_i\cos\phi_i(t)E_{\mathrm{ac}}(t)$ that yields after an expansion in $\delta\phi_i(t)$,

$$H_{int} = \mu\cos\phi(t)E_{\mathrm{ac}}(t) \approx \mu_{\parallel}E_{\mathrm{ac}}(t) - \mu_{\perp}\delta\phi(t)E_{\mathrm{ac}}(t). \tag{10}$$

We note $\mu_{\parallel}=\mu\cos\phi^0$ and $\mu_{\perp}=\mu\sin\phi^0$ the components of the dipole parallel and perpendicular to the electric field, respectively. In this expression and in the following we omit the indices for convenience. The mobile dipoles are subjected to friction as a consequence of their interaction with the environment that can be modeled in several ways.[25,27,28,52] To be consistent with our present understanding of the molecular junctions,[15,23] a satisfying and rather general model of the environment should include the harmonic modes of the monolayer (vibration and rotation modes) and a set of two-level systems that model defects such as the ones considered to analyze the $1/f$ current noise[15] or the interfacial peak of Fig. 1.[23] These are the so-called harmonic oscillator[25] and spin baths,[52] respectively. They are known to give different behaviors.[53] In particular, the part of the dissipated energy from the oscillating mobile dipoles to a spin bath decreases strongly at high temperatures on the contrary to the part given to the harmonic oscillator bath that increases. Since the experiments are done at room temperature, we expect the effects of a spin bath to be weak. Therefore, as a first step, we consider in this work oscillator bath only. It has to be understood that the consequences of this approximation should be tested in future works, by varying the temperature for instance.

The mobile dipoles interact with an infinite number of harmonic modes (bath). These harmonic modes can be, for instance, the rotation or vibration modes of the monolayer. We neglect explicit dipole-dipole interaction terms. The total Hamiltonian is then written as

$$H = \frac{J\delta\dot{\phi}(t)^2 + k\delta\phi(t)^2}{2} - \mu_{\perp}\delta\phi(t)E_{\mathrm{ac}}(t) + \frac{1}{2}\sum_{\alpha=1}^{N} J_{\alpha}\delta\dot{\phi}_{\alpha}(t)^2 + k_{\alpha}\left[\delta\phi_{\alpha}(t) - \frac{c_{\alpha}}{k_{\alpha}}\delta\phi(t)\right]^2, \tag{11}$$

where $J$ is the inertial moment of the dipole. The first term of $H_{int}$ has been dropped out since it does not contribute to the dynamics of the dipole. The last term of this Hamiltonian

models the harmonic bath ($N$ modes, $N$ assumes to be "infinite") that interacts linearly with the dipole. $J_\alpha$ and $k_\alpha$ are the inertial moment and the elastic constant of the mode $\alpha$, $c_\alpha$ is the coupling between the mode and the dipole. This is a Caldeira-Leggett type of Hamiltonian introduced to study quantum dissipation.[25,28] The central ingredient in such model is the product of the density of modes of the bath times the squared coupling strength; this is the so-called spectral density of the environmental coupling[28]

$$\gamma(\omega) = \sum_{\alpha=1}^{N} \frac{c_\alpha^2}{J_\alpha \omega_\alpha} \delta(\omega - \omega_\alpha) \tag{12}$$

with $\omega_\alpha = \sqrt{k_\alpha / J_\alpha}$. If the noise (the bath) is characterized the dynamics of the system is fully determined. The spectral density $\gamma$ could be, in principle, derived from detailed microscopic calculations. In practice, it is more often taken as a phenomenological function to be determined by experiments. This is the strategy followed in this work. Our objective is to determine this quantity giving the experimental susceptibility $\chi_{dip}(\omega) \propto \chi_{\mathrm{DH}}(\omega)$. In this approach the admittance spectroscopy can be seen as a kind of fluctuation spectroscopy.

In the following, we neglect quantum fluctuations (high-temperature limit). From Hamiltonian (11) the equations of motion for $\delta\phi$ and $\delta\phi_\alpha$ can be readily written down and, after elimination of the bath variables, the dipole coordinates are shown to follow the generalized Langevin equation (GLE),[28]

$$J\delta\ddot{\phi} + \int_0^t \eta(t-t')\,\delta\dot{\phi}(t')dt' + k\,\delta\phi(t) = \xi(t) + \mu_\perp E_{\mathrm{ac}}(t), \tag{13}$$

where

$$\eta(t) = \sum_\alpha \frac{c_\alpha^2}{J_\alpha \omega_\alpha^2} \cos\,\omega_\alpha t = \int_0^{+\infty} d\omega \frac{\gamma(\omega)}{\omega} \cos\,\omega t \tag{14}$$

and $\xi(t)$ is a Gaussian random field related to the damping kernel—or memory-friction kernel $-\eta(t-t')$ by the fluctuation-dissipation theorem,

$$\langle \xi(t)\xi(t') \rangle = k_B T \eta(t-t'). \tag{15}$$

$\langle\ \rangle$ represents the mean over thermal noise. The average is taken by considering the system bath plus dipole frozen at coordinates $\delta\phi(0)$ and $\delta\dot{\phi}(0)$ in thermal equilibrium.[28] $T$ is the equilibrium temperature of the bath. In this new formulation, the memory kernel is the central quantity. We note $\eta(t) = \eta_S f(t)$, $\eta_S$ being the friction coefficient (Stoke coefficient) and $f(t)$ a function without dimension. $\eta_S$ is related to the bath parameters [Eq. (14)].

We can derive from the GLE [Eq. (13)], an equation for the relaxation function [see Eq. (4)] defined as a time correlation function at zero field,

$$\varphi(t) = \overline{\langle \delta\phi(t)\,\delta\phi(0) \rangle}. \tag{16}$$

The symbol $\bar{O}$ ($O$ a function) means that an additional averaging over the initial fluctuation $\delta\phi(0)$ has been performed. By multiplying each term of Eq. (13) by $\delta\phi(0)$ and doing the different averages considering $\overline{\delta\phi(0)} = 0$, we get

$$J\ddot{\varphi} + \int_0^t \eta(t-t')\dot{\varphi}(t')dt' + k\varphi(t) = 0. \tag{17}$$

This procedure corresponds to our macroscopic experiment where we probe not a single mobile dipole but a huge assembly of them each supposed to respond independently. From Eq. (17) we can derive the fluctuation dissipation theorem [Eq. (13)]. This theorem is valid only because we have performed the additional averaging procedure.[26,43]

The dipole dynamics is assumed to be highly overdamped ($J \to 0$) as in the first model of Debye.[44] The Langevin equation [Eq. (13)] is then solved by Laplace's transform.[26] $\tilde{O}$ denotes the Laplace transform of $O$,[26,43]

$$\delta\tilde{\phi}(s) = \tilde{\eta}(s)\tilde{\chi}(s)\,\delta\phi(0) + \tilde{\chi}(s) \times \left( \tilde{\xi}(s) + \frac{1}{2}\mu_\perp E_{\mathrm{ac}} \left[ \frac{1}{s - j\omega} + \frac{1}{s + j\omega} \right] \right) \tag{18}$$

with

$$\tilde{\chi}(s) = \frac{1}{k + s\tilde{\eta}(s)} \tag{19}$$

the Laplace transform of the dielectric susceptibility. The first term on the right-hand side of Eq. (18) gives the relaxation of the dipole starting from the initial fluctuation $\delta\phi(0)$. It also corresponds to the relaxation function of the system [Eq. (16)] obtained by solving directly Eq. (17) by Laplace transform,

$$\tilde{\varphi}(s) = \tilde{\eta}(s)\tilde{\chi}(s) = \frac{\tilde{\eta}(s)}{k + s\tilde{\eta}(s)}. \tag{20}$$

With the model, Eq. (13), we have $\chi_0 = 1/k$—meaning that the more the dipoles are constraint the less important is the dipolar contribution to the admittance—and $\tau = \eta_S / k$—meaning that the more the dipole is constraint the more rapidly it goes back to equilibrium and that the more the friction is important the more this way back is slowed down.

Before studying in more details the solution of the GLE it is necessary to connect the local and the macroscopic susceptibilities [Eq. (1)]. We assume the local and the macroscopic fields to be the same, for simplicity. This approximation should be reasonable since the organic monolayers are weakly polar. The Fourier transform of the average dipole displacement is obtained from Eq. (18) by performing averaging over the thermal noise and initial fluctuations,

$$\overline{\langle \delta\mu(\omega) \rangle} = \mu_\perp \overline{\langle \delta\phi(\omega) \rangle} = \mu_\perp^2 \chi(\omega) E_{\mathrm{ac}}(\omega). \tag{21}$$

From the last equation the macroscopic dipolar polarization vector by unit volume is obtained

$$P_{dip}(\omega) = M\overline{\langle \delta\mu(\omega) \rangle} = M\mu_\perp^2 \chi(\omega) E_{\mathrm{ac}}(\omega), \tag{22}$$

where $M$ is the number of dipoles (or molecules) by unit volume. Writing, as usual, $P_{dip}(\omega) = \epsilon_0 \chi_{dip}(\omega) E(\omega)$ we get the expected simple relation

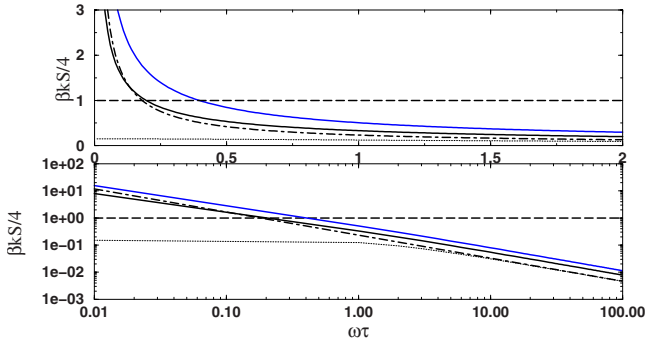


FIG. 4. (Color online) Spectral density (linear and log-log plot) of the dielectric noise [Eq. (24)] in units of $k_BT/k$ related to the DH susceptibilities (full lines) with $n=0.85$ and $m=0.2$ (the down curve in black) and $n=0.85$ and $m=0.1$ (the top curve in blue), to the Debye susceptibility (dashed line) Ref. 44), to the Cole-Cole susceptibility (Ref. 45) with $n=0.85$ (dotted-dashed line), and to the Cole-Davidson susceptibility (Ref. 46) with $n=0.85$ (dotted line).

$$\chi_{dip}(\omega) = \frac{M\mu_\perp^2}{\epsilon_0}\chi(\omega). \tag{23}$$

This last relation establishes connection between solutions of the GLE and the experimental data.

Simple manipulations summarized in Appendix A, allow to relate the local dielectric susceptibility to the spectral density of the random field, $\xi(t)$,

$$S(\omega) = 4k_BT\frac{\Im\chi(\omega)}{\omega|\chi(\omega)|^2}. \tag{24}$$

In Fig. 4 (linear and log-log plot), we show two examples of spectral density derived from our data corresponding to the relaxation functions of Fig. 3. As a matter of illustration, the spectral densities of usual model susceptibilities given in Appendix B are also shown. These are models that produce simple analytical expressions to compare with. They reflect very different type of dynamics of the mobile dipoles. The Debye model[44] corresponds to usual Brownian motion,[54] the Cole-Cole model[45] to stochastic motion with fractional Gaussian noise.[30] The Cole-Davidson model[46] presents the two characteristics: it is Debye type at low frequencies and Cole-Cole type at high frequencies.

As can be seen in Fig. 4, at high enough frequencies the DH, and Cole-Davidson spectral densities are reduced to simple power laws as the Cole-Cole case. With the Havriliak-Negami susceptibility,[47] not explicitly considered here, we also obtain the same qualitative behaviors. Therefore, we expect similar noise properties at high frequencies ($\omega\tau \gg 1$) for all these different models, except Debye. Moreover, in our case, on the contrary to the Cole-Davidson case, we expect the same type of dynamics not only at high frequencies, but also at lower frequencies where the spectral density again tends to power laws but with slightly different exponents. To summarize, the spectral densities that we extract from our data of dielectric susceptibilities are qualitatively similar to the Cole-Cole model: we expect therefore the dipoles to follow a subdiffusion.[30] However, contrary to the Cole-Cole model the characteristics of the fluctuating bath are changing with frequencies: they are always characteristics of a fractional Gaussian noise but with a value of the Hurst index that slightly depends on the frequency window considered.

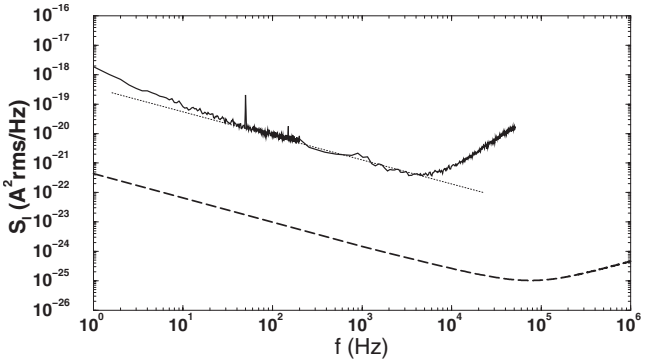


FIG. 5. Spectral density of tunnel current noise. The experimental data (full line) are obtained for an OD junction at $V_{dc}=0.8$ V. The power law is well reproduced by the theory (dashed line) but not the amplitude.

The spectral density of the bath is simply related to the spectral density of polarization fluctuations, $S_P$. Indeed, starting from Eq. (18) without external field we get after averaging over the initial fluctuation the following simple relation between autocorrelation functions:

$$\overline{\langle \delta\tilde{\phi}(j\omega)\delta\tilde{\phi}(-j\omega)\rangle} = |\chi(\omega)|^2\overline{\langle \delta\tilde{\xi}(j\omega)\delta\tilde{\xi}(-j\omega)\rangle}. \tag{25}$$

From this last equation we can straightforwardly write

$$S_P(\omega) = \frac{M\mu_\perp^2}{\epsilon_0}|\chi(\omega)|^2 S(\omega) = \frac{M\mu_\perp^2}{\epsilon_0}\frac{\Im\chi(\omega)}{\omega} = \frac{\Im\chi_{dip}(\omega)}{\omega}. \tag{26}$$

Such spectral density gives a Lorentzian in the case of Debye and power laws for the other models. This is an important expression to be tested by future experiments. It synthesized all the approximation contained in our model [Eqs. (11), (13), and (23)]. This quantity cannot be measured directly but appears in the spectral density of voltage and current fluctuations as explained below.

The $1/f$ current noise of molecular junctions was already investigated in the frequency range from 0 to 100 Hz (see Fig. 5).[15] It shows two main characteristics. (i) The background noise power spectrum is proportional to $(\partial I/\partial V)^2$, $I$ the tunnel current, $V$ the applied voltage, suggesting pure capacitive effects. (ii) Strong local increase in noise appear at certain bias voltages. As usual, we have interpreted the data in terms of fluctuating defects modeled by independent two-level systems:[15,55] each defect is described by two possible states, the population of those states fluctuating with time. The first point was attributed to voltage fluctuations induced by the fluctuating two-level systems. The second point was explained by important changes in tunnel resistance at certain voltages induced by the modifications of the defect states through assisted tunneling mechanisms.[15] However, to our opinion this common interpretation suffers several drawbacks.[56] (i) The physical nature of the two-level systems

remains unknown. (ii) Arbitrary assumptions on the energy and time relaxation densities have to be done to get the expected $1/f$ behavior. (iii) More importantly, to reproduce the very large noise amplitude that we observed we are forced to consider unphysically large density of such defects: in some cases we obtain more defects than atoms present in the molecular dielectric. We have then to look for better interpretation with better physical grounds. For instance, is the $1/f$ polarization noise characterized in this work a possible candidate for the background noise observed in experiments?

In a dielectric, the voltage noise is due to the thermal fluctuations of the polarization.[57] In particular, there is no thermal motion of charge carriers as in any conductor. The Nyquist formula for the spectral density of voltage fluctuations, $S_V$, across a (macroscopic) capacitor gives[57]

$$S_V(\omega) = 4k_B T \frac{\Im C(\omega)}{\omega |C(\omega)|^2}. \tag{27}$$

Considering only the molecular fluctuations characterized in this work, we write

$$S_V(\omega) = \frac{4k_B T d}{A\epsilon_0} \frac{S_P(\omega)}{|[\epsilon_{r\infty} + \chi'_{dip}(\omega)]^2 + \chi''^2_{dip}(\omega)|}, \tag{28}$$

where $\epsilon_{r\infty}$ is the dielectric constant at high frequencies due to electrons (to be related to $C_\infty$). This prediction may be tested by measuring the voltage fluctuation at zero dc field instead of the current fluctuations. This will be done in future work. Here we focus on the $1/f$ tunnel current noise to see if it is consistent with these voltage fluctuations. Note that in general there is also an interfacial contribution to this polarization which, however, could be considerably reduced by heating process.[23]

The polarization noise produces a fluctuating current—a polarization current—that shows an increasing spectral density with frequency[57]

$$S_I^P(\omega) = 4k_B T \omega \Im C(\omega). \tag{29}$$

This kind of noise is not explicitly observed in the frequency window considered in Ref. 15 (see Fig. 5) but could be seen at higher frequencies. This point needs to be further investigated. On the other hand the current flowing through the tunnel resistance is also fluctuating because of the fluctuating voltage. The experimental data suggest that these fluctuations are predominant in our systems at low frequencies.[15] Assuming a nonfluctuating tunnel resistance, the current fluctuations are simply related to voltage fluctuations,

$$\langle \delta I(t) \delta I(t') \rangle = \left( \frac{\partial I}{\partial V} \right)^2 \langle \delta V(t) \delta V(t') \rangle, \tag{30}$$

where $\delta O(t) = O(t) - \langle O \rangle$. The spectral density of current noise is then related to the spectral density of voltage noise,

$$S_I(\omega) = \left( \frac{\partial I}{\partial V} \right)^2 S_V(\omega). \tag{31}$$

With this expression, the spectral density of current shows a $(\partial I/\partial V)^2$ dependence as observed in experiment.

In Fig. 5, we compare the prediction of Eq. (31) with typical data (obtained at $V_{dc}=0.8$ V). The power law is well reproduced but not the amplitude: a factor of about $10^3$ or $10^4$ is missing in the theory. In this expression we consider only the voltage fluctuations caused by the permanent dipoles of the SAMs. Adding the interface [Eq. (2)] and the displacement current contributions [Eq. (29)] increases $S_I$ but certainly not in a sufficient way. As a matter of illustration, the latter contribution is added to the spectral density in Fig. 5 and shown to contribute significantly to the total signal for frequencies higher than $10^5$ Hz only. It seems therefore clear that the polarization noise alone cannot explain the large amplitude of the current noise. An important drawback of Eq. (31) concerns the assumption of constant tunnel resistance, consistent with the use of Eq. (27). Indeed, fluctuations of the dielectric properties, as the ones evidenced in this work, will induce fluctuations in the potential profile through the junction and, therefore, changes in the tunnel resistance. Additional investigations including both polarization and resistance noise induced by the same molecular fluctuations are needed to see whether the molecular fluctuations considered in this work are large enough, or not, to explain the unusual magnitude of the tunnel current noise. It is interesting to note that we have also seen effects of the low-frequency peaks in the tunnel current noise that perturb locally the $1/f$ law but in a way that cannot be simply explained by including the interfacial contribution in $S_V(\omega)$. This point is still under investigation and goes beyond the scope of the present work.

## VI. EFFECTS OF THE dc ELECTRIC FIELD

In the experiments we apply a weak ac field plus a static potential varying from 0 to 1 V. Two main effects have been observed and summarized in Fig. 6. (i) The inverse of the characteristic time $\tau$ increases linearly with the dc field. (ii) The exponent $m$ decreases. The first point is naturally explained with the GLE: this is the purpose of this section. The second point is beyond the scope of the effective theory used in this work.

The interaction of the dipole with the applied fields becomes

$$H_{int} = \mu \cos \phi(t) [E_{ac}(t) + E_{dc}]. \tag{32}$$

Expanding this expression yields

$$H_{int} \approx \mu_\parallel [E_{ac}(t) + E_{dc}] - \mu_\perp \delta\phi(t) [E_{ac}(t) + E_{dc}] - \frac{1}{2} \mu_\parallel [\delta\phi(t)]^2. \tag{33}$$

With this new interaction term, one can derive a generalized Langevin equation that is formally similar to Eq. (13) at the condition to consider shifted dynamical variables

$$\delta\phi \to \delta\phi + \frac{\mu_\perp}{k + \mu_\parallel E_{dc}} \tag{34}$$

and a new elastic constant

$$k \to k + \mu_\parallel E_{dc}. \tag{35}$$

These two transformations have clear meanings. (i) The center of mass of the harmonic oscillator is shifted by the con-

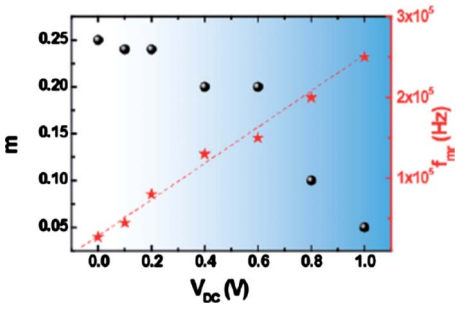


FIG. 6. (Color online) Typical evolution of $m$—one of the two exponents of the Dissado-Hill susceptibility (see text)—and $f_m = 1/\tau$ as function of $V_{\rm dc}$ for a particular OD junction.

stant field. (ii) The harmonic potential is strengthened by the dc potential, i.e., the constant field tends to align the mobile dipoles in its direction and therefore to reduce the angle fluctuations. The new Langevin equation is solved exactly as before. As a first consequence the inverse of $\tau$ is shifted up linearly by the constant electric field in agreements with experimental data,

$$\frac{1}{\tau} = \frac{k + \mu_{\parallel} E_{\rm dc}}{\eta_S}. \tag{36}$$

The dc potential perturbs also the harmonic modes of the environment in the same way it perturbs the dynamics of the dipoles. Since the dissipation is caused by the interaction between the permanent dipoles and the harmonic modes of the SAM, changes in the density of states should induce changes in the exponents of the Dissado-Hill susceptibility, Fig. 6.

## VII. LOW-FREQUENCY VIBRATION MODES—QUALITATIVE ARGUMENTS

The energy dissipation is caused by the interaction of the dipoles with the harmonic modes of the bath, here the vibration and rotation modes of the monolayer. To get insight into the physical mechanisms at the origin of the particular response functions that we observe, a detailed knowledge both of these modes and of the way they interact with the permanent dipoles are needed. A full microscopic study of the mechanical properties of the monolayers is however a very complicated task. In this work we limit ourselves to a simple procedure assuming that $c_\alpha = \bar{c}$ and $J_\alpha = \bar{J}$ are $\alpha$ independent (these parameters remain constant for all harmonic modes). They can then be taken out of the summation in Eq. (14). The spectral density of environmental fluctuations is in this way simply related to the density of harmonic modes of our monolayer,

$$\rho(\omega) = \frac{1}{L^2} \sum_n \delta(\omega - \omega_n) \approx \frac{\bar{J}}{L^2 \bar{c}^2} \omega \gamma(\omega) = \frac{\bar{J}}{k_B T L^2 \bar{c}^2} \omega^2 S(\omega). \tag{37}$$

$L$ being the characteristic size of the system. This crude approximation gives for the Debye susceptibility $\rho_{Debye}(\omega)$

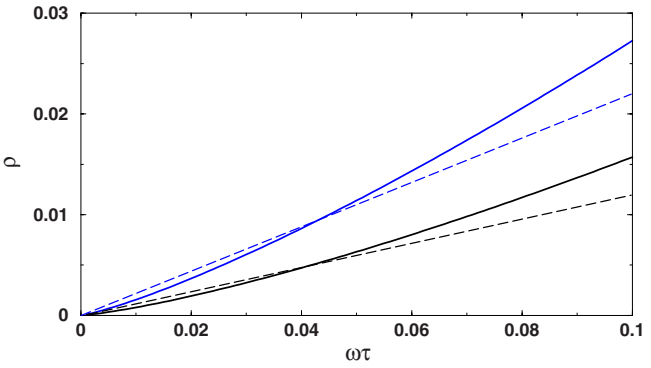


FIG. 7. (Color online) Density of harmonic modes related to the DH susceptibility with $n=0.85$, $m=0.2$ (the down curves in black) and $n=0.85$, $m=0.1$ (the top curves in blue), taking [see Eq. (37)]. The first case corresponds to the OD based devices without dc field, the second either to the OD with constant field [cf. Fig. 3(b)] or the OTS based devices without field. The two dashed curves are guide lines that serve to estimate the variations between the data and the linear densities expected for perfect monolayers.

$\propto \omega^2$ that corresponds to the density of independent three-dimensional isotropic harmonic oscillators, in agreements with the original statements of the Debye model.[44] For the more general susceptibility of Dissado and Hill, that corresponds to our observations, we get $\rho_{\rm DH}(\omega) \propto \omega^\sigma$ with $\sigma$ depending on the frequency window considered but being always such that $1 < \sigma < 2$. In the case of the Cole-Cole model which should be strictly equivalent to ours for $\omega\tau > 1$ (see Fig. 4), $\sigma = 2 - n$ at all frequencies,

$$\rho_{Cole\text{-}Cole}(\omega) = \frac{4\bar{J}\tau^{1-n}}{L^2 \bar{c}^2 \chi_0} \omega^{2-n} \sin(1-n)\frac{\pi}{2}. \tag{38}$$

The densities of states, $\rho_{\rm DH}$, corresponding to the DH spectral densities of Fig. 4 are shown in Fig. 7.

Are the densities obtained in Fig. 7 close to what could be expected for our systems? The complete phonon (or rotation) spectrum of the SAMs is very complex simply because the number of atoms per unit cell is large. However, as far as we are concerned with long-wavelength modes compared to a scale defined by the molecular interaction, we can, in principle, forget all the details of the motif and describe the equilibrium properties of the system with a continuum elastic theory. We assume in the following that the films we are considering could be described by such theory. In the two types of monolayer studied in this work the molecules are organized in a triangular lattice. Due to symmetry consideration, it is well known that such a lattice can be described by a unique pair of Lamé coefficients $(\lambda, \mu)$.[58] The displacement field is then a sum of two independent contributions, a longitudinal and a transverse components. The wave equation to be considered is[58]

$$\left(\Delta + \frac{\omega^2}{\nu^2}\right) u(\vec{r}) = 0, \tag{39}$$

where $u(\vec{r})$ is any component, longitudinal or transverse, of the displacement field and $\nu$ the corresponding sound veloc-

ity. Equation (39) may be considered as the simplest possible candidate to describe the mechanical properties of the SAMs. The density of states obtained with this model gives a reference to compare to the results of Fig. 7,

$$\rho(\omega) = \frac{1}{2\pi\nu^2}\omega. \tag{40}$$

With this simple continuum elastic theory, the density of harmonic modes at low frequencies is linear and characterized solely by the speed of sound. Considering the linear density [Eq. (40)] suppresses dissipation. This is particularly clear with the Cole-Cole model [Eqs. (B4) and (38)]: taking $n=1$ gives $S_{Cole\text{-}Cole}(\omega)=0$. If our systems were perfectly ordered at the macroscopic scale probed in the frequency window considered in this work, the motion of the permanent dipoles would occur without any dissipation. Since we observe dissipation the density of states cannot be perfectly linear as in Eq. (40). Indeed, in the two examples shown in Fig. 7, clear deviations to the linear relation are evidenced.

Considering the model structure of the SAMs described in Sec. III, nonlinearities in the density of states are induced by disorder. There is several ways to introduce disorder in the continuum elastic theory. A direct generalization of Eq. (39) is investigated in Ref. 59. As a matter of illustration we base our following discussion on this particular example which has the merit to propose analytical expressions. Considering polycrystalline materials, such as our monolayers, and special type of disorder where λ is taken as the only random variable, the original continuum elastic theory is simplified to a wave equation for a displacement field that is reduced to a scalar instead of a two-component vector[59]

$$\left[\Delta + \frac{\omega^2}{\nu^2(\vec{r})}\right]u(\vec{r}) = 0. \tag{41}$$

$\nu(\vec{r})$ is the random sound velocity field. Correlated noise is considered by the authors of Ref. 59 with mean $\nu$ and spatial correlation $\langle\nu(\vec{r})\nu(\vec{r}')\rangle=\exp(-|\vec{r}-\vec{r}'|/l_c)$, $l_c$ being the correlation length. Standard perturbation theory gives the density of states for $\omega \ll v/l_c$,[59]

$$\rho(\omega) = \frac{1}{2\pi\nu^2}\omega\left[1 + \alpha\left(\frac{l_c}{\nu}\right)^2\omega^2 + \cdots\right]. \tag{42}$$

$\alpha$ is a positive constant to be determined. We note in the above equation a nonlinear increase, $\delta\rho$, of the density of states

$$\delta\rho(\omega) = \alpha\frac{l_c^2}{2\pi\nu^4}\omega^3. \tag{43}$$

The nonlinear part of the density of states of harmonic modes is at the origin of the friction in the generalized Langevin equation. In other words, there is dissipation only because some sort of disorder exists in our systems. An example of such nonlinear contribution induced by disorder is given by Eq. (43). In this relation, the amplitude of $\delta\rho$ depends on $l_c$ and $\nu$. If the first parameter is certainly related to the particular model used in Ref. 59, the second one is much more general. If one omits the Poisson ratio, the average speed of sound is expressed as $\nu \propto \sqrt{E/\rho_M}$, where $E$ is the Young's modulus and $\rho_M$ the mass density of the SAM.[58] The Young's modulus expresses the property of a body to be elongated (or compressed) by a uniform extension (or compression) along the direction where the stress is applied. Equations such as Eqs. (37) and (43) build therefore a natural connection between the dynamic of relaxation of the permanent dipoles and the mechanical properties of the molecular junctions, a key parameter that controls these properties being the Young's modulus. As it was pointed out in the introduction of Ref. 21, it seems suitable to complement the admittance spectroscopy by investigations of the mechanical properties of the self-assembled monolayers. A few questions related to the present work could concern the comparison of the speed of sound in OTS- and OD-based junctions or the effects of a perpendicular dc electric field on the Young's modulus. Note that the Young's modulus was very recently measured for similar SAMs as ours and shown to be close to the one of bulk polyethylene, giving a speed of sound $\nu = 2000$ m s$^{-1}$.[60] The parameters of the dielectric susceptibility $(n, m, 1/\tau)$ found for our systems are also close to the ones of bulk saturated polymers.

## VIII. CONCLUSIONS

In this work we focus on the dipolar component of the complex admittance.[23] It is attributed to permanent dipoles present in the monolayer. The measured response is a system average which contains elements both from the dipoles and from the mechanical interaction of these dipoles with the electrically inactive structure of which the dipoles are an intrinsic part. This has been modeled in terms of the GLE that considers a permanent dipole trapped in a harmonic potential and interacting with a non-Markovian bath.[26] This equation allows us to connect the spectral density of polarization noise to the measured dielectric susceptibility. From our experimental data we have determined the power spectrum of this noise: it is of $1/f$ type. It is of importance since all fluctuating mechanisms existing in our systems ($1/f$ current noise, random telegraph signal, etc.) should be considered by taking into account explicitly this high-level noise. We suggest, for instance, that the polarization noise could be the source of the $1/f$ current noise observed earlier in the same systems.[15] Finally, we stress that in order to get more physical insight into the mechanisms at the origin of the particular complex admittance investigated in this work, studies of the mechanical properties of the molecular junctions should be carried on.

## APPENDIX A: SPECTRAL DENSITY OF THE RANDOM FIELD

In this appendix, we derive a relation between the local susceptibility, $\chi$, and the spectral density of the random field, $\xi$. From Eq. (19) we write

$$\tilde{\eta}(s) = \frac{1}{s}\left[\frac{1}{\chi(js)} - \frac{1}{\chi_0}\right]. \tag{A1}$$

According to Eq. (14), the memory function and the spectral density are related by an integral relation. Inverting this relation gives[28]

$$\gamma(\omega) = \lim_{\epsilon \to 0^+} [\tilde{\eta}(\epsilon + j\omega) + \tilde{\eta}(\epsilon - j\omega)]. \quad \text{(A2)}$$

Using these two equations we can determine the spectral density of the environmental coupling from the dielectric susceptibility

$$\gamma(\omega) = \frac{\Im\chi(\omega)}{|\chi(\omega)|^2}. \quad \text{(A3)}$$

Inserting the last expression into Eq. (14) we get a relation between the friction kernel and the local susceptibility ($\beta = 1/k_B T$),

$$\eta(t) = \beta\langle\xi(t)\xi(0)\rangle = \int_0^{+\infty} d\omega \frac{\Im\chi(\omega)}{\omega|\chi(\omega)|^2}\cos\,\omega t. \quad \text{(A4)}$$

By virtue of Wiener-Khintchine's theorem the spectral density of the random field is deduced

$$S(\omega) = 4k_B T \frac{\Im\chi(\omega)}{\omega|\chi(\omega)|^2}. \quad \text{(A5)}$$

## APPENDIX B: MODEL SPECTRAL DENSITIES OF NOISE

In this appendix, we derive from Eq. (24) the noise spectral density corresponding to dielectric model susceptibilities: the Debye,[44] Cole-Cole,[45] and Cole-Davidson[46] susceptibilities.

The Debye susceptibility,

$$\chi_{Debye}(\omega) = \frac{\chi_0}{1 + j\omega\tau} \quad \text{(B1)}$$

gives a white noise

$$S_{Debye}(\omega) = \frac{4k_B T}{\chi_0}. \quad \text{(B2)}$$

This is typical of usual Brownian motion where, in the free-particle case (without trapping potential), the system experiences a normal diffusion under the action of a memoryless damping function, $\eta_{Debye}(t) = \eta_S \delta(t)$.[54] This type of motion is characterized, for instance, by a mean-square displacement linear in time. Note that this simple case is also of direct interest for us since the low-frequency peak is Debye type (see Fig. 1).[23]

The Cole-Cole susceptibility[45]

$$\chi_{Cole\text{-}Cole}(\omega) = \frac{\chi_0}{1 + (j\omega\tau)^{1-n}} \quad \text{(B3)}$$

yields a completely different result

$$S_{Cole\text{-}Cole}(\omega) = \frac{4k_B T}{\chi_0}\tau(\omega\tau)^{-n}\sin(1-n)\frac{\pi}{2}. \quad \text{(B4)}$$

$S_{Cole\text{-}Cole}$ decreases following the same power law in the whole frequency range. This is the signature of a fractional Gaussian noise with Hurst index $H = (n+1)/2$.[29,30] In the free-particle case, this is typical of a strict subdiffusion with a non-Markovian damping kernel $\eta(t) \propto t^{n-1}$. This type of dynamics is characterized, for instance, by a mean-square displacement increasing in time as a power law with an exponent less than 1.

Last, the Cole-Davidson susceptibility[46]

$$\chi_{Cole\text{-}Davidson}(\omega) = \chi_0(1 + j\omega\tau)^{n-1} \quad \text{(B5)}$$

shows two distinct regimes

$$S_{Cole\text{-}Davidson}(\omega) = \frac{4k_B T}{\chi_0}\frac{\sin(1-n)\omega\tau}{\omega}(1 + \omega^2\tau^2)^{(1-n)/2}. \quad \text{(B6)}$$

It gives a plateau at small frequencies ($\omega\tau \ll 1$) and a power law, $\omega^{-n}$, at high frequencies ($\omega\tau \gg 1$).

The Debye and Cole-Cole models are both well studied. They serve here as references illustrating two different types of dynamics to compare with. The Cole-Davidson model in a sense is an extrapolation between these two different cases: it shows a Debye character at low frequencies and a Cole-Cole character at high frequencies.


[1] F. Schreiber, Prog. Surf. Sci. **65**, 151 (2000).
[2] J. Collet, O. Tharaud, A. Chapoton, and D. Vuillaume, Appl. Phys. Lett. **76**, 1941 (2000).
[3] M. Halik, H. Klauk, U. Zschieschang, G. Schmid, C. Dehm, M. Schütz, S. Maisch, F. Effenberger, M. Brunnbauer, and F. Stellacci, Nature (London) **431**, 963 (2004).
[4] A. Facchetti, M. H. Yoon, and T. K. Marks, Adv. Mater. **17**, 1705 (2005).
[5] E. Stern, J. F. Klemic, D. A. Routenberg, P. N. Wyrembak, D. B. Turner-Evans, A. D. Hamilton, D. A. LaVan, T. M. Fahmy, and M. A. Reed, Nature (London) **445**, 519 (2007).
[6] Z. Liu, A. A. Yasseri, J. S. Lindsey, and D. F. Bocian, Science **302**, 1543 (2003).
[7] V. Ferri, M. Elbing, G. Pace, M. D. Dickey, M. Zharnikov, P. Samori, M. Mayor, and M. A. Rampi, Angew. Chem., Int. Ed. Engl. **47**, 3407 (2008).
[8] C. Dri, M. Peters, J. Schwarz, S. Hecht, and L. Grill, Nat. Nanotechnol. **3**, 649 (2008).
[9] N. Katsonis, T. Kudernac, M. Walko, S. Van der Molen, B. Van Wees, and B. Feringa, Adv. Mater. **18**, 1397 (2006).
[10] J. M. Mativetsky, G. Pace, M. Elbing, M. A. Rampi, M. Mayor, and P. Samori, J. Am. Chem. Soc. **130**, 9192 (2008).
[11] A. Salomon, D. Cahen, S. M. Lindsay, J. Tomfohr, V. B. Engelkes, and C. D. Frisbie, Adv. Mater. **15**, 1881 (2003).
[12] H. Haick and D. Cahen, Prog. Surf. Sci. **83**, 217 (2008).
[13] W. Wang, T. Lee, T. Krestchmar, and M. A. Reed, Nano Lett. **4**, 643 (2004).
[14] A. Troisi, J. M. Beebe, L. B. Picraux, R. D. van Zee, D. R. Stewart, M. A. Ratner, and J. G. Kushmerick, Proc. Natl. Acad. Sci. U.S.A. **104**, 14255 (2007).

[15] N. Clément, S. Pleutin, O. Seitz, S. Lenfant, and D. Vuillaume, Phys. Rev. B **76**, 205407 (2007).
[16] A. Badia, R. B. Lennox, and L. Reven, Acc. Chem. Res. **33**, 475 (2000).
[17] V. V. Tsukruk, Adv. Mater. **13**, 95 (2001).
[18] A. Haran, D. H. Waldeck, R. Naaman, E. Moons, and D. Cahen, Science **263**, 948 (1994).
[19] M. Pursch, D. L. Vanderhart, L. C. Sander, X. Gu, T. Nguyen, S. A. Wise, and D. A. Gajewski, J. Am. Chem. Soc. **122**, 6997 (2000).
[20] H. Schmitt, A. Badia, L. Dickson, L. Reven, and R. B. Lennox, Adv. Mater. **10**, 475 (1998).
[21] Q. Zhang, Q. Zhang, and L. A. Archer, J. Phys. Chem. B **110**, 4924 (2006).
[22] M. C. Scott, D. R. Stevens, J. R. Bochinski, and L. I. Clarke, ACS Nano **2**, 2392 (2008).
[23] N. Clément, S. Pleutin, D. Guérin, and D. Vuillaume, Phys. Rev. B **82**, 035404 (2010).
[24] A. K. Jonscher, Nature (London) **267**, 673 (1977).
[25] A. O. Caldeira and A. J. Leggett, Ann. Phys. **149**, 374 (1983).
[26] I. Goychuk, Phys. Rev. E **76**, 040102(R) (2007).
[27] P. C. E. Stamp, Stud. Hist. Philos. Mod. Phys. **37**, 467 (2006).
[28] U. Weiss, *Quantum Dissipative Systems*, 3rd ed. (World Scientific, Singapore, 2008).
[29] B. B. Mandelbrot and J. W. Van Ness, SIAM Rev. **10**, 422 (1968).
[30] S. C. Kou and X. S. Xie, Phys. Rev. Lett. **93**, 180603 (2004).
[31] D. K. Aswal, S. Lenfant, D. Guerin, J. V. Yakhmi, and D. Vuillaume, Anal. Chim. Acta **568**, 84 (2006).
[32] A. Salomon, T. Boecking, C. K. Chan, F. Amy, O. Girshevitz, D. Cahen, and A. Kahn, Phys. Rev. Lett. **95**, 266807 (2005).
[33] E. H. Nicollian and J. R. Brews, *MOS (Metal Oxide Semiconductor) Physics and Technology* (Wiley, New York, 1982).
[34] Y. Wang, Rev. Sci. Instrum. **74**, 4212 (2003).
[35] G. G. Raju, *Dielectrics in Electric Fields* (Marcel Dekker, New York, Basel, 2003).
[36] M. R. Linford, P. Fenter, P. M. Eisenberger, and C. E. D. Chidsey, J. Am. Chem. Soc. **117**, 3145 (1995).
[37] K. I. Iimura, Y. Nakajima, and T. Kato, Thin Solid Films **379**, 230 (2000); I. Doudevski and D. K. Schwartz, J. Am. Chem. Soc. **123**, 6867 (2001).
[38] I. M. Tidswell, B. M. Ocko, P. S. Pershan, S. R. Wasserman, G. M. Whitesides, and J. D. Axe, Phys. Rev. B **41**, 1111 (1990).
[39] I. M. Tidswell, T. A. Rabedeau, P. S. Pershan, S. D. Kosowsky, J. P. Folkers, and G. M. Whitesides, J. Chem. Phys. **95**, 2854 (1991).
[40] L. Romaner, G. Heimel, C. Ambrosch-Draxl, and E. Zojer, Adv. Funct. Mater. **18**, 3999 (2008).
[41] R. Kubo, J. Phys. Soc. Jpn. **12**, 570 (1957).
[42] L. F. Cugliandolo, J. Kurchan, and G. Parisi, J. Phys. I **4**, 1641 (1994).
[43] N. Pottier, Physica A **317**, 371 (2003).
[44] P. Debye, *Polar Molecules* (Dover, New York, 1965).
[45] K. S. Cole and R. H. Cole, J. Chem. Phys. **9**, 341 (1941).
[46] D. W. Davidson and R. H. Cole, J. Chem. Phys. **19**, 1484 (1951).
[47] S. Havriliak and S. Negami, Polymer **8**, 161 (1967).
[48] L. A. Dissado and R. M. Hill, Nature (London) **279**, 685 (1979); Proc. R. Soc. London **390**, 131 (1983).
[49] L. J. Slater, *Generalized Hypergeometric Functions* (Cambridge University Press, Cambridge, England, 2008).
[50] R. M. Hill, Phys. Status Solidi B **103**, 319 (1981).
[51] S. Corezzi, E. Campani, P. A. Rolla, S. Capaccioli, and D. Fioretto, J. Chem. Phys. **111**, 9343 (1999).
[52] N. V. Prokof'ev and P. C. E. Stamp, Rep. Prog. Phys. **63**, 669 (2000).
[53] A. O. Caldeira, A. H. Castro Neto, and T. O. de Carvalho, Phys. Rev. B **48**, 13974 (1993).
[54] S. Chandrasekhar, Rev. Mod. Phys. **15**, 1 (1943).
[55] K. S. Ralls, W. J. Skocpol, L. D. Jackel, R. E. Howard, L. A. Fetter, R. W. Epworth, and D. M. Tennant, Phys. Rev. Lett. **52**, 228 (1984).
[56] S. M. Kogan, *Electronic Noise and Fluctuations in Solids* (Cambridge University Press, Cambridge, 1996).
[57] N. E. Israeloff, Phys. Rev. B **53**, R11913 (1996).
[58] L. D. Landau and E. M. Lifshitz, *Theory of Elasticity* (Pergamon, New York, 1970).
[59] V. Gurarie and A. Altland, Phys. Rev. Lett. **94**, 245502 (2005).
[60] F. W. DelRio, C. Jaye, D. A. Fischer, and R. F. Cook, Appl. Phys. Lett. **94**, 131909 (2009).

# Low Frequency Dielectric Loss of Metal/Insulator/Organic Semiconductor Junctions in Ambient Conditions

*R. Ledru*[a], *S. Pleutin*[a,b]*, *B. Grouiez*[a], *D. Zander*[a], *H. Bejbouji*[a,b], *K. Lmimouni*[b], *and D. Vuillaume*[b]

[a] CReSTIC, University of Reims, Moulin de la Housse
F-51687 Reims Cedex 2 (France).

[b] Institute for Electronics, Microelectronics and Nanotechnology (IEMN), CNRS, University of Lille, BP 60069, Avenue Poincaré,
F-59652 Cedex, Villeneuve d'Ascq (France).

* Corresponding author, E-mail: stephane.pleutin@isen.iemn.univ-lille1.fr

Keywords: Metal-Oxide-Organic semiconductor junctions, dielectric relaxation, anomalous diffusion, admittance spectroscopy

Abstract: The complex admittance of metal/oxide/pentacene thin film junctions is investigated under ambient conditions. At low frequencies, a contribution attributed to proton diffusion through the oxide is seen. This diffusion is shown to be anomalous and is believed to be also at the origin of the bias stress effect observed in organic field effect transistors. At higher frequencies, two dipolar contributions are evidenced, attributed to defects located one at the organic/oxide interface or within the organic, and the other in the bulk of the oxide. These two dipolar responses show different dynamic properties that manifest themselves in the admittance in the form of a Debye contribution for the defects located in the oxide, and of a Cole-Cole contribution for the defects related to the organic.

## 1. Introduction.

As Organic Field-Effect Transistors (OFET) are now close to applications, questions about their reliability under realistic atmospheric conditions become more and more important.[1] Electrical instabilities are evidenced, for instance, in the bias stress effect where under a prolonged application of a gate potential the device characteristics, such as the threshold voltage, evolve with time.[1,2] Several mechanisms were proposed to understand these degradations of the device properties. Some are intrinsic mechanisms such as trapping of charges, in the organic film[3-5] or at the organic/oxide interface, [6] or pairing of mobile charges to heavier bipolarons.[7] Some others are extrinsic mechanisms needed especially when the measurements are done in the air since humidity was shown to amplify these instabilities.[8] An example of such mechanism was proposed recently based on proton production by electrochemical reactions involving water molecules adsorbed at the organic/oxide interface, followed by proton diffusion through the oxide.[9,10]

We have considered $Si^{+}/SiO_2$/Pentacene/Au junctions that are the two terminal pendants of thin film transistors with the same layer structure. We study the dynamic electrical response of these junctions under ambient conditions over a large frequency window as function of a superimposed dc voltage ($V_{dc}$). This technique has proven in the past to be powerful because of its sensitivity and its ability to separate the different process involved.[11,12] It was already applied to several organic based junctions[13,14] but the results were interpreted based on models relying on the Shokley-read-Hall statistics not appropriated to organic materials.[11,12] Compared to these previous works[13,14] our frequency range is more extended, going down to $10^{-1}$ Hz, and the analysis of our data insist on the crucial role played by the interactions of the defects with their surroundings which determine the shape of the measured response functions.[15-18] We have identified two types of defects with different dynamic properties: one located inside the oxide shows a Debye type of response, the other located at the

oxide/organic interface, or in the bulk of the organic, shows a Cole-Cole type of response.[17,19,20] At lower frequencies (< 100 Hz) we observe anomalous Low Frequency Dispersion (LFD)[21] that is consistent with the ionic diffusion current proposed in Refs. [9,10] but instead of normal diffusion considered in these works, our results evidence fractional diffusion to occur.[22,23]

## 2. Material and methods.

### 2.1. *Device preparation.*

The samples are fabricated using 70 (± 7) nm thick $SiO_2$ layer which was thermally grown on a heavy phosphorus doped n-typed silicon (100) (0.001 – 0.003 Ω cm). Prior to the pentacene deposition, the substrate was cleaned in an ultrasonic bath with acetone and isopropanol, and then blown with dry nitrogen. Subsequently, it was exposed to UV-ozone for 20 min. Then the thermal evaporation of the 40 nm thick pentacene organic active layer was done under the base pressure of $2.8 – 3.10^{-6}$ mbar. The deposition rate of pentacene was maintained at 0.1 Å/s on the substrate kept at room temperature. After the deposition of the pentacene, the sample was transferred to the metallization chamber in order to deposit 120 nm of gold electrodes.

### 2.2. *Admittance measurements.*

We have considered about 20 devices in ambient conditions showing all the same qualitative features. We present below results mostly for one of then that is very representative. For each sample, a small part of the surface is left free of pentacene. This allows us to access on the $Si^+/SiO_2/Au$ junctions that constitute the "reference" measurements which can be compared with the organic based systems. We have measured the admittance in the frequency range $10^{-1}$ – $10^5$ Hz as function of a static potential ($V_{dc}$) varying between -20 V and +20 V. The $V_{dc}$ bias and the small superimposed $V_{ac}$ signal (100 mV) was applied to the gold electrode. Three

different sizes of $9.10^{-4}$, $3.6.10^{-3}$ and $10^{-2}$ $cm^2$ of contact electrode were accessible on our devices but no size effects were noticed. The complex admittance, $Y(\omega)$, was measured using a frequency response analyzer (Solartron 1260) coupled with an interface dielectric (Solartron 1296) that provides directly the parallel conductance and capacitance. We write the response as[16]

$$\frac{Y(\omega)}{\omega} = j\left(C'(\omega) - jC''(\omega)\right) = j\left(\chi'(\omega) + C_\infty\right) + \chi''(\omega) \quad (1)$$

where all the terms are supposed to be normalized by the contact surface area. As usual, we define $\omega = 2\pi f$, $f$ the signal frequency. $C'$ contains information about the polarization properties, $C''$ about the energy dissipated by the system during the polarization process. $C_\infty$ is the part of the capacitance that includes the response of the "fast" species (electrons, polarons, phonons,…) able to follow instantaneously the electric field (considering our frequencies range). In other words, it is the capacitance of an ideal junction (junction without defects) for which the amplitude is fixed, as in standard Metal/Oxide/Semiconductor junctions, by the density profile of the free carriers present in the semiconductor. At the frequencies considered in this work, the electric energy is transferred without any loss to the free carriers and therefore $C_\infty$ is a real quantity. $\chi$ is the part of the dielectric susceptibility that includes the response of the "slow" species present in the junctions. They could be slow ions, defects able to trap free carriers or impurities carrying permanent dipoles, for instance. In other words, $\chi$ includes the response of various defects that contribute to increase the ideal capacitance, $C_\infty$, by adding new mechanisms of polarization but which dissipate part of the electric energy in the surrounding. $\chi$ is therefore a complex quantity: the real part describes the polarization processes of the defects, the imaginary part the way part of the electric energy is lost.

**3. Results and discussions.**

Typical results are shown in Figs. 1a and 1b giving $C'$ and $C''$, respectively, for different dc voltages ($V_{dc}$). The results for a corresponding reference junction are also shown on the same graphs. These results show a loss part (Fig. 1b) structured and weakly frequency dependent with a minimum loss ~ $10^{-10}$ S.s.cm$^{-2}$ ($\tan\delta$ about $10^{-3}$).[20] As for all the junctions that we have investigated, our data clearly show that the admittance is decomposed in two qualitatively different types of independent contributions (see Figs. 1). The first type of contributions ( $\chi_{Ion}$ ) observed at low frequencies (<100 Hz) for all of our devices shows a decrease both in the real and the imaginary part of $Y(\omega)/\omega$ following a fractional power law. We identify this contribution with a LFD observed in systems where the polarization is controlled by currents of slow charges.[21] The second type of contribution ($10^2$-$10^5$ Hz) is dipolar type that manifests itself as a peak in the loss part of the admittance.[16,17,20] Our data are very well reproduced if we consider only two different dipolar contributions ( $\chi_{Organic}, \chi_{SiO_2}$ ). Because they are visible for different range of $V_{dc}$ they can be attributed to defects located one in the bulk of the $SiO_2$ and the other on the organic/oxide interface or within the organic film. The dielectric susceptibility of Eq. (1) is then written as a sum of three components

$$\chi(\omega) = \chi_{SiO_2}(\omega) + \chi_{organic}(\omega) + \chi_{Ion}(\omega). \quad (2)$$

The relative amplitude of each of these components fluctuates from device to device and varies with $V_{dc}$. We do the same analysis for the "reference" junctions for which no contribution of the pentacene appears. In the example of Figs. 1, the reference junction shows clearly an ionic but no sizable dipolar contribution. Indeed, for frequencies above 10 Hz the imaginary part of the dielectric susceptibility becomes so weak to reach the sensitivity limitation of our experiment resulting in the wide fluctuations shown in Fig. 1.b. For frequencies above 10 Hz, the capacitance of this reference junction is then close to the

geometric capacitance. Another example of reference junction, with more pronounced dipolar contribution, will be shown later.

The three contributions of Eq. (2) are detailed farther. In particular, simple analytic expressions for each of these three contributions are given (Eqs. (3), (4) and (7)). With the Eqs. (1) and (2), together with these analytic expressions, we accurately fit the complex admittance at every $V_{dc}$ as will be seen below (examples are shown in Figs. 3 and Figs. 4, for specific values of $V_{dc}$). In particular, the fitting procedure gives us the $C_\infty$-$V_{dc}$ curves that we first comment before presenting the different contributions of Eq. (2).

### 3.1. $C_\infty$-$V_{dc}$ *characteristics.*

An example of $C_\infty$-$V_{dc}$ curves that corresponds to the measurements of Figs. 1 is shown in Fig. 2. This quantity contains only the contributions of the fast degrees of freedom (hole, polarons,…) to the polarization and gives information about the electrostatic properties of a pure junction where all the slow contributions contained in $\chi$ have been removed.

The infinite frequency capacitance of the "reference" junctions has been shown to be bias independent, as it should be, and shows good agreements with the theoretical expectations: the case of Figure 1a, for instance, corresponds to an oxide of 77 nm width once the frequency dependant part of the admittance has been subtracted (see Fig. 2). The $C_\infty$-$V_{dc}$ curves of the pentacene based junctions (an example is shown in Fig. 2) appear to be similar to the ones of classical Metal/Oxide/Semiconductor junctions but we have to keep in mind that the organic semiconductors differ noticeably from their inorganic counter part.[24,25] First, the organic semiconductor is not doped: so, charges come from the electrodes and by changing the applied voltage we modify both the charge density and the charge profile within the organic film. Moreover, the organic semiconductors are strongly polarizable and the free charge carriers are polarons, or bipolarons, that can not be described as easily as the quasi-electrons

or quasi-holes of Si.[24,25] Nevertheless, we verify that for sufficiently strong $V_{dc}$, charges have been accumulated at the pentacene/oxide interface and the junctions tend to the full accumulation regime where the capacitance is given by the one of the oxide only that is shown in Fig. 2. However, the full accumulation regime is not reached in the potential range that we have investigated: our data shows a transition region between depletion and accumulation much smoother than the one commonly observed in Si based MOS junctions that could be due to the differences between the free charges found in these two systems.[11,12] In decreasing $V_{dc}$ the carrier density decreases (Fig 2) and drives continuously the system from the accumulation to the full depletion (starting from $V_{dc}$=-5 V). Finally for small enough potential values the organic layer is well free of charges and reacts as a dielectric. In this regime the equivalent capacitance corresponds to the series of oxide and pentacene capacitances which is lead to a pentacene dielectric constant of about 3.5, in agreement with values recently reported in literature.[26] It should be stressed that, as commonly observed for organic field effect transistors, our junctions are not ambipolar (p-semiconductor). Even after applying a strong negative potential ($V_{dc}$<-40 V) the capacitor remains in the depletion regime: no negative charges are accumulated at the interface.

3.2. *Dipolar contributions*.

The two first contributions of the dielectric susceptibility (Eq. (2)) are of dipolar type. In general, the term dipolar should be understood in a broad sense referring to the frequency range where the responses take place. They are associated to particular entities that could be permanent dipoles carried by impurities present in the structure [17,18] or traps that can be successively charged and discharged,[27] for instance. In our cases, we argue (as explain below) that the two dipolar contributions are likely to be caused by permanent dipoles, $\vec{\mu}_{SiO_2}$ and $\vec{\mu}_{Organic}$, located in the oxide and in the organic film, respectively. The origin

of these dipoles remains to be clarified but they could be due, for instance, to substitution atoms coming from the doped silicon to the oxide and adsorbed polar molecules – such as water molecules – at the organic/oxide interface, respectively. In all cases, the permanent dipoles are driven out of their equilibrium position by the electric field and oscillate under the action of $V_{ac}$ giving contributions to the polarization. These motions can be modeled in terms of damped harmonic oscillators. [17,18] With this formalism, it was shown in Ref. [17] that the characteristic frequency of each oscillator depends on the dc electric field in the following way

$$1/\tau_{SiO_2/Organic}(\omega) \propto \vec{\mu}_{SiO_2/Organic}\vec{E}_{local}\,. \qquad (3)$$

$\vec{E}_{local}$ is the electric field seen by the dipole considered. We have to include in Eq. (3) the local electric field instead of the applied field as done in Ref. [17], because the polarons may screen the applied potential. According to this equation, the behaviors of the characteristic frequencies as function of $V_{dc}$ give information about the dipole orientation and the electrostatic properties of the junctions. Moreover, the permanent dipoles are not isolated systems but instead interact with their surroundings that could be materialized by the vibration modes of the junctions, for instance. These interactions cause energy dissipation and the characteristics of the surroundings (the bath) influence the dynamical properties of the oscillators.[17,18] Roughly speaking, if the bath has the faculty to forget instantaneously the perturbations induced by the oscillators (compared to the characteristic time of observation),[28] the dielectric susceptibility will be of Debye type. On the contrary, if the bath possesses a long term memory of these perturbations, [28] the time response of the oscillators will be slow down that shows up in the dielectric susceptibility as fractional power laws. This is a Jonscher type of response [15] that could be modeled by several empirical functions.[19,29,30] In our junctions the two types of response are observed depending on the location of the oscillators.

A single dipolar contribution is seen in the admittance of the "reference" junctions. It is of Debye type

$$\chi_{SiO_2}(\omega) = A_{SiO_2}\left(1 - j\omega\tau_{SiO_2}\right)^{-1}. \quad (4)$$

$A_{SiO_2}$ is the amplitude, proportional to the density of such dipoles.[17] $\tau_{SiO_2}$ is the characteristic relaxation time of these dipoles that is found between $10^{-5}$s and $10^{-7}$s depending on cases. Two examples that differ by their characteristic relaxation time are shown: a first one in Figs. 1 with $\tau_{SiO_2} \approx 10^{-6}$ s, and a second one in Figs. 3 with $\tau_{SiO_2} \approx 10^{-5}$ s. As a remark we may notice that the loss part of the admittance, $C''$, of the two examples differ by one order of magnitude: in case of Figs. 1, as already stressed, it is close to the sensitivity limitation of our experiment what explains the wide fluctuations observed in the data. In all cases, the amplitude, $A_{SiO_2}$, and the characteristic frequency, $1/\tau_{SiO_2}$ ,do not vary with $V_{dc}$.

In the case of the organic MOS junctions, in the accumulation regime, the dielectric response of the organic thin film is strongly dominated by the one of the free carriers. As a consequence, again the bulk of the oxide only is probed and indeed, we obtain the same response (see Figs. 4a and 4b) where the two parameters of Eq. (4), $A_{SiO_2}$ and $\tau_{SiO_2}$, are potential independent with fixed values at all $V_{\mathrm{dc}}$: $A_{SiO_2} \approx 7.10^{-9}$ and $1/\tau_{SiO_2} \approx 2.10^{6}$ Hz for the example shown in Figs. 1 and 4. Surprisingly, the characteristic frequency is the same for the reference and MOS junctions. As a remark, we may notice that the same kind of response was already obtained in the past for MOS capacitors that was interpreted in terms of charging and discharging of surface states.[31] First, since the reference junctions are of metal/oxide/metal type, the response should concern different kind of impurities located deep in the bulk and then not accessible by tunneling. Furthermore, the fact that the characteristic frequency is electric field independent is not consistent with such scenario, whereas independent permanent dipoles located in the bulk of the oxide would be a good assumption if we add an hypothesis concerning their orientation in space. The data correspond to the sum of the

responses of all of them. According to Eq. (3), it then means that there is no preferential orientation for the permanent dipoles carried by these defects: they can take all accessible orientations in space with equal probability. Therefore, for some of them, the characteristic frequency will increase with the electric field, for some others, it will decrease, giving in total a field independent behavior.

As usual in MOS capacitor, the organic/oxide interface is probed when the junction is driven from accumulation to depletion regime. Decreasing progressively the voltage from accumulation, a second dipolar contribution appears at lower frequencies (see Figs. 1 from $10^2$ to $10^4$ Hz). It is of Jonscher type and well described by the Cole-Cole susceptibility

$$\chi_{Organic}(\omega) = A_{Organic}\left(1 + \left(-j\omega\tau_{Organic}\right)^{\alpha}\right)^{-1} \quad (5)$$

where $0 < \alpha < 1$.[19] The amplitude, $A_{Organic}$, the characteristic frequency, $1/\tau_{Organic}$, and $\alpha$ ($\approx$ 0.5) change slightly with $V_{dc}$. We discuss in the following only the changes of characteristic frequencies from which we are able to obtain some information. An example is given in Fig. 5. First, we remark that our data can not be produced by successive charges and discharges in traps. Indeed, in this case the electric charges should come from the organic semiconductor and this contribution is also seen in the complete depletion regime where no free carriers are present in the pentacene film. In these conditions, the dipolar contribution can not be attributed to traps but, instead, is likely due to permanent dipoles. With this assumption and at the light of Eq. (3), the variations of $1/\tau_{Organic}$ seen in Fig. 5, indicate that the projection of the corresponding permanent dipoles is directed toward the substrate. Moreover, we clearly see different behaviors between the depletion regime ($V_{dc}$ < -5 V), where the variations are linear, and the transition to the accumulation regime ($V_{dc}$ > -5 V), where non-linearities are evidenced. These changes could be explained by the modification of the electrostatic properties of the junction induced by the formation of the space charges: the local electric field of Eq. (3) is progressively screened by the free carriers accumulated in the organic film.

Notice that the figure 5 is limited to the negative values of the dc potential for simplicity because this is the region where the Cole-Cole contribution is more pronounced.

3.3. *Ionic contributions*.

The last contribution of the dielectric susceptibility (Eq. (2)) is a LFD type of contributions which is usually attributed to diffusion current of slow charges.[21] Moreover, in some heterostuctures it was shown to be related to adsorbed water layer on one of the interfaces in the inside of the structure.[21] Under ambient condition such layer is expected to be formed in our systems at the surface oxide: water molecules is known to diffuse through the organic film.[9] They would then react with the Si-OH bonds present at the surface. This layer is supposed, on the one hand, to be at the origin of the Cole-Cole contribution (Eq. (5)) as discussed above and, on the other hand, to be the source of electrochemical reactions such as the one proposed in Refs. [9,10] that could be a possible origin to the LFD as explained in details below. When hole polarons (h) – or simply hole in the case of the reference junctions - are accumulated at this interface, protons are produced according to the coupled reactions $2H_2O + 4h \rightarrow 4H^+ + O_2(g)$ and $2H^+ \rightarrow 2h + H_2(g)$. The protons $H^+$ then migrate through the oxide, probably in the $H_3O^+$ state. The diffusion of particles through amorphous systems is known to follow, in general cases, a continuous time random walk in which the ions may remain after each jump at the same position for infinitely long time.[32,23] This type of random walk can be described by the fractional diffusion equation[23,33] characterized by a parameter $\beta$ ($0 \leq \beta \leq 1$), the case $\beta = 1$ corresponding to normal diffusion considered in Refs. [9,10]. This parameter controls the dynamics of the ions and can be measured in our experiment.

Because of the diffusive intrusion of protons in the oxide the capacitance becomes a function of time, $C(t)$. The time needed for an ion to cross the oxide layer can be estimated to $10^7$ s, by taking $K_1 \approx 2.10^{-19}$ $cm^2s^{-1}$given in Ref. [10], but is certainly longer for anomalous diffusion.

As a consequence, during the time of our experiment, the protons remain very close to the interface and we may reasonably assume that the changes of capacitance are a linear function of the amount of ions inside the oxide. Taking the time derivative, we may then write (see appendix)

$$\dot{C}(t) = -A_C J_\beta(0,t). \tag{6}$$

$J_\beta$ is the anomalous diffusion current of protons taken at the interface ($x = 0$) and the constant $A_C$ takes account for the effects of the ions on the capacitance. According to Eq. (6), the dielectric susceptibility of the LFD is directly related to the admittance of the ionic anomalous diffusion, $Y_{Ion}$, which was calculated in Refs. [22,34]. In the limit of high frequencies (compared to the characteristic frequency $10^{-7}$ Hz for ion diffusion) that corresponds to our experiments, we finally obtain:

$$\chi_{Ion}(\omega) = -\frac{A_c}{j\omega} Y_{Ion}(\omega) \approx A_{Ion}(-j\omega)^{-\beta/2} \tag{7}$$

that reproduces very well our data (Figs 3 and 4). The detailed expression of the amplitude $A_{Ion}$ can be found in the appendix. For the reference junctions we get $\beta = 1$ that corresponds to normal diffusion (see Figs. 3). For the organic based junctions we find anomalous diffusion with $\beta$ between 0.2 and 0.4. In the example of Fig. 4, the Cole-Cole contribution is strong enough to spoil the characteristics of the LFD contribution that are more apparent in some other examples such as the one shown in Fig. 6.a. We find $\beta = 0.4$ in the example of Figs. 4 and $\beta = 0.3$ in the example of Fig. 6.a. Moreover, we notice that the amplitude, $A_{Ion}$, increases when $V_{dc}$ decreases in a way shown in Fig. 6.b that corresponds to the junction investigated in Figs. 1 and 4. According to Eq. (A12) of the appendix, $A_{Ion}$ is inversely proportional to the proton density at the interface. With the chemical reactions described above that explain the mechanism of proton production, this density is directly related to the density of holes accumulated at the interface – a linear relation between these two quantities is assumed in Ref. [10]. Following this assumption, $A_{Ion}$ becomes inversely proportional to the density of

holes at the interface. This is in agreements with our findings (Fig. 6.b): in the depletion regime, the hole density is very weak and $A_{Ion}$ is maximal, on the opposite, in the accumulation regime, the hole density increases implying a decrease of $A_{Ion}$. The reasons why the diffusion characteristics are different in the two types of junctions remain unclear. It may be explained by the structural characteristic of the two interfaces, Au/oxide and pentacene/oxide, that should be very different. However, we do not have clear ideas on the way a particular structural organization influences the proton diffusion.

## 4. Conclusions.

In summary, we have measured the low frequency admittance of Metal/Oxide/Organic semiconductor junctions and identified both dipolar and diffusive current contributions to the polarization. The dynamical responses of the polarizable species (dipoles or ions) are strongly influenced by their surroundings. If they are markovian (without memory) we get a Debye response for the dipoles and a normal diffusion for the ions as measured for "reference" junctions. If they are non-markovian (with memory) the responses are more complex; in their simplest forms we get a Cole-Cole response for the dipoles and a fractional diffusion for the ions. Our data show anomalous behavior in presence of organic layer. We believe these observations could be the signature of particular structural organizations which can be located either, in the organic layer itself or, in the organic/oxide interface.

*Acknowledgement*
We thank Nicolas Clement for fruitful discussion and the *Region Champagne-Ardenne* for financially supporting of PhD of Romuald Ledru. This work has been supported by the ANR under contract N°ANR-09-BLAN-0329-02 (CADISCOM).

## References.

_[1] H. Sirringhaus, *Adv. Mater*. **2009**, 21, 3859.

_[2] A.R. Brown, C.P. Jarrett, D.M. de Leeuw, and M. Matters, *Synth. Met.* **1997**, 88, 37.

_[3] J.B. Chang and V. Subramanian, *Appl. Phys. Lett.* **2006**, 88, 233513.

_[4] A. Salleo, F. Endicott, and R.A. Street, *Appl. Phys. Lett.* **2005**, 86, 263505.

_[5] M. Tello, M. Chiesa, C.M. Duffy, and H. Sirringhaus, *Adv. Funct. Mater.* **2008**, 18, 3907.

_[6] R.A. Street, M.L. Chaninyc, F. Endicott, and B. Ong, *J. Appl. Phys.* **2006**, 100, 114518.

_[7] R.A. Street, A. Salleo, and M.L. Chaninye, *Phys. Rev. B* **2003**, 68, 085316.

_[8] S.J. Zilker, C. Detcheverry, E. Cantatore, and D.M. de Leeuw, *Appl. Phys. Lett.* **2001**, 79, 1124.

_[9] A. Sharma, S.G.J. Mathijssen, M. Kemerink, D.M. de Leeuw, and P.A. Bobbert, *Appl. Phys. Lett.* **2009**, 95, 253305.

_[10] A. Sharma, S.G.J. Mathijssen, E.C.P. Smits, M. Kemerink, D.M. de Leeuw, and P.A. Bobbert, *Phys. Rev. B.* **2010**, 82, 075322.

_[11] E.H. Nicollian and A. Goetzberger, *Bell Syst. Tech. J.* **1967**, 46, 1055.

_[12] E.H. Nicollian and J.R. Brews, *MOS (Metal Oxyde Semiconductor) Physics and Technology*, Wiley, New York **1982**.

_[13] a) N. Alves and D.M. Taylor, *Appl. Phys. Lett.*. **2008**, 92, 103312; b) I. Torres and D.M. Taylor, *J. Appl. Phys.* **2005**, 98, 073710.

_[14] S. Grecu, M. Roggenbuck, A. Opitz, and W. Brütting, *Org. Elect.* **2006**, 7, 276.

_[15] A.K. Jonscher, *Nature (London)* **1977**, 267, 673.

_[16] N. Clément, S. Pleutin, D. Guérin, and D. Vuillaume, *Phys. Rev. B.* **2010**, 82, 035404.

_[17] S. Pleutin, N. Clément, D. Guérin, and D. Vuillaume, *Phys. Rev. B.* **2010**, 82, 125436.

_[18] I. Goychuk, *Phys. Rev. E.* **2007**, 76, 040102(R).

_[19] K.S. Cole and R.H. Cole, *J. Chem. Phys.* **1941**, 9, 341.

_[20] G.G. Raju, *Dielectrics in Electric Field (Marcel Dekker, New York, Basel,* **2003)**.

_[21] L.A. Dissado and R.M. Hill, *J. Chem. Soc. Faraday Trans. 2* **1984**, 80, 291.

_[22] J. Bisquert and A. Compte, *J. Electroanal. Chem.* **2001**, 499, 112.

_[23] a) R. Metzler and J. Klafter, *Phys. Rep.* **2000**, 339, 1; b) J. Klafter and I.M. Sokolov, *Physics World* **2005**, 18, 29.

_[24] N. Tessler, Y. Preezant, N. Rappaport, and Y. Roichman, *Adv. Mater.* **2009**, 21, 2741.

_[25] S. Coropceanu, J. Cornil, D.A. da Silva Filho, Y. Olivier, R. Silbey, and J.L. Bredas, *Chem. Rev.* **2007**, 107, 926.

_[26] C.H. Kim, O. Yaghmazadeh, D. Tondelier, Y.B. Jeong, Y. Bonnassieux, and G. Horowitz, *J. Appl. Phys.* **2011**, 109, 083710.

_[27] P.P. Boix, G. Garcia-Belmonte, U. Munecas, M. Neophytou, C. Waldauf, and R. Pacios, *Appl. Phys. Lett.* **2009**, 95, 233302; T. Walter, R. Herberholz, C. Müller, and H.W. Schock, *J. Appl. Phys.* **1996**, 80, 4411.

_[28] U. Weiss, *Quantum Dissipative Systems,* 3rd ed. *(World Scientific, Singapor,* **2008)**.

_[29] D.W. Davidson and R.H. Cole, *J. Chem. Phys.* **1951**, 19, 1484.

_[30] S. Havriliak and S. Negami, *Polymer* **1967**, 8, 161.

_[31] M.J. Uren, S. Collins, and M.J. Kirton, *Appl. Phys. Lett.* **1989**, 54, 1448.

_[32] H. Scher and E.W. Montroll, *Phys. Rev.B* **1975**, 12, 2455.

_[33] A. Compte, *Phys. Rev. E* **1996**, 53, 4191.

_[34] J. Bisquert, G. Garcia-Belmonte, F. Fabregat-Santiago, and P.R. Bueno, *J. Electroanal. Chem.* **1999**, 475, 152.

_[35] D. H. Zanette, *Physica A.* **1998**, 252, 159.

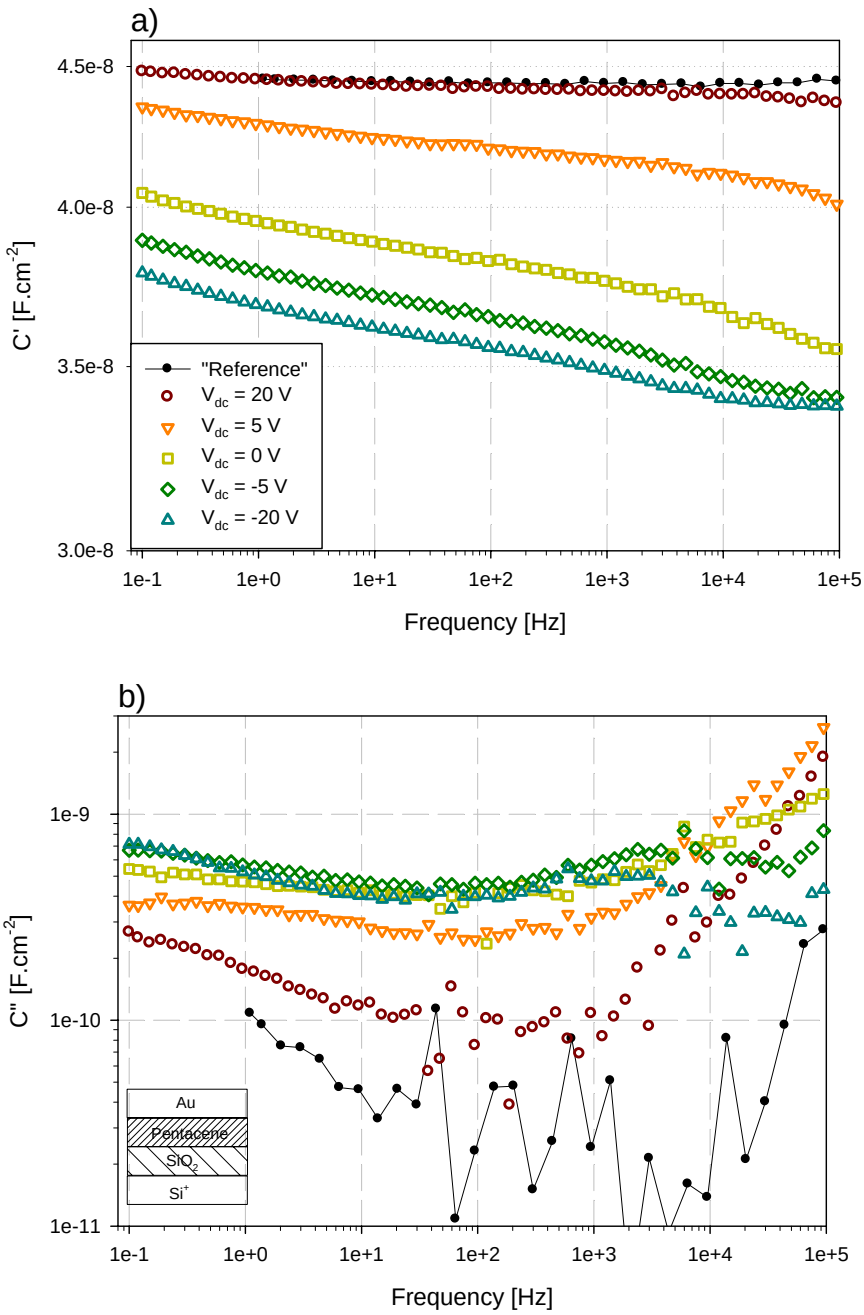


***Figure 1.*** *Typical capacitance, a) real part, C′, and b) imaginary part, C″, for $V_{dc}$=20 V to -20 V. Results for the reference junction at $V_{dc}$ = 0V are also shown (dots). Insert of b): Schematic of the layer structure of the junctions.*

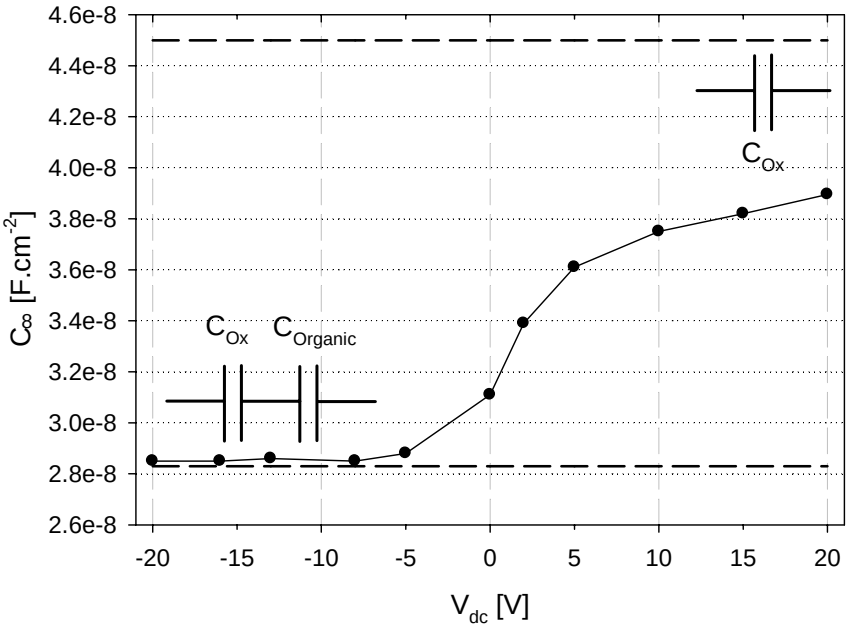


***Figure 2.*** *Infinite frequency capacitance, $C_\infty$, extracted from the results shown in Fig. 1 following the fitting procedure described in the text, as function of $V_{dc}$. The two limiting values are also shown. The upper limit is the capacitance in the full accumulation regime that corresponds to the infinite capacitance of the corresponding reference junction, $C_{Ox}$. The lower limit is the capacitance in the full depletion regime given by the capacitance of a 40 nm layer of pentacene (with $\varepsilon = 3.5$), $C_{Organic}$, and $C_{Ox}$ in series.*

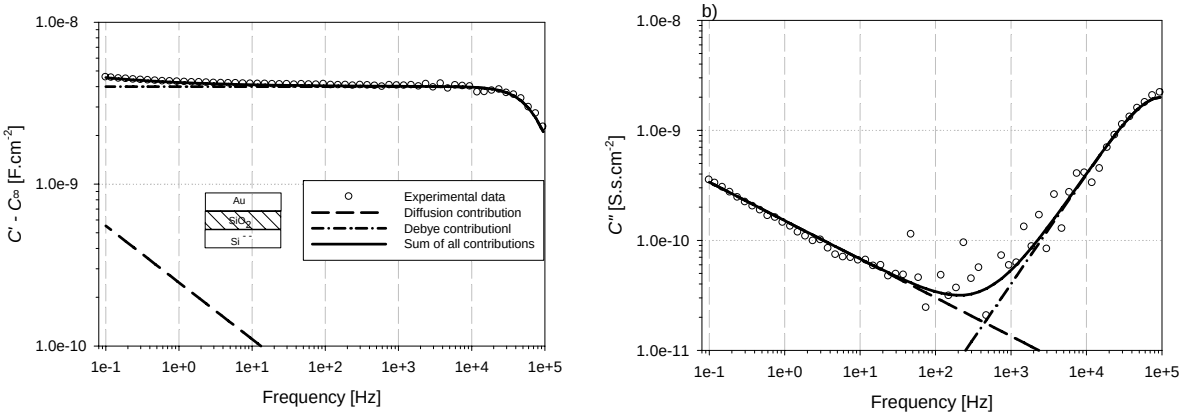


***Figure 3.*** *Typical capacitance of a "Reference" $Si^+/SiO_2/Au$ a) real part, b) imaginary part at $V_{dc}=0$ V. The experimental data are fitted with two contributions: a Debye contribution for $SiO_2$ defects (Eq. (3)) and a LFD contribution for ion diffusion in the oxide (Eq. (6)). The fitting parameters are $A_{SiO_2}=4.10^{-9}$, $\tau_{SiO_2}=10^5$s, $A_{Ion}=5.5\ 10^{-10}$ and $\beta=1$.*

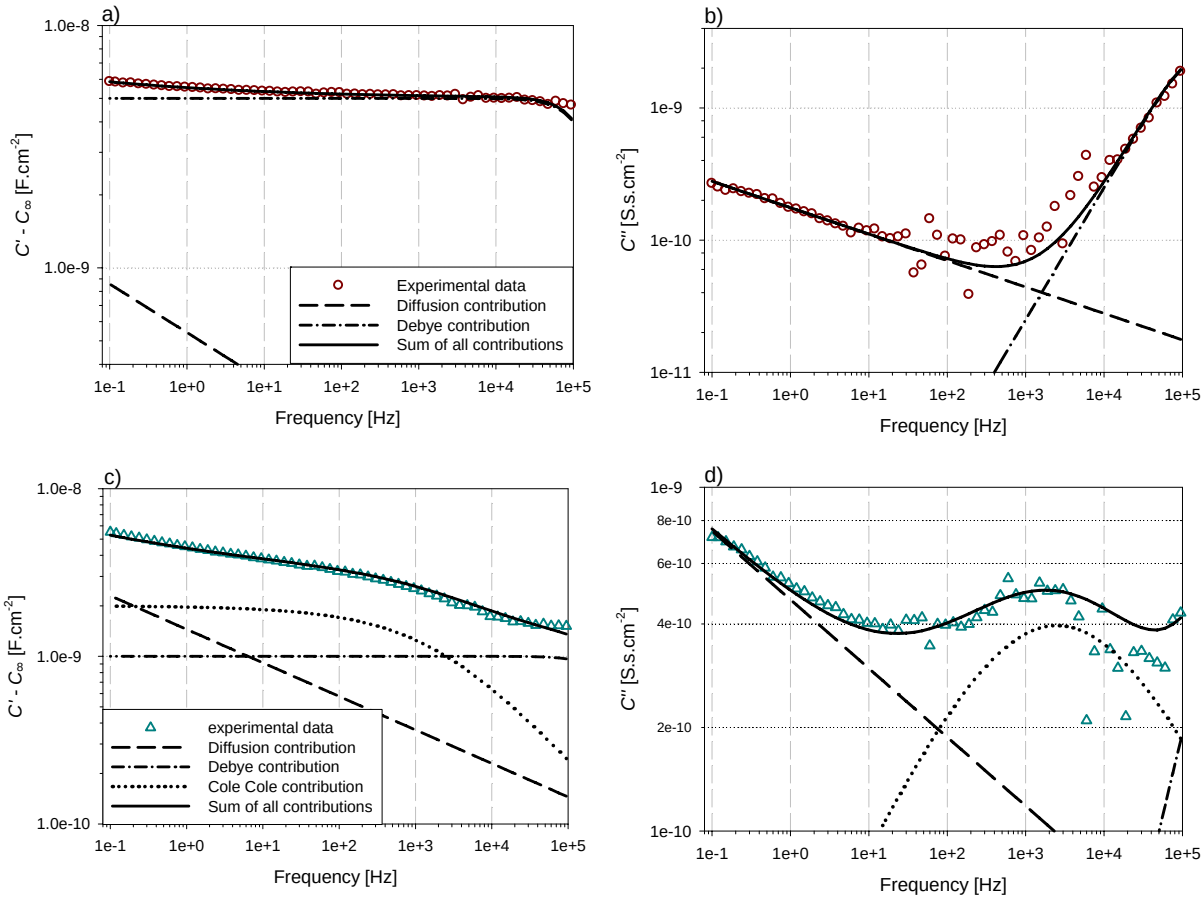


***Figure 4.*** *Focus on two particular examples of Fig. 1 at $V_{dc}$=+20 V a) real part, b) imaginary part, and at $V_{dc}$=-20 V c) real part, d) imaginary part. The experimental data are fitted with two or three contributions: a Debye contribution for $SiO_2$ defects (Eq. 3) - doted-dashed lines, a Cole-Cole contribution for organic defects (Eq. 4) – doted lines, and a LFD contribution for ions at the $SiO_2$/pentacene interface (Eq. 6) – doted line. The values of the parameters are discussed in the text.*

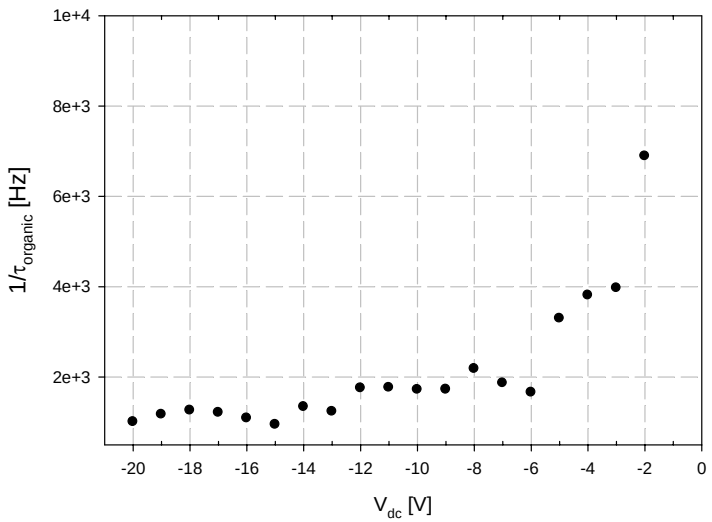


***Figure 5.*** *$1/\tau_{organic}$ as function of $V_{dc}$: a change of behavior may be noticed between the depletion regime ($V_{dc}$ < -5 V) and the transition to the accumulation regime ($V_{dc}$ > -5 V).*

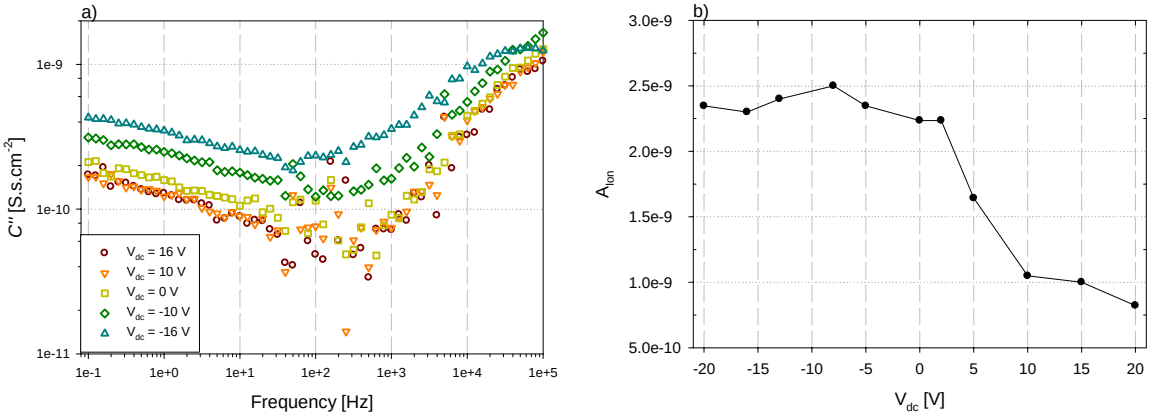


***Figure 6.*** *a) C″ for a junction with a weak Cole-Cole contribution showing more clearly the LFD contribution at all $V_{dc}$: Some examples are shown from the accumulation to the depletion regime. The $\beta$ parameter is bias independent - in this case $\beta = 0.3$, and the amplitude of the ionic contribution increases when $V_{dc}$ decreases. b). Amplitude of the ionic contribution, $A_{Ion}$, as function of $V_{dc}$ for the example shown in Figs. 1 and 4.*

**Appendix: Model for the anomalous Low Frequency Dispersion (LFD).**

We note $p(x,t)$ the time dependant volume density of protons in the oxide at distance $x$ from the organic/oxide interface. The thickness of the oxide layer is $L \approx 70$nm. As it is usual for amorphous systems, the protons are assumed to follow a continuous time random walk through the oxide.[31,23] It means that after each jump the protons may remain at the same position for infinitely long time. In practice this could happen in deep traps. This type of random walk can be described by the fractional diffusion equation [33]

$$\frac{\partial p(x,t)}{\partial t} = {}_0D_t^{1-\beta} K_\beta \frac{\partial^2 p(x,t)}{\partial x^2} = \frac{K_\beta}{\Gamma(\beta)} \frac{\partial}{\partial t} \int_0^t dt' \frac{1}{(t-t')^{1-\beta}} \frac{\partial^2 p(x,t')}{\partial x^2}. \quad \text{(A1)}$$

${}_0D_t^{1-\beta}$ is the fractional Riemann-Liouville operator with definition given by the second equality of Eq. (A1), $\beta$ is a constant such that $0 \leq \beta \leq 1$, $\Gamma$ is the Gamma function and $K_\beta$ generalizes the diffusion coefficient with dimension $cm^2.s^{-\beta}$. The case $\beta = 1$ corresponds to normal diffusion. This density should also fulfill the charge conservation equation

$$\frac{\partial p(x,t)}{\partial t} = -\frac{\partial J_\beta(x,t)}{\partial x}. \quad \text{(A2)}$$

$J_\beta$ is the anomalous diffusion current of protons that may be written as [35]

$$J_\beta(x,t) = -q \frac{K_\beta}{\Gamma(\beta)} \frac{\partial}{\partial x} \left[ t^{\beta-1} p(x,0) + \int_0^t dt' p(x,t') (t-t')^{\beta-1} \right]. \quad \text{(A3)}$$

$q$ is the electric charge of the diffusing ions. On the contrary to normal diffusion ($\beta$=1), the current is non-local in time: at each time it depends on the previous history. Moreover, the first term of Eq. (A3) shows that the initial condition contributes at all times.

Because the protons diffuse through the oxide, the capacitance of our junction becomes time dependant, $C(t)$. The proton diffusion is very slow: it takes about $10^7$ s for an ion to cross the oxide so that during the time of our experiments, they all remain close to the organic/oxide interface.[10] We therefore suppose

$$C(t) = C(0) - A_C \int_0^L dx\, p(x,t). \quad \text{(A4)}$$

The ions modify the capacitance by Coulomb interaction but since the ions are all approximately at the same distance from the interface the complicated space dependence due to these interactions may be reduced to a single constant $A_C$. Taking the time derivative of Eq. (A4) and with the help of the charge conservation equation (Eq. (A2)) we obtain

$$\dot{C}(t) = -A_C J_\beta(0,t). \tag{A5}$$

The dot is for the time derivative. We have considered that $J_\beta(L,t) = 0$ since all the ions remain near $x = 0$.

The ions continuously diffuse through the oxide. Applying in addition a small ac potential introduces a perturbation to the main contribution. We write

$$p(x,t) = p_0(x,t) + p_1(x,t). \tag{A6}$$

$p_0$ is the dc component, $p_1$ the ac perturbation. In the same way we can decompose the surface potential at the organic/oxide interface

$$\psi(t) = \psi_0(t) + \psi_1(t). \tag{A7}$$

To determine the admittance associated to the ion displacement we need to consider only the ac components; $p_0(x,t)$ and $\Psi_0(t)$ may indeed be considered as time independent in the time spend to do the experiments. Taking the Laplace transform of Eq. (A5) yields

$$\chi_{Ion}(s) = -\frac{A_C}{s} Y_{Ion}(s) \tag{A8}$$

where the admittance of the ionic current is defined as

$$Y_{Ion}(s) = \frac{\tilde{J}_\beta(0,s)}{\tilde{\psi}_1(s)}. \tag{A9}$$

$\tilde{J}_\beta(0,s)$ and $\tilde{\psi}_1$ are the Laplace transforms of the diffusion current, $J_\beta$, at $x = 0$ and of $\Psi_1$, respectively. Eq. (A9) was solved in Ref. [22] assuming a linear relation between $p_1(x,t)$ at the interface and $\psi_1(t)$. With ideal conditions for the electrochemical reaction it may be written[34]

$$\psi_1(t) = \frac{k_B T}{p_0(0,0)} p_1(0,t). \tag{A10}$$

$T$ is the temperature and $k_B$ the Boltzmann constant. Different boundary conditions at the other interface were considered by the authors of Ref. [22] but, it is important to stress that at

the frequencies we consider in this work they do not play any role. We quote their solution for absorbing boundary conditions, $p_1(L,t)=0$. In terms of frequency instead of Laplace coordinate we finally get

$$\chi_{Ion}(\omega) = -\frac{A_c}{j\omega} Y_{Ion}(\omega) = \frac{q k_B T K_\beta}{L} \frac{\omega_d^{1-\beta}}{p_0(0,0)} \left( \frac{-j\omega}{\omega_d} \right)^{-\beta/2} \frac{1}{\tanh\left( (-j\omega/\omega_d)^{\beta/2} \right)}, \tag{A11}$$

with $\omega_d = \left( K_\beta / L^2 \right)^{1/\beta}$. At high frequencies, $\omega/\omega_d \to +\infty$, this equation gives

$$\chi_{Ion}(\omega) \approx q \frac{k_B T K_\beta}{L} \frac{\omega_d^{1-\beta}}{p_0(0,0)} \left( \frac{-j\omega}{\omega_d} \right)^{-\beta/2} = A_{Ion} (-j\omega)^{-\beta/2} \tag{A12}$$

that corresponds to Eq. (7) of the main text. It would be the same with open boundary conditions, for instance.

ADVANCED FUNCTIONAL MATERIALS
www.afm-journal.de



# An Organic Nanoparticle Transistor Behaving as a Biological Spiking Synapse

By *Fabien Alibart, Stéphane Pleutin, David Guérin, Christophe Novembre, Stéphane Lenfant, Kamal Lmimouni, Christian Gamrat,* and *Dominique Vuillaume**

**Molecule-based devices are envisioned to complement silicon devices by providing new functions or by implementing existing functions at a simpler process level and lower cost, by virtue of their self-organization capabilities. Moreover, they are not bound to von Neuman architecture and this feature may open the way to other architectural paradigms. Neuromorphic electronics is one of them. Here, a device made of molecules and nanoparticles—a nanoparticle organic memory field-effect transistor (NOMFET)—that exhibits the main behavior of a biological spiking synapse is demonstrated. Facilitating and depressing synaptic behaviors can be reproduced by the NOMFET and can be programmed. The synaptic plasticity for real-time computing is evidenced and described by a simple model. These results open the way to rate-coding utilization of the NOMFET in dynamical neuromorphic computing circuits.**

## 1. Introduction

It is now well recognized that electronic circuits based on the von Neuman paradigm are unable to catch the behavior of the complex, real-world environment, as can biological neural systems (e.g., the human brain). One of the reasons is the so-called ''von Neuman bottleneck''[1] due to the physical separation of computing units and memories. In the brain, memory and computation are mixed together and allow the processing of information both in time and space via the time-dependent properties of interconnected neurons.[1,2] This challenge for the development of a new generation of computers has induced a lot of effort in neuroscience computation activities and the framework for the spatiotemporal processing of information seems to be theoretically achievable.[2] One key element that is still a limitation concerns the integration of neurons and synaptic connections in order to realize a brain-like computer. Even though silicon CMOS (complementary metal-oxide-semiconductor) chips have been designed and fabricated to emulate the brain behaviors,[3,4] this approach is limited to small systems because it takes several (at least seven) silicon transistors to build an electronic synapse.[5] As the human brain contain more synapses than neurons (by a factor of approximately $10^7$), it is essential to develop a nanoscale, low power, synapse-like device if we want to scale neuromorphic circuits towards the level of the human brain. This feature has recently prompted the research for nanoscale synaptic devices. Proposals for such programmable memory devices include optically-gated carbon-nanotube field-effect transistors (OGCNTFETs),[6,7] organic/hybrid Si nanowire transistors,[8] and memristors.[9–12]

Here, we show that mixing nanoparticles (NPs) and molecules to implement computation and memory in a single synapse-like device is a powerful approach towards such objectives. NPs and molecules are nanosize objects suitable for nanodevice fabrication; they can be manipulated and assembled by low-cost, bottom-up, techniques (e.g., self-assembly),[13,14] and are prone to work on flexible, plastic substrates (as shown by the tremendous efforts expended on plastic, printable, organic electronics).[15–17]

The nanoparticle organic memory field-effect transistor (NOMFET) demonstrated here can be programmed to work as a facilitating or depressing synapse; it exhibits short-term plasticity (STP) for dynamical processing of spikes. This behavior is obtained by virtue of the combination of two properties of the NOMFET: the transconductance gain of the transistor and the memory effect due to charges stored in the NPs. The NPs are used as nanoscale capacitors to store the electrical charges and they are embedded into an organic semiconductor (pentacene). Thus, as detailed in Section 4, the transconductance of the transistor can be dynamically tuned by the amount of charge in the NPs. We previously demonstrated that this type of device works as a memory[18] but with a ''leaky'' behavior. The retention times are in the range of a few seconds to a few thousands of seconds. This

[*] Dr. F. Alibart, Dr. S. Pleutin, Dr. D. Guérin, Dr. S. Lenfant, Dr. K. Lmimouni, Dr. D. Vuillaume
Molecular Nanostructures and Devices group
Institute for Electronics Microelectronics and Nanotechnology (IEMN)
CNRS, University of Lille
BP60069, avenue Poincaré, F-59652 cedex, Villeneuve d'Ascq (France)
E-mail: dominique.vuillaume@iemn.univ-lille1.fr
Dr. C. Novembre, Dr. C. Gamrat
CEA, LIST/LCE (Advanced Computer technologies and Architectures)
Bat. 528, F-91191, Gif-sur-Yvette (France)

**DOI: 10.1002/adfm.200901335**





**Final page numbers not assigned**

behavior is used here to implement the synaptic weight $w_{ij}$ with a possible dynamic working in this time range, a necessary condition to obtain the training/learning capabilities of a spiking neural network.[19] A transistor is basically a multiplier, it is used to realize the basic function of the synapse described as $S_j = w_{ij}\ S_i$, where $S_i$ and $S_j$ are the pre- and post-synaptic signals (here the source/drain current and voltage of the NOMFET). The synaptic weight $w_{ij}$ is a time-dependent parameter whose value depends on the activity of the pre- and post-synapse neurons. We demonstrate that we can tailor the dynamic behavior of the NOMFET in the frequency/time domain (0.01–10 Hz) by adjusting the size of both the NPs (5–20 nm in diameter) and the size of the NOMFET (channel length $L$ from 200 nm to 20 μm). We also demonstrate that models developed to explain and simulate the plasticity of biological synapses can be successfully adapted to the NOMFET behavior. These results open the way to the rate-coding utilization[20] of the NOMFET in neuromorphic computing circuits.[21]

## 2. NOMFET—Materials and Fabrication

The NOMFET (Fig. 1) consists of a bottom-gate, bottom source–drain contacts organic transistor configuration. We immobilized the gold NPs (20, 10 and 5 nm in diameter) into the source–drain channel using surface chemistry (self-assembled monolayers or SAM). They were subsequently covered by a thin film (35 nm thick) of pentacene (see the Experimental Section). This device gathers the behavior of a transistor and a memory.[18] We selected several sizes for the NPs and channel lengths of the NOMFET (200 nm to 20 μm) to study their impact on the synaptic behavior of the NOMFET. We also studied the dependence of this behavior as a function of the NP density. Figure 1 shows scanning electron microscopy (SEM) images of NP arrays with NP densities ranging from approximately $10^{10}$ cm$^{-2}$ to a quasi-continuous 2D film. The density of the NP network is controlled by the density of NPs in solution and the duration of the reaction (see the Experimental Section). The optimum NP density to observe the synaptic behavior reported here is between $10^{11}$ and $10^{12}$ cm$^{-2}$, as shown in Figure 1b–d for the 5, 10 and 20 nm NPs, respectively. A density that is too low, $<10^{11}$ NP cm$^{-2}$, (Fig. 1a) leads to the memory and synaptic behaviors of the NOMFET being too weak. At high density, $>10^{12}$ NP cm$^{-2}$, (above the percolation threshold, such as in Fig. 1e), the device does not exhibit a transistor behavior due to metallic shorts between source and drain, and screening of the gate voltage by the metallic film of NPs.

In the following, we focus on devices with a NP density of around $10^{11}$ cm$^{-2}$. In all cases (Fig. 1b–d), we obtained a rather uniform distribution of NPs (no NP aggregation) with a density of approximately $10^{11}$ NP cm$^{-2}$. Even though we optimized the process (see the Experimental Section) to got a reproducibility (i.e., a density of about $10^{11}$ NP cm$^{-2}$ without aggregation) of nearly 100% in the case of the 10 and 20 nm NPs (tested on three different fabrication runs), we observed in a few cases the formation of some aggregates (see the Supporting Information, Fig. S3). A reproducibility of only 50% is obtained for the 5 nm NPs, mainly due the lack of reproducibility in forming the thiol-terminated self-assembled monolayer (SAM) on the gate oxide (see the Experimental Section). It is noteworthy that we always observed synaptic behavior in the NOMFET, even when the arrays of NPs seem under less control (see Section 4). This feature means that the synaptic behavior of the NOMFET is very robust and defect tolerant, and this can be viewed as an important advantage for the envisioned applications in neuronal computing at the nanoscale.

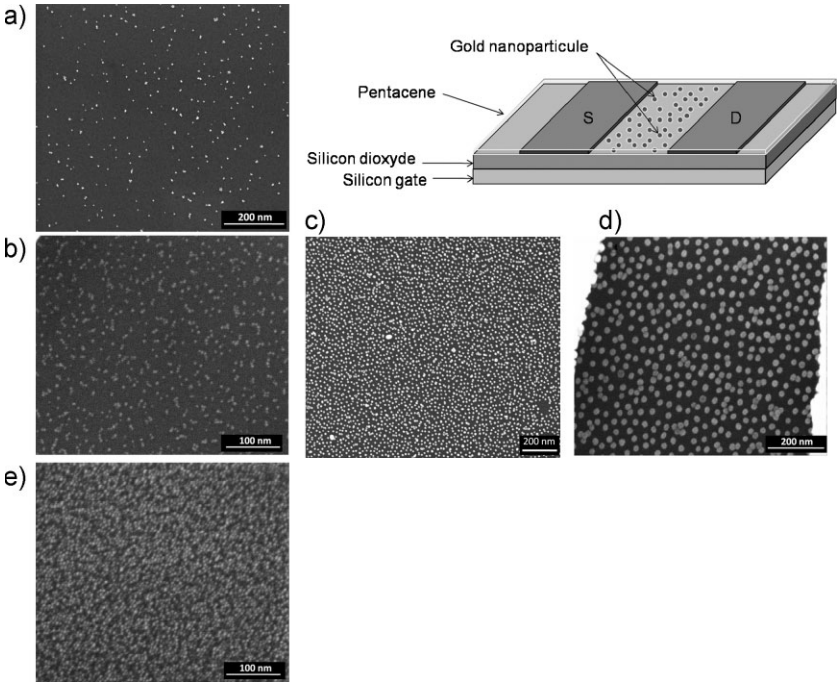


**Figure 1.** Scanning electron microscope image of the NP arrays before the pentacene deposition. a) 5 nm NP with a low density of $4.4 \times 10^{10}$ NP cm$^{-2}$, b–d) 5, 10 and 20 nm NP with a medium densities of $3.7 \times 10^{11}$, $1.8 \times 10^{11}$ and $0.9 \times 10^{11}$ NP cm$^{-2}$, respectively, e) 5 nm NP with a high density $>10^{12}$ NP cm$^{-2}$ showing a quasi 2D film with a strong percolation.

We checked, by tapping-mode atomic force microscopy (TM-AFM), the morphology of the pentacene layer deposited over the NP networks. Figure 2 shows the pentacene morphology for the reference sample (no NPs) and for the 10 nm NP NOMFET. The film without NPs shows the usual polycrystalline structure of pentacene film with large grain size and terraces, each terrace corresponding to a monolayer of pentacene molecules.[22] The pentacene film is more disordered in the presence of the NPs with a smaller grain size, and the terraces are more difficult to see. This result may be due to both the presence of NPs that hinders the surface diffusion of pentacene molecules during the deposition, and the presence of the organic SAM used to anchor the NPs on the surface. A smaller grain size has been often observed for organic field-effect transistors (OFETs) with a gate dielectric functionalized by a SAM.[23] This more-disordered pentacene film explains the decrease in the output drain current $I_D$ and hole mobility $\mu_h$

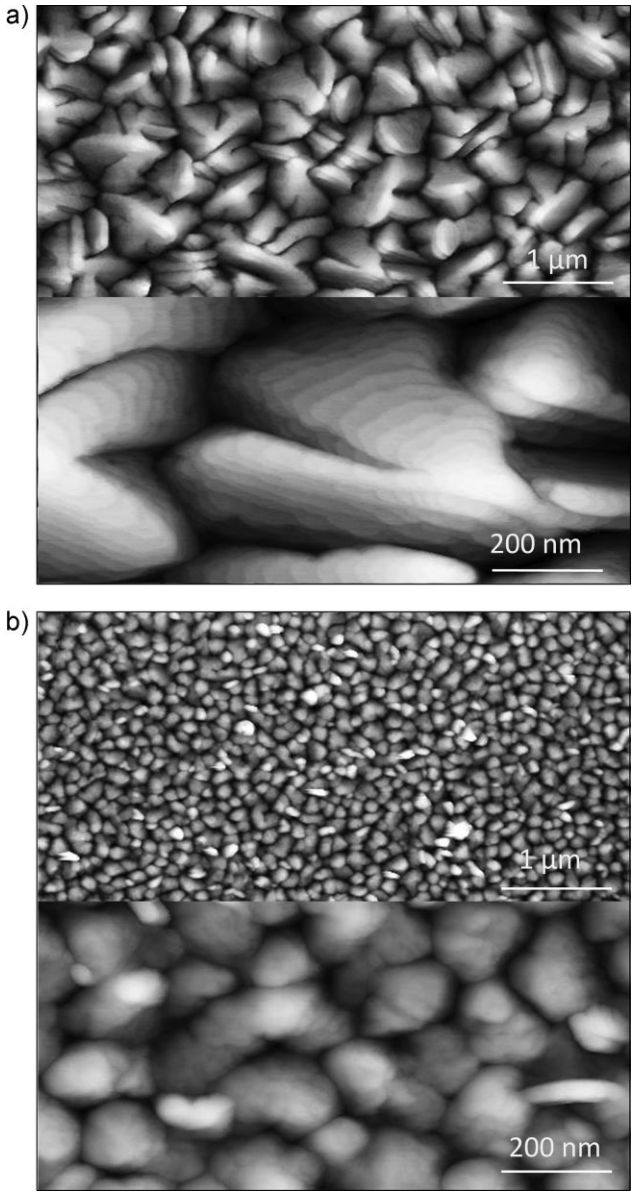


**Figure 2.** TM-AFM images of the 35 nm thick pentacene films at two magnifications: a) without the NPs and b) with an array of 10 nm NPs at a density of around $10^{11}$ NP $cm^{-2}$, as in Figure 1b.

measured for the NOMFET (approximately $10^{-3}$ $cm^2$ $V^{-1}$ $s^{-1}$) compared to the reference device (approximately 0.1 $cm^2$ $V^{-1}$ $s^{-1}$), as shown in Table 1. These values are averaged over 6–8 devices, and we notice that the presence of NPs induces a larger dispersion of the FET parameters. The error bars given in Table 1 are the standard deviation of a normal distribution fitted on the data; however, we did not observe a specific trend as function of the NP size.

## 3. Basic Behavior of a Biological Synapse

For the sake of clarity and comparison with the NOMFET, let us start with a brief description of how a biological synapse works. The most important feature of a synapse is its ability to transmit, in a given way, an action potential (AP) from one pre-synapse neuron N1, to a post-synapse neuron N2. When a sequence of APs is sent by N1 to N2, the synaptic behavior determines the way the information is treated. The synapse transforms a spike arriving from the presynaptic neuron into a chemical discharge of neurotransmitters (NTs) detected by the post-synaptic neuron and transformed into a new spike. Markram and Tsodyks[24,25] have proposed a phenomenological model to describe the synapse behavior. The synapse possesses a finite amount, $U$, of resources: the chemical neurotransmitters. Each spike activates a fraction $aU$ ($a < 1$) of these resources and the amplitude $I$ of the transmitted spike is a function of this fraction. The fraction of neurotransmitters spent to transmit the information is then recovered with a characteristic time $\tau_{rec}$ (typically in the range of a second). The response of a synapse to a train of pulses depends on the time interval between successive pulses that determines the amount of available NTs. Depending on the nature of the synapse, the response to a constant frequency train of pulses can be either depressing or facilitating (cf. Fig. 3a). Moreover, the biological synapse can process dynamical information when the frequency of the train of pulses is changed (Fig. 3b). In the case of a purely depressive synapse, a depressing behavior is obtained for a "high" frequency train of pulses (i.e., a decrease of the NTs available due to the low recovery between each spike separated by a time interval $< \tau_{rec}$), while the response of the synapse increases (facilitating behavior) at a lower frequency (the NTs get enough time to recover completely). This property has been extensively studied in biological synapses and is referred to as short-term plasticity (STP).[20,25] This simple behavior gives the synapse the main property that is necessary[2] for dynamical processing of information.

Varela et al. developed a simple iterative model[26] to simulate the STP of biological synapses. Based on the work of Magleby et al.,[27] they describe the amplitude $I$ of a given spike in the post-synapse neuron by:

$$I = \tilde{I} F_1 \ldots F_n D_1 \ldots D_m \quad (1)$$

Where the $F$ and $D$ terms are attributed to different facilitating or depressing mechanisms with specific time constants. Thus, the

**Table 1.** Main transistor parameters of the NOMFET with different NP size and of the reference device (no NP). All measurements for a channel length $L = 5$ µm NOMFET. Average values and error bars correspond to the mean and standard deviation of a normal distribution fitted to the experimental data. The threshold voltage shift is the difference between the threshold voltages after and before charging the NP by a negative pulse voltage applied on the gate (−50 V for 30 s). Note that the small value measured for the reference device is known and due to traps in the pentacene or at the $SiO_2$/pentacene interface (see Ref. [18] and references therein).

| | Average $I_D$ [A] | Average mobility [$cm^2$ $V^{-1}$ $s^{-1}$] | $V_t$ shift [V] |
|---|---|---|---|
| Reference | $1.8 \times 10^{-4}$ ($\pm$ $8.5 \times 10^{-5}$) | 0.13 ($\pm$ 0.05) | 1.1 ($\pm$ 0.4) |
| 5 nm NP | $2.3 \times 10^{-6}$ ($\pm$ $1.6 \times 10^{-5}$) | $2 \times 10^{-3}$ ($\pm$ $2 \times 10^{-3}$) | 7.5 ($\pm$ 1.4) |
| 10 nm NP | $4.1 \times 10^{-7}$ ($\pm$ $7.5 \times 10^{-7}$) | $7.6 \times 10^{-4}$ ($\pm$ $7.9 \times 10^{-4}$) | 9.4 ($\pm$ 0.9) |
| 20 nm NP | $3.3 \times 10^{-7}$ ($\pm$ $2.8 \times 10^{-7}$) | $2.0 \times 10^{-3}$ ($\pm$ $2.9 \times 10^{-3}$) | 12.8 ($\pm$ 1.8) |

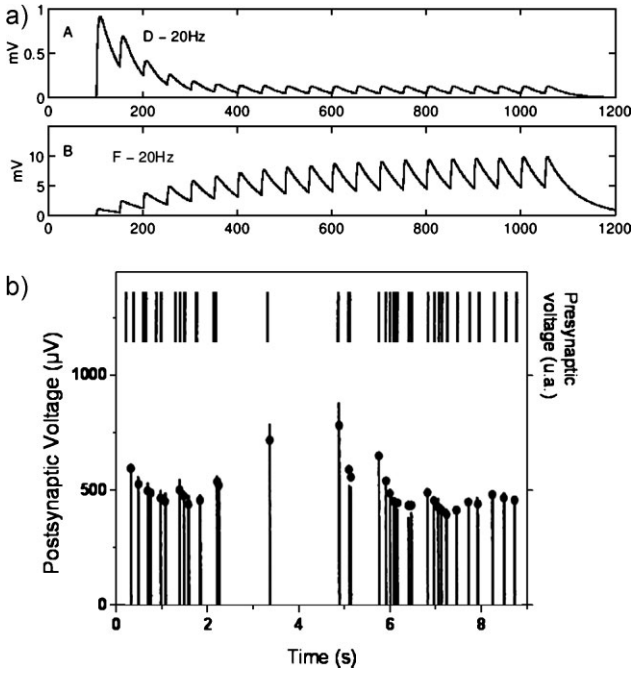


**Figure 3.** a) Simulation of post-synaptic potential for a depressing (top) and a facilitating (bottom) synapse submitted to the same pre-synaptic pulse train at 20 Hz (adapted from Ref. [24]). b) Comparison between the frequency-dependent post-synaptic potential response of a depressing synapse (lines) and the iterative model of Varela et al. (dots), adapted from Ref. [26], as a function of frequency of the pre-synaptic input signal.

output of the simplest depressing synapse follows $I = \tilde{I}D$, where only one depressive term is considered (this expression is also used by Abbott et al.[20]). $\tilde{I}$ is the intrinsic spike intensity delivered by the synapse (i.e., the intensity of the first spike after a long period of rest) and $D$ is a dynamical factor representing the depression ($0 < D < 1$). The response of a synapse to a train of pulses at variable frequency is calculated by an iterative model: at each pulse arriving to the input, the output is calculated by combining the depression factor $D$ and the amount of NTs recovered (with a time constant $\tau_{rec}$) between two successive pulses. This quantitative model has shown a good agreement with biological synapse behavior. Figure 3b shows the comparison between the biological synapse response and the iterative model of Varela et al. with one facilitating and two depressing contributions (from Ref. [26]). We now demonstrate how the NOMFET can mimic these typical synapse behaviors.

## 4. NOMFET-Device Behavior Results and Synapse Analogy

We first express the NOMFET output current taking into account the effect of the charged NPs. The pentacene being a p-type semiconductor, the NOMFET is active for negative gate voltage only. Such voltage has two effects: i) As for standard transistors, it creates holes in the pentacene thin film at the interface with the insulator; and, ii) It charges positively the gold particles via the organic material. Adapting the percolation theory of Vissenberg and Matters[28] for organic thin-film transistors, the drain/source current of the NOMFET is expressed as (see the Supporting Information):

$$I_{DS} = GV_{DS} \quad with \quad G = A_0 e^{\beta\varepsilon_F} e^{-\beta\Delta} \tag{2}$$

Where $G$ is the channel conductance, $\beta = 1/k_B\Theta$, $\Theta$ the temperature, $A_0$ a temperature-dependent parameter, $\varepsilon_F$ the Fermi energy fixed by the gate voltage and $\Delta$ the shift of the Fermi energy induced by the charged NPs. The last term is caused by the repulsive electrostatic interaction between the holes trapped in the NPs and the ones in the pentacene. The effect of the positively charged NPs is to reduce the current. As an analogy with the biological synapses, the holes play the role of the neurotransmitters. They modify the output signal, $I_{DS}$, in a way that depends on the numbers of trapped charges via the $\Delta$ term: the more charges stored in the NPs, the more the current is reduced. Note that with electrons trapped in the NPs, the result is the opposite: the charges then increase the Fermi energy and the current. These behaviors correspond to our experimental observations, as reported elsewhere.[18] Charging NPs with holes by applying a negative voltage pulse on the gate induces a negative threshold voltage shift as measured on the drain current–gate voltage ($I_D$–$V_G$) curves of the NOMFET, and (at fixed $V_D$ and $V_G$), a decrease in the current. A positive gate voltage pulse shifts the NOMFET characteristics backward.[18] From these threshold voltage shifts (Table 1) and for the optimized NOMFET with a NP density of around $10^{11}\,cm^{-2}$ (such as those shown in Fig. 1b–d), we estimated the number of charge per NP (for a gate voltage pulse of $-50$ V during 30 s, measured on a 5 μm channel length NOMFET at $V_D = -30$ V). They are typically approximately 2, 6 and 15 holes per NP for the 5, 10 and 20 nm NP NOMFETs, respectively.

Using these properties, we can mimic the different behaviors of the biological synapses by initially charging the NPs with holes (negative gate voltage) or discharging the NPs (positive gate voltage) depending whether we want a depressing or a facilitating behavior, respectively, before measuring the response of the NOMFET to a train of spikes. The input signal is the drain–source voltage, the output is the drain/source current (the transistor is used in a pass-transistor configuration, source and drain are reversible). The gate has two functions. In a first phase (see a chronogram of the signals in the Supporting Information, Fig. S2), we used it to program the NOMFET by applying a gate voltage pulse $V_P$ while source and drain were grounded, and during the working phase, we applied a dc voltage $V_G$ to maintain the transistor in its "on" regime while an input spiking voltage (between $V_{D1}$ and $V_{D2}$) was applied on the drain. Figure 4a and b demonstrate that the facilitating and depressing behaviors are obtained on the same NOMFET, for rigorously the same application of pulses at the input, by initially programming the device with the gate signal $V_P$. For the depressing case (Fig. 4a), we applied $V_P > 0$ before running the device, while for the facilitating case $V_P < 0$ (Fig. 4b). In a biological synapse, the facilitating behavior means that an incoming signal with a given frequency and duty cycle induces a post-synaptic signal having an increasing trend, whereas in the case of a depressing synapse, the post-synaptic signal tends to decrease, as shown in Fig. 3a. We demonstrated in Figure 4 exactly the same behavior for the NOMFET, where the programming

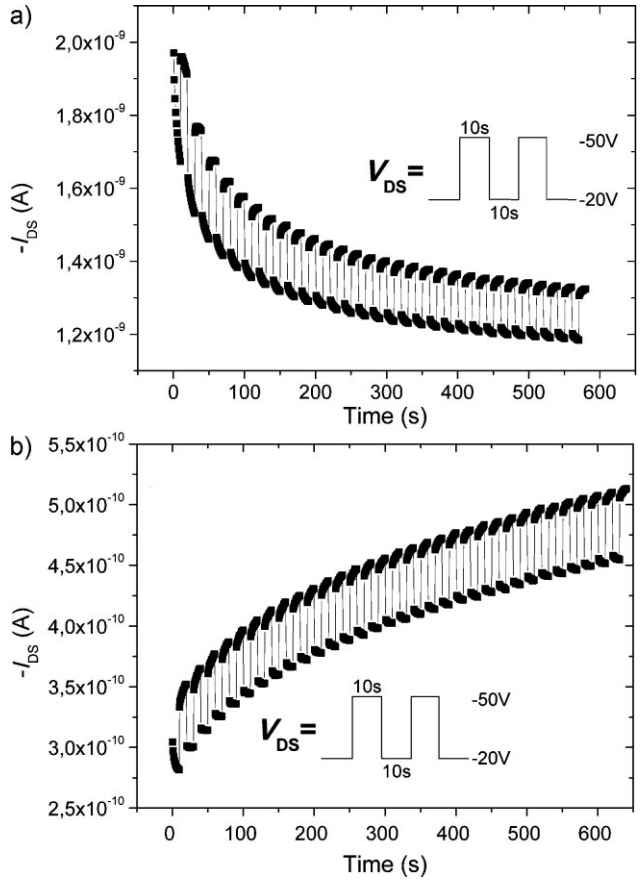


**Figure 4.** a) Response (drain current) of the NOMFET (5 nm NP, $L/W = 12\,\mu m/113\,\mu m$) to a constant frequency (0.05 Hz) train of pulses ($V_{D1} = -20$ V, $V_{D2} = -50$ V) after programming the device by a $V_P = 50$ V (40 s) gate pulse to discharge the NPs. The decreasing trend of the output current (in absolute value) mimics a depressing biological synapse. b) Response (drain current) of the NOMFET (5 nm NP, $L/W = 12\,\mu m/113\,\mu m$) to a constant frequency (0.05 Hz) train of pulses ($V_{D1} = -20$ V, $V_{D2} = -50$ V) after programming the device by a $V_P = -50$ V (40 s) gate pulse to charge the NPs. The increasing trend of the output current (in absolute value) mimics a facilitating biological synapse.

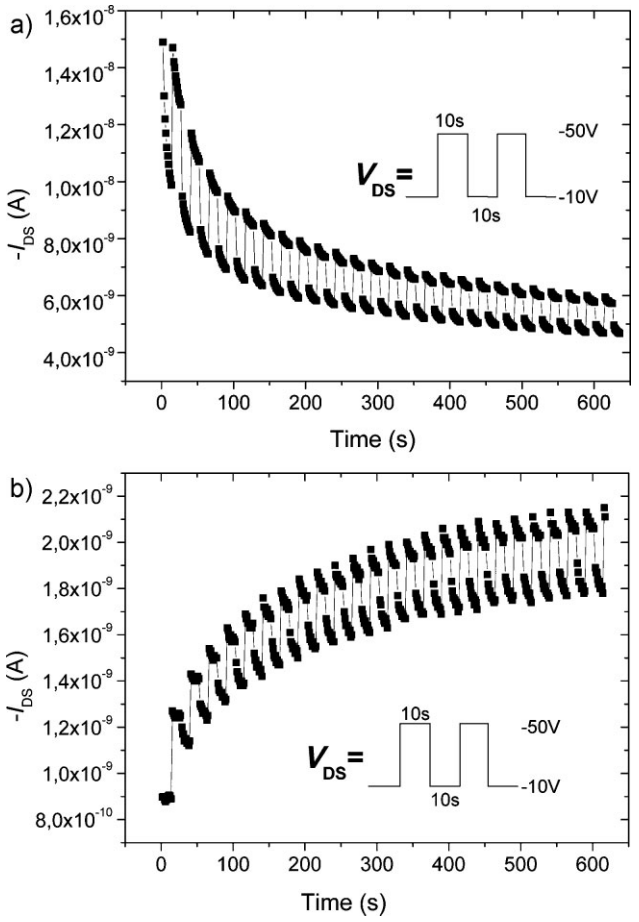


**Figure 5.** a) Response (drain current) of the NOMFET (20 nm NP, $L/W = 12\,\mu m/113\,\mu m$) to a constant frequency (0.05 Hz) train of pulses ($V_{D1} = -10$ V, $V_{D2} = -50$ V) after programming the device by a $V_P = 50$ V (20 s) gate pulse to discharge the NPs. The decreasing trend of the output current (in absolute value) mimics a depressing biological synapse. b) Response (drain current) of the NOMFET (20 nm NP, $L/W = 12\,\mu m/113\,\mu m$) to a constant frequency (0.05 Hz) train of pulses ($V_{D1} = -10$ V, $V_{D2} = -50$ V) after programming the device by a $V_P = -50$ V (20 s) gate pulse to charge the NPs. The increasing trend of the output current (in absolute value) mimics a facilitating biological synapse.

negative or positive gate voltage pulses induce facilitating or depressing behavior, respectively. Interestingly, the same behavior (Fig. 5) is also obtained for NOMFET with a less-controlled deposition of NPs (i.e., NPs forming aggregates, Fig. S3 in the Supporting Information). This result means that the synaptic behavior of the NOMFET is robust against process variations.

More importantly, we can reproduce the STP behavior without initial programming. We used the NOMFET as a ''pseudo-two-terminal device''. The gate receives the same input voltage (a train of pulses at frequency $1/T$, where $T$ is the period, and amplitude $V_P$) as the drain/source electrode (see the Supporting Information, Fig. S2). We measured the response of the NOMFET to sequences of pulses with different periods, $T$ (Fig. 6). During such experiments, the NPs are alternately charged during the pulse time and discharged between pulses.[18] The value of the current at a certain time (i.e., after a certain number of spikes) depends on the past history of the device, which determines the amount of charge presents in the NPs. To illustrate this point, let us consider the NOMFET ($L = 12\,\mu m$, 5 nm NPs) at the beginning of a particular sequence with period $T$ (Fig. 6a), where the NPs contain some charges. If $T << \tau_d$ ($\tau_d$ is the NP discharge time constant, of about 20 s here; see below), more and more holes are trapped in NPs and the NOMFET presents a depressing behavior, as observed for the 0.5 and 2 Hz spike sequences. As expected, the depressing behavior is more pronounced when increasing the frequency. This result is also in good agreement with the behavior of a spiking biological synapse (see the Supporting Information). Then, for a larger period $T$ (0.05 Hz signal in Fig. 6a), the NPs have enough time to be discharged between pulses and the sequence presents a facilitating behavior. This feature exactly reproduces the behavior of a biological synapse (Fig. 3b). The holes trapped in the NPs play the role of the neurotransmitters and the output signal, $I_{DS}$, is a decreasing function of the number of holes stored in the NPs[18] (Fig. 6). At each spike, a certain number of holes are trapped in the

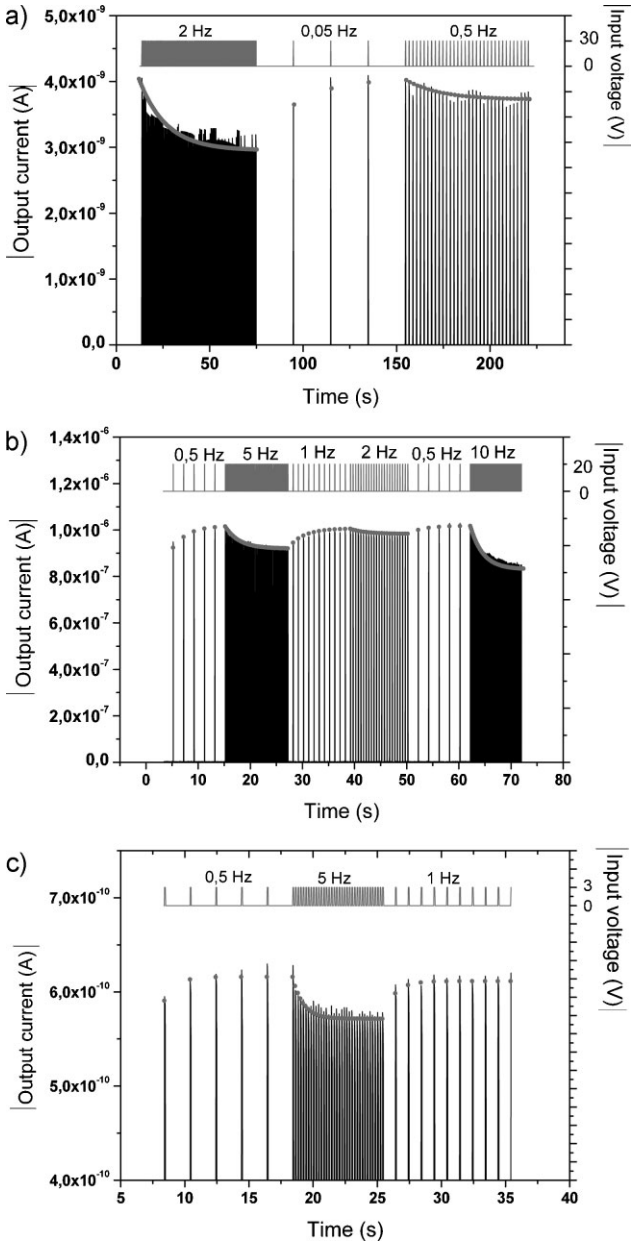


**Figure 6.** a) Response (drain current) of NOMFET with $L/W$ ratio of 12 μm/113 μm and NP size of 5 nm to sequences of spikes at different frequencies (pulse voltage $V_P = -30$ V). b) Response of NOMFET with $L/W$ ratio of 2 μm/1 000 μm and NP size of 5 nm (pulse voltage $V_P = -20$ V). c) Response of NOMFET with $L/W$ ratio of 200 nm/1 000 μm and NP size of 5 nm (pulse voltage $V_P = -3$ V). In all cases, the grey circles correspond to the iterative model calculation (see text), the black lines are the output current measurements. Increasing the frequency evidences a depressing behavior and a facilitating one is observed by decreasing the frequency.

NPs. Between pulses the system relaxes: the holes escape with a characteristic time $\tau_d$. We did not observe such a synaptic behavior for the reference pentacene OFET (no NPs; see the Supporting Information, Fig. S4).

Based on Equation 2 for the output current, we adapted the simplest iterative model of Varela et al.[26] to simulate the dynamical behavior of the NOMFET, and we developed an analogous modelisation. A pulse induces positive charges in the NPs: the NOMFET channel conductance is then reduces by a multiplicative factor $K < 1$. Between each pulse, the NPs tend to discharge with a characteristic time $\tau_d$. The general equation describing the iterative model is (see supporting information):

$$I_{n+1} = I_n K e^{-(T-P)/\tau_d} + \tilde{I}\left(1 - e^{-(T-P)/\tau_d}\right)K \quad (3)$$

Where $I_{n+1}$ and $I_n$ are the current of the NOMFET at the end of the $(n+1)^{th}$ and $n^{th}$ voltage pulses sent to the NOMFET, $\tilde{I}$ is the intrinsic drain current of the NOMFET, i.e., the current that the device would have if the charges in the NPs were kept in the equilibrium configuration (i.e., after a long period of rest, with no charge, or with a constant residual charge induced by the static dc bias of the device), $T$ is the period between two pulses and $P$ is the width of the pulses.

We fitted the iterative model to simulate the NOMFET behavior (gray dots in Fig. 6). The same fitted parameters, $\tilde{I}$ and $K$, and $\tau_d$ (here $4.1 \times 10^{-9}$ A, 0.9 and 20 s, respectively) are used in the three successive sequences shown in Figure 6a, proving a good agreement between the model and the experiments. For instance, let us consider the system at the beginning of a particular sequence with period $T$ ($T = 0.5$ s or $F = 2$ Hz in Fig. 6a), where the NPs contain some charges. Since $T << \tau_d$, the first term of the iterative function, $I_n K e^{-(T-P)/\tau_d}$, is the most important one and the sequence of spikes present a depressing behavior ($I_{n+1} < I_n$). On the other hand, for a larger period $T$ ($T = 20$ s, $F = 0.05$ Hz), the second term $\tilde{I}\left(1 - e^{-(T-P)/\tau_d}\right)K$ becomes the larger one and the sequence presents a facilitating behavior ($I_{n+1} > I_n$). Again, the depressing behavior for $T = 2$ s ($F = 0.5$ Hz) is well reproduced by the model.

We applied this model to different NOMFET with various $W/L$ ratios (where $L$ is the distance between electrodes and $W$ the width of the electrodes) down to $L = 200$ nm. For instance, the fits shown in Figure 6b for the $L = 2$ μm NOMEFT correspond to $\tau_d = 3$ s ($\tilde{I} = 10^{-6}$ A, $K = 0.99$) and for the $L = 200$ nm NOMFET (Fig. 6c) to $\tau_d = 0.9$ s ($\tilde{I} = 6.3 \times 10^{-10}$ A, $K = 0.98$). We report in Figure 7 the evolution of $\tau_d$ with the channel length and size of the NPs. For comparison, we also plot (for some devices) the time constant extracted from basic charge/discharge measurements (see the Supporting Information, Fig. S5). We note that: i) the characteristic time from the fitted model and the direct discharge measurement are of the same order of magnitude, ii) the characteristic time, and thus the working frequency range of the NOMFET, can be adjusted by changing the channel length $L$ of the NOMFET, and, iii) $\tau_d$ is weakly dependent on the NP size. The RC charge/discharge time constant is roughly governed by the channel resistance $R$ of the NOMFET, which scales as $L$, and the self-capacitance of a NP $C_{self} = 2\pi\varepsilon D$, which scale as the NP diameter $D$ ($\varepsilon$ is the dielectric constant), thus scaling down $L$ and $D$ should, in principle, decrease $\tau_d$. This feature is clearly observed for $L$.

At the macroscopic scale, we have to take into account the total capacitance, which is $NC_{self}$ with $N$ being the number of NPs in the channel. This number, while controlled to be around $10^{11}$ NP cm$^{-2}$ (see Fig. 1), varies from device to device, and we believe that these dispersions can hinder the intrinsic role of the NP size. Moreover, the NPs are capped with surfactant molecules (see the

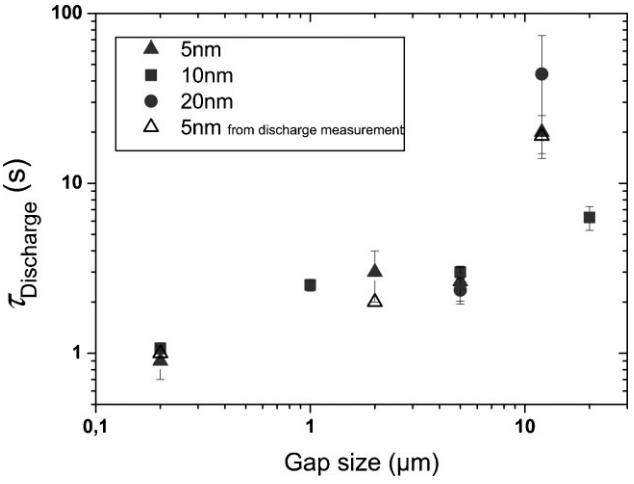


**Figure 7.** Evolution of the NP discharge time constant as function of the NOMFET channel length and for the different sizes of NP. Full symbols are from data extracted by fitting the model on the experiments (as in Fig. 6), open symbols are from discharge experiments (see the Supporting Information, Fig. S5).

Experimental Section), which can act as a tunnel barrier between the NPs and the pentacene. It is likely that this tunnel barrier play a role in the discharge phenomena (a thicker tunnel barrier will increase the discharge time constant). We did not control the structural quality of this tunnel barrier, which can represent an additional source of dispersion. More detailed experiments, for instance by systematically varying the length of the alkanethiol capping the NPs, will be necessary to increase the control of the charging/discharging phenomena in the NOMFET. A more accurate description of the relationship between these time constants, the size of the NPs and geometry of the NOMFET would require a more sophisticated modelization using a 2D network of distributed RC time constants (taken into account statistical dispersion) rather than a single macroscopic one.

Finally, we note that the iterative model used here to fit the experimental data can be implemented in usual device simulator (SPICE-like) allowing a reliable conception and simulation of hybrid NOMFET/CMOS neuronal circuits.[29] These device/circuit simulations can easily take into account the experimental dispersion of the NOMFET performances to test the robustness of these neuronal circuits against the actual device variation. Recently, a simple associative memory was built using a purely CMOS-based emulator of memristor (acting as the synapse) and neurone.[30] In this work, the memristor-synapse is emulated using a combination of CMOS analog-to-digital converter and microcontroller. It is likely that the NOMFET can be used as the synapse in such associative memory architecture. Such hybrid NOMFET/CMOS neuromorphic computing circuits and architectures are currently under investigation in our laboratory. At this stage, an interesting question can be raised: whether the NOMFET is more related to a memristor device[9] or more related to a memcapacitor as defined by Di Ventra et al. [31] While a definitive answer would probably require more experiments and simulations of the NOMFET, we believe that the NOMFET is more related to a charge-controlled memristor ( or charge-controlled memconductance) as defined in Ref. [31], since the channel conductance of the NOMFET is history-dependent of the amount of charges stored in the NPs.

## 5. Conclusions

We demonstrated a hybrid nanoparticle-organic device, a NOMFET, that makes use of the charge storage capability of the nanoparticles and the amplification factor of the organic transistor to mimic the short-term plasticity of a biological synapse. The NOMFET can be programmed to exhibit either a facilitating or a depressing behavior. By adjusting the size of the device down to 200 nm and the diameter of the nanoparticle down to 5 nm, we can range the working frequency between 0.01 and 10 Hz. We simulated the synapse behavior of the NOMFET by adapting a model developed for the biological synapse. Varela et al.[26] describe the output of biological synapses as a product of several depression (*D*-terms) and facilitation (*F*-terms) factors (Eq. 1), each of these factors being associated with a particular characteristic time. For the NOMFET, by approximating the relaxation function of the NP discharge by a simple exponential, we get the simplest model of this type: our NOMFET behaves within this approximation as the simplest depressive synapse with only one *D*-term.

## 6. Experimental

*Fabrication of Devices*: The NOMFETs were processed using a bottom-gate electrode configuration. We used highly-doped ($\rho = 10^{-3}\ \Omega$ Cm) p-type silicon covered with a thermally grown 200 nm thick silicon dioxide. Before use, these wafers were cleaned by sonication in chloroform for 5 min then by a piranha solution ($H_2SO_4$ /$H_2O_2$, 2:1 v/v) for 15 min and then by ultraviolet irradiation in an ozone atmosphere (ozonolysis) for 30 min (*caution: preparation of the piranha solution is highly exothermic and it reacts violently with organics*). Electrodes (titanium/gold, 20/200 nm) were deposited on the substrate by vacuum evaporation and patterned by optical lithography (for channel length *L* between 1 and 20 μm). Smaller NOMFETs ($L = 0.2$ μm) were fabricated on thinner oxide (10 nm thick) by usual electron-beam lithography.

The $SiO_2$ (gate dielectric) was then functionalized as a self-assembled monolayer (SAM) to anchor gold nanoparticles (NPs) on the surface. For the largest NPs (20 and 10 nm in diameter), the $SiO_2$ surface was functionalized by an amino-terminated SAM before the NP deposition [13,32,33]. First, gold (Au) electrodes were functionalized by dipping in a 2-amino ethanethiol solution in ethanol (10 mg $mL^{-1}$) for 5 h. The sample was then rinsed 3 times with isopropanol and subsequently dried in argon stream. Second, the $SiO_2$ surface was functionalized by immersion in a solution of (3-aminopropyl) trimethoxysilane (APTMS) molecules (supplied by ABCR) diluted in anhydrous toluene at a concentration 1.25 μL $mL^{-1}$ and at 60 °C for 4 min [34]. The reaction took place in a glove-box with a controlled atmosphere (nitrogen, with less than 1 ppm of oxygen and water vapor). Excess, non-reacted, molecules were removed by rinsing with toluene, and then in isopropanol under sonication. This sample was subsequently dried under an argon stream. The static water contact angle was 19°, a common value for hydrophilic $NH_2$-terminated surfaces [34]. This sample was then dipped in an aqueous solution of citrate-stabilized Au-NP (colloidal solution purchased from Sigma Aldrich, $20 \pm 3$ nm and $10 \pm 3$ nm diameter) overnight under an argon atmosphere. The NP concentration in the solution and duration of the reaction were changed to adjust the NP density on the surface. The sample was then cleaned with deionized water and isopropanol, and dried under argon stream. Finally, Au-NPs were encapsulated by dipping in a solution of 1,8-octanedithiol (from Aldrich) in ethanol (10 μL $mL^{-1}$) for 5 h to help the

formation of a network of NPs. The sample was subsequently rinsed in alcohol and dried in argon stream. For the smallest NPs, we used a solution of 4–5 nm diameter dodecanethiol-functionalized gold nanoparticles (2% in toluene) supplied by Aldrich. The oxidized silicon with gold electrodes wafer was placed overnight in the presence of vapors of freshly distilled mercaptopropyltrimethoxysilane (MPTS) in laboratory glassware at 0.2 Torr [35,36]. This freshly prepared substrate was immersed in a gold nanoparticles (NPs) solution. The starting solution supplied by Aldrich was diluted 100 times in toluene. Again, NP concentration in the solution and duration of the reaction were changed to adjust the NP density on the surface. As expected, thiol capped Au NPs readily reacted with thiol-terminated SAM by ligand exchange forming a covalent bond with the surface.

Finally, a 35 nm thick pentacene film was evaporated at a rate of 0.1 Å $s^{-1}$. The substrate was kept at room temperature. A reference device of pentacene without NPs (and without SAM) was also realized in the same run of deposition to evidence the effect of NPs on the electrical properties. Note that a second reference sample with a SAM between the $SiO_2$ and the pentacene film did not show any memory effect [37].

*Electrical Measurements*: The NOMFET electrical characteristics were measured with an Agilent 4155C semiconductor parameter analyzer, the input pulses were delivered by a pulse generator (Tabor 5061). The electrodes of the NOMFET were contacted with a micro-manipulator probe station (Suss Microtec PM-5) placed inside a glove box (MBRAUN) with a strictly controlled nitrogen ambient (less than 1 ppm of water vapor and oxygen). Such a dry and clean atmosphere is required to avoid any degradation of the organics (SAMs and pentacene). So the devices are not exposed to air from the beginning of the fabrication process to the end of the electrical characterization.

## Acknowledgements

This work was funded by the European Union through the FP7 Project NABAB (Contract FP7-216777) and partly by the Micro and Nanotechnology Program from the French Ministry of Research under the grant RTB: ''Post CMOS moléculaire''. We thank R. Baptist (CEA-LETI) for his support. Supporting Information is available online from Wiley InterScience or from the corresponding author.

Received: July 20, 2009
Revised: October 5, 2009
Published online:

[1] J. Backus, *Commun. ACM* **1978**, *21*, 613.
[2] D. V. Buonomano, W. Maass, *Nat. Rev. Neurosci.* **2009**, *10*, 113.
[3] G. Le Masson, S. Renaud-Le Masson, D. Debay, T. Bal, *Nature* **2002**, *417*, 854.
[4] FACETS: Fast Analog Computing with Emergent Transient States, http://facets.kip.uni-heidelberg.de (accessed October 2009).
[5] M. Boegerhausen, P. Suter, S.-C. Liu, *Neural Comput.* **2003**, *15*, 331.
[6] J. Borghetti, V. Derycke, S. Lenfant, P. Chenevier, A. Filoramo, M. Goffman, D. Vuillaume, J. P. Bourgoin, *Adv. Mater.* **2006**, *18*, 2535.
[7] G. Agnus, W. Zhao, V. Derycke, A. Filoramo, Y. Lhuillier, S. Lenfant, D. Vuillaume, C. Gamrat, J.-P. Bourgoin, *Adv. Mater.* **2009**, in press.
[8] Q. Lai, Z. Li, L. Zhang, X. Li, W. F. Stickle, Z. Zhu, Z. Gu, T. I. Kamins, R. S. Williams, Y. Chen, *Nano Lett.* **2008**, *8*, 876.
[9] D. B. Strukov, G. S. Snider, D. R. Stewart, R. S. Williams, *Nature* **2008**, *453*, 80.
[10] J. J. Yang, M. D. Pickett, X. Li, A. A. OhlbergDouglas, D. R. Stewart, R. S. Williams, *Nat. Nanotechnol.* **2008**, *3*, 429.
[11] J. Borghetti, Z. Li, J. Straznicky, X. Li, D. A. A. Ohlberg, W. Wu, D. R. Stewart, R. S. Williams, *Proc. Natl. Acad. Sci. USA* **2009**, *106*, 1699.
[12] G. S. Snider, in *IEEE/ACM International Symposium in Nanoscale Architectures* **2008**, 85.
[13] M.-C. Daniel, D. Astruc, *Chem. Rev.* **2004**, *104*, 293.
[14] W. Lu, C. M. Lieber, *Nat. Mater.* **2007**, *6*, 841.
[15] M. F. Sybille Allard, B. Souharce, H. Thiem, U. Scherf, *Angew. Chem. Int. Ed.* **2008**, *47*, 4070.
[16] H. Yan, Z. Chen, Y. Zheng, C. Newman, J. R. Quinn, F. Dotz, M. Kastler, A. Facchetti, *Nature* **2009**, *457*, 679.
[17] J. H. Cho, J. Lee, Y. Xia, B. Kim, Y. He, M. J. Renn, T. P. Lodge, C. Daniel Frisbie, *Nat. Mater.* **2008**, *7*, 900.
[18] C. Novembre, D. Guérin, K. Lmimouni, C. Gamrat, D. Vuillaume, *Appl. Phys. Lett.* **2008**, *92*, 103314.
[19] S. Haykin, *Neural Networks. A Comprehensive Foundation*, Macmillian, New York **1994**.
[20] L. F. Abbott, J. A. Varela, K. Sen, S. B. Nelson, *Science* **1997**, *275*, 220.
[21] J. J. Hopfield, *Proc. Natl. Acad. Sci. USA* **1982**, *79*, 2554.
[22] C. D. Dimitrakopoulos, D. J. Mascaro, *IBM. J. Res. & Dev.* **2001**, *45*, 11.
[23] M. Shtein, J. Mapel, J. B. Benziger, S. R. Forrest, *Appl. Phys. Lett.* **2002**, *81*, 268.
[24] M. Tsodyks, K. Pawelzik, H. Markram, *Neural Computation* **1998**, *10*, 821.
[25] M. V. Tsodyks, H. Markram, *Proc. Natl. Acad. Sci. USA* **1997**, *94*, 719.
[26] J. A. Varela, K. Sen, J. Gibson, J. Fost, L. F. Abbott, S. B. Nelson, *J. Neurosci.* **1997**, *17*, 7926.
[27] K. L. Magleby, J. E. Zengel, *J. Gen. Physiol.* **1982**, *80*, 613.
[28] M. C. J. M. Vissenberg, M. Matters, *Phys. Rev. B* **1998**, *57*, 12964.
[29] O. Bichler, W. Zhao, F. Alibart, S. Pleutin, D. Vuillaume, C. Gamrat, unpublished.
[30] Y. V. Pershin, M. di Ventra, *arXiv:cond-mat/0905.2935* **2009**.
[31] M. di Ventra, Y. V. Pershin, L. O. Chua, *Proc. IEEE* **2009**, *97*, 1717.
[32] H. X. He, D. Zhang, Q. G. Li, T. Zhu, S. F. Y. Li, Z. F. Liu, *Langmuir* **2000**, *16*, 3846.
[33] T. Sato, H. Ahmed, D. Brown, B. F. G. Johnson, *J. Appl. Phys.* **1997**, *82*, 696.
[34] D. F. Siqueira Petri, G. Wenz, P. Schunk, T. Schimmel, *Langmuir* **1999**, *15*, 4520.
[35] J. J. Senkevitch, C. J. Mitchell, G.-R. Yang, T.-M. Lu, *Langmuir* **2002**, *18*, 1587.
[36] D. K. Aswal, S. Lenfant, D. Guerin, J. V. Yakhmi, D. Vuillaume, *Small* **2005**, *1*, 725.
[37] M. Ternisien, *PhD Thesis*, University of Lille **2008**.

ADVANCED FUNCTIONAL MATERIALS

**Supporting Information.**

# An organic-nanoparticle transistor behaving as a biological spiking synapse

F. Alibart,[1] S. Pleutin,[1] D. Guerin,[1] C. Novembre,[2] S. Lenfant,[1] K. Lmimouni,[1]

C. Gamrat,[2] & D. Vuillaume.[1*]

*1. Molecular Nanostructures and Devices group, Institute for Electronics Microelectronics and Nanotechnology, CNRS, University of Lille, BP60069, avenue Poincaré, F-59652cedex, Villeneuve d'Ascq, France.*

*2. CEA, LIST/LCE (Advanced Computer technologies and Architectures), Bat. 528, F-91191, Gif-sur-Yvette, France.*

* dominique.vuillaume@iemn.univ-lille1.fr

## ***Supporting information***

## I. Drain current of the NOMFET, role of the NPs

The transport properties of organic thin film transistors are reasonably well understood in terms of a percolation theory developed already ten years ago by Vissenberg and Matters (VH)[1]. The advantage of this theory is to provide an analytical expression for the conductance of the transistor channel. We start by summarizing the main features of the model. A thin film of pentacene is not perfectly organized, and it is likely that the disorder increases in the presence of the network of NPs. For small bias (linear regime) the organic film can be viewed as an electrical network with a quantum localized state of energy $\varepsilon_i$ at each node i.[2] The site energies are exponentially distributed. The density of states (DOS) is given by

$$g(\varepsilon) = \frac{N_t}{k_B\theta_0}\exp\left(\frac{\varepsilon}{k_B\theta_0}\right) \quad \text{(S1)}$$

with $N_t$ the number of localized state per unit volume, $k_B\theta_0$, a measure of the energy width of the distribution (Fig. S1). The energies are such that $-\infty < \varepsilon \leq 0$. It is important to note that this type of DOS introduced by VH is not arbitrary and has been recently observed by Kelvin probe force microscopy for thin films of copper phthalocyanine[3], for instance.

Each pair of nodes, i and j, distant by $R_{ij}$ is connected by a bond with a conductance $G_{ij}=G_0 exp(-S_{ij})$ where[1,2]

$$S_{ij} = 2\alpha R_{ij} + \frac{\left|\varepsilon_i - \varepsilon_F\right| + \left|\varepsilon_j - \varepsilon_F\right| + \left|\varepsilon_i - \varepsilon_j\right|}{2k_B\theta} \tag{S2}$$

The first term takes account for usual tunneling processes and the second for thermally assisted tunneling. $\alpha$ is an effective overlap parameter, $\varepsilon_F$ is the Fermi energy imposed by the reservoirs (electrodes) which fixes the number of careers and $\theta$ is the temperature. The second term is crucial to understand the conductivity in organic thin film transistor. It selects the quantum states with energy sufficiently close to the Fermi level to participate to the charge transport: the more the DOS is high at the Fermi level, the more the conductance will be high. Because of the exponential DOS, by increasing the gate voltage we increase the number of states at the Fermi level and consequently the conductance. This is the usual behavior for an organic transistor but, in this case, the conducting channel is disordered (more or less random distribution of $R_{ij}$). Solving the percolation problem, VH have found the channel conductance

$$G = G_0\left(\frac{\pi N_t(\theta_0/\theta)^3}{(2\alpha)^3 B_C}\right)e^{\beta\varepsilon_F} = A_0 e^{\beta\varepsilon_F} \tag{S3}$$

where $G_0$ is a parameter and $B_C$ a constant (~2).

In the NOMFET, when the gold particles are positively charged, there is a Coulomb repulsion between the trapped charges in the NPs and the holes created in the pentacene thin film by the gate voltage. We assume that the only effect of the charged NPs is on the energy of the localized states. The gold NPs are assumed to be all perfectly identical. Every lattice site i feels a repulsive Coulomb interaction

$$\delta_i = \frac{q^2}{4\pi\varepsilon_0\varepsilon_r}\sum_\alpha \frac{n_\alpha}{\left|\vec{r}_\alpha - \vec{r}_i\right|} \tag{S4}$$

where the summation runs over all the NPs which are labelled by $\alpha$. $n_\alpha$ is the number of holes stored in the NP α ($n_\alpha$=0, 1, 2,…), $q$ is the elementary electric charge, $\varepsilon_0$ and $\varepsilon_r$ denote as usual the permittivity of the vacuum and of the material, respectively. $\vec{r}_\alpha$ and $\vec{r}_i$ are the position vectors of the NP α and the quantum state i, respectively. Note that the summation does not show any divergence since the NPs and the quantum state never occupy the same spatial location. $\delta_i$ is a stochastic variable. We face a new percolation problem where all the site energies are shifted up by the repulsive terms, $\varepsilon_i \rightarrow \varepsilon_i+\delta_i$.

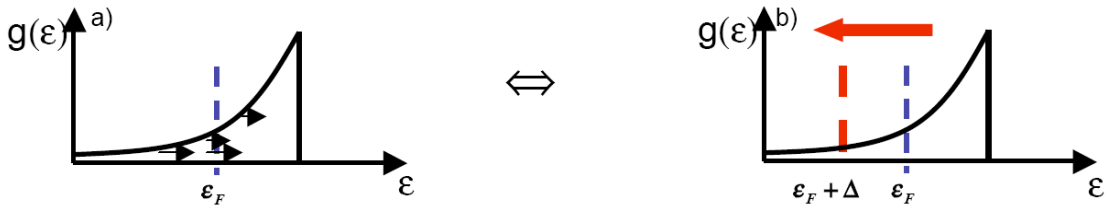


**Figure S1**. **a**, The quantum state energies are shifted up by the interaction with the charged NPs. **b**, Equivalently the Fermi level is shifted down by the same interaction.

When the NPs are positively charged the conductance of the pentacene thin film decreases. This is due to the exponential DOS. The Fermi level is fixed by the electrodes. The site energies are all shifted up by the repulsive Coulomb interaction (Figure S1) and consequently the number of states at the Fermi level is reduced. Since we are only interested to calculate the conductance of the NOMFET this is, to a first approximation, the only important information. This decrease of the conductance can be simply modeled by keeping the unperturbed DOS and shifting down the Fermi level by a constant $\Delta$ (Figure S1). We further assume that the value of $\Delta$ depends only on the applied gate voltage. Choosing a particular voltage fixes the number of positive charges trapped in the NPs. It is clear however that the precise way these charges are distributed in the NPs should in principle influence the transport properties but, how this is done and how large is this dependence remain to be understood. Nevertheless, it turns out that our approximation is sufficient to model our data with a reasonable accuracy.

To summarize, the effect of the repulsive interaction due to positive charges in the NPs is to reduce the Fermi energy by an amount $\Delta$ that is related to the total number of charges trapped in the particles. In other terms, it is a function of $V_G$. Then

$$G = A_0 e^{\beta\varepsilon_F} e^{-\beta\Delta} \quad \text{(S5)}$$

meaning that the amplitude of the current, $I=GV_{sd}$, is reduced by the holes stored in the particles. This is indeed what is experimentally observed[4].

## II. Chronograms.

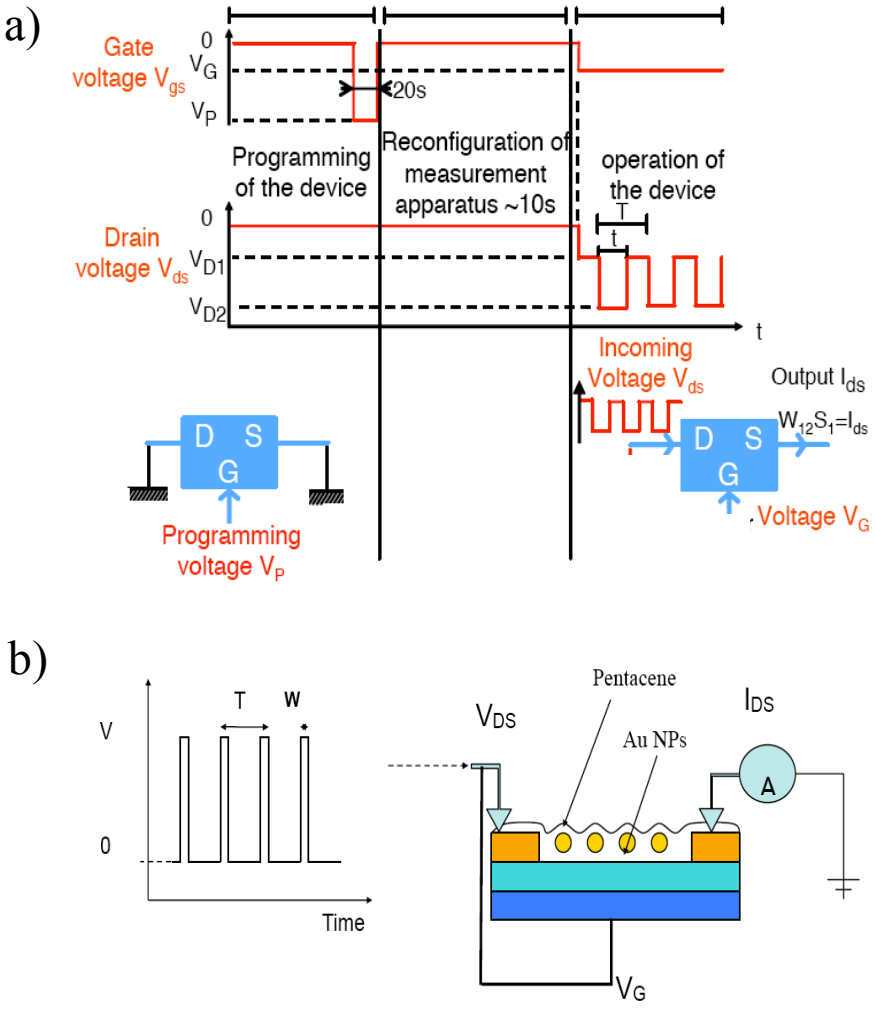


**Figure S2**. **a)** Typical gate and drain voltage chronogram for the programming period (pulse $V_P$ applied on the gate) and functioning period (a train of pulse voltages between $V_{D1}$ and $V_{D2}$ is applied on the drain/source, while the gate is dc biased at $V_G$ = - 20V). **b)** Typical signal chronogram for the STP experiment.

## III. Aggregated NP networks.

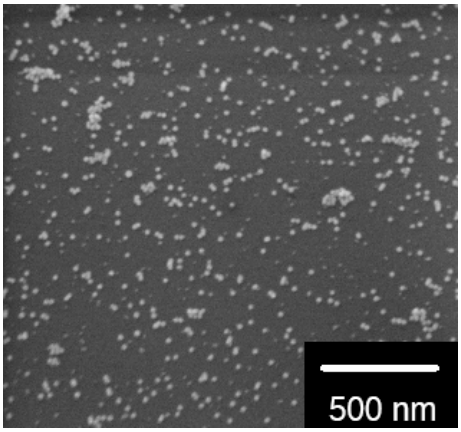


**Figure S3.** Scanning electron microscope images of aggregated 20 nm NP networks such as those used in the NOMFET reported in Fig. 5.

## IV. Reference device (no NP)

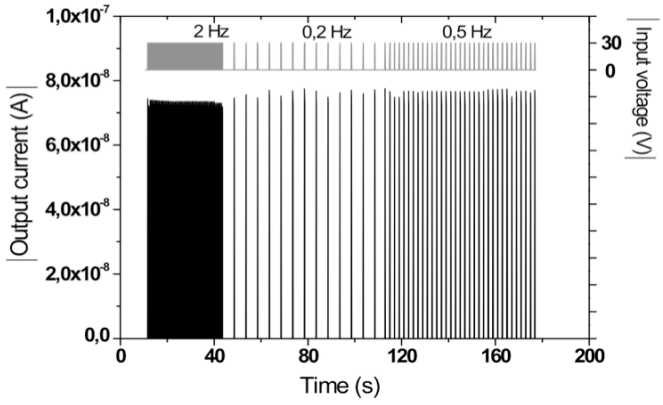


**Figure S4.** Same experiment as in Figure 6 (main text) for a reference device without NPs and W/L ratio of 12µm/113µm. We did not observe a STP behavior.

## V. Iterative model adapted to the NOMFET

The next step is to model the response of the NOMFET to a sequence of spikes. Here, we first consider a train of pulse voltage of frequency *1/T* and amplitude $V_P$, each pulse has a time width *P* (as in Figs. 4-6 in the main text). To model the NOMFET response, we consider the iteration $I_n$, the value of the current at the end of the $n^{th}$ pulse. During the pulse the particles are charged with a certain

dynamic characterized by a function $f_c(t)$, t being the time variable. For a pulse with an infinite width the charges stored in the NPs is such that we get the exponential prefactor $e^{-\beta\Delta}$ in the conductance. We further assume to be as close as possible to Varela's model[5] developed for biological synapses (see main text), that the amount of charges entering the NPs at each spike depends only on the properties of the pulse ($V_P$, the amplitude, $P$, the width) but not on the history of the device. Overcoming this constraint does not change significantly the results for the typical sequences of spikes considered in this work: the approximation of constant charging gives very good agreements with experiments (Fig. 6, main text). Between pulses, the particles are discharged according to a dynamic described by a function $f_d(t)$. For an infinite period, the particles are completely empty giving a factor 1 in the conductance. Collecting these informations together we get the general iteration

$$I_{n+1} = I_n\left(e^{-\beta\Delta} - \left(e^{-\beta\Delta} - 1\right)f_c(P)\right)f_d(T-P) + \tilde{I}\left(1 - f_d\left(T-P\right)\right)\left(e^{-\beta\Delta} - \left(e^{-\beta\Delta} - 1\right)f_c(P)\right) \quad \text{(S6)}$$

where $\tilde{I}$ is the current that would carry the device within the same voltage conditions but without NPs. The two relaxation functions are such that $f_c(0) = f_d(0) = 0$. The starting value $I_0$ of the iteration depends on the initial charging condition of the NPs (that can be adjusted by an initial pulse on the gate). Since we consider only pulses with constant width $P$ and amplitude $V_P$ during a sequence (only the period varies), we can replace the charging part of the iteration by a constant multiplicative factor

$$K = e^{-\beta\Delta} - (e^{-\beta\Delta} - 1)f_c(P) \quad \text{(S7)}$$

The discharging function $f_d(t)$ of the NPs is then evaluated by fitting the iterative model to the sequences of pulses measurements such as those shown in Fig. 6 (main text). This function is approximated by a single exponential with a reasonable accuracy

$$f_d(t) \approx f_d(0)e^{-t/\tau_d} \quad \text{(S8)}$$

The resulting iterative function that will be used for the modeling has the simple form:

$$I_{n+1} = I_n K e^{-(T-P)/\tau_d} + \tilde{I}\left(1 - e^{-(T-P)/\tau_d}\right)K \quad \text{(S9)}$$

It is important to note that with this simplification, good agreements are obtained with experiments even if the discharging function should be more complex, and we are in the same approximation limit than Abbott et al.[6] when these authors discussed the role of short term plasticity in biological synapses.

As a matter of illustration, let us write down the two very first iterations for the case where $I_0 = \tilde{I}$. The time origin is chosen to be the start of the 1st pulse. At $t=P$, we get $I_1 = \tilde{I}K$. The initial

current is reduced by the multiplicative factor caused by the charges stored in the NPs during the pulse. At *t*=*T*+*P*, we get $I_2 = \tilde{I}\left(1-(1-K)e^{-(T-P)/\tau_d}\right)K$. The term between brackets is due to the discharge between the two first pulses; if *T* is very long the NPs will be completely empty and this term will give a factor 1. The additional *K* factor is caused by the charges trapped in the NPs during the second pulse. By doing so, the general formula (S6) can be obtained.

## VI. Simple charge/discharge experiments

An alternative measurement has been performed on the NOMFET to get more information about the discharging phenomena. We first applied a negative bias on the gate (of the same value as those used in the spike experiments shown in Fig. 6, i.e. -30V) during a sufficiently long time to be close to the maximal charge of the NPs (defined as the time for which the drain current reaches a steady state). Then, we switched the gate to 0V and we measured the time-dependent variation of the drain current corresponding to the discharge of the NPs. We fitted the discharging curves with a linear combination of exponentials

$$f_{Rd}(t) = \sum_i a_{Rid} e^{-t/\tau_{Rid}} \qquad \text{(S10)}$$

with $\tau_{R1d} << \tau_{R2d} <<$...an so forth.

Two typical examples are shown in Fig. S2 that gives typical values for the discharge $\tau_{R1d}$ = 3.7 s and $\tau_{R2d}$ = 19.1s (for the NOMFET with the 5 nm NPs and L= 12 µm as on figure 6), and $\tau_{R1d}$ = 0.4 s and $\tau_{R2d}$ = 2.2 s (for the NOMFET with the 5 nm NPs and L= 2 µm). The fitting of the discharge current is not significantly improved by using three exponential terms (we get $R^2 >$ 0.999 with two exponentials). Comparing (Fig. 7, main text) these time constants with those obtained from the fit of the iterative models on the spike experiments (Fig. 6), we find that the second relaxation time constant $\tau_{R2d}$ is very similar to $\tau_d$ for all the NOMFET with various channel lengths L and NPs sizes. It means that $\tau_{R1d}$ is too short to lay any role in the spiking experiments done here. Even if the response of the device to a sequence of pulses should be improve by adding more terms in the discharging function in equations (S6), (S9) and (3 main text),we found that the contribution of the shortest time is not

necessary to reproduce the general behavior of the NOMFET to the sequences of pulses considered in this work.

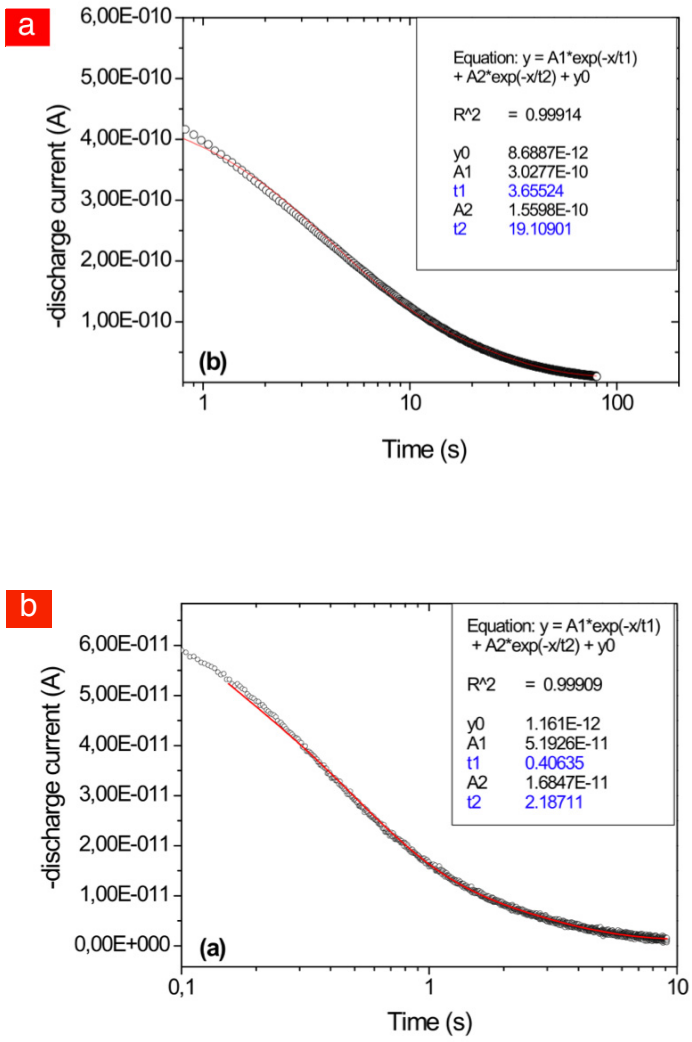


**Figure S5. a**, semi-log plot of the time dependent variation of the NOMFET (L=12 µm and 5 nm NPs) drain current during the discharge of the NPs (all terminals grounded). The red lines are the fit with equation (S10) given $\tau_{R1d}$ = 3.7 s and $\tau_{R2d}$ = 19.1s. **b**, same experiments for the NOMFET L=2 µm and 5 nm NPs. The fit gives $\tau_{R1d}$ = 0.4 s and $\tau_{R2d}$ = 2.2 s.

## VII. Amplitude of the STP versus the frequency

We observed that the amplitude of the depressing and facilitating behavior during the STP experiments (Fig. 6) depends on the frequency of the signal. For instance, the decrease in the $I_{DS}$ current is more important at 2 Hz than at 0.5 Hz (fig. 6-a). This is expected because at 2 Hz, the time

interval between two subsequent pulses is shorter than a t 0.5 Hz, and the charges stored in the NPs during the pulse period have less time to relax. At a consequence, at the end of the train of pulses, more charges remain stored in the NPs and the decrease in the current is also more important. The amplitude of the depressing behavior increases with the frequency of the pulses. The model catches this behavior satisfactorily.

Let us consider the limit for a large number of pulses, where $I_n$ reaches a steady state (Fig. S6)

$$I_n \xrightarrow[n\to+\infty]{} \tilde{I}\left(e^{(T-P)/\tau_d}-1\right)\frac{Ke^{-(T-P)/\tau_d}}{1-Ke^{-(T-P)/\tau_d}} \tag{S11}$$

In the particular case where $T << \tau_d$ (depressing behavior) this limit becomes

$$\lim_{n\to\infty} I_n = \frac{1}{1+\frac{\tau_d}{T-P}\left(K^{-1}-1\right)} \approx \frac{1}{f} \tag{S12}$$

with $f = 1/T$. This particular behavior is indeed observed experimentally (Fig. S6). This 1/f behavior was also observed by Tsodyks et al.[7] and Abbott et al.[6] in the case of a biological synapse (for instance, see figure 1 in Ref. [6]).

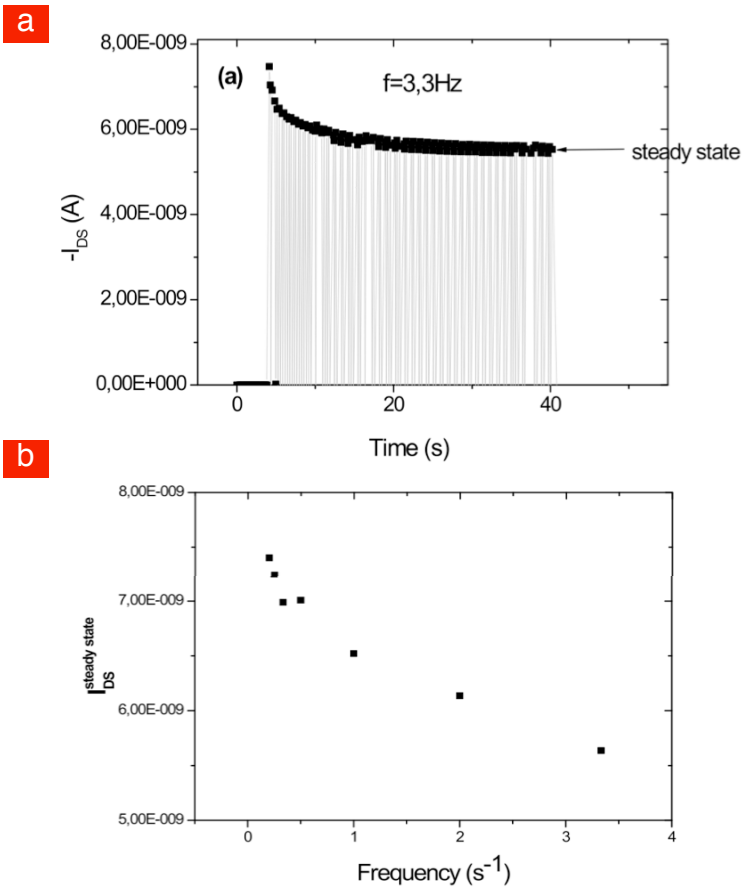


**Figure S6. a,** response of the NOMFET for a long sequence of pulses. The output current reaches a steady-state. **b**, evolution of the steady-state current as a function of the frequency of the pulses. Data for the NOMFET with the 5 nm NPs and L= 12 μm.

## REFERENCES

[1] Vissenberg, M.C.J.M. & Matters, M., Theory of the field-effect mobility in amorphous organic transistors. *Phys. Rev. B* 57, 12964-12967 (1998).

[2] Ambegaokar, V., Halperin, B.I., & Langer, J.S., Hopping Conductivity in Disordered Systems. *Physical Review B* 4 (8), 2612 (1971).

[3] Celebi, K., Jadhav, P.J., Milaninia, K.M., Bora, M., & Baldo, M.A., The density of states in thin film copper phthalocyanine measured by Kelvin probe force microscopy. *Applied Physics Letters* 93 (8), 083308 (2008).

[4] Novembre, C., Guérin, D., Lmimouni, K., Gamrat, C., & Vuillaume, D., Gold nanoparticle-pentacene memory transistors. *Appl. Phys. Lett.* 92 (10), 103314 (2008).

[5] Varela, J.A. *et al.*, A quantitative description of short-term plasticity at excitatory synapses in layer 2/3 of rat primary visual cortex. *J. Neurosci.* 17 (20), 7926-7940 (1997).

[6] Abbott, L.F., Varela, J.A., Sen, K., & Nelson, S.B., Synaptic depression and cortical gain control. *Science* 275, 220-224 (1997).

[7] Tsodyks, M.V. & Markram, H., The neural code between neocortical pyramidal neurons depends on neurotransmitter release probability. *Proc. Natl. Acad. Sci. USA* 94 (2), 719-723 (1997).

# A Memristive Nanoparticle/Organic Hybrid Synapstor for Neuroinspired Computing

*Fabien Alibart, Stéphane Pleutin, Olivier Bichler, Christian Gamrat, Teresa Serrano-Gotarredona, Bernabe Linares-Barranco, and Dominique Vuillaume**

**A large effort is devoted to the research of new computing paradigms associated with innovative nanotechnologies that should complement and/or propose alternative solutions to the classical Von Neumann/CMOS (complementary metal oxide semiconductor) association. Among various propositions, spiking neural network (SNN) seems a valid candidate. i) In terms of functions, SNN using relative spike timing for information coding are deemed to be the most effective at taking inspiration from the brain to allow fast and efficient processing of information for complex tasks in recognition or classification. ii) In terms of technology, SNN may be able to benefit the most from nanodevices because SNN architectures are intrinsically tolerant to defective devices and performance variability. Here, spike-timing-dependent plasticity (STDP), a basic and primordial learning function in the brain, is demonstrated with a new class of synapstor (synapse-transistor), called nanoparticle organic memory field-effect transistor (NOMFET). This learning function is obtained with a simple hybrid material made of the self-assembly of gold nanoparticles and organic semiconductor thin films. Beyond mimicking biological synapses, it is also demonstrated how the shape of the applied spikes can tailor the STDP learning function. Moreover, the experiments and modeling show that this synapstor is a memristive device. Finally, these synapstors are successfully coupled with a CMOS platform emulating the pre- and postsynaptic neurons, and a behavioral macromodel is developed on usual device simulator.**

## 1. Introduction

Spike-timing dependent plasticity (STDP) is widely believed today to be one of the fundamental mechanisms of the unsupervised learning in biological neural networks. STDP in biological systems is a refinement of Hebb's learning rule.[1] Grant et al,[2] Markram et al,[3] Bi, and Poo[4] observed STDP in biological synapses. The principle of STDP is to tune the response of a synapse as a function of the pre- and post- synaptic neurons spiking activity - **Figure 1**a. Depending on the correlation or anti-correlation of the spiking events of the pre- and post-synaptic neurons, the synapse's weight is reinforced or depressed, respectively. The so-called "STDP function" or "STDP learning window" is defined as the relationship between the change in the synaptic weight or synaptic response versus the relative timing between the pre- and postsynaptic spikes (Figure 1b).[5] The implementation of STDP with nanodevices is strongly driven by a bio-inspired approach to enable local and unsupervised learning capability in large artificial SNN in an efficient and robust way. To this end, it is envisioned to use the nanodevices as synapses and to realize the neuron functionality with complementary metal oxide semiconductor (CMOS) technology. This approach is supported by the fact that the limiting integration factor is really the synapse density, as realistic applications could require as much as $10^3$ to $10^4$ synapses per neuron. Snider[6] proposed an implementation of STDP with nanodevices, where the synapses are realized with a crossbar of memristors[7] and the neurons with a "time-multiplexing CMOS" circuit. Using these two elements, it should be possible to reproduce exactly the "STDP learning window" of a biological synapse (Figure 1b). Linares-Barranco et al. simulated the implementation of the STDP function with memristive nanodevices.[8,9] Using a specific shape of the spikes and the nonlinearity of the memristor, they showed that the conductivity of the memristor can be tuned depending on the precise timing between the postsynaptic and presynaptic spikes. More interestingly, they showed that the shape of the STDP learning window can be tuned by changing the shape of the spike (Figure 1c). We have to emphasize that our aim is to be inspired by the behavior of a biological synapse for neural computation applications (and not to build a model system of the synapse), thus the important point is to reproduce qualitatively the STDP behavior, even if the spike signals applied to the synapstor are not close to the real biological spike.

Dr. F. Alibart, Dr. S. Pleutin, Dr. D. Vuillaume
Institute for Electronics Microelectronics and Nanotechnology (IEMN)
CNRS, University of Lille
BP60069, avenue Poincaré, F-59652cedex, Villeneuve d'Ascq, France
E-mail: dominique.vuillaume@iemn.univ-lille1.fr
O. Bichler, Dr. C. Gamrat
CEA, LIST/LCE (Advanced Computer technologies and Architectures)
Bat. 528, F-91191, Gif-sur-Yvette, France
Prof. T. Serrano-Gotarredona, Prof. B. Linares-Barranco
Instituto de Microelectrónica de Sevilla (IMSE)
CNM-CSIC, Av. Americo Vespucio s/n, 41092 Sevilla, Spain

**DOI: 10.1002/adfm.201101935**

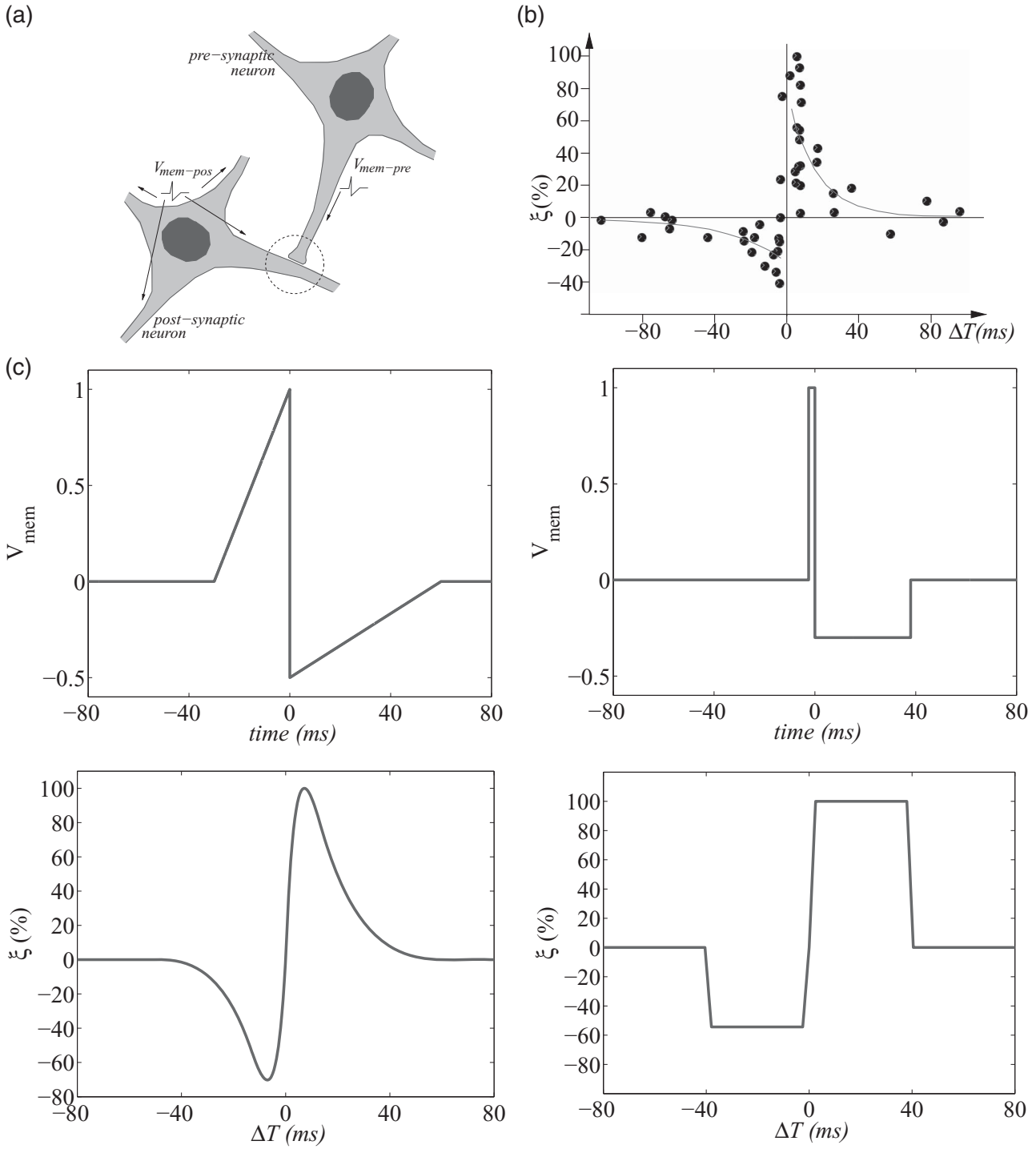


**Figure 1.** a) Illustration of a synapse connecting two neurons: the presynaptic and the postsynaptic neurons. Reproduced with permission.[9] b) STDP function, i.e., change in the synaptic weight versus spike timing interval, measured on a biological synapse. Reproduced with permission;[9] data from Bi and Poo.[4] c) Two shapes of spikes (left side) and the corresponding STDP functions (right side) calculated for a memristive device. Reproduced with permission.[9]

We recently demonstrated that the nanoparticle–organic memory field-effect transistor (NOMFET) is able to mimic the short-term plasticity (STP) behavior of a spiking biological synapse.[10] When a sequence of voltage pulses is applied across the device, the current transmitted by the NOMFET is modulated depending on the frequency of the pulses and the past input activity of the device,[10,11] mimicking the facilitating or depressing behavior of a biological spiking synapse.[12] Research

on artificial synapse devices mimicking the plasticity of a biological synapse is a burgeoning field. Recently, Jo et al.[13] have observed STDP in Ag/Si-based memristor, Lai et al.[14] in polymer/Si nanowire transistor, Seo et al.[15] in oxide resistive memory, Kuzum et al. in phase-change memory.[16] Here, we demonstrate the STDP behavior of the NOMFET. First, we carefully analyze the behavior of this synapstor and show that it can be modelized by the memristor equations.[17,18] Thus, we follow the Linares-Barraco et al. suggestions[8,9] to successfully implement the STDP behavior with the NOMFET. Beyond the demonstration at a single device level, we also demonstrate that the NOMFET can be efficiently coupled with a CMOS platform emulating the pre- and postsynaptic neurons. Finally, we developed a behavioral macromodel suitable for device/circuit simulations using commercially available simulators (*Spectre-Cadence*).[19]

## 2. The Nanoparticle–Organic Memory Field-Effect Transistor: A Memristive Device

The NOMFET is based on a standard bottom gate/bottom source-drain organic transistor with gold nanoparticles (NPs) fixed at the gate dielectric/organic semiconductor (OSC) interface by surface chemistry (see the Experimental Section, and a previously reported detailed material characterization[10]). The STP behavior of the NOMFET is due to the internal charge/discharge dynamics of the NP/OSC system with typical time constants that can be adjusted between 1 to $10^2$ s.[10] While we have demonstrated some simple neuroinspired plasticity for NOMFETs with a channel length L down to 200 nm, and NP diameter of 5 nm, working at a nominal bias of –3 V,[10] here for the sake of demonstration, all the experiments are reported for L = 5 µm NOMFETs and 20 nm diameter NPs working at a nominal voltage of –30 V, because these devices previously showed the largest plasticity amplitude (i.e., the largest modulation of the NOMFET output current, here analogous to the synaptic weight, by the applied spike sequence).[10] The channel width ($W$) is 1000 µm for the 5 µm length NOMFET, to maximize the output current, given the relative low mobility of the device (ca. $10^{-3}$ cm$^2$ V$^{-1}$ s$^{-1}$).[10] Optimization of the OSC properties (not done here) will allow reaching a state-to-the art mobility of about 1 cm$^2$ V$^{-1}$ s$^{-1}$, and will allow reducing the actual width by a factor $10^3$. Further optimization would be the use of high-k dielectric to reach the same output current while downscaling $W$ accordingly. Downscaling the NOMFET channel length to 30 nm (with 5 nm diameter NPs) is possible (we have already demonstrated a 30 nm channel length OFET[20]), but such a task would require a hard work for technological optimization, out of the scope of this proof of principle demonstration.

The NOMFET is used as a pseudo two-terminal device (**Figure 2**a): the drain (D) and gate (G) electrodes are connected together and used as the input terminal of the device, and the source (S) is used as the output terminal (virtually grounded through the ampmeter). To establish that it works as a memristive device, we write the output current - input voltage relation in the NOMFET according to the formalism proposed by Chua,[17] and we discuss the significance of the terms in this equation:

$$I_{DS}(t) = G(Q_{NP}(t), V_{DS}(t), t)\,V_{DS}(t) \quad (1)$$

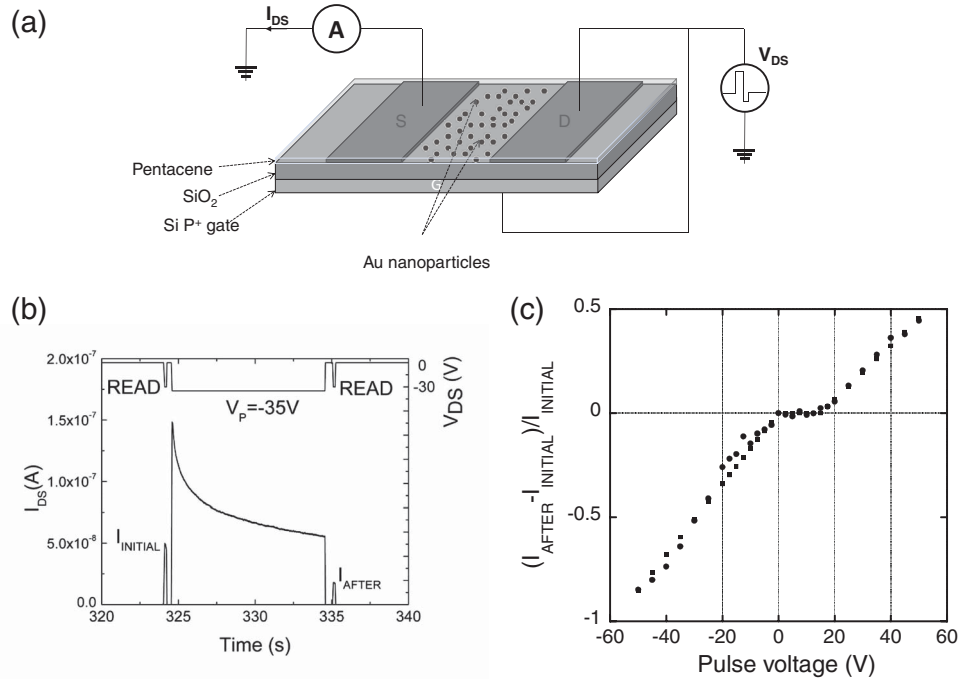


**Figure 2.** a) Schematic representation of the NOMFET and pseudo two-terminal connections of the device. b) Typical "single pulse measurement" used to characterized the NOMFET as a memristive device. The current is measured just before and after a large pulse of 10s in order to estimate the effect of the pulse voltage $V_P$ on the NPs charge. c) Relative variation of the current as a function of the pulse voltage $V_P$. Dots are the experimental measurements and squares from the physical model (see the Supporting Information).

$$\dot{Q}_{NP}(t) = g(Q_{NP}(t), V_{DS}(t), t) \quad (2)$$

where $G$ is the conductance of the device that includes the field effect, $V_{DS}(t)$ is the applied signal of time varying shape, and $Q_{NP}(t)$ the charges trapped in the NPs. For the NOMFET, $Q_{NP}(t)$ is the relevant internal parameter, and its first-order time derivative is given by the $g$ function, which is the "memristive" function that describes how this internal parameter is updated as function of the internal state, the external voltage and time. A non-linear behavior of $g$ is very interesting to implement synaptic plasticity and STDP.[6,8,9,18] A $g$ function with a null value between negative and positive threshold voltages and increasing/decreasing parts above/below (respectively) these thresholds has been used to simulate STDP and learning capabilities in memristor-based neuroinspired circuits.[8,9]

To characterize the memristive behavior of the NOMFET, we measure the change of its internal parameter $\delta Q_{NP}$ when voltage signal $V_{DS}(t)$ is a pulse of amplitude $V_P$ and duration 10 s. This value of 10 s has been fixed in order to maximize the effect of the NP charge. This time is longer than the typical charging/discharging time constants (about 2–3 s)[10] for a NOMFET with a channel length of 5 µm and 20 nm NPs used for these experiments. Reducing the width of the charging pulse will give smaller variations of the current, but does not change the conclusions. The output current, before ($I_{initial}$) and after ($I_{after}$) the application of the charging pulse, are measured with a short read pulse (100 ms). This pulse is short enough to not modify the charge state of the NPs. Plotting $(I_{after}-I_{initial})/I_{initial}$, which is proportional to $\delta Q_{NP} = Q_{NP}^{after} - Q_{NP}^{initial}$ (Eq. S24, Supporting Information), versus $V_P$ gives a representation of the g-function of the NOMFET. As the current at a given time t depends on the history of the device, we have developed a specific reset protocol (see Experimental Section, and Figure S1, Supporting Information) that sets the charge state of the NPs to the same $Q_{NP}^{initial}$ before each measurement at different $V_P$. Figure 2c shows the measured relative variation of the current (dots) as a function of $V_P$, i.e., the internal memristive-like function of the NOMFET. This function displays the three expected regions similarly to the resistance change in a voltage-controlled memristance:[8,9,17,18] i) For the negative voltage, the NPs are charged with holes, the Coulomb repulsion between the positively charged NPs and the OSC reduces the hole density in the conducting channel, the conductivity of the NOMFET is decreased. ii) For intermediate voltages ($V_{th1} < V < V_{th2}$), the effect of the input voltage on the charge state of the NPs is null. The charge state of the NPs cannot be changed. The physical meanings of the two threshold voltages, $V_{th1} \approx 0$ V and $V_{th2} \approx 15$ V, are discussed in the Supporting Information. iii) For large positive voltages, holes can be detrapped from the NPs, leading to a reverse effect, i.e., an increase in the conductivity of the NOMFET. The memristive $g$ function shown in Figure 2c can be calculated using Equation S31 (Supporting Information) considering the three parts of the experimental curve. For simplicity, we assume the same time constants in Equation S31 ($\tau = \tau_0 = \tau_+ = \tau_- = 5$ s). This value is in good agreement with experimental values for the NOMFET.[10,11] The squares in Figure 2c are the fit of this model. Equation S31 gives two linear relationships for the two branches that fit relatively well our data.

## 3. Spike-Timing Dependent Plasticity Behavior of the Nanoparticle–Organic Memory Field-Effect Transistor

In a previous report,[10] the STP (short-term plasticity) is obtained by virtue of the unbalanced charging (during the application of a pulse at the input terminal) and discharging (between two successive pulses at the input terminal) behaviors of the NPs, respectively. Here, as detailed below, we play with the same charging/discharging dynamics to modulate (i.e., increase or decrease) the amount of charges trapped in the NPs when two pulses are now applied, one at the input and one at the output terminals of the NOMFET separated by a given time interval, leading to the long-term depression (LTD) or long-term potentiation (LTP) behavior of STDP, respectively. More precisely, **Figure 3**a shows the two different shapes of the spikes that are applied to the NOMFET, in agreement with the spike shape suggested previously[8] (Figure 1c). These spikes are designed so that – when applied alone – they do not induce any significant variation of conductivity. It means that NPs charging and discharging are well balanced between the negative and positive parts of the spike, respectively. The integral of the negative part of the signal ($V < V_{th1} \approx 0$ V) is equal to the integral of the positive part $V > V_{th2} \approx 15$ V), Figure 3a. To facilitate the measurement with the probe-station, the postsynaptic spike (that must be applied to the $V_S$ terminal of the device) is inverted and applied to the $V_D$ presynaptic terminal. Thus, the effective signal (Figure 3b) applied to the $V_D$ terminal becomes equivalent to the application of the presynapse spike at the $V_D$ terminal and the postsynapse spike at the $V_S$ terminal (as a feedback). We check in section 4 that this procedure gives the same results as if we had applied the pre- and postsynaptic pulses directly to each of the two terminals. Note that the postsynaptic shape (Figure 3b) is slightly different from the presynaptic one to take into account the asymmetry of the memristive $g$ function of the NOMFET (Figure 2c).

In a first stage, the presynapse spike is applied alone at the input terminal of the NOMFET. This step is crucial to verify that the presynapse spike alone does not change the conductivity of the NOMFET. In a second stage, we apply the pre- and postsynaptic spikes with a fixed time shift $\Delta t$ between them (Figure 3b). The spikes have a frequency of 0.1 Hz and the conductivity of the NOMFET is read with a short pulse (100ms) synchronized with the spike sequence and applied 1s after the end of the pre-/postsynapse spike sequence (Figure 3b). The superposition of the pre- and postsynaptic spikes leads to an effective voltage across the NOMFET (bottom Figure 3b) in which the positive and negative contributions are no longer equal. This unbalanced contribution allows reproducing the basic principle of the STDP (Figure 3c). i) When the presynaptic neuron fires alone, the weight of the synapse is not changed. In the first part of Figure 3c (labeled "No postspike"), 10 presynaptic spikes are applied alone to the NOMFET. The conductivity of the NOMFET remains in its initial state. ii) When a presynaptic spike is correlated with a postsynaptic spike, the conductivity of the NOMFET is increased (Figure 3c labeled "With postspike", $\Delta t = +2$ s, 13 correlated spikes) due to the more important contribution of the positive part of the effective voltage across the NOMFET (i.e., the NPs are progressively discharged). The

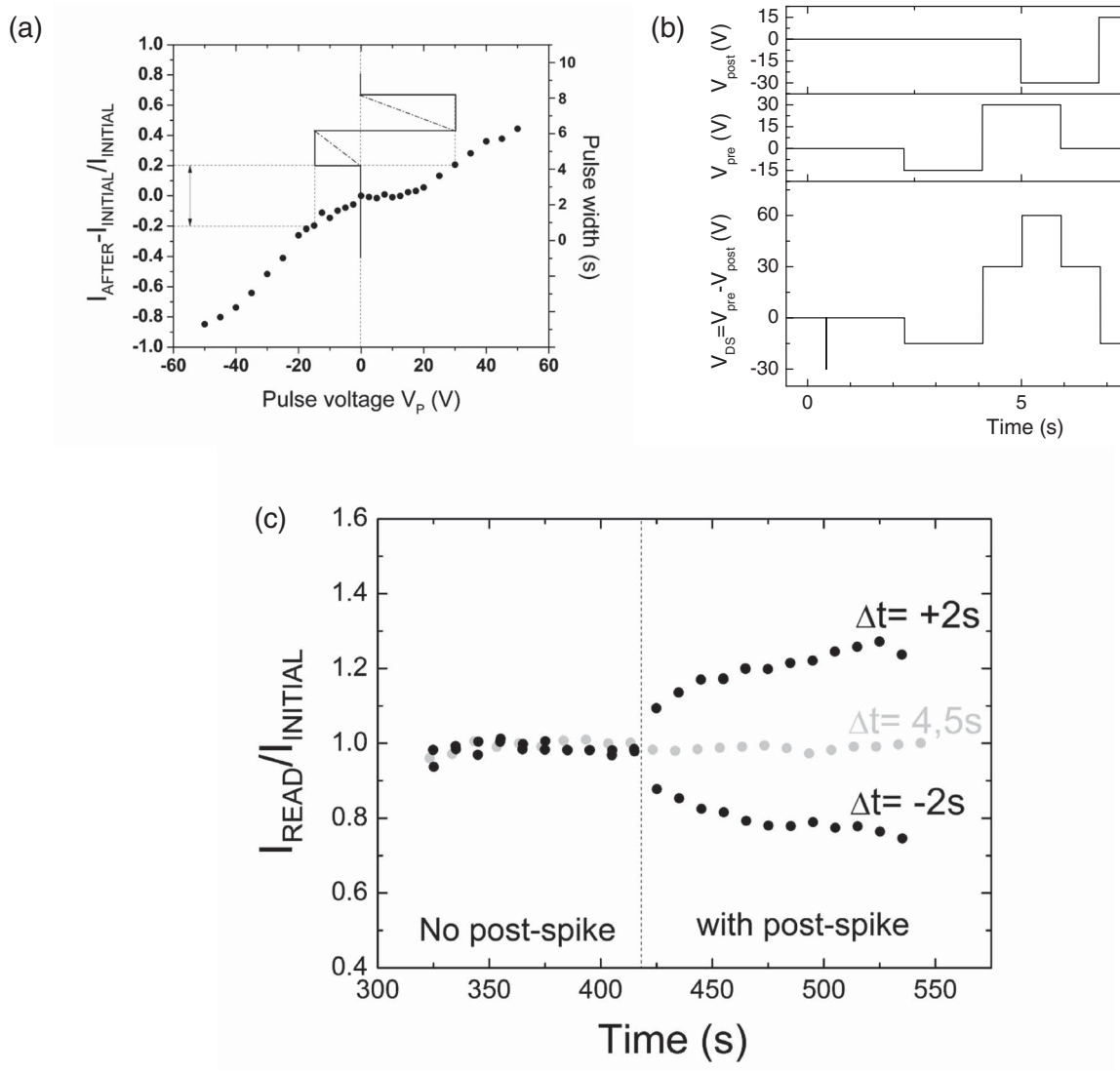


**Figure 3.** a) The two different pulses used to reproduce the STDP: square signal (solid lines), triangular signal (dash-dot line). In the case of the presynaptic pulse, the effect of the negative part, $V^- = -15$ V for 2 s, on the conductivity is equal to the effect of the positive part of the pulse, $V^+ = 30$ V for 2 s. b) Pre- and postsynaptic pulses superposition: the effective potential across the device is $V_{PRE}$- $V_{POST}$ (in this case, $\Delta t$ is 3 s). Note that the postsynaptic pulse is $V^- = -30$ V and $V^+ = 15$V to take into account the asymmetry of the memristive $g$ function of the NOMFET. In this situation, the effect of the postsynaptic pulse alone on the conductivity is null. c) Typical STDP measurement. First, 10 presynaptic pulses are applied alone at 0,1 Hz in order to verify that the conductivity is not changed by the presynaptic signal alone. Next, 13 pre- and postsynaptic pulses are applied with 3 different $\Delta t$ values.

synaptic weight is reinforced. iii) When the post- and presynaptic neuron spikes are anti-correlated ($\Delta t = -2$ s), the conductivity decreases, the contribution of the negative potential part dominates and the NPs are gradually more charged. The weight of the synapstor is depressed.

The same data are plotted as $\Delta I/I$ versus $\Delta t$ curves (STDP learning curve) in **Figures 4**a and b for a sequence of 12 successive triangular and square spikes, respectively. Figure 4a (triangular spike) qualitatively looks like the one reported by Bi and Poo[4] for a biological synapse, by other groups with inorganic devices[13–16] and Linares-Barranco et al.[8,9] for simulations on memristors, i.e., a more or less sharp STDP function as shown in Figure 1c (right upper corner). Results in Figure 4b obtained with a rectangular spike show that the shape of the STDP learning window can be modulated successfully by changing the shape of the pulses, in good agreement with the behavior predicted by Linares-Barranco for a memristive device[8,9] (Figure 1c). Recent results on synapses based on phase change memory also showed experimentally that it is possible to change the shape of the STDP curves, albeit with a much more complicated sequence of spikes in this case.[16] Now, we obtain a more "squared" or "rounded" shape for the NOMFET STDP function, comparable with the simulation (right-lower corner in Figure 1c). Our model reproduces the experiments with a good qualitative agreement (squares Figure 4) considering five different values for the charge/discharge time constants depending on the voltage (Equation S32 and S34, Supporting Information). These time constants $\tau_i$ ($-2 < i < +2$, Equation S34)

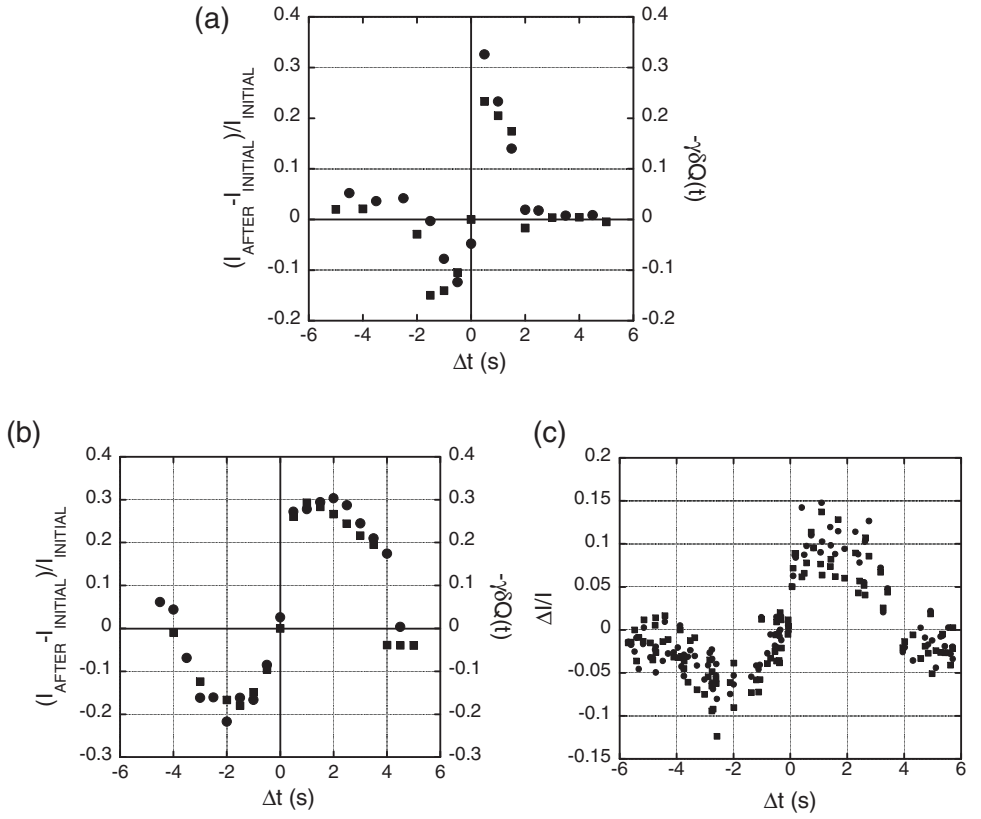


**Figure 4.** The relative variation of current is measured after 12 repetitions of the pre and post pulses pattern with a given $\Delta t$ (as described in Figure 3b). The dots correspond to the experimental measurement $(I_{after} - I_{initial})/I_{initial}$ and the squares are the model calculation – $\gamma\delta Q_{NP}$ (see the Supporting Information). a) STDP function obtained with the triangle-shape pulses. b) STDP function obtained with the square-shape pulses. c) STDP learning function acquired with the electronic-board for two NOMFETs (dots and squares) measured simultaneously.

are in the range 0.3 to 5 s, in good agreement with previous measurements showing that the charging/discharging of the NPs follows a multi-time constant dynamics in this time-scale range (Figure S5 in the Supporting Information in Ref. [10]). Finally, we can note that the approximation used in Eq. S24 ($\gamma\delta Q_{NP} << 1$) is justified (see Figure 2c) at low bias and is reasonable for bias voltages in the range ± 30V used in the STDP experiments. Nevertheless, the model-experiment agreement seems not strongly affected when $\gamma\delta Q_{NP}$ approaches 1 at higher voltages. Finally, we note that the STDP amplitude (from –15% to 30%, Figure 4) is lower than for biological synapse (–40 to 100%) as reported by Bi and Poo,[4] however, our results are larger or similar to the ones reported by other groups.[13–16] We expect that these performances can be improved by a careful technology optimization, for instance, recent STDP results with phase change memory (PCM)[16] – a much more mature technology – reached a dynamic between –40 and 110%.

## 4. Hybrid Nanoparticle–Organic Memory Field-Effect Transistor/Complementary Metal Oxide Semiconductor System

Instead of using a single device connected to a probe-station, a more realistic demonstration of the STDP behavior of the NOMFET is obtained by interfacing these synapstors with a CMOS-based electronic board to emulate the neurons and generate pre- and postsynaptic spikes, which are now directly applied to the input and output of several NOMFETs. Several NOMFETs were mounted in a TO case and plugged on the electronic board (see Figure S2, Supporting Information). This board is driven by an FPGA and is remotely controlled by a PC (see details in the Supporting Information). Series of rectangular spikes, identical to those used for the previous measurements, are applied simultaneously to two NOMFETs, with a randomly generated time interval $\Delta t$ between the pre- and postsynaptic spikes. The output currents of these NOMFETs are acquired with the electronic-board (see Figure S2, Supporting Information). The $\Delta I/I$ versus $\Delta t$ measured simultaneously for two NOMFETs are shown in Figure 4c. The STDP function obtained with this NOMFET/CMOS system is in good agreement with the one measured point-by-point for a NOMFET connected with the probe-station as shown in Figure 4b. In addition this is, to the authors' best knowledge, the first actual implementation of STDP on a dynamic device that meets the following conditions: i) The correct behavior is achieved regardless of the initial state of the device, as the timing between the pre- and postsynaptic spikes is random between each measurement (the same STDP behavior, Figure 4c, has been obtained here with random $\Delta t$, while the data shown in Figures 4a and 4b have

been recorded for a linear sequence of $\Delta t$ from –5 to +5 s). ii) The behavior remains consistent and very well reproducible regardless of the characteristics of the devices. Indeed, there is a factor 10 in the mean conductivity ratio between the two NOMFETs used in Figure 4c and yet the relative change in conductivity is the same for the two devices, i.e., the variability on the dynamical behavior of the NOMEFT is very low. This behavior is due to the fact that the STDP is based on a temporal coding, and only the relative variation of the NOMFET conductivity obtained through the applied pulses, and the natural relaxation of the NPs, impose the dynamics. This means that with STDP, we have a reliable way of programming conductivity changes using temporal information coding with seemingly unreliable devices. As a consequence, STDP and NOMFET can be useful to implement some learning algorithms in neural network circuits without to pay too much attention to some common variability sources, such as physical dimensions, reproducibility and control of the technological steps.

## 5. Behavioral Macromodel for Neuroinspired Circuit Simulation

The physical model developed for such a diode-connected NOMFET (**Figure 5**a) is implemented in *Spectre-Cadence*[19] for simulating neuroinspired circuits using STDP and NOMFET. The NOMFET device can be described behaviorally using the macro model circuit shown in Figure 5b. The terminal drain and source voltage $V_D$ and $V_S$ are copied to an internal diode in series with a resistor, attenuated by a scaling factor $\alpha$. This is to adapt the operating voltage (few tens of volts) of the NOMFET to a regular silicon diode used in CADENCE. The current through the diode $i_{ds0}$ is sensed and copied to the bottom input of element $m()$. Element $m()$ computes the following function:

$$m(i_{ds0}, w) = Ai_{ds0}e^{-w/w_0} \quad (3)$$

where $w$ is a circuit variable (a voltage) that describes the evolution of the charge in the NPs, $w(t)$ is proportional to $\delta Q_{NP}(t)$ (Equation S36 in the Supporting Information). Internal voltage $w$ is generated by feeding a resistor $R$ and a capacitor $C$ with a current source of value $-C\rho(V_{DS})$. The time constant in eqs. (S35–S39) is such that $\tau = RC$. This way this circuit implements Equation S38. This macromodel is used to simulate the behavior of the NOMFET when stimulated by a signal such as the one shown in Figure 2b, a pulse $V_P = -35$ V during 10s. By holding $V_S = 0$ and applying a negative –35 V pulse during 10 s at $V_D$, we obtain the signal evolutions shown in Figure 5c. The different parameters were optimized to best fit the measured $I_{DS}$ signal in Figure 2b: $\tau = 2.2$ s ($C = 1$ F, $R = 2.2\ \Omega$), $A = 10^{-6}$, $R_d$ the diode resistance = 20 kΩ, $V_{th} = 15$V, $w_0 = 0.16$V and $\alpha = 0.1$. The internal diode is described by $i_{ds0} = I_{d0}e^{V_{diode}/U_T}$ where $U_T = kT/q$ is the thermal voltage (≈ 26mV) and $I_{d0} = 8 \times 10^{-20}$ A. Simulated results in Figure 5c are in very good agreement with the experiments (Figure 2b). Again, note that the fitted time constant is in good agreement with experimental values for the NOMFET as reported elsewhere.[10] These results validate the macromodel that can be further used to simulate neuroinspired circuits using STDP learning rules.

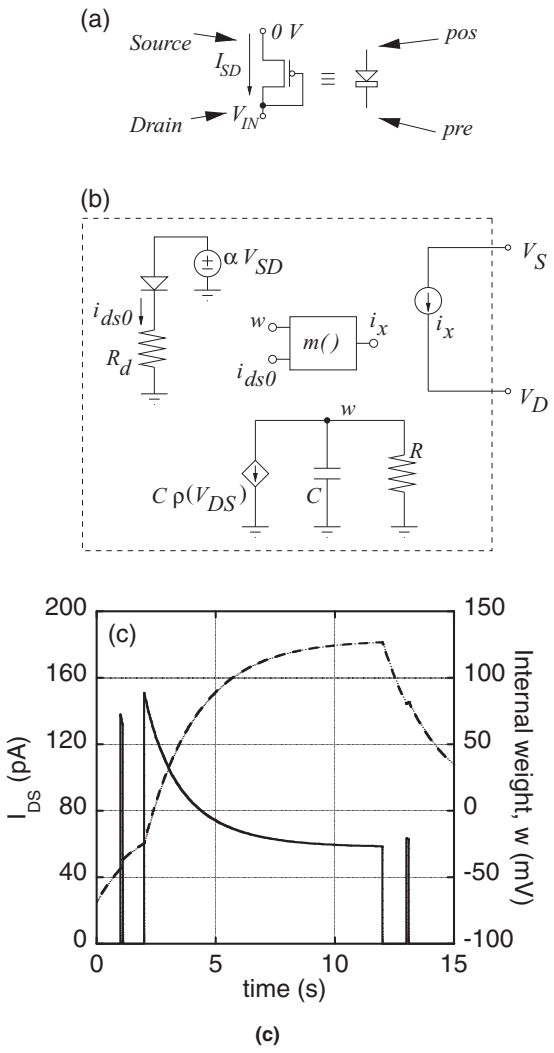


**Figure 5.** a) The NOMFET is a p-type FET, it is used in a diode-like connected configuration. Source S is the top terminal, drain D is the bottom terminal. $I_{DS}$ is either zero or positive. It is equivalent to a diode. When used as an STDP synapse (see Figure 2a), bottom terminal is the presynaptic connection and top terminal is the postsynaptic connection. b) NOMFET macromodel implemented in *Spectre-Cadence*.[19] c) Simulation of the NOMFET with the macromodel: output current (solid line, left scale) and evolution of the internal weight parameter $w$ (dashed line, right scale).

## 6. Discussion and Conclusion

Finally, we can notice that the potentiation (depression) reported here for the correlated (anticorrelated) spikes resembles that of a biological synapse (albeit with spike signals adapted to the NOMFET for which the physical mechanisms responsible for the STDP behavior are clearly different from the ones in a biological synapse) as reported by Markram et al.[3] and by Bi and Poo,[4] while at different time scales due to the different internal dynamics of the two systems. We have already demonstrated that NOMFET with a smallest channel length ($L$ = 200 nm, and 5 nm NPs), working at a lower voltage (–3 V) exhibit neuroinspired short-term plasticity (STP) with smaller time constants (~1 s, see Figure 6c in Ref. [10]), while with a

weaker amplitude.[10] So we believe there is room to improve the neuroinspired behavior of these synapstors and their future use in neuroinspired computing circuits and architectures. For instance, the actual low time scale response of NOMFET can be ascribed to two features. i) The fist one is the low charge/discharge time constants of the NPs, which are capped by alkyl chains (see the Experimental Section) acting as tunnel barrier. ii) The relatively low mobility of charges in the pentacene/NP channel,[10] which reduces the functioning speed of the device. Improvements (i.e., shorter time-scale, closer to the one of a biological synapse) can probably be attainable by changing the nature of the NP capping molecules (e.g., using more conducting $\pi$-conjugated molecules), and/or optimizing the deposition/nature of the organic semiconductor to increase the charge-carrier mobility.

## 7. Experimental Section

*Device Fabrication*: The synapstors are made on a highly doped (~$10^{-3}$ Ω.cm) p-type silicon covered with a thermally grown 200 nm thick silicon dioxide. After a usual wafer cleaning (sonication in chloroform for 5 min, piranha solution ($H_2SO_4/H_2O_2$, 2/1 v/v) for 15 min – *caution: the preparation of the piranha solution is highly exothermic and reacts violently with organics*, ultraviolet ozone cleaning (ozonolysis) for 30 min), we evaporated titanium/gold (20/200 nm) electrodes, patterned by optical lithography and lift-off. To attach the NPs, the gold (Au) electrodes were functionalized with a 2-amino ethanethiol molecules (10 mg $mL^{-1}$ in ethanol) during 5 h. After rinse (isopropanol) and subsequent drying in argon stream, the $SiO_2$ surface was functionalized at 60 °C during 4 min by 3-aminopropyl trimethoxysilane (APTMS) molecules (from ABCR) at 1.25 µL $mL^{-1}$ (in anhydrous toluene).[21] The reaction took place in a glove-box (MBRAUN) filled with nitrogen (less than 1 ppm of oxygen and water vapor). We removed non-reacted molecules by rinse in toluene, and then in isopropanol under sonication, and the samples were dried under argon stream. This sample was then dipped in an aqueous solution of citrate-stabilized Au-NP (colloidal solution purchased from Sigma–Aldrich, 20 ± 3 nm in diameter) overnight under argon atmosphere, followed by cleaning with deionized water and isopropanol, and drying under argon stream. NP concentration in the solution and duration of the reaction are selected from our previous work to have a NP density on the surface of about $10^{11}$ NP $cm^{-2}$ that gives the best results for the synaptic behavior of the NOMFET.[10] Then, the Au-NPs were encapsulated by dipping in a solution of 1,8-octanedithiol (from Aldrich) in ethanol (10 µL $mL^{-1}$) during 5h. The sample was finally rinsed in alcohol and dried in argon stream. The device is completed by evaporating (substrate kept at room temperature during the evaporation) 35 to 50 nm thick of pentacene at a rate of 0.1 Å $s^{-1}$ More details on the structural characterizations of the NPs networks and pentacene films (SEM, AFM,…) have been provided previously.[10]

*Electrical Measurements*: The NOMFET were contacted with a micromanipulator probe station (Suss Microtec PM-5) inside a glove box (MBRAUN) with controlled nitrogen ambient (less than 1 ppm of water vapor and oxygen). Such a dry and clean atmosphere is required to avoid any degradation of the organics. The input spikes were delivered by an arbitrary waveform generator (Tabor Electronics 5062) remote controlled by a PC. The pulse and spike sequences were designed with Matlab. The output currents were measured with an Agilent 4155C semiconductor parameter analyzer.

*Reset Potocol*: The reset signal is based on the same principle than the one used to remove the permanent magnetization of a magnet. We impose a decreasing sinusoidal input voltage (see Figure S1, Supporting Information) with a large period and a large initial voltage (the period and initial voltage must be large enough in comparison to the input voltage used during the operation/characterization of the device). The NPs are alternatively charged and discharged with a decreasing magnitude. Even if this initial state of charge of the NPs is different from the virgin state of charge of the NPs (i.e.,in the as-deposited state), it allows starting a specific measurement from the same initial condition.

## Supporting Information

Supporting Information is available from the Wiley Online Library or from the author.

## Acknowledgements

This work was funded by the European Union through the FP7 Project NABAB (Contract FP7-216777). We thank D. Guérin, K. Lmimouni, S. Lenfant (CNRS-IEMN) for help and advises during the device fabrication, and D. Querlioz (CNRS-IEF) for helpful discussions.

Received: August 17, 2011
Revised: October 24, 2011
Published online:

[1] D. Hebb, *The Organization of Behavior*, Wiley, New York **1949**.
[2] K. Gant, C. Bell, V. Han, *J. Physiol. Paris* **1996**, *90*, 233.
[3] H. Markram, J. Lubke, M. Frotscher, B. Sakmann, *Science* **1997**, *275*, 213.
[4] G. Q. Bi, M. M. Poo, *J. Neurosci.* **1998**, *18*, 10464.
[5] J. Sjöström, W. Gerstner, *Scholarpedia* **2010**, *5*, 1362.
[6] G. S. Snider, *Proc. IEEE ACM Int. Symp. Nanoscale Architectures* **2008**, 85.
[7] D. B. Strukov, G. S. Snider, D. R. Stewart, R. S. Williams, *Nature* **2008**, *453*, 80.
[8] B. Linares-Barranco, T. Serrano-Gotarredona, *Proc. 9th IEEE Conf. Nanotechnol.* **2009**, 601.
[9] C. Zamarreno-Ramos, L. Camuñas-Mesa, T. Serrano-Gotarredona, B. Linares-Barranco, *Front. Neurosci.* **2011**, **5**, 26.
[10] F. Alibart, S. Pleutin, D. Guérin, C. Novembre, S. Lenfant, K. Lmimouni, C. Gamrat, D. Vuillaume, *Adv. Funct. Mater.* **2010**, *20*, 330.
[11] O. Bichler, W. Zhao, F. Alibart, S. Pleutin, D. Vuillaume, C. Gamrat, *IEEE Trans. Electron Devices* **2010**, *57*, 3115.
[12] J. A. Varela, K. Sen, J. Gibson, J. Fost, L. F. Abbott, S. B. Nelson, *J. Neurosci.* **1997**, *17*, 7926.
[13] S. H. Jo, T. Chang, I. Ebong, B. B. Bhadviya, P. Mazumder, W. Lu, *Nano Lett.* **2010**, *10*, 1297.
[14] Q. Lai, L. Zhang, Z. Li, W. F. Stickle, R. S. Williams, Y. Chen, *Adv. Mater.* **2010**, *22*, 2448.
[15] K. Seo, I. Kim, S. Jung, M. Jo, S. Park, J. Park, J. Shin, K. P. Biju, J. Kong, K. Lee, B. Lee, H. Hwang, *Nanotechnology* **2011**, *22*, 254023.
[16] D. Kuzum, R. G. D. Jeyasingh, B. Lee, H.-S. P. Wong, *Nano Lett.* **2011**, DOI:10.1021/nl201040y.
[17] L. O. Chua, *IEEE Trans. Circuit Theory* **1971**, *18*, 507.
[18] M. Di Ventra, Y. V. Pershin, L. O. Chua, *Proc. IEEE* **2009**, *97*, 1717.
[19] Cadence Virtuoso platfom with Spectre simulator. Cadence Design Systems, Inc. www.cadence.com.
[20] J. Collet, O. Tharaud, A. Chapoton, D. Vuillaume, *Appl. Phys. Lett.* **2000**, *76*, 1941.
[21] D. F. Siqueira Petri, G. Wenz, P. Schunk, T. Schimmel, *Langmuir* **1999**, *15*, 4520.

ADVANCED FUNCTIONAL MATERIALS

# Supporting Information

for *Adv. Funct. Mater.*, DOI: 10.1002/adfm.201101935

# A Memristive Nanoparticle/Organic Hybrid Synapstor for Neuroinspired Computing

*Fabien Alibart, Stéphane Pleutin, Olivier Bichler, Christian Gamrat, Teresa Serrano-Gotarredona, Bernabe Linares-Barranco, and Dominique Vuillaume**

ADVANCED FUNCTIONAL MATERIALS

**Supporting Information**.

# A memristive nanoparticle/organic hybrid synapstor for neuro-inspired computing.

F. Alibart,[1] S. Pleutin,[1] O. Bichler,[2] C. Gamrat,[2]
T. Serrano-Gotarredona,[3] B. Linares-Barranco[3] & D. Vuillaume.[1]

*(1). Institute for Electronics Microelectronics and Nanotechnology (IEMN),*
*CNRS,*
*Avenue Poincaré, F-59652 Villeneuve d'Ascq, France.*
*(2). CEA, LIST, Embedded Computers Laboratory,*
*91191 Gif-sur-Yvette Cedex, France.*
*(3). Instituto de Microelectrónica de Sevilla (IMSE),*
*CNM-CSIC, Av. Americo Vespucio s/n,*
*41092 Sevilla, Spain.*

*E-mail : dominique.vuillaume@iemn.univ-lille1.fr*

## Supporting information.

### Theory

1- *Carriers number and source-drain current: effects of trapped charges in the nanoparticles*.

The charge transport in organic thin film is usually interpreted in terms of incoherent hopping of charges via localized states randomly distributed in space and in energy. A particularly simple theory within this line was proposed twenty years ago by Vissenberg and Matters (VM) [2]. The principle merit of their work is to provide simple analytic formula. The important point for us is to describe the changes in the conductivity and in the number of carriers induced by the charges trapped in the gold nanoparticles (NPs). In our previous work [1, 3], we have therefore extended the VM model to take account of these effects. We start to recall the main formula of Refs. [1-3], and then show that the NOMFET enters in the class of memristive devices defined by Chua [4, 5].

Due to disorder an organic thin film can be considered as an electrical network of quantum localized states with hopping transport from site-to-site. The energies of those states, ε (<0, below the vacuum level), are assumed by VM to be exponentially distributed

$$D(\varepsilon) = \frac{N_t}{k_B\theta_0}\exp\left(\frac{\varepsilon}{k_B\theta_0}\right) \quad \text{(S1)}$$

$N_t$ is the number of localized states per unit volume, $k_B\theta_0$ a measure of the energy width of the distribution ($k_B$, the Boltzmann constant). Each pair of sites, *i* and *j*, distant by $R_{ij}$ is connected by a bond with conductance $G_{ij}=G_0\exp(-S_{ij})$ where

$$S_{ij} = 2\alpha R_{ij} + \frac{\left|\varepsilon_i - \varepsilon_F\right| + \left|\varepsilon_j - \varepsilon_F\right| + \left|\varepsilon_i - \varepsilon_j\right|}{2k_B\theta} \quad \text{(S2)}$$

The first term takes account for usual tunnelling processes and the second for thermally assisted tunnelling. $\alpha$ is an effective overlap parameter, $\varepsilon_F$ the Fermi energy imposed by the electrodes and $\theta$ the temperature. Solving the percolation problem, VM found the conductance of the organic thin film [R1]

$$G = A_0\exp(\beta\varepsilon_F) \quad \text{(S3)}$$

where $\beta$=1/ $k_B\theta$ and $A_0$ is a dimensionless function of $N_t$, $\theta_0$, $\theta$ and $\alpha$. The charge carrier density at the organic semiconductor/dielectric interface is given by the following integral

$$N_P = \int_{-\infty}^{+\infty} d\varepsilon\, D(\varepsilon) f(\varepsilon,\varepsilon_F) \approx B_0 N_t \exp(\beta_0\varepsilon_F) \quad \text{(S4)}$$

where *f* is the Fermi-Dirac distribution, $\beta$=1/ $k_B\theta$, and $B_0$ is a function with no dimension of $\theta$ and $\theta_0$. The last equality is valid for low carrier density [R1].

When a gate potential is applied, an accumulation layer is formed at the interface between the film and the dielectric as discussed above (eq. [S4]), but charges are also stored in the NPs. We note $Q_P(t)$ and $Q_{NP}(t)$, the number of holes in the accumulation layer and in the NPs, respectively. $Q_P(t)=\Omega N_P(t)/e$, $\Omega$ is the volume of the thin film, *e* the elementary charge. We write $Q_T(t)= Q_P(t) + Q_{NP}(t)$, the total number of holes. The charges $Q_P(t)$ and $Q_{NP}(t)$ interact via Coulomb interaction changing the site energies of the electrical network, ε. These modifications were modelled in Ref.

[R2] by a shift, up or down, depending on the sign of the charges, of the Fermi level by an amount of -$\Delta$. We wrote

$$G = A_0 \exp(\beta\varepsilon_F - \beta\Delta) \tag{S5}$$

for the conductance. In the same way, we can write

$$Q_P = \Omega/e \int_{-\infty}^{+\infty} d\varepsilon\, D(\varepsilon) f(\varepsilon,\varepsilon_F - \Delta) \approx \Omega/e \exp(-\beta\Delta) \int_{-\infty}^{+\infty} d\varepsilon\, D(\varepsilon) f(\varepsilon,\varepsilon_F) \tag{S6}$$

for the number of holes in the accumulation layer. The second equality is valid if $\beta\Delta$ << 1. Combining Eqs. (S4) and (S6), we get

$$Q_P \approx \Omega/e\, B_0 N_t \exp(\beta_0\varepsilon_F - \beta\Delta) \tag{S7}$$

Starting from Eqs. (S6) and (S7) we show in the following that the NOMFET is a memristive device as defined by Chua [R4,R5]. Since the NOMFET is used as a pseudo two terminal device, there is only one control parameter, $V_{DS}$, the potential applied between the source and gate/drain (these later connected together). When $V_{DS}$ is applied, both $Q_P(t)$ and $Q_{NP}(t)$ are changed. As a consequence, at time $t$, the drain-source current, $I_{DS}$, can be written as usual for memristive devices [R4,R5]

$$I_{DS}(t) = \sigma_0(V_{DS}) f(Q_{NP}(t)) V_{DS}(t) \tag{S8}$$

$\sigma_0$ is the conductivity of our device that includes the field effect. $f(Q_{NP})$ is the memristive function of the device that contains the effects of the charges trapped in the NPs [R4,R5]. $Q_{NP}(t)$ is the so-called internal parameter of the NOMFET. Based on our previous analysis, we write

$$f(Q_{NP}(t)) = e^{-\gamma Q_{NP}(t)} \tag{S9}$$

Comparing with Eq. (S5) we identify $\sigma_0(V_{DS}) = A_0 \exp(\beta\varepsilon_F(V_{DS}))$ and $\gamma Q_{NP} = \Delta\beta$ . We assume in the following that the $V_{DS}$ dependence in the second expression is uniquely due to $Q_{NP}$ and consider $\gamma$ as a constant. We note that $1/\gamma$ behaves as a capacitance times $k_B\theta$. We next simplify further Eq. (S8) considering the effect of the trapped charges as a perturbation: we write

$$I_{DS}(t) \approx \sigma_0(V_{DS})(1 - \gamma Q_{NP}(t)) V_{DS}(t) \tag{S10}$$

In the same way, starting from Eq. (S7) we do the following series expansion

$$Q_P(t) \approx \Omega/e\, B_0 N_t \left(1 - \beta_0\varepsilon_F - \gamma Q_{NP}(t)\right) \tag{S11}$$

Finally, we rewrite the second term showing explicitly the $V_{DS}$ dependence

$$Q_P(t) \approx \overline{N} - \eta(V_{DS})V_{DS}(t) - \gamma\overline{N}Q_{NP}(t) \quad \text{(S12)}$$

where $\overline{N} = \Omega B_0 N_t / e$ and $\eta$ is a function of $V_{DS}$ to be fitted on experiments. The term $\eta(V_{DS})V_{DS}$ models the Fermi level shift. The carrier density depends on the gate potential, as usual, but also on $Q_{NP}$ that shifts the Fermi level.

This model was already used to describe the facilitating and depressing synaptic behaviours of our device [R2]. It gives very good agreements with experiments but all the measurements were done at fixed $V_{DS}$. In the present work we need to consider explicitly the $V_{DS}$ dependence. Moreover, the time trajectory of $I_{DS}$ depends on the details of the charge/discharge dynamics of the nanoparticles that needs to be specified further.

2- *Dynamics of charge/discharge of the gold nanoparticle*.

We choose to describe the charge/discharge dynamics of the NPs by the simplest as possible kinetic equations

$$\begin{cases} \dot{Q}_{NP} = -k_{NP\to P}(V_{DS})Q_{NP} + k_{P\to NP}(V_{DS})Q_P \\ \dot{Q}_P = -k_{P\to NP}(V_{DS})Q_P + k_{NP\to P}(V_{DS})Q_{NP} + SQ_P(V_{DS}) \end{cases} \quad \text{(S13)}$$

The dot is for the time derivative. The rate coefficients, $k_{P\to NP}(V_{DS})$ - NP charging, and $k_{NP\to P}(V_{DS})$ - NP discharging, depend on the control parameter $V_{DS}$. The number of charges in the pentacene film is not constant but depends on $V_{DS}$ and on the number of charges trapped in the NPs, $Q_{NP}$. $SQ_P$ is the source term that gives the amount of positive charges created at time $t$ coming from source and drain electrodes. From Eq. (S12) we can deduce

$$SQ_P(V_{DS}) = -\eta(V_{DS})\dot{V}_{DS} - \gamma\overline{N}\dot{Q}_{NP} \quad \text{(S14)}$$

At fixed $V_{DS}$, once stationarity is reached the charge variables fulfil

$$\begin{cases} 0 = -k_{NP\to P}(V_{DS})Q_{NP}^{st} + k_{P\to NP}(V_{DS})Q_P^{st} \\ 0 = -k_{P\to NP}(V_{DS})Q_P^{st} + k_{NP\to P}(V_{DS})Q_{NP}^{st} \end{cases} \quad \text{(S15)}$$

with the condition

$$Q_T(t) = Q_T^{st} = Q_{NP}^{st} + Q_P^{st} \quad \text{(S16)}$$

meaning that the number of holes and their repartition between pentacene and particles are time independent. They however depend on $V_{DS}$. We get

$$Q_{NP}^{st}(V_{DS}) = \frac{k_{P\to NP}(V_{DS})}{k_{NP\to P}(V_{DS}) + k_{P\to NP}(V_{DS})} Q_T^{st}(V_{DS}) \tag{S17}$$

To characterize efficiently our device we systematically apply the same relaxation procedure described in the main text before any sequences of measurements. We assume then the device to be at equilibrium (or at rest). This state is characterized by $Q_{NP}^0$, $Q_P^0$ and $Q_T^0$ defined as $Q_{NP}^0 = Q_{NP}^{st}(0)$, $Q_P^0 = Q_P^{st}(0)$ and $Q_T^0 = Q_T^{st}(0)$. We then measure the variation of charges trapped in the NPs, $\delta Q_{NP}$, with respect to this reference state after various types of excitations described in the main text and below. This gives us a rational way to characterize our device.

If we suddenly switch on $V_{DS}$ just after the relaxation step the current reads

$$I_0 \approx \sigma_0(V_{DS})(1-\gamma Q_{NP}^0)V_{DS} \tag{S18}$$

This is the reference current at voltage $V_{DS}$. Out of stationarity, we write Eqs (S13) as

$$\dot{Q}_{NP} = -\left(k_{NP\to P}(V_{DS}) + k_{P\to NP}(V_{DS})\right)Q_{NP} + k_{P\to NP}(V_{DS})Q_T(t) \tag{S19}$$

with

$$Q_T(t) = Q_T^0 + \delta Q_T(t) = Q_T^0 - \gamma\overline{N}(Q_{NP}(t) - Q_{NP}^0) - \eta(V_{DS})V_{DS}(t) \tag{S20}$$

We then obtain a simple first order differential equation for $Q_{NP}$

$$\dot{Q}_{NP} = -\frac{1}{\tau(V_{DS})}Q_{NP} + \frac{1}{\tau_0(V_{DS})}Q_{NP}^0 - \eta(V_{DS})V_{DS}(t) \tag{S21}$$

where the characteristic time constants are

$$\begin{cases} \dfrac{1}{\tau(V_{DS})} = k_{P\to NP}(V_{DS}) + k_{NP\to P}(V_{DS}) + \gamma\overline{N}k_{P\to NP}(V_{DS}) \\ \dfrac{1}{\tau_0(V_{DS})} = k_{P\to NP}(V_{DS})\left(\dfrac{k_{P\to NP}(0) + k_{NP\to P}(0)}{k_{P\to NP}(0)} + \gamma\overline{N}\right) \end{cases} \tag{S22}$$

At $V_{DS}$=0, starting from an initial charge, Eq. (S21) gives an exponential relaxation. We have seen in Ref. [R2] that the charge relaxations of our device follow power laws that can be in general approximated by a single exponential but in a limited time interval. It is therefore clear that our

simple set of equations (Eqs. (S21) and (S22)) could only work in such limited time interval. For larger time window of observation, more sophisticated theory would be needed. It turns out that this simple modelling is sufficient for our purpose.

The complete determination of the rate coefficients implies a microscopic study of the hole tunnelling between pentacene and nanoparticles. This is a complex problem that goes far beyond the scope of the present study. Instead we apply series of reasonable approximations detailed below.

The first approximation concern the source term (Eq. (S14)) that is a key ingredient of the kinetic equation (Eqs. (S13)). It characterizes the amount of holes created at time *t* in the accumulation layer of the pentacene. The NOMFET, as all the organic thin film transistors, is not bipolar. It means that accumulations of holes or electrons are not equivalent and obey different properties: it is more difficult to accumulate electrons than holes. We decompose the source term in two different components: one for negative voltage (accumulation of holes) and one for the positive voltage (depletion of holes). Guided by our experimental results (see Fig. 2-c in the main text) – as it will be clear below - we assume that the depletion of holes becomes efficient only for voltages higher than a threshold, $V_{th}$. We write

$$SQ_P(V_{DS}) = -\left[\eta_-(V_{DS})\Theta(-V_{DS}) + \eta_+(V_{DS})\Theta(V_{DS}-V_{th})\right]\dot{V}_{DS} - \gamma\overline{N}\dot{Q}_{NP} \quad \text{(S23)}$$

introducing two new functions $\eta_-$ and $\eta_+$ for the negative and positive branches, respectively. $\Theta$ is the Heaviside function. Doing so we divide the voltage space in three regions: $V_{DS} < 0$, $0 < V_{DS} < V_{th}$ and $V_{DS} > V_{th}$.

The second set of approximations concern the $V_{DS}$ dependence of the rate coefficients. It is detailed in the next section.

### 3- *Comparisons with experiments.*

To characterize our device, starting from the reference point we apply sequences of pulses and consider

$$\frac{I_{DS}(t)-I_0}{I_0} = e^{-\gamma\delta Q_{NP}(t)} - 1 \approx -\gamma\delta Q_{NP}(t) = -\gamma(Q_{NP}(t) - Q_{NP}^0) \quad \text{(S24)}$$

which is approximately proportional to the changes of charges trapped in the NPs at time *t* after a particular history of the external parameter $V_{DS}$. Note that we assume that the trapped charges are small enough to have $\gamma\delta Q_{NP} \ll 1$. This will be check on the experiments (see main text, section 3). We

have applied three different types of signal: A single pulse (Fig. 2-b, main text) and two different sequences of spikes that differ by the shape of those spikes (Spike 1 - rectangular shape and Spike 2 – triangular shape, see Fig. 3-a, main text). In the following we detail the results that we obtain with our model to describe each of these experiments.

Single pulse experiments. This type of experiment gives an easy way to characterize our devices through the variations of the internal parameter. The current depends on three parameters: the amplitude, $V_{DS} = V_P$, and the width, $W$, of the pulse and on the final time, $t$, of the experiment where the final current is measured. We get

$$\frac{I(V_{DS},W,t)-I_0}{I_0} = e^{-\gamma\delta Q_{NP}(V,W,t)} - 1 \approx -\gamma\delta Q_{NP}(V_{DS},W,t) = -\gamma(Q_{NP}(V_{DS},W,t) - Q_{NP}^0) \quad \text{(S25)}$$

that can be written as

$$-\gamma\delta Q_{NP}(V_{DS},W,t) = \gamma\left[\tau(V_{DS})\eta(V_{DS})V_{DS} + Q_{NP}^0\left(1-\frac{\tau(V_{DS})}{\tau_0(V_{DS})}\right)\right]\left(1-\exp\left(-\frac{W}{\tau(V_{DS})}\right)\right)\exp\left(-\frac{(t-W)}{\tau(0)}\right) \quad \text{(S26)}$$

To go further, we need to specify the different functions of $V_{DS}$ appearing in the above expression. In a first approximation (Approximation 1), we simply neglect the voltage dependence in each region of $V_{DS}$ of the rate coefficients. This could be justified by the fact that the particles and the pentacene molecules involved in the tunnelling process are very close in space and so at approximately the same potential. We write

$$k_{\substack{NP\to P\\ P\to NP}}(V_{DS}) = \begin{cases} k^{-}_{\substack{NP\to P\\ P\to NP}}, V_{DS} < 0 \\ k^{0}_{\substack{NP\to P\\ P\to NP}}, 0 < V_{DS} < V_{th} \\ k^{+}_{\substack{NP\to P\\ P\to NP}}, V_{DS} > V_{th} \end{cases} \quad \text{(S27)}$$

To reproduce the data in the simplest way, the best strategy is to consider together with the above rate coefficients, the following source term

$$SQ_P = -\left(\eta_-\Theta(-V_{DS}) + \eta_+\Theta(V_{DS}-V_{th})\right)\dot{V}_{DS} - \gamma\bar{N}\dot{Q}_{NP} \quad \text{(S28)}$$

where $\eta_-$ and $\eta_+$ are constants to be determined. We must then assume also

$$\tau(V_{DS}) = \tau_0(V_{DS}) \quad \text{(S29)}$$

to avoid any discontinuity as function of $V_{DS}$ in the internal parameter. These approximations are equivalent to consider three different time constants

$$\tau(V_{DS}) = \begin{cases} \tau_-, V_{DS} < 0 \\ \tau_0, 0 < V_{DS} < V_{th} \\ \tau_+, V_{DS} > V_{th} \end{cases} \quad \text{(S30)}$$

The internal parameter takes then a particularly simple form

$$-\gamma\delta Q_{NP}(V_{DS}, W, t) = \begin{cases} \gamma\tau_-\eta_- V_{DS}\left(1-\exp\left(-\frac{W}{\tau_-}\right)\right)\exp\left(-\frac{(t-W)}{\tau_0}\right), & V_{DS} < 0 \\ 0, \quad 0 < V_{DS} < V_{th} \\ \gamma\tau_+\eta_+(V_{DS}-V_{th})\left(1-\exp\left(-\frac{W}{\tau_+}\right)\right)\exp\left(-\frac{(t-W)}{\tau_0}\right), & V_{DS} > V_{th} \end{cases} \quad \text{(S31)}$$

It gives two linear relations: one starting at $V_{DS}$=0 and the other at $V_{DS}$=$V_{th}$ that fit relatively well our data (see Fig. 2-c, main text). There are six parameters to optimize: $V_{th}$, $\tau_0$, $\tau_-$, $\tau_+$, $\gamma\eta_-$ and $\gamma\eta_+$. It is obvious that an infinite set of parameter values give the same proposed function. However $V_{th}$ is unambiguously fixed by the shape of the memristive function to $V_{th}$=15V. We choose to fix the characteristic time constants to reasonable values taken from experiments [1, 3] (typically $\tau_0$, $\tau_-$, $\tau_+ \approx$ 1-5s); the two remaining parameters are then uniquely determined, to fit the experimental curve (Fig. 2-c) to $\gamma\tau_-\eta_-$=1.7x10$^{-2}$ and $\gamma\tau_+\eta_+$=1.3x10$^{-2}$.

Spike 1 and Spike 2. Different sequences of pre- and post- synaptic spikes distant by a certain time interval $\Delta t$ are applied to the NOMFET. They allow us to evidence the STDP properties of our device. Two kind of spike are used that give different outcomes (Figs. 4-a and 4-b, main text). To get the corresponding STDP functions (Eq. (S24)), one has to solve the first order differential equation (S21) with the appropriate $V_{DS}(t)$: to each sequence of spikes with a given $\Delta t$ corresponds a particular $V_{DS}(t)$. We have then, as for the previous case, to specify the different functions of $V_{DS}$ that appear in Eq. (S21). Applying the simple Approximation 1 does not give good results especially for the spike 2. For spike 1 (rectangular), the tendency could be reproduced by choosing very long characteristic times ($\tau_0$, $\tau_-$, $\tau_+ \approx$ 1000s) but the amplitude of the response is then by far too low; for spike 2 (triangular), the response is totally inconsistent with the data. In a second approximation (Approximation 2), we do not consider the rate coefficients as simple constants in each voltage region (Eq. (S27)) but instead recognize that the voltage dependences could become important

above thresholds: $V_-$ and $V_+$ in the negative and positive region, respectively. These dependences are taken in the simplest way

$$k_{\substack{NP\to P\\P\to NP}}(V_{DS})=\begin{cases} k^{-2}_{\substack{NP\to P\\P\to NP}}, V_{DS}<V_- \\ k^{-1}_{\substack{NP\to P\\P\to NP}}, V_-<V_{DS}<0 \\ k^{0}_{\substack{NP\to P\\P\to NP}}, 0<V_{DS}<V_{th} \\ k^{+1}_{\substack{NP\to P\\P\to NP}}, V_+>V_{DS}>V_{th} \\ k^{+2}_{\substack{NP\to P\\P\to NP}}, V_{DS}>V_+ \end{cases} \quad \text{(S32)}$$

We consider with Eq. (S32) the corresponding source term

$$SQ_P=-\left((\eta_{-2}-\eta_{-1})\Theta(-V_{DS}+V_-)+\eta_{-1}\Theta(-V_{DS})+\eta_{+1}\Theta(V_{DS}-V_{th})+(\eta_{+2}-\eta_{+1})\Theta(V_{DS}-V_+)\right)\dot{V}_{DS}-\gamma\dot{Q}_{NP} \quad \text{(S33)}$$

These approximations are equivalent to consider five different time constants

$$\tau(V_{DS})=\begin{cases} \tau_{-2}, V_{DS}<V_- \\ \tau_{-1}, V_-<V_{DS}<0 \\ \tau_0, 0<V_{DS}<V_{th} \\ \tau_{+1}, V_+>V_{DS}>V_{th} \\ \tau_{+2}, V_{DS}>V_+ \end{cases} \quad \text{(S34)}$$

With this new set of approximation, the differential equation (S21) is decomposed in different pieces depending on the $V_{DS}$ amplitude, according to Eq. (S34), and then solved. We impose Approximation 2 to give the same result for the memristive function (Fig. 2-c, main text). During the fitting procedure, once the time characteristics are chosen the different $\eta$ constants are fixed by imposing the linear relations shown in Fig. 2-c (main text). Choosing $\tau_0$, $\tau_{-1}$, $\tau_{+1}$ = 5s, $\tau_{-2}$ = 1s and $\tau_{+2}$ = 0.3s for the characteristics time constants and $V_-$ = -25V and $V_+$ = 40V give the best fits shown in Figs. 4-a and 4-b (main text). With the same collection of parameters, the whole set of data is reasonably well fitted by Approximation 2.

**Reset Protocol.**

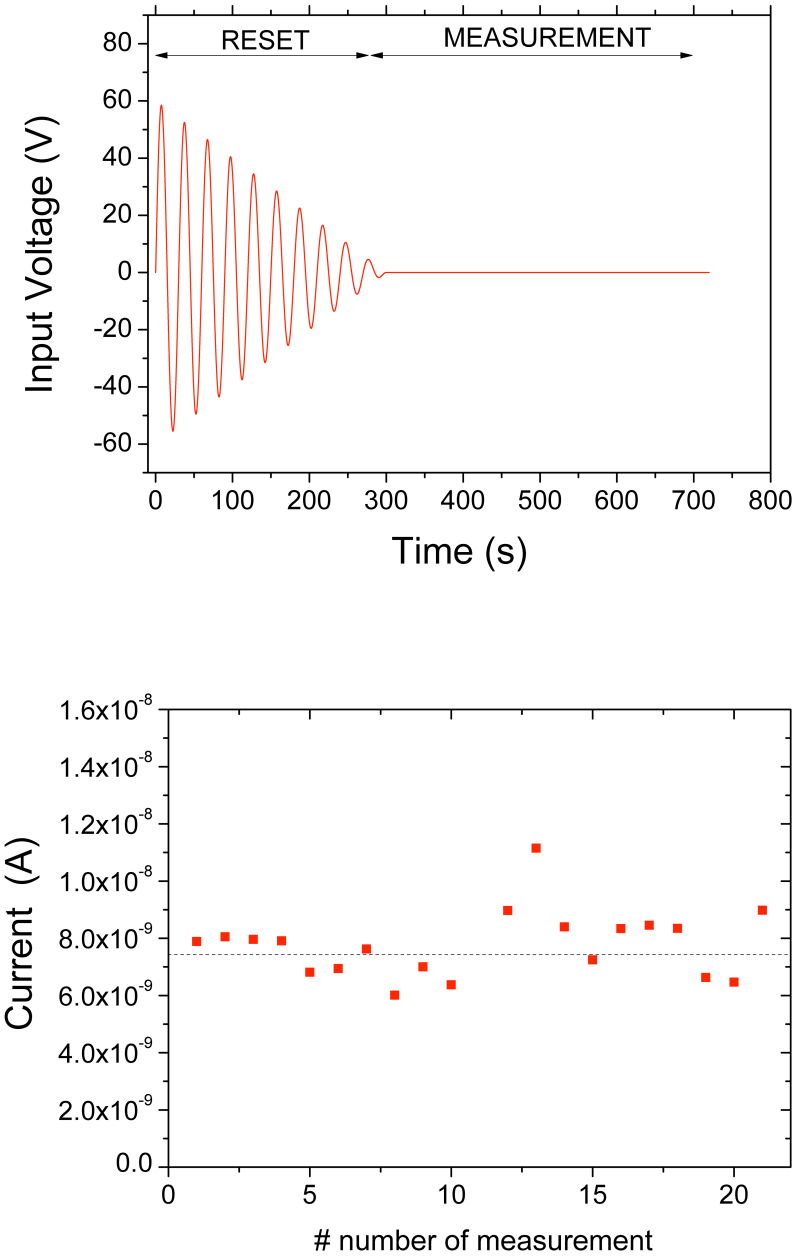


***Figure S1. (a)*** *Typical reset signal applied to the NOMFET to reset the same intial state (i.e. almost the same charge in the NPs and same output drain current) before each new SDTP measurements.* ***(b)*** *Typical drain current measured after the reset signal for more than 20 experiments.*

### Physical meaning of threshold voltages in curve 2-c (memristive function)

For VDS < Vth1, when the NOMFET is in its ON state, the NP charging mechanism is likely hole tunneling through the organic capping layer of the NP (typically alkylthiol, see Experimental section). This tunnel trapping can start as soon as holes are present in the OSC at the interface, since the turn-on voltage of the NOMFET is around 0 V (albeit with a large device-to-device dispersion, ± 5 V), it explains Vth1 ≈ 0 V. The slope of this part is about 1.7x10-2 (or 1/59) V-1. For V > Vth2, the OSC is in depletion, and the hole detrapping occurs probably through field-assisted emission. In that case, Vth2 relies on the minimum internal field required to overcome the energy barrier at the NP/OSC interface for charge detrapping. The slope of this part is about 1.3x10-2 (or 1/79) V-1. The difference in the slopes would indicate that tunneling trapping is more efficient than field-assisted detrapping in the present case. A detailed analysis of these charging/discharging phenomena in the NOMFET is beyond the scope of this paper and will require more voltage-dependent and temperature-dependent experiments.

### Electronic board for hybrid CMOS/NOMFET measurements.

Basically, the electronic board comprises three essential parts. 1) The pulse (Fig. S2-b) are generated with an analog multiplexer (MAX14752) which can wwitch voltages up to ± 36V). 2) The current is measured on board with an op-amp current-to-voltage converter (OPA445) supporting a large voltage up to ± 45V and having a low input bias current (ca. 10 pA), required to measure current down to the nA. It is followed by an analog-to-digital converter (ADC, model LTC1856) to obtain a digital value of the current. 3) This electronic board is fully controlled with a FPGA (Field Programmable Gate Array) board, which is driven by a PC.

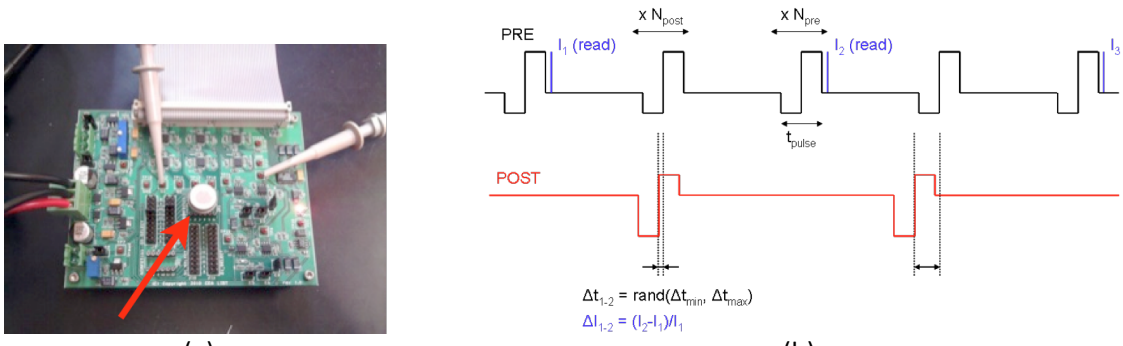


(a) (b)

**Figure S2.** ***(a)*** *Photography of the NOMFETs in a TO case (arrow) plugged on the electronic-board.* ***(b)*** *Typical spike signals applied at the input (pre-synaptic spikes) and at the output (pots-synaptic spike)*

*of the NOMFET for measing data shown in Fig. 4-c. For each Δt, a first sequence of $N_{pre}$ = 20 pre-synaptic spikes are applied before the conductivity is measured, followed by a sequence of $N_{post}$ = 20 pre-post spike interactions, after which the conductivity is measured again and compared to the previous one to obtain the change of conductivity. The pre-synaptic spike's duration is 4 s (-15 V during 2 s followed by 30 V during 2 s), as the post-synaptic spike (-30 V during 2 s followed by 15 V during 2 s).*

**Behavioral model equations.**

From Eqs. 1-2 and S9, S10, S21, S24, we can rewrite Eq. 1 and 2 as:

$$\begin{aligned} I_{DS}(t) &= \sigma_0(V_{DS}(t))V_{DS}(t)e^{-\gamma Q_{NP}(t)} \\ \gamma\tau\dot{Q}_{NP}(t) &= -\gamma Q_{NP}(t) - \gamma\tau\eta(V_{DS}(t))V_{DS}(t) \end{aligned} \quad \text{(S35)}$$

For macro-modeling convenience, let us define a circuit variable (a voltage) *w(t)* to describe the evolution of NP charges in the NOMFET:

$$w(t)/w_0 = \gamma Q_{NP}(t) \quad \text{(S36)}$$

where $w_o$ is a normalization constant that takes the value of 1*V*. Similarly, let us redefine the second right hand side term of bottom equation (S35) as a single function of the NOMFET terminal voltages as:

$$\rho(V_{DS}(t)) = \gamma w_0 \eta(V_{DS}(t))V_{DS}(t) \quad \text{(S37)}$$

As a result, eq. (S35) becomes

$$\begin{aligned} I_{DS} &= \sigma_0(V_{DS})V_{DS}e^{-w/w_0} \\ \frac{\tau\dot{w}}{w_0} &= -\frac{w}{w_0} - \frac{\tau}{w_0}\rho(V_{DS}) \end{aligned} \quad \text{(S38)}$$

The function $\rho(V_{DS})$ can be described by (see S31):

$$\frac{\tau}{w_0}\rho(V_{DS}) = \gamma\tau\eta(V_{DS})V_{SD} = \begin{cases} (V_{DS} - V_{th})\gamma\tau\eta^+ & , \quad V_{DS} > V_{th} \\ 0 & , \quad 0 < V_{SD} < V_{th} \\ V_{DS}\gamma\tau\eta^- & , \quad V_{DS} < 0 \end{cases} \quad \text{(S39)}$$

with $V_{th}$ = 15 V, $\gamma\tau\eta^+ \approx 0.013\ V^{-1}$ and $\gamma\tau\eta^- \approx 0.017\ V^{-1}$ as given after fitting Eq. (S31) to data of Fig. 2-c.

**REFERENCES**

[1] F. Alibart*, et al.*, "An Organic Nanoparticle Transistor Behaving as a Biological Spiking Synapse," *Advanced Functional Materials,* vol. 20, pp. 330-337, 2010.

[2] M. C. J. M. Vissenberg and M. Matters, "Theory of the field-effect mobility in amorphous organic transistors," *Phys. Rev. B,* vol. 57, pp. 12964-12967, 1998.

[3] O. Bichler*, et al.*, "Functional Model of a Nanoparticle-Organic Memory Transistor for Use as a Spiking Synapse," *IEEE Trans. Electron Devices,* vol. 57, pp. 3115-3122, 2010.

[4] L. O. Chua, "Memristor - the missing circuit element," *IEEE Trans. on Circuit Theory,* vol. 18, pp. 507-519, 1971.

[5] L. O. Chua and S. M. Kang, "Memristive devices and systems," *Proc. of the IEEE,* vol. 64, pp. 209-223, 1976.